

RESEARCH PROGRESS REPORT  
THE INTERACTION OF RADIATION WITH MATTER

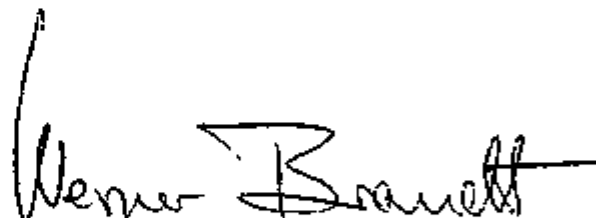
Submitted to  
DEPARTMENT OF ENERGY  
Division of Biomedical and Environmental Research

by  
Radiation and Solid State Laboratory  
Physics Department  
New York University

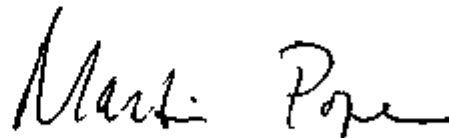
NOTICE  
This report was prepared as an account of work sponsored by the United States Government. Neither the United States nor the United States Department of Energy, nor any of their employees, nor any of their contractors, subcontractors, or their employees, makes any warranty, express or implied, or assumes any legal liability or responsibility for the accuracy, completeness, or usefulness of any information, apparatus, product or process disclosed, or represents that its use would not infringe privately owned rights.

for the period November 1, 1977 to October 31, 1978

PROJECT DIRECTORS:



Professor Werner Brandt, Director  
Radiation and Solid State Laboratory



Professor Martin Pope  
Associate Director  
Radiation and Solid State Laboratory

N O T I C E

This report was prepared as an account of work sponsored by the United States Government. Neither the United States nor the United States Department of Energy, nor any of their employees, nor any of their contractors, subcontractors, or their employees, makes any warranty, express or implied, or assumes any legal liability or responsibility for the accuracy, completeness, or usefulness of any information, apparatus, product or process disclosed or represents that its use would not infringe privately owned rights.

DISTRIBUTION OF THIS DOCUMENT IS UNLIMITED 

## **DISCLAIMER**

**This report was prepared as an account of work sponsored by an agency of the United States Government. Neither the United States Government nor any agency Thereof, nor any of their employees, makes any warranty, express or implied, or assumes any legal liability or responsibility for the accuracy, completeness, or usefulness of any information, apparatus, product, or process disclosed, or represents that its use would not infringe privately owned rights. Reference herein to any specific commercial product, process, or service by trade name, trademark, manufacturer, or otherwise does not necessarily constitute or imply its endorsement, recommendation, or favoring by the United States Government or any agency thereof. The views and opinions of authors expressed herein do not necessarily state or reflect those of the United States Government or any agency thereof.**

## **DISCLAIMER**

**Portions of this document may be illegible in electronic image products. Images are produced from the best available original document.**

This report presents highlights of our research during the period from 1 October 1977 to 30 September 1978. Our efforts in the elucidation of basic processes underlying the physics and chemistry of pollution have continued. Some of the new avenues have found their reflection in a separate research proposal now under evaluation.

This year emphasis is given to Professor Brandt's program of charged-particle penetration processes. Professor Pope's program will come under detailed review during the next period. The first part summarizes the work of Professor Brandt and his group. The second describes the work of Professor Pope and his colleagues.

Werner Brandt

Martin Pope

May 1978

LABORATORY PERSONNEL 1977-1978

Supervisors:

W. Brandt  
M. Pope

Faculty:

N. E. Geacintov  
R. Laubert

Research Scientists:

M. Arista  
S. Arnold  
M. El Hamamsy  
M. Khalifa  
G. Lapicki  
W. Losonsky  
K. Stanton

Research Assistants:

M. Binder  
F. Chen  
T. Flamer  
B. Fowlkes  
H. Hu  
D. Husiak  
D. Isaacson  
V. Ivanovic  
J. Khosrofian  
K. Kim  
M. Mourino  
T. Prusik  
S. Rudolph  
R. Schachter  
K. Slotvick  
S. Stern  
C. Strom

LABORATORY PERSONNEL (continued)

Technical Personnel:

E. Hesnault  
C. Peterson

Undergraduate Assistants:

D. Schwartzman

Secretarial Staff:

L. Bloom  
A. Loblack

Scientific Consultants:

J. Burgos  
H. Kallman  
R. Lophiemer  
A. Schwartzchild  
R. Selsby  
C. E. Swenberg  
N. Wotherspoon

Visitors:

J. B. Aladekomo  
R. H. Ritchie  
M. Silver

## ABSTRACT

- (1) Innershell Coulomb ionization cross sections show significant relativistic effects even for the lighter atoms, because ionization occurs near the nucleus in our range of low particle energies.
- (2) Atomic excitation and ionization in deep atom-atom collisions can be described in terms of a model with random walk in energy space to the continuum. This model may be best suited for the analysis of heavy ion-atom encounters.
- (3) Energy straggling of charged particles in matter are affected by inhomogeneities in and surface conditions of the medium.
- (4) Using molecular ions as incident projectiles we conclude that moving protons do not have bound states in solids. Projectiles in close proximity to each other exhibit larger energy losses than isolated projectiles indicating interactions of the electron density fluctuations established behind moving projectiles in solids.
- (5) Heterogeneous oxidation of  $\text{SO}_2$  by holes has been found at an organic (PAH) aqueous interface. The process has a reasonably high quantum efficiency ( $\approx 0.1$ ) for anthracene. Various experiments are being carried out to determine whether  $\text{SO}_3^-$  or  $\text{HSO}_3^-$  is involved.

- (6) Photoemission from PAH organic aerosols has been investigated. The rate of emission from tetracene is found to go as the maximum electron kinetic energy cubed. It is found that the particle may be used as an electron spectrometer for determining the electron kinetic energy distribution.
- (7) A new way of characterizing small aerosols by mass has been found. The method utilizes the detection of a single electron imbalance in a Millikan chamber. Aerosol masses as small as 1pgm can be measured to better than 1%.
- (8) The potent carcinogen benzo (a) pyrene (BP) when metabolized in vivo is found to have a physical structure in which the BP7,8-dihydrodial 9,10-oxide adduct (BPDE) is bound on the outside of the helix. Both structural models and physical measurements support this conclusion.



## TABLE OF CONTENTS

I.	INSTRUMENT DEVELOPMENT	1
II.	INNERSHELL EXCITATION	3
	1. Relativistic Effects	3
	2. Coulomb Deflection Effects	8
	3. Screening effect	11
	4. Pauli Excitation	14
III.	PENETRATION PHENOMENA	40
	1. Introduction	40
	2. Screening of Ions in Solids	40
	3. Cluster Penetration through Solids	57
	4. Stopping Power Maxima	68
	5. Projectile-Charge Dependence of Stopping Powers	72
	6. Effective Charge Theory of Stopping Powers	87
	7. Energy Straggling of Ions in Solids	121
IV.	INFORMAL WORKSHOP ON CURRENT STOPPING POWER PROBLEMS	136
V.	PUBLICATIONS	140
VI.	ORAL PRESENTATIONS	149

SECTION I  
HEAVY ION PHYSICS

## 1. Instrument Development (Laubert, Peterson)

The main research tool of the heavy ion physics program is the New York University heavy ion accelerator. During the past year the accelerator produced ion beams for 1749 hours which averages to more than 8 hours per working day. This indicates the importance of the accelerator in our research efforts as well as the small amount of "down" time of the facility.

To achieve such low "down" times preventive maintenance as well as availability of crucial components is required. In the past year the major components we had to replace were the high voltage power supplies for the ion source located in the dome of the accelerator and the main 6" oil diffusion vacuum pump. Both of these items have been in continuous operation for close to ten years and suffered many symptoms of old age.

In order for us to maintain our competitive advantage with respect to other accelerators in this energy domain we installed an accurate magnetic field measuring system. The new system consists of a nuclear magnetic resonance probe which allows us to measure the magnetic field to an accuracy of 1 part per  $10^5$ , which is two orders of magnitude better than we were able to achieve with our previous system employing a rotating coil gaussmeter.

A perpetual problem in accelerator experiments is the buildup of carbon on the target surface. Recently new diffusion pump fluids (Santovac 5 and Fomblin) have been developed that claim to be superior in preventing such buildup. We plan

to test these new fluids in actual working systems utilizing the method of observing the decrease in the characteristic x-ray yield with surface-layer buildup. Technological advances in cryogenic vacuum pumps have made these pumps reasonably priced. We plan to test this pumping system for carbon deposition if sufficient funds are available.

## II. Inner-shell excitation

### 1. Relativistic effects (Brandt, Lapicki)

As was noticed already a quarter century ago,<sup>1</sup> a relativistic description of inner shells is required, especially when heavy target atoms and slow collisions are considered. The relativistic effect has been investigated in the context of K-shell ionization<sup>2</sup>, but only a few plane-wave Born approximation<sup>3</sup> (PWBA) or straight-line semiclassical<sup>4</sup> (SCA) calculations for ionization cross sections were performed with relativistic wavefunctions during the intervening years. Various schemes were proposed to reproduce this effect without involved numerical calculations.<sup>5-11</sup> Following Hönl<sup>5</sup>, Merzbacher and Lewis<sup>6</sup> suggested that one may continue to employ the nonrelativistic screened hydrogenic wavefunctions but with a reduced value of the binding energy parameter  $\theta_S$  to correct for the relativistic increase in the binding energy of a screened hydrogen atom. It has been argued that the Merzbacher-Lewis reduction factor should be changed<sup>9,11</sup> to yield slightly lower values of  $\theta_S$ . Hardt and Watson<sup>7</sup> proposed instead to decrease the orbital velocity  $v_{2S}$  in accord with the relativistic expression for kinetic energy in the virial theorem.

Such approximate methods are, however, inadequate since they mimic the relativistic effect only by a change of the average quantities that characterize inner shells; they can reproduce numerical calculations with the relativistic wavefunctions only when  $v_1 \sim v_{2S}$  and the important impact parameters in the collision are comparable to  $a_{2S}$ . ( $v_1$  is the projectile

velocity and  $a_{2S}$  is the inner shell radius.) In slow collisions ionization takes place deeply inside of the inner shell where relativistic effects can be significant even for L-shells of relatively light atoms; they are underestimated by incorporating a relativistic change merely in the mean binding energy or velocity of the electron. Hansen<sup>8</sup> used the relativistic mass and velocity to approximate a relativistic electron velocity distribution that is used in the binary encounter approximation (BEA). It is not possible to apply this procedure straightforwardly in the PWBA. The Hansen correction, presented as a table of  $(\sigma_K^R/\sigma_K)^{BEA}$  for different projectile velocities and target atoms, still underestimates the relativistic effect in the slow collision regime when compared with  $(\sigma_K^R/\sigma_K)^{PWBA}$  when  $\sigma_K^R$  is based on the relativistic wavefunctions.

We proposed the procedure that simulates the relativistic PWBA cross sections through a substitution of mass of the electron  $M_e$  (equal to 1 in atomic units) by its relativistic value  $M_e^R$  evaluated at the distance at which ionization is most probable. In terms of the nonrelativistic  $\sigma_S^{PWBA}(\zeta_S\theta_S)$ , the relativistic PWBA cross section,  $\sigma_S^{PWBAR}$ , can be simply evaluated as

$$\sigma_S^{PWBAR} = \sigma_S^{PWBA}(M_e^R \zeta_S, \theta_S) / M_e^{R^2},$$

where  $\zeta_S = v_1 / \frac{1}{2} v_{2S} \theta_S$ .

Figures 1 and 2 demonstrate that this method agrees remarkably well with the numerical PWBA calculations which are based on the relativistic wavefunctions. Recently Amundsen et al.<sup>10</sup>

extracted various analytical factors to account for the relativistic effect in slow collisions. These factors were derived for K shell ionization and their use is restricted to the low velocities of the projectile where our procedure reproduces equally well the full, numerical calculation of Amundsen.<sup>4</sup>

#### References:

- 1) H. W. Lewis, B. E. Simmons, and E. Merzbacher, *Phys. Rev.* 91, 943 (1953); C. Zupancic and T. Huus, *Phys. Rev.* 94, 205 (1954).
- 2) P. D. Miller, Master thesis (Rice University, Houston, 1956) (unpublished); G. Basbas, *Bull. Am. Phys. Soc.* 13, 80 (1968) and Ph.D. thesis (North Carolina University, Chapel Hill, 1968) (unpublished); C. B. O. Mohr, *Adv. At. Mol. Phys.* 4, 221 (1968).
- 3) D. Jamnik and C. Zupancic, *K. Dan. Vidensk. Selsk. Mat.-Fys. Medd.* 31, No. 2 (1959); B.-H. Choi, *Phys. Rev. A* 4, 1002 (1971) and Proceed. Inter. Conf. Inner Shell Ionization Phenomena and Future Applications, Atlanta, 1972, ed. by R. W. Fink et al. (U.S. AEC, Oak Ridge, TN, 1973), p. 1093.
- 4) P. A. Amundsen, *J. Phys. B* 9, 971 (1976) 9, 2163 (1976) (E).
- 5) H. Hönl, *Z. Phys.* 84, 1 (1930).
- 6) E. Merzbacher and H. W. Lewis, in Hanbuch der Physik, edited by S. Flügge (Springer, Berlin, 1958), Vol. 34, p. 166.

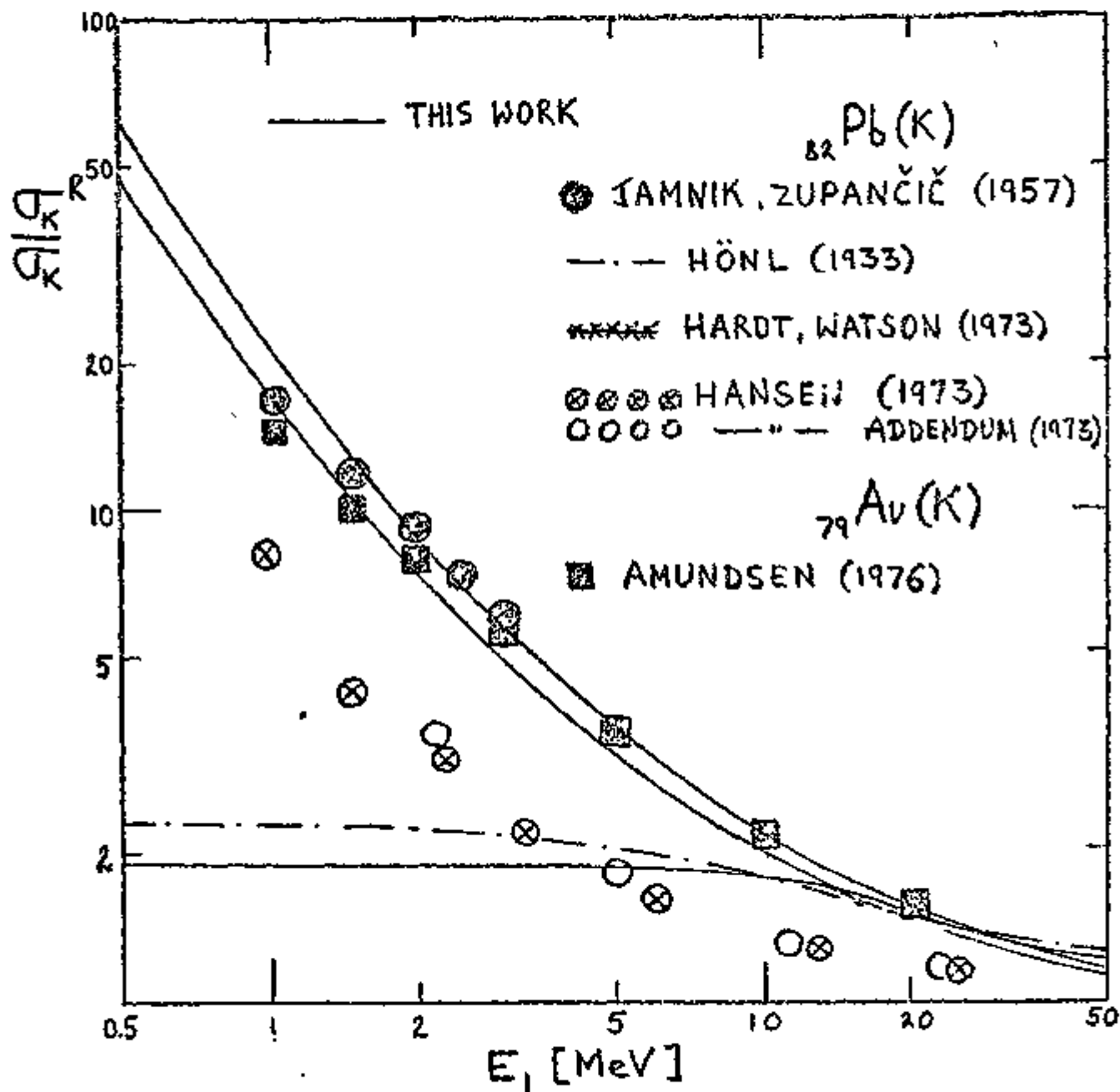


FIG. 1



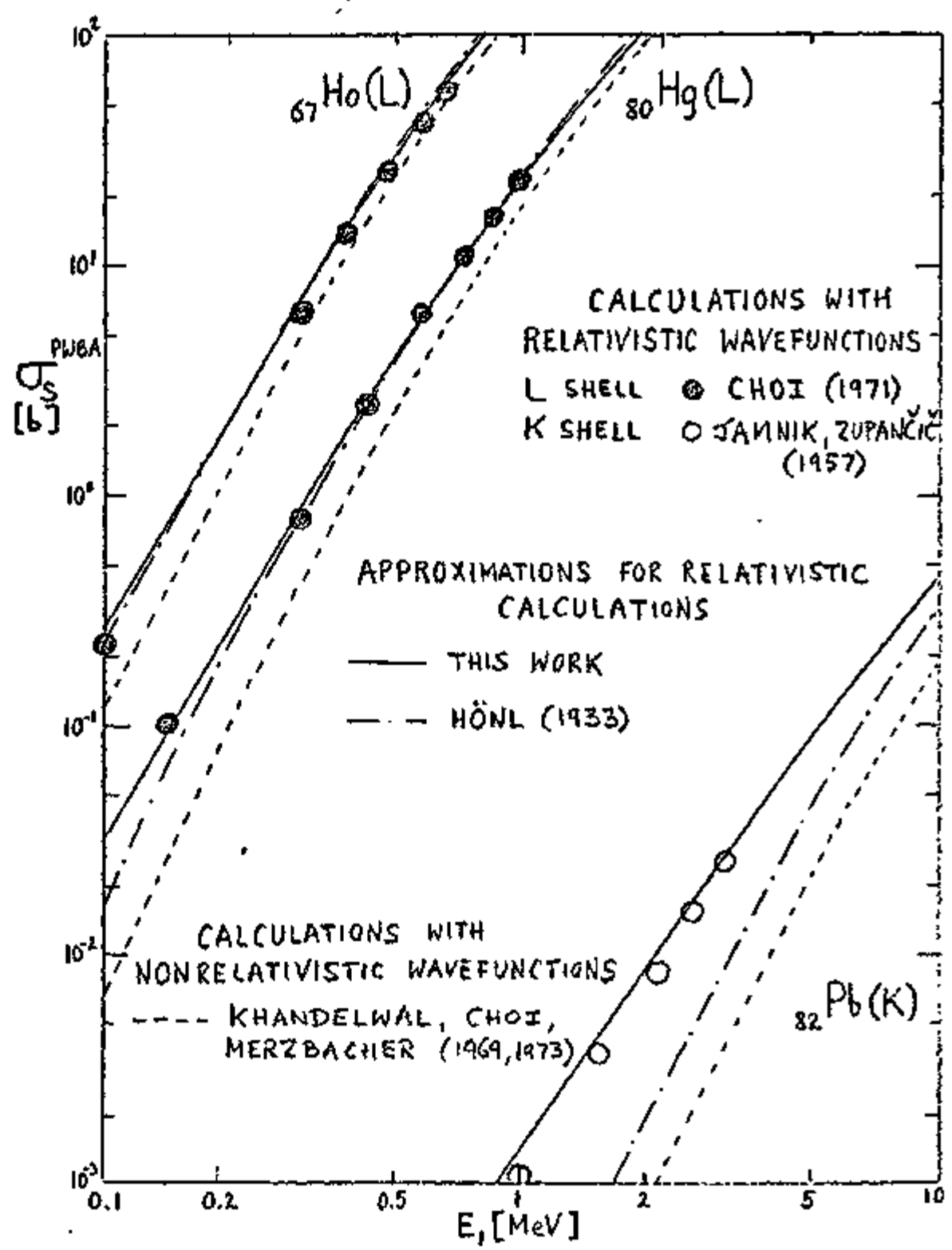


FIG. 2

- 7) T. L. Hardt and R. L. Watson, Phys. Rev. A 7, 1917 (1973).
- 8) J. S. Hansen, Phys. Rev. A 8, 822 (1973); Appendix (1973, unpublished).
- 9) G. Lapicki, Ph.D. thesis (New York University, New York, 1975). (unpublished).
- 10) P. A. Amundsen, L. Kocbach, and J. M. Hansteen, J. Phys. B. 9, L203 (1976) 9, 2755 (E).
- 11) E. Caruso and A. Cesati, Phys. Rev. A 15, 432 (1977).

## 2. Coulomb deflection effect (Brandt, Lapicki, Laubert)

Brandt et al.<sup>1-5</sup> extracted the Coulomb deflection factor

$$C = \exp(-\pi\zeta) \quad (1)$$

from the semiclassical treatment of Bang and Hansteen<sup>2</sup> for inner shell ionizations. Its validity has been questioned<sup>3</sup> and its values were found to be above recent numerical calculations<sup>4</sup> and analytical results.<sup>5</sup> Here  $\zeta \equiv dq_{0S}$  denotes the adiabaticity parameter which determines the ratio of the characteristic time in Coulomb scattering,  $d/v_1$ , to the transition time,  $1/(\omega_{2S} + E_f)$  with  $d = Z_1 Z_2 / Mv_1^2$  being the half distance of closest approach in a head on collision and  $q_{0S} \equiv \frac{\omega_{2S} + E_f}{v_1}$  the minimum momentum transfer for the ejection of electron of energy  $E_f$ .

The existing data cover the  $0 \leq \zeta \leq 0.9$  range and lie somewhat inconclusively between the new predictions for the Coulomb deflection factor and old ones according to Eq. (1), although

the latterd predictions seem to be favored by the data when the small and large values of  $\zeta$  from the experimental range of  $\zeta$  are considered. A particularly sensitive measure of the Coulomb deflection factor is offered when the ratio of ionization cross sections by deuterons to those by protons at the same velocity are taken at the highest possible values of  $\zeta$ .

We have measured this ratio in the 50-150 keV/amu range of proton/deuteron energies in L-shell ionization of silver which, at the lowest energy, corresponds to  $\zeta = 1.3$ . As seen in Fig. 1 the data agree with the Eq. (1) for  $\zeta = 1$ ; a result that appears to be disagree with recent predictions<sup>4,5</sup>. Studies of the Coulomb deflection effect are still needed, and the Coulomb deflection effect remains to be reexamined in the light of the disagreement between these prediction and experimental evidence.

- 1) W. Brandt, R. Laubert, and I. Sellin, Phys. Lett. 21, 518 (1966) and Phys. Rev. 151, 56 (1966); G. Basbas, W. Brandt, and R. Laubert, Phys. Rev. A 7, 783 (1973); W. Brandt and G. Lapicki, Phys. Rev. A 10, 474 (1974).
- 2) J. Bang and J. M. Hansteen, K. Dan. Vidensk. Selsk. Mat.-Fys. Medd. 31, No. 13 (1959).
- 3) K. Brunner, Ph.D. thesis (Würzburg University, Würzburg, 1972) (unpublished); K. Brunner and W. Hink, Z. Phys. 262, 181 (1973).
- 4) L. Kocbach, Physica Noyvegica 8, 187 (1976).
- 5) P. A. Amundsen, J. Phys. B 10, 2177 (1977).

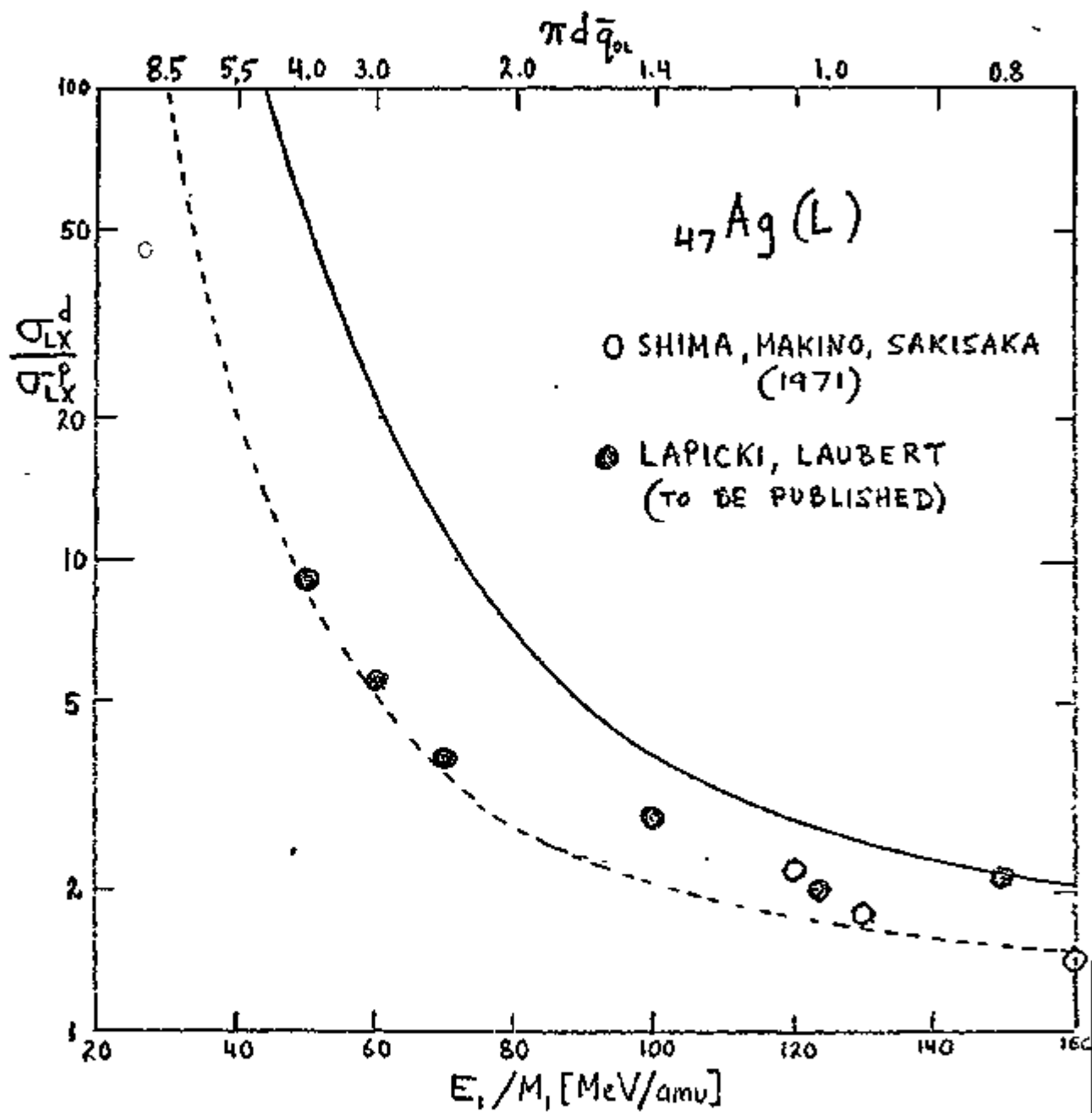


FIG. 1

### 3. Screening effects (Losonsky)

The effect of the projectile electrons in causing excitation or ionization of inner shells in heavy-ion collisions are usually neglected on the assumption that the relevant impact parameters are small compared to the shell radii of projectile electrons. However, even in Coulomb K-shell ionization when the projectile atomic number  $Z_1$  is much smaller than the target atomic number  $Z_2$ , screening effects on the cross sections as large as 10-20% have been calculated.<sup>1</sup>

We have investigated theoretically a system, excitation of 2p and 3p states of fluorine for  ${}_{18}\text{Ar} \rightarrow {}_{9}\text{F}^{+8}$  (where  $Z_1 = 2Z_2$ ), for which a large screening effect is expected. This system has the advantage that Auger data<sup>2</sup> are available for comparison. Thus we can accurately test our procedure for calculating screening effects.

The following assumptions are made:

- (1) Only Coulomb forces are considered in the scattering potential.
- (2)  $\Delta E / (2 \mu v^2) \ll 1$  where  $\Delta E$  is the difference in energy of the final and initial state of the target atom;  $\mu$  is the reduced mass and  $v$  is the relative velocity of projectile to target atom.
- (3) The transition amplitude is expanded in powers of  $1/M_1$  and  $1/M_2$ , keeping only the lowest-order term ( $M_1, M_2$  are the projectile and target atomic masses, respectively).
- (4) The wave function of the projectile atom can be represented by the product of one-electron screened-hydrogenic eigenfunctions.

(5) The first plane-wave Born approximation is used.

A general formula,<sup>3</sup> involving a single integral is obtained. This integral can be easily evaluated numerically. In Fig. 1 the results of our calculation are compared with experiment. The theory without screening disagrees with the data by a factor of 2.5; the theory with screening coincides with the data. This indicates that, at least for one-electron targets, the procedure outlined here can be used to account for even large screening effects. Attempts are now being made to extend our results to two-electron target systems.

- 1) G. Basbas in: Abstracts of papers, 9th Intern. Conf. on the Physics of electronic and atomic collisions, eds. J. R. Risley and R. Geballe (University of Washington Press, Seattle, 1975), p. 502.
- 2) F. Hopkins, R. Brenn, A. R. Whittmore, N. Cue, V. Dutkiewicz, and R. P. Chaturvedi, Phys. Rev. A 13, 74 (1976).
- 3) W. Losonsky, Phys. Rev. A 16, 1312 (1977).

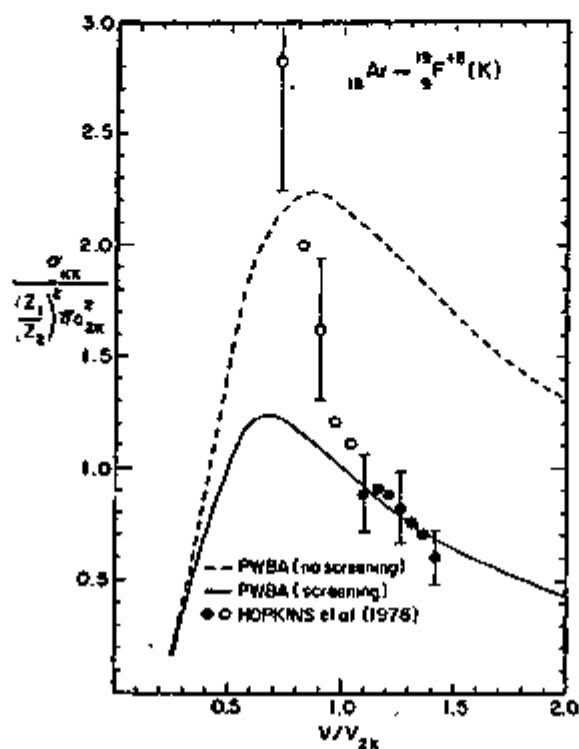


FIG. 1. Cross section  $\sigma_{KX}$  for K x-ray production in excitation of  $^{19}\text{F}^{+8}$  by neutral  $^{16}\text{Ar}$  bombardment, as a function of relative velocity  $v$ . The cross section is in units of  $(Z_1/Z_2)^2 \pi a_{KX}^2$  with  $a_{KX} = 1/Z_2$  being the fluorine K-shell radius in a.u.; relative velocity is in units of the fluorine K-shell velocity  $v_{2K} = Z_2$  in a.u. The data are taken from Ref. 1:  $\bullet$ , data for which electron capture by  $\text{F}^{+8}$  contributes less than or approximately equal to the error bar;  $\circ$ , data for which electron capture cannot be neglected. The PWBA theory without screening (---) scales in the plotted units; the full PWBA, including screening (—), cannot be scaled to a single universal curve. As discussed in the text, the calculations include excitation to  $2p$  and  $3p$  states only.

4. Pauli Excitation (Brandt with Johnson, Jones, Jundt, Guillaume, Kruse, BNL)

Measurements of the cross sections for production of characteristic x-rays in heavy-ion-atom collisions have been in progress for many years. Detailed knowledge of the systematics of these collisions as a function of projectile atomic number,  $Z_1$ , target atomic number,  $Z_2$ , and the laboratory kinetic energy of the projectile,  $E$ , derives from the production of K-shell x rays. Total K-vacancy cross section measurements have been made in several experiments of solid targets. Kubo et al.<sup>1</sup> reported target and projectile cross sections for  $_{28}\text{Ni}$  and  $_{35}\text{Br}$  beams as a function of  $Z_2$  at several projectile energies and observed strong variations in the cross section which are attributed to electronic shell effects. Meyerhof et al.<sup>2</sup> carried out similar experiments with beams of  $_{35}\text{Br}$ ,  $_{36}\text{Kr}$ ,  $_{53}\text{I}$ ,  $_{54}\text{Xe}$ , and  $_{82}\text{Pb}$  at energies up to 470 MeV. Cross sections at low energies were reported by Jones et al.<sup>3</sup>, for 5 MeV  $_{10}\text{Ne}$  and  $_{18}\text{Ar}$  beams. A common trend for given  $Z_1$  is the strong variation of total K-shell-vacancy production as a function of  $Z_2$ . Measurements of the probability,  $P_K$ , of vacancy production as a function of impact parameter,  $b$ , have been reported for relatively light ions and targets.<sup>4-6</sup> Recently, experiments by Johnson et al.<sup>7</sup> with a  $_{28}\text{Ni}$  beam on solid  $_{25}\text{Mn}$  and  $_{82}\text{Pb}$  targets and Cocke et al.<sup>8</sup> with a  $_{17}\text{Cl}$  beam on a gaseous  $_{18}\text{Ar}$  target have started to give information for ranges of higher  $Z_1$ ,  $Z_2$ , and  $E$  where total cross section measurements have been performed.

The mechanisms for vacancy production in atomic collisions are complex and can range between two limiting cases. On the one hand is the production of a K vacancy by direct Coulomb ionization caused by the



Coulomb field of a completely stripped projectile.<sup>9</sup> On the other is the vacancy production during the interaction of the electron clouds of the projectile and target atoms, Pauli excitation.<sup>10</sup> Under such conditions, the cross sections are usually much larger than direct Coulomb excitation cross sections.

A basis for the discussion of Pauli excitation is the molecular orbital (MO) model of Fano and Lichten.<sup>11,12</sup> It has been developed by Briggs and Macek<sup>13</sup> and by Taulbjerg et al.<sup>14</sup> to give detailed predictions of the impact parameter dependence of ionization probabilities, and of the scaling of the total cross sections. This approach requires specific assumptions about a few orbitals taken to be prevalent in a given collision. In collisions involving a large number of molecular-orbital crossings, the vacancy production can be studied in terms of a statistical model, first developed by Mittleman and Wilets<sup>15</sup> for total ionization. The statistical model has been applied by Brandt and Jones<sup>5</sup> to K-vacancy production. As is shown below, a simple development based on random-walk between level crossings illuminates the physical content of this approach. The statistical model is effective in representing differential and total cross section data on disparate collision systems in a concise manner.<sup>7,16</sup>

The present experiment was undertaken to extend the work of Johnson et al.<sup>7</sup> by measuring the impact-parameter dependent probability of inner-shell-vacancy production by 45-138 MeV  $^{28}\text{Ni}$  beams on  $^{25}\text{Mn}$ ,  $^{50}\text{Sn}$ , and  $^{82}\text{Pb}$  solid targets. The targets were chosen because corresponding total cross sections represent maxima (Mn, Pb) and a minimum (Sn) in the  $Z_2$  dependence of the Ni measurements of Kubo et al.<sup>1</sup> The experimental results are discussed in terms of the statistical model and are compared with predictions of the molecular orbital model.

## II. Experimental Procedure

Beams of  $^{58}_{28}\text{Ni}$  ions at 45, 94, and 138 MeV were obtained from the Brookhaven MP-tandem Van de Graaff accelerator facility with currents in the range of 1-10 nA/ion charge. The beam was collimated with two 0.25 mm diam apertures spaced 20 cm apart, followed by a 0.5 mm diam scraper slit at a distance of 6 cm, limiting the beam dispersion to at most  $0.15^\circ$ . Targets were prepared by vacuum evaporation of natural  $^{25}\text{Mn}$  and  $^{82}\text{Pb}$  in films of  $20 \mu\text{g}/\text{cm}^2$ , and  $^{50}\text{Sn}$  in films of  $100 \mu\text{g}/\text{cm}^2$  with uncertainties in target thickness of  $\pm 20\%$ , onto  $20 \mu\text{g}/\text{cm}^2$  carbon foils. They were positioned 8 cm downstream from the scraper slit and inclined at an angle of  $45^\circ$  to the beam direction.

After passing through the target material and the supporting carbon foil, the beam was stopped in a small Faraday cup mounted at the center of an annular particle detector. The cup current to ground was used for monitoring the accelerator operation. The particle detector consisted of a 0.5 mm thick annular collimator with inner radius 4.0 mm and outer radius 4.8 mm positioned in front of a silicon surface-barrier detector with a sensitive depth of 100  $\mu\text{m}$  and an active area of  $200 \text{ mm}^2$ . The mean scattering angle subtended by the annular collimator was varied by moving the detector assembly coaxially with the beam direction on a sliding shaft. At the minimum and maximum target-to-detector distances of 3.3 and 53 cm, particles were detected that had been scattered through angles  $(7.5 \pm 1)^\circ$  and  $0.5 \pm 0.1)^\circ$ , respectively. The range of accepted scattering angles resulted

in detection of scattered particles which had undergone collisions with the target atoms over a range of impact parameters approximately  $\pm 10\%$  of the calculated mean value. The solid angle of the detector was reduced at small distances by the finite thickness of the collimator rings for which corrections were made. The energy resolution of the surface barrier detector deteriorated with radiation damage, but the results of the experiment were insensitive to this resolution, as demonstrated in repeated runs with used and new particle detectors under otherwise equal conditions.

A liquid-nitrogen-cooled Si(Li) x-ray detector with an active area of  $80 \text{ mm}^2$  and an energy resolution of 200 eV for the 5.9 keV  $K\alpha$  line of Mn registered x-rays produced during the passage of the beam through the target. The  $25.4 \mu\text{m}$  beryllium window of the detector was directly coupled to the vacuum chamber at a distance of 2.5 cm from the target at  $90^\circ$  to the incident beam. A calibrated  $^{55}_{26}\text{Fe}$  x-ray source at the target position determined the value of the product of acceptance solid angle and detection efficiency for the x-ray detector at the 5.9 keV Mn  $K\alpha$  x-ray energy. Corrections were made for changes in the transmission of the Be entrance window for Ni, Sn, and Pb x-rays, and for Al absorbers placed between the detector and the Sn, and Pb targets to reduce the counting rate from radiative electron capture and low-energy L and M x-rays.

Signals from the preamplifiers of the x-ray and particle detectors were split to handle separately the circuitry for the x-ray and particle coincidences, and for the high-resolution energy spectra. The start and stop pulses for a time-to-pulse height converter were derived from timing filter amplifiers followed by constant-fraction timing discriminators.

Their levels were set to accept particles scattered in the target films and x-rays emitted from the projectile and target atoms. Coincident x-rays from projectile and target atoms were recorded through gates derived from the high resolution x-ray circuitry. A typical time resolution was 20 nsec for the 7.5 keV Ni K $\alpha$  x-ray.

The probability,  $P_K$  or  $P_L$ , for producing a K- or L-shell vacancy was calculated for each detector position from the relationship  $P = 4\pi N_C / (N_S \gamma \Omega_x \epsilon_x)$ , where  $N_C$  is the number of coincidences,  $N_S$  the number of scattered particles,  $\gamma$  the static fluorescence yield,<sup>17</sup> and  $\Omega_x \epsilon_x$  the solid angle-efficiency for the x-ray detector. The x-rays from the beam and target were taken to be emitted isotropically.

Although it was not the primary aim of the experiment, it was also possible to measure total vacancy production cross sections at each detector position. The agreement of these values with previous measurements<sup>1</sup> established the validity of the calibration for the absolute values of  $P_K$  and  $P_L$ . The cross sections,  $\sigma_K$  or  $\sigma_L$ , were calculated from the relationship  $\sigma = (4\pi N_x / N_S \gamma) (d\sigma/d\Omega)_S (\Omega_S \epsilon_S / \Omega_x \epsilon_x)$ , where  $N_x$  is the number of x-rays,  $(d\sigma/d\Omega)_S$  the appropriate cross section for scattering particles into the particle detector, and  $\Omega_S \epsilon_S$  the solid-angle efficiency for the particle detector. The mean values of  $\sigma$  obtained from this procedure are listed in Table I.

Data taken with bare carbon foils showed that Ni x-ray emission at 45 MeV was negligible. At the higher beam energies, 94 and 138 MeV, appreciable beam x-ray production was observed and the data were corrected for contributions from the carbon backing.

The effects of multiple scattering in the target were estimated from the theory of Mayer.<sup>18</sup> We conclude that multiple scattering should not affect the results compared to instrumental uncertainties at scattering angles greater than a few degrees corresponding to the small impact parameters. At small angles corresponding to the large impact parameters multiple scattering becomes significant. The value of  $P$  at the largest impact parameter was taken to be indicative of contributions from multiple scattering and long range processes such as direct Coulomb ionization.

Inner-shell vacancy production in heavy ion-atom collisions can be a strong function of the degree of ionization and particular electronic configurations of the collision partners. It has been shown<sup>19</sup> that many electrons can be removed in a single collision, resulting in a distribution of final charge states and electronic configurations even though the initial states are well defined. In our experiments the projectiles move in solids, and their electronic state as they enter x-ray producing close collisions with target atoms is largely determined by electron stripping and excitation of the ion core by electron impact. Specifically the thickness of our target films was  $\approx 20$  nm as compared to the predicted charge equilibrium distances which, depending on  $v_1$ , ranged from  $\approx 20$ -40 nm.<sup>20</sup> In consequence, the mean charge of the  $^{28}\text{Ni}$  projectile must have ranged between the initial values (6-8)e in the beam and the expected equilibrium charges (13-18)e.<sup>21</sup> Such effects may influence the inner-shell vacancy production

relative to that in single-collision experiments performed with gaseous targets.<sup>22</sup>

### III. Discussion

Heavy ion-atom collisions in general are expected to be characterized by a distribution of charge and electronic states in a quasi-molecular system with complex and densely spaced level crossings. Following the first attempt,<sup>6</sup> the data are discussed in terms of the statistical model which is especially appropriate for complex collision systems. The effects of various electronic configurations and the complexity of the collision are incorporated in one adjustable parameter of the model, which scales in the atomic numbers of the collision pair.

We display the physical content of the statistical approach by treating inner-shell ionization as a random-walk process<sup>23</sup> of electron promotion between densely spaced, interacting level crossings of transient molecular orbitals. The probability,  $dP_n$ , that an electron starting from an energy level  $E_n$  at  $t = 0$  will reach the threshold to unoccupied states,  $E_{thr}$ , during the time between  $t$  and  $t+dt$  is given by

$$dP_n = \frac{\epsilon_n}{2t(\pi\delta_n t)^{1/2}} \exp\left(-\frac{\epsilon_n^2}{4\delta_n t}\right) dt, \quad (1)$$

where  $\epsilon_n = E_{thr} - E_n$  and the electron-promotion parameter,  $\delta_n$ , is related as  $\delta_n = (1/2) \gamma_n \epsilon^2$ , to  $\gamma_n$ , the mean number of level crossings per unit time between levels of average spacing  $\epsilon$ . For  $n = 1, 2$  we write also  $\epsilon_K, \epsilon_L$  etc.

Following Wilets,<sup>24</sup> one may set  $\delta_n = C_n \dot{R}^2$ , where  $\dot{R}$  is the radial velocity during collision. The parameter  $C_n$  is treated as a constant when the internuclear distance,  $R$ , is less than an effective interaction range  $R_0$  over which the atomic electron clouds interact strongly; and when  $R > R_0$ ,  $C_n \approx 0$ . We defer an extension of the treatment of excitations through rotational level coupling or "Coriolis mixing" via dependences of  $\delta_n$  on the time-dependent angular velocity of the internuclear radius vector.

Without loss in generality, we can simplify matters by replacing the promotion parameter,  $\delta_n(t)$ , by its value  $\bar{\delta}(v, R_0)$  averaged over the collision time,  $t_{col}$ , and assume a straight projectile path with impact parameter  $b$  and constant velocity  $v$ . Integration of Eq. (1) over the collision time,  $t_{col}$ , given by

$$t_{col} = \frac{2R_0}{v} (1-x^2)^{1/2} \Theta(1-x), \quad (2)$$

with  $x \equiv b/R_0$  and  $\Theta(y) = (1/2) (1 + y/|y|)$ , yields, in terms of the error function complement, erfc,

$$P_n = \text{erfc} \left( \frac{1}{S_n^{1/2}} \right), \quad (3)$$

where

$$S_n = \frac{2 R_0 v}{\bar{D}_n} \left( 1 - \frac{b^2}{R_0^2} \right)^{1/2} \Theta(1-x^2) \equiv W_n (1-x^2)^{1/2} \Theta(1-x^2) \quad (4)$$

with the abbreviation

$$W_n = (2R_0 v / \bar{D}_n) (v / v_n), \quad (5)$$

in terms of the orbital velocity  $v_n$ , and

$$\bar{D}_n = \frac{e^2 v^2}{4\bar{\delta}_n} \quad (6)$$

Since the mean promotion parameter in energy space,  $\bar{\delta}_n$ , is proportional to  $v^2$ ,  $\bar{D}_n$  is taken to be a constant and, because of its dimensions [ $L^2 T^{-1}$ ], is referred to as diffusion constant. The total cross section becomes

$$\begin{aligned} \sigma_n &= 2\pi R_o^2 \int_0^1 x dx P_n(x) \\ &= 2\pi R_o^2 \int_1^\infty \frac{dy}{y^3} \operatorname{erfc} \left( \frac{y^{1/3}}{W_n^{1/2}} \right) \end{aligned} \quad (7)$$

We integrate and obtain to leading terms (with error < 10%)

$$\sigma_n \approx \pi R_o^2 \frac{2E_3\left(\frac{1}{W_n}\right)}{1 + \sqrt{\frac{\pi}{W_n}}} \quad (8)$$

where  $E_3(x) = \int_1^\infty e^{-xt} t^{-3} dt$ .

A detailed treatment of the time dependent diffusion problem of excitation to the continuum for total ionization was given by Mittleman and Willets<sup>15</sup>. It was developed for inner-shell ionizations and applied to K-shells by Brandt and Jones.<sup>6</sup> It is used here for the first time to interpret L-shell data. In the diffusion model the probability for vacancy production per electron in the n shell is given by



$$P_n(b) \approx 1 - \frac{2}{\pi} \sum_{\nu=0}^{\infty} \frac{(-1)^\nu}{(\nu+\frac{1}{2})} \exp[-(\nu+\frac{1}{2})\pi^2 s_n(b)], \quad (9)$$

where

$$s_n(b) = \frac{2R_0 v}{D_n} F\left(\frac{b}{R_0}\right) = w_n F(x) \quad (10)$$

with

$$F(x) = [(1-x^2)^{\frac{1}{2}} - x \arccos x] \theta(1-x^2). \quad (11)$$

with the notation  $w_n = (2R_0 v_n / D_n)(v/v_n)$ , where  $D_n = \epsilon_n^2 / C_n$ . The total vacancy production cross section becomes

$$\sigma_n = 2\pi \int_0^{R_0} P_n(b) b db = \pi R_0^2 S(w_n), \quad (12)$$

where the function  $S(w_n)$  is given in Ref. 15.

Figure 1(a) compares Eq. (3) with Eq. (9) and Fig. 1(b) compares Eq. (8) with Eq. (12). The two approaches lead to essentially the same impact parameter and velocity dependencies. The coefficients  $D_n \propto \delta_n^{-1}$  contain in principle all the quantum mechanical information about electron promotion between interacting level crossings in the molecular orbital picture. The parameters,  $\bar{D}_n$  and  $D_n$ , in the two approximations differ merely by a model-dependent numerical factor of the order of 1. In particular, these coefficients change with  $\epsilon_n$ , the gap to unoccupied states, which can be affected by the degree of ionization and by vacancies in the core of the projectiles as they are prepared, prior to the colli-

sion, by the conditions of the experiment and may be affected during the time of strong interaction.

The main results of the experiment are shown in Figs. 2-7. The uncertainties due to counting statistics are indicated. Total cross sections are given in Table I. The K-shell data for  $P$  and  $\sigma$  are divided by 2, the number of electrons in the shell, and reported in the form of the summed probabilities,  $P_K(L) + P_K(H)$ , and summed cross sections,  $\sigma_K(L) + \sigma_K(H)$ , per K-shell electron. The notation (L) and (H), respectively, refers to the light and heavy member of the collision pairs. Ionization probabilities and cross sections for the individual collision partners in the Pauli excitation regime can be culled by use of the Meyerhof charge sharing formalism.<sup>25</sup> The variation with impact parameter for the Mn, Sn and Pb targets seem to be very similar in Figs. 2-4. Apparently the differences in reaction mechanisms which cause the  $Z_2$  dependent structure in the total cross section data of Kubo et al.<sup>1</sup> are not strongly reflected in the impact-parameter dependence of  $P_K$ . There is some weak evidence for additional structure in the 45 MeV data which deserves further study.

We present in Figs. 6 and 7 the L-shell data in a similar manner by dividing the measured  $P_L(H)$  and  $\sigma_L(H)$  by 8, the number of electrons in the L-shell. Summed L-shell probabilities and cross sections are not available because the low energy of Ni L x-rays precluded the simultaneous measurement of  $P_L(L)$  and  $\sigma_L(L)$ , and the systematics of the sharing of L-shell vacancies is unknown. The magnitudes found for  $\sigma_L(H)$  and the dependence of  $P_L(H)$  on impact parameter and bombarding energy are similar to those observed for the K-shell vacancy production.

Figures 2-7 compare the impact-parameter-dependent data with the

statistical model predictions via Eqs. (9) to (11). For definiteness,  $R_0$  is set equal to the Thomas-Fermi radius of the combined atom,  $R_0 = 0.885 a_0 Z_{\text{eff}}^{-1/3}$  with  $Z_{\text{eff}} = (Z_1^{2/3} + Z_2^{2/3})^{3/2}$  and  $a_0 = 0.0529$  nm. The diffusion coefficients,  $D_K$  and  $D_L$ , were chosen to achieve a best fit to the experimental data and are listed in Table I together with the experimental and calculated Eq. (12) total cross sections. Inspection of the figures shows that the particular choice of  $R_0$  does not affect sensitively the curves calculated according to Eq. (9) in the range of  $b$  where the ionization probabilities are large. In fact, if the  $P$  values at the largest impact parameters in Figs. 3-7 are taken to be indicative of the contributions from multiple scattering and long-range processes such as direct Coulomb ionization, and are subtracted (open circles), the experimental ionization probabilities for the smaller impact parameters drop towards zero as the  $b$  values approach  $R_0$  consistent with the simple form of Eq. (11).

Values for  $D_K$  in nearly symmetric collisions are expected to have the form  $D_K = [(Z_1 + Z_2)/A]^\alpha (\pi/m)$ , where  $A$  and  $\alpha$  are parameters weakly dependent on  $Z_1$  and  $Z_2$ . In the validity range of the statistical model the exponent,  $\alpha$ , is expected to have values near 2.<sup>6</sup> For this  $\alpha$  value, the  $D_K$  values in Table I indicate that  $A \approx 13$  for  ${}_{28}\text{Ni} + {}_{25}\text{Mn}$  and  $A \approx 14$  for  ${}_{28}\text{Ni} + {}_{50}\text{Sn}$ . For the most asymmetric collision,  ${}_{28}\text{Ni} + {}_{82}\text{Pb}$ ,  $D_K$  is smaller, corresponding to  $A \approx 26$ . The values of  $D_K$  for Mn and Pb targets are in reasonable agreement with our earlier work at a single bombarding energy of 45 MeV.

It should be emphasized that the number and values of  $D_K$  just cited are found by comparing our experimental data with the values of  $P(b)$  predicted in Eqs. (9) to (11). Early work<sup>5</sup> on limited ranges of light atoms and in nearly symmetric collisions with  $Z_1 + Z_2$  was described by

$D_K$  given by  $D_K \simeq [(Z_1 + Z_2)/18]^3 \hbar/m$ , but can be equally well be represented by  $D_K = [(Z_1 + Z_2)/12]^2 \hbar/m$  consistent with the present work.

We analyzed the  $P_K$  data for 45 MeV  $^{28}\text{Ni}$  ions on  $^{25}\text{Mn}$  and  $^{50}\text{Sn}$  targets in terms of the MO model.<sup>13,14</sup> Vacancies in the  $2p\pi$  orbital brought into the collision are transferred to the  $2p\sigma$  orbital by rotational coupling and so produce K-shell vacancies in the light member of the interacting pair. Vacancies in the K-shell of the heavy atom can be produced by radial coupling between the  $2p\sigma$  and  $2p\pi$  orbitals. The  $P_K$  were calculated using the method of Taulbjerg et al.<sup>14</sup> For proper comparison with experiment we have averaged these values over the range of impact parameters accepted at each position by our annular detector as described in Section II., with the result shown as dashed curves in Fig. 5. In the lower Z collision of  $^{17}\text{Cl}$  ions on gaseous  $^{18}\text{Ar}$ , Cocke et al.<sup>8</sup> found agreement with these predictions. For comparison the statistical model curves from Figs. 2 and 3 are included as solid curves.

The theoretical fits to the  $P_L$  data shown in Figs. 6 and 7 were obtained by adjusting the value of  $D_L$  without changing the choice of the Thomas-Fermi radius for the interaction range  $R_D$ . The general shape of  $P_L$  as a function of impact parameter is well reproduced. The energy dependence of  $P_L$  is somewhat weaker than that displayed by the experiments. This could represent a stronger dependence of  $P_L$  on the charge state of the incident ion than was observed for  $P_K$ . The use of the statistical model permits a unified description of the production of different types of vacancies in ion-atom interactions and illustrates the power of the theory in collating different types of experimental data.

#### IV. Summary and Conclusions

We have reported inner-shell vacancy production probabilities,  $P_K$  and  $P_L$ , and total cross sections,  $\sigma_K$  and  $\sigma_L$ , derived from x-ray production measurements for  $Z_1 = 28$  ions on solid targets with  $Z_2 = 25, 50$  and  $82$ . Inner-shell ionization is described in terms of the statistical model as a random walk process from an initial inner-shell state to a threshold which depends on the unoccupied levels and vacancies of the projectile. The impact-parameter dependence of the  $P_K$  and  $P_L$  data can be represented well by the statistical model through the choice of two parameters in the diffusion coefficient for all collision pairs. Given these diffusion coefficients, the statistical model predicts accurately the values of the measured K- and L-shell cross sections. The  $P_K$  data do not show the pronounced peak at small impact parameters expected from a model of electron promotion through  $2p_{11} - 2p_{00}$  MO coupling.

Our results, then, extend the study of inner-shell vacancy production under Pauli excitation conditions to intermediate  $Z_1, Z_2$  values. The comparison between experiment and theory can be influenced by various factors, such as the distribution of charge and excitation states of projectiles moving in dense targets. This circumstance, which differs from measurements performed with gaseous targets, may "fill in" the structure predicted for isolated collisions through a statistical average over the electronic states of the moving collision partners. Experiments are needed on solid and gaseous targets to ascertain such effects. As to the theory, the scaling with atomic number of the coupling scheme in the MO model may over-estimate the impact parameter at which  $P_K$  has a maximum in our  $Z_1, Z_2$  domain. On the other hand, channels opened by the crossing

of higher molecular orbitals, as subsummed by the statistical model, may have gained importance to such an extent that they, in fact, govern the vacancy-formation probabilities. As measurements are extended to larger  $Z_1$  and  $Z_2$ , one may expect that the statistical model provides an increasingly effective basis for the prediction of inner-shell vacancy production probabilities.

## References

1. F. C. Jundt, H. Kubo, and K. H. Purser, in Proceedings of the International Conference on Inner Shell Ionization Phenomena and Future Applications, edited by R. W. Fink, S. T. Manson, J. H. Palms, and P. V. Rao (U. S. ERDA, Oak Ridge, Tennessee, 1973), p. 1450; H. Kubo, F. C. Jundt, and K. H. Purser, *Phys. Rev. Lett.* 31, 674 (1973); H. Kubo, Ph.D. Thesis, University of Rochester.
2. W. E. Meyerhof, R. Anholt, T. K. Saylor, S. M. Lazarus, and A. Little, *Phys. Rev. A* 14, 1653 (1976); W. E. Meyerhof, R. Anholt, and T. K. Saylor, *Phys. Rev. A* 16, 169 (1977); R. Anholt and W. E. Meyerhof, *Phys. Rev. A* 16, 190 (1977).
3. K. W. Jones, F. C. Jundt, G. Guillaume, and P. Fintz, in Proceedings of the Tenth International Conference on the Physics of Electron and Atomic Collisions, (Paris, France, 1977) p. 326; K. W. Jones, F. C. Jundt, G. Guillaume, P. Fintz, and B. M. Johnson, (unpublished).
4. H. O. Lutz, in Proceedings of the Second International Conference on Inner-Shell Ionization Phenomena, edited by W. Melhorn and R. Brenn (University of Freiburg, Freiburg, Germany, 1976), p. 104.
5. K. W. Jones, H. W. Kraner, and W. Brandt, *Phys. Lett.* 57A, 33 (1976).
6. W. Brandt, and K. W. Jones, *Phys. Lett.* 57A, 35 (1976), and references cited therein.
7. B. M. Johnson, K. W. Jones, and D. J. Pisano, *Phys. Lett.* 59A, 21 (1976).
8. C. L. Cocke, R. R. Randall, S. L. Varghese, and B. Curnutte, *Phys. Rev. A* 14, 2026 (1976).
9. J. M. Hantzen, Advances in Atomic and Molecular Physics, edited by G. K. Bates and E. Hodson, (Academic Press, New York, 1975), Vol. II., p. 299.

10. W. Brandt and R. Laubert, Phys. Rev. Lett. 24, 1037 (1970).
11. U. Fano and W. Lichten, Phys. Rev. Lett. 14, 627 (1965).
12. M. Barat and W. Lichten, Phys. Rev. A, 6, 211 (1972).
13. J. S. Briggs and J. H. Macek, J. Phys. B 5, 579 (1972); ibid 6, 982 (1973).
14. K. Taulbjerg, J. S. Briggs, and J. Vaaben, J. Phys. B 9, 1351 (1976).
15. M. H. Middleman and L. Willets, Phys. Rev. 154, 12 (1967).
16. R. Schuch, J. Volpp, I. Tserruya, K. E. Stiebing, R. Schule, H. Schmidt-Bücking, and G. Gaukler, in Proceedings of the Tenth International Conference on the Physics of Electron and Atomic Collisions (Paris, France, 1977) p. 330.
17. W. Bambynek, B. Crasemann, R. W. Fink, H. U. Fround, H. Mark, C. D. Swift, R. E. Price, and V. P. Rao, Rev. Mod. Phys. 44, 716 (1972).
18. L. Meyer, Phys. Status Solidi B 44, 253 (1971).
19. N. Stolterfoht, D. Schneider, R. Mann, and F. Folkmann, J. Phys. B10, L281 (1977) and references cited.
20. W. Brandt, R. Laubert, M. Mourino, and A. Schwarzschild, Phys. Rev. Lett. 30, 358 (1973); ibid 31, 1095 (1973).
21. W. Brandt, in Atomic Collisions in Solids, edited by S. Datz, B. R. Appleton, and C. D. Hoak (Plenum, New York, 1975), Vol. 1, p. 261.
22. For recent work on projectile excitation in solids see F. Bell and H. D. Betz, J. Phys. B 10, 483 (1977); T. J. Gray, P. Richard, K. A. Jamison, J. M. Hall, and R. K. Gardner, Phys. Rev. A 14, 1333 (1976); F. Hopkins, J. Sokolov, and A. Little, ibid 15, 588 (1977).  
W. Meyerhof, Phys. Rev. Lett. 31, 1341 (1973).
23. S. Chandrasekhar, Rev. Mod. Phys. 15, 1 (1943).
24. L. Willets in Proceedings of the Second International Conference on The Physics of Electronic and Atomic Collisions (W. A. Benjamin, Inc., New York, 1961) p. 47; Phys. Rev. 116, 372 (1959).



Table I. Total inner-shell vacancy production cross sections,  $\sigma_K$  or  $\sigma_L$ , in  $\text{cm}^2$ . Data listed under Experiment I are from this work, and data under II are from Ref. 1 with mean experimental uncertainties of  $\pm 30\%$ . Theoretical values are calculated from Eq. (4) with the listed constants  $D_K$ ,  $D_L$ , and  $R_0$  as obtained by fitting Eq. 1 to the experimental probabilities,  $P_K$  and  $P_L$ , shown in Figs. 1 to 6. Theoretical values for  $\sigma_K(L)$  and  $\sigma_K(H)$  for  $^{28}\text{Ni} + ^{25}\text{Mn}$  collisions were obtained by calculating  $\sigma_K$  according to Eq. 12 and applying the charge sharing formalism of Ref. 22 to  $\sigma_K = \sigma_K(L) + \sigma_K(H)$ . Numbers in parentheses are powers of 10.

Collision	Observed x-rays	Cross Section Identification	$D_K$ or $D_L$ ( $\text{cm}^2/\text{sec}$ )	$R_0$ (cm)	$\sigma_K/2$ or $\sigma_L/8$ ( $\text{cm}^2$ )							
					$E_1 = 45$ MeV		94 MeV		138 MeV			
					Experiment I	Theory II	Experiment I	Theory II	Experiment I	Theory		
$^{28}\text{Ni} + ^{25}\text{Mn}$	NiK	$\sigma_K(H)$		1.1(-9)	2.0(-21)	5.7(-21)	1.5(-21)	1.7(-20)	2.0(-20)	2.0(-20)	3.9(-20)	4.0(-20)
$^{28}\text{Ni} + ^{25}\text{Mn}$	MnK	$\sigma_K(L)$		1.1(-9)	1.0(-20)	1.3(-20)	7.2(-21)	4.2(-20)	2.2(-20)	2.5(-20)	5.0(-20)	4.0(-20)
$^{28}\text{Ni} + ^{25}\text{Mn}$	NiK+MnK	$\sigma_K(T)$	19	1.1(-9)	1.2(-20)	1.9(-20)	2.9(-20)	5.9(-20)	4.2(-20)	7.3(-20)	8.9(-20)	1.1(-19)
$^{50}\text{Ni} + ^{50}\text{Sn}$	NiK	$\sigma_K(T)$	35	9.8(-10)	6.0(-22)	3.6(-22)	1.2(-21)	7.0(-21)	4.5(-21)	6.6(-21)	1.0(-20)	1.2(-20)
$^{82}\text{Ni} + ^{82}\text{Pb}$	NiK	$\sigma_K(T)$	21	8.8(-10)	1.2(-20)	5.0(-21)	5.8(-21)	8.0(-20)	2.3(-20)	2.1(-20)	1.5(-19)	5.8(-20)
$^{50}\text{Ni} + ^{50}\text{Sn}$	SnL	$\sigma_L(H)$	14	9.8(-10)	3.4(-21)	1.9(-20)	3.6(-20)	2.3(-20)	5.9(-20)	8.8(-20)	3.6(-20)	1.4(-19)
$^{82}\text{Ni} + ^{82}\text{Pb}$	PbL	$\sigma_L(H)$	39	8.8(-10)	2.1(-21)	3.5(-22)	2.4(-22)	2.5(-21)	1.1(-21)	2.1(-21)	3.0(-21)	4.9(-21)

### Figure Captions

Fig. 1 Predictions of the statistical model in the random walk(—) and diffusion(---) approximation agree in essence.

Fig. 1(a) displays the product,  $P_n \times b/R_0$ , of the probability for ionization of an inner shell level,  $n$ , and the reduced impact parameter as a function of  $b/R_0$ . The solid curve is calculated from Eqs. (3) and (4) with  $w_n = 1$ , Eq. (5), and the dashed curve from Eqs. (9) and (10) with  $w_n = W_n/3$ .

Fig. 1(b) displays the reduced inner shell vacancy production cross section,  $\sigma_n/nR_0^2$ , for a level  $n$  as a function of  $W_n$ . The solid curve is calculated from Eq. (8), and the dashed curve from Eq. (13) with  $w_n = W_n/3$ . By Eq. (5), the abscissa values are equal to the reduced projectile velocities,  $v/v_n$ , for  $2R_0 v/\bar{D}_n = 1$ .

Fig. 2 Probabilities,  $P_K = P_K(L) + P_K(H)$ , for the K-shell vacancy production in light (L) and heavy (H) collision partners, for  ${}_{28}^{Ni} + {}_{25}^{Mn}$  as a function of impact parameter,  $b$ , for three collision energies. The curves present the predictions of the statistical model, with the diffusion constant,  $D_K$ , and interaction radius,  $R_0$ , as listed in Table I.

Fig. 3 K-shell vacancy production probabilities,  $P_K \equiv P_K(L) + P_K(H) \simeq P_K(L)$ , for  ${}_{28}^{Ni} + {}_{50}^{Sn}$  as a function of impact parameter,  $b$ , for three collision energies. The curves present the predictions of the statistical model with  $D_K$  and  $R_0$  as listed in Table I.

Fig. 4 K-shell vacancy production probabilities,  $P_K \equiv P_K(L) + P_K(H) \simeq P_K(L)$ , for  ${}_{28}^{Ni} + {}_{82}^{Pb}$  as a function of impact parameter,  $b$ , for three collision energies. The curves present the predictions of the statistical model with  $D_K$  and  $R_0$  as listed in Table I.

Fig. 5 Comparison of experimental K-shell ionization probabilities,  $P_K$ , for  $^{28}\text{Ni} + ^{25}\text{Mn}$  and  $^{28}\text{Ni} + ^{50}\text{Sn}$  at 45 MeV with the predictions of the statistical and molecular orbital models. Data and solid curves are from Figs. 1 and 2. Vertical bars represent uncertainties in counting statistics. Solid curves: predictions of the statistical model with  $D_K$  and  $R_0$  as listed in Table I; dashed curves: predictions based on  $2p\pi-2p\sigma$  MO coupling from Ref. 14.

Fig. 6 L-shell vacancy production probabilities,  $P_L = P_L(H)$ , for  $^{28}\text{Ni} + ^{50}\text{Sn}$  as a function of impact parameter,  $b$ , for three collision energies. The curves present the predictions of the statistical model with  $D_L$  and  $R_0$  listed in Table I.

Fig. 7 L-shell vacancy production probabilities,  $P_L = P_L(H)$ , for  $^{28}\text{Ni} + ^{82}\text{Pb}$  as a function of impact parameter,  $b$ , for three collision energies. The curves present the predictions of the statistical model with  $D_L$  and  $R_0$  listed in Table I.

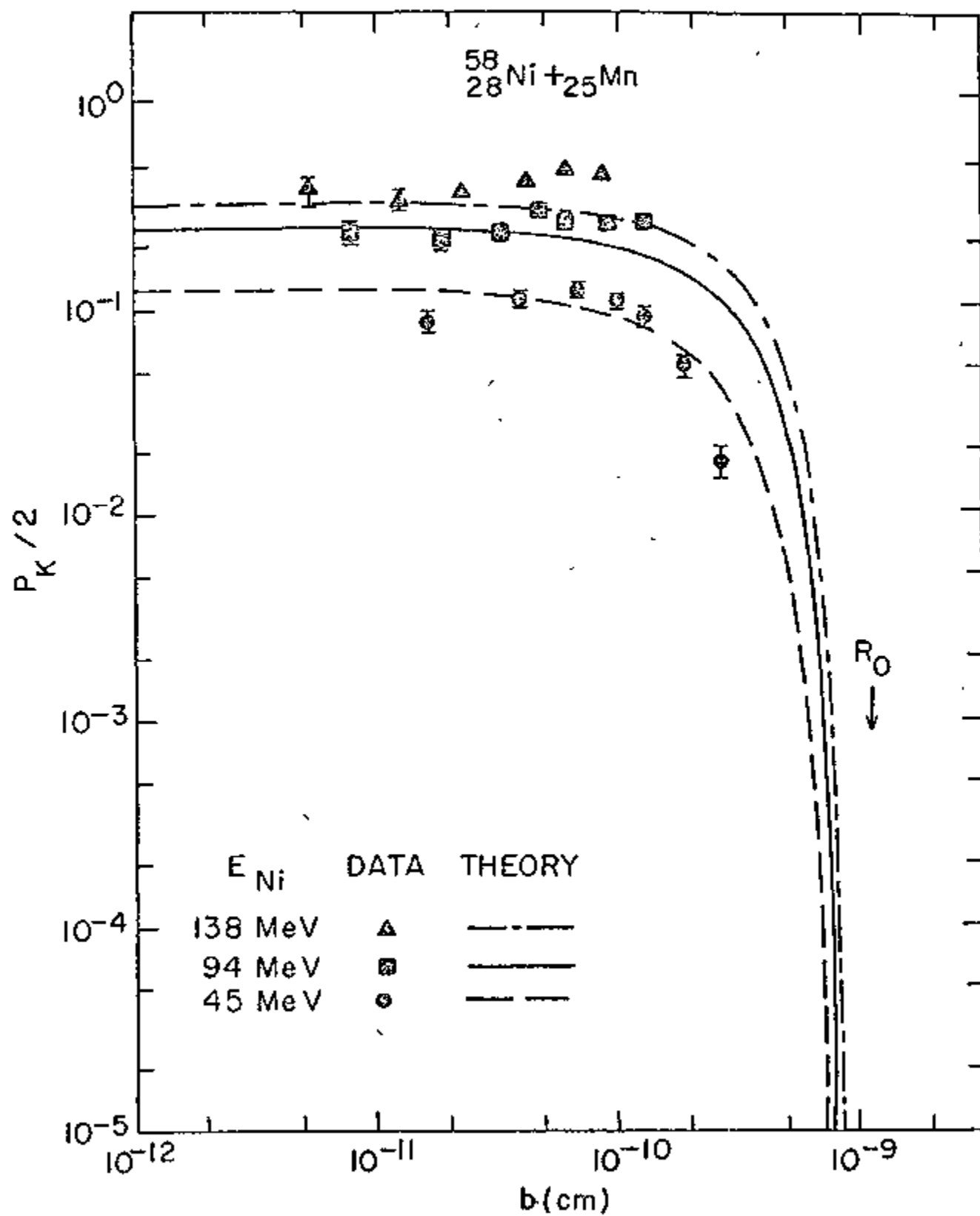


Figure 2

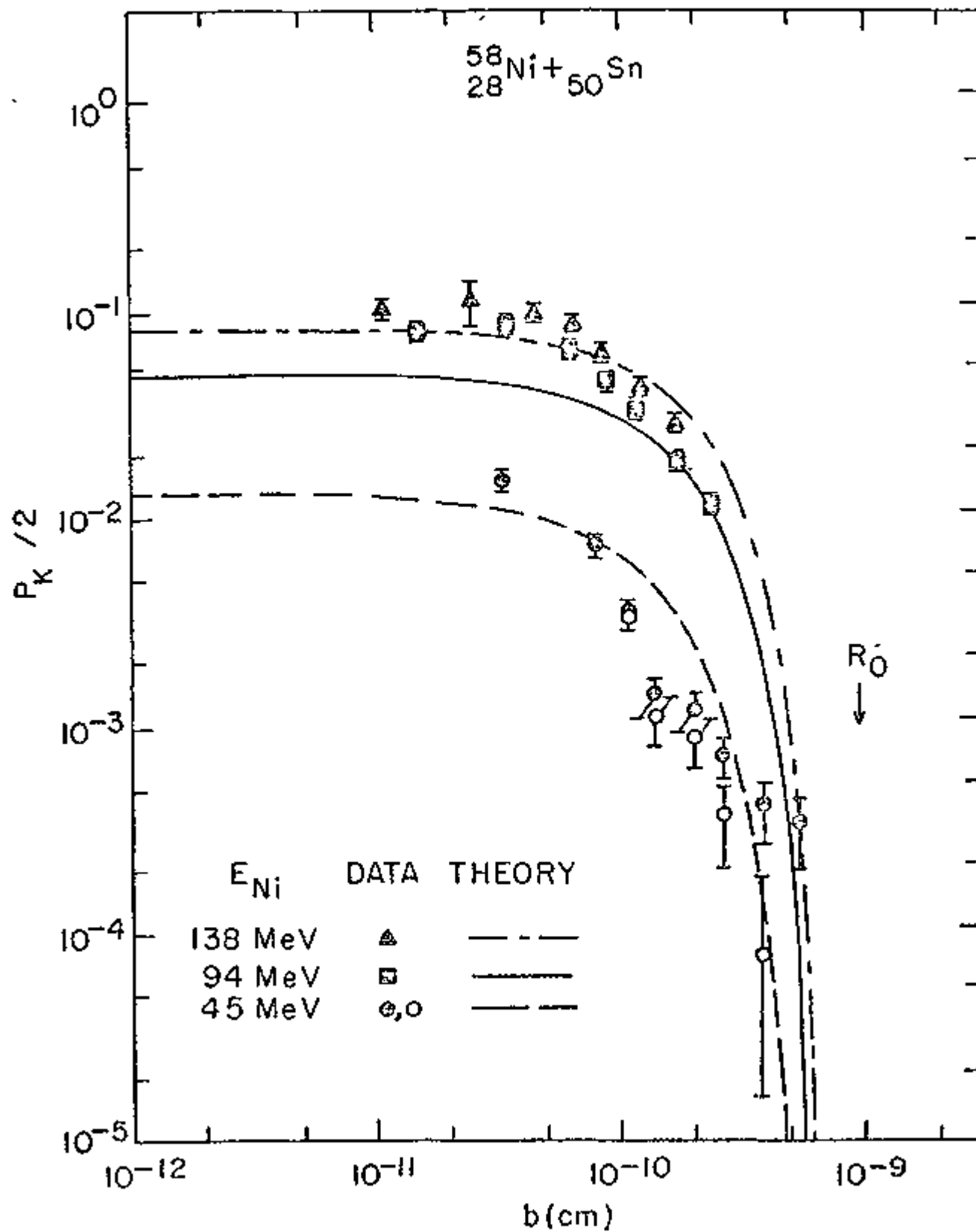


Figure 3

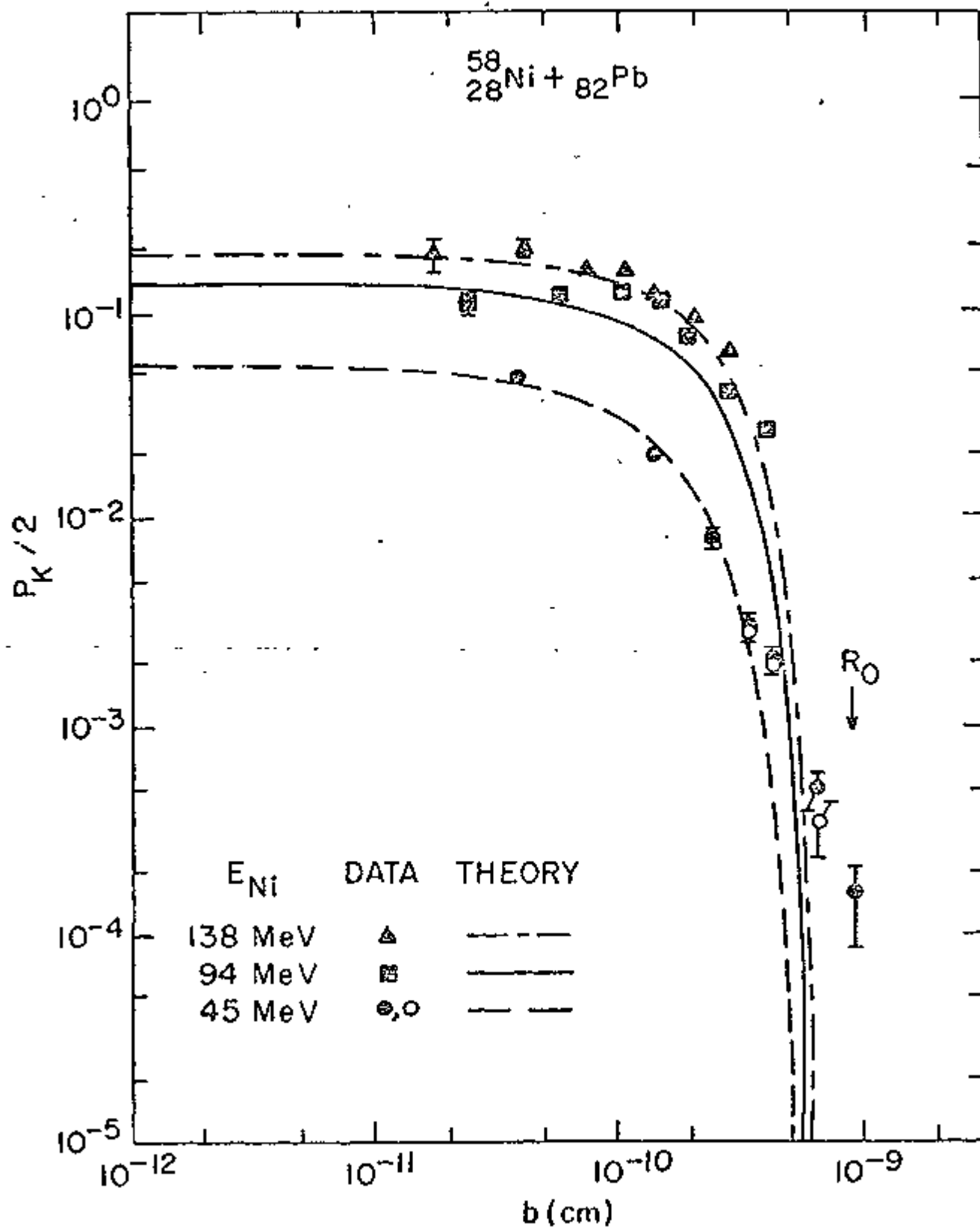


Figure 4

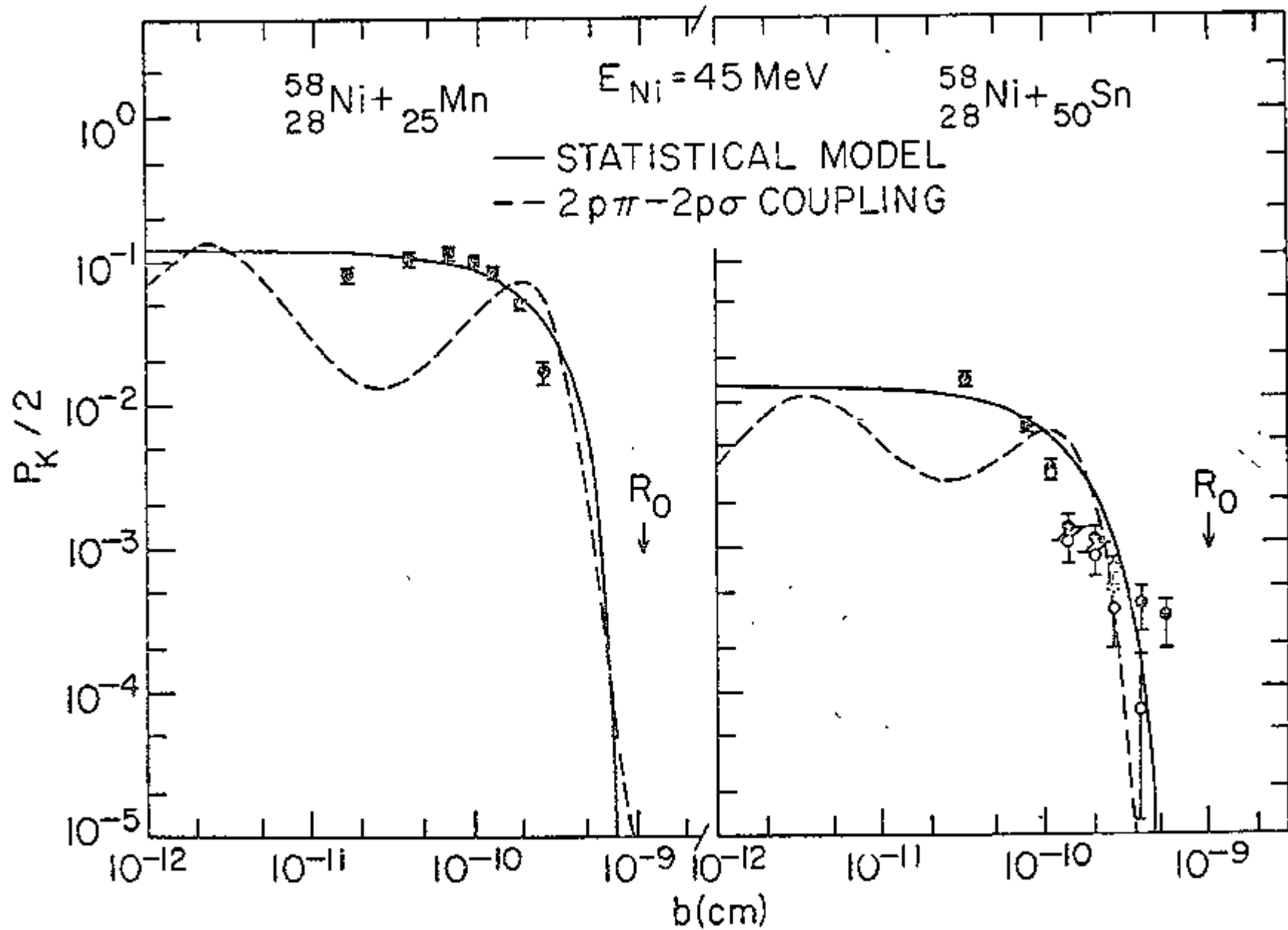


Figure 5

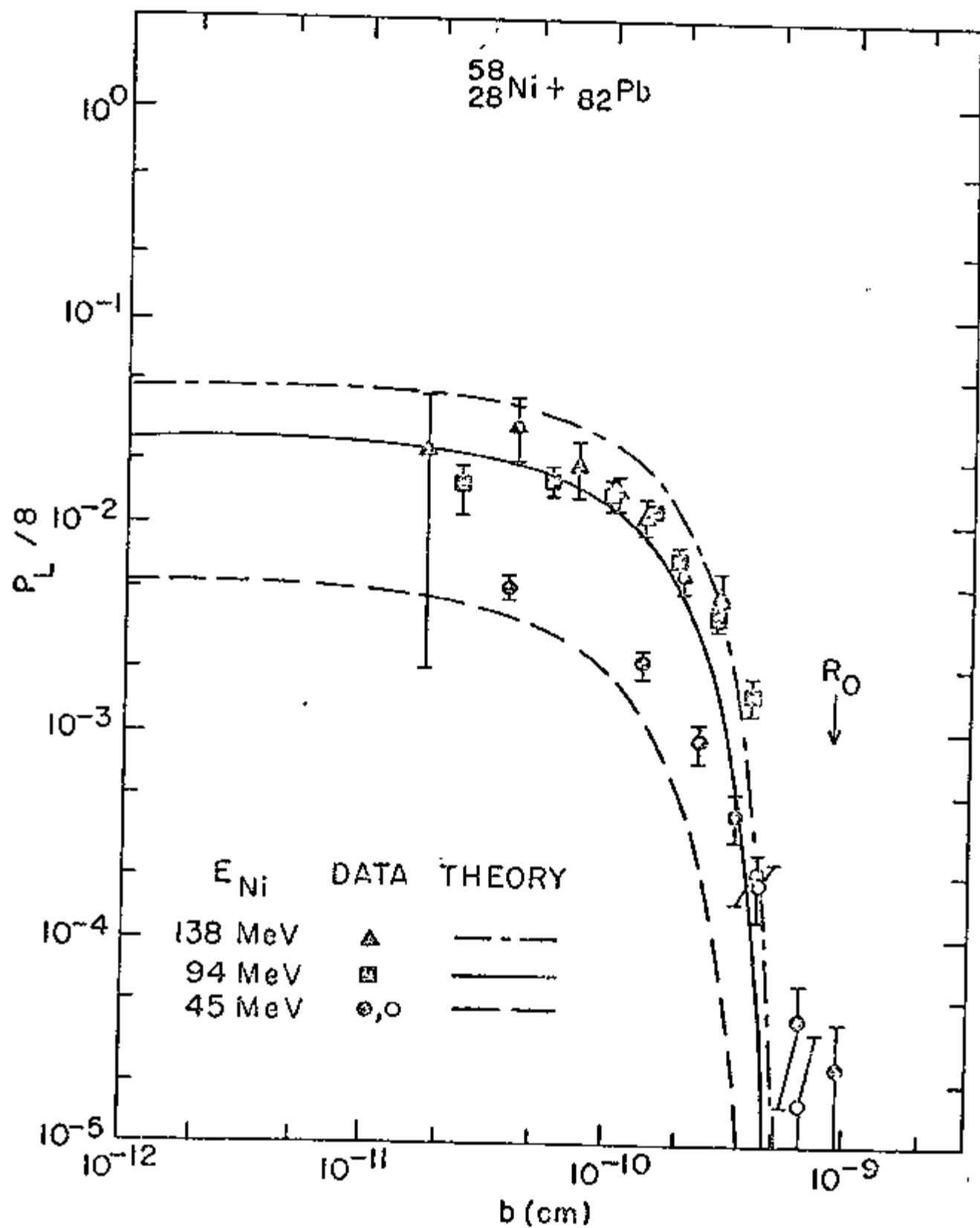


Figure 7



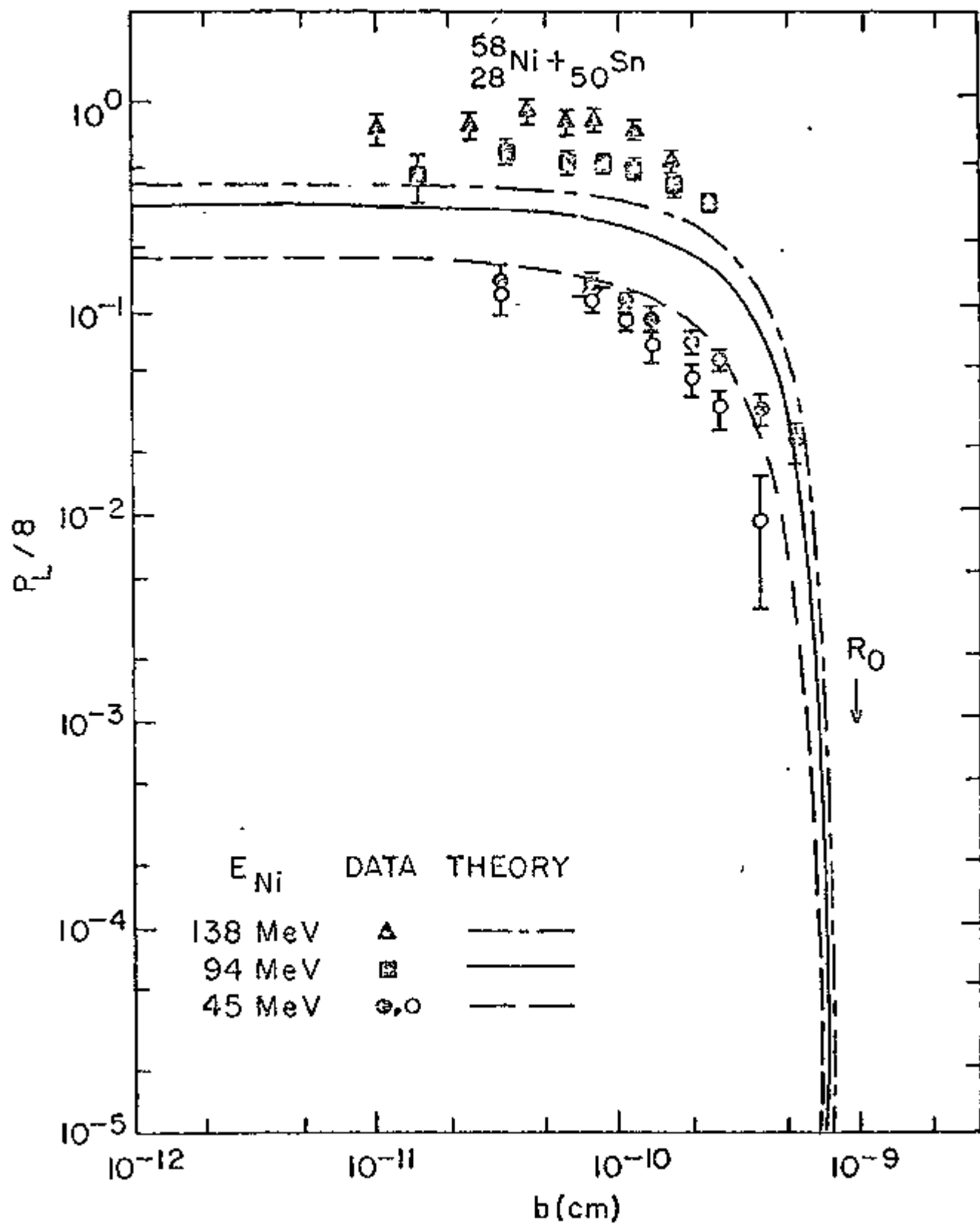


Figure 6

### III. Penetration Phenomena

#### 1. Introduction

A major program at this laboratory is the investigation of the interaction of fast charged particles with matter and different pathways of energy-loss mechanisms. To this end we have sustained experimental and theoretical programs in the energy loss and energy straggling of fast particles in matter, and in the potential distribution in the vicinity of the fast particle as it penetrates an ensemble of atoms which characterize the solid. Knowledge of this potential permits calculations of stopping powers and energy straggling. It creates a theoretical framework within which the experimental results can be assessed.

#### 2. Screening of ions in solids (Laubert, Chen, Kim)

The potential established by a swift charged particle as it penetrates a solid target is one of the basic problems of collisional atomic physics. We have embarked on an experimental program with the intent of determining this quantity directly, and to compare our results to theoretical estimates.

The method uses molecules as incident projectiles. This constrains the initial internuclear separation between the nuclei of the atoms. Upon entering the target the bonding electrons of the molecule are removed by scattering.<sup>1,2</sup> The nuclei experience forces due to the medium and to the cluster of nuclei moving in close proximity. This will cause the constituents of the cluster to separate. The separation is

given by the internuclear potential in the moving cluster, and proportional to the transitive of the cluster.<sup>3</sup> When leaving the target the cluster can capture electrons, and the separation continues in vacuum in a well defined potential. The total explosion experienced by the nuclei of the molecule in an apparatus can be determined by measuring the final energy difference of the cluster constituents. The final energy distribution of neutral and charged particles is indicative of the internuclear potential inside the target medium.

The experimental arrangement employed in these studies is shown schematically in Fig. 1. A magnetic spectrometer (MI) selects the desired particles from the New York University heavy-ion accelerator. Following MI a pair of crossed slits, separated by ~ 40 cm, restrict the angular divergence of the beam to  $\pm 0.2$  mrad and prevent slit-scattered or dissociated particles from reaching the target. The targets were located inside a liquid nitrogen cooled cylinder to reduce carbon deposition on the entrance and exit surfaces of the target.<sup>4</sup> The target thickness was determined by measuring the energy loss of 75 keV protons and using a value of  $0.75 \text{ keV}/\mu\text{g}/\text{cm}^2$  for the stopping power of carbon.<sup>5</sup> Typically a beam size of  $\sim 10^{-3}$  cm diam reached the target with an intensity of  $(1 \text{ to } 5) \times 10^{-11}$  A. The uniformity of the carbon target was checked over an extended area by measuring the energy loss and straggling of the emerging protons. Target areas that were uniform within  $\pm 10\%$  were selected for this experiment. A second set of crossed slits, located 15 cm downstream from the

target, selected particles about the forward direction having an angle of 0.2 to 1.0 mrad. The total angular distribution of the emerging particles was 3 to 15 mrad. A second magnetic spectrometer (MII) analyzed the energy of the selected particles. The magnetic field is swept by a programmable power supply and measured by a differential gaussmeter whose amplified output is connected to a linear gate. A solid state particle detector, located in the focal plane of the analyzing magnet, coupled to a single channel analyzer provided the second input for the linear gate. The linear gate signals were stored in a pulse height analyzer (PHA) whose channel number is then proportional to the energy of the detected particles. Converting from momentum to energy distribution we find the energy resolution,  $\Delta E_1/E_1$ , of this system to be  $(1 \text{ to } 5) \times 10^{-4}$ . To average the beam intensity fluctuations during the collection time (typically 10-20 minutes) the magnetic field of MII was swept twice per minute.

The composition of the molecular beam was ascertained by removing the target and measuring the intensities of the dissociated molecules. In all cases the dissociated fraction was less than  $10^{-3}$ .

Typical results obtained with carbon targets are shown in Fig. 2. The narrow distributions, open symbols, are obtained with proton beams. Their energy straggling, as measured by the full width at half maximum (FWHM), after correction for target nonuniformity<sup>6</sup> agrees with theory.<sup>7</sup> The broad distributions, full symbols, are obtained with  $H_2^+$  beams. As the widths of these distributions increase with increasing projectile energy

(Fig. 2a-2c), three distinct peaks are resolved. For brevity we label the high energy peak as 1, the middle peak as 2, and the low energy peak as 3. We note that the FWHM of peak 3 is greater than those of peak 1 and 2 whose FWHM equals that of proton energy straggling. The intensity of peak 2 increases linearly from ~ 20% for a 300 keV  $H_2^+$  beam to ~ 60% for a 100 keV  $H_2^+$  beam. Increasing the target thickness from 1.4 to  $4.5 \mu\text{g}/\text{cm}^2$  (Fig. 1c-1d) results in a two-peak distribution and the disappearance of the clearly resolved center peak.

Peaks 1 and 3 are attributed to the leading and trailing particles in the exploding clusters. The higher intensity of peak 3 relative to peak 1 results from wake forces which tend to align the trailing particle behind the leading particle.<sup>8</sup> Peak 2 has not been observed previously. Its properties coincide with those one expects from clusters that did not experience explosion inside the target.

As a first step, we separated post-target explosion from processes inside the target through coincidence measurements between emerging H and  $H^+$  particles. The  $0^\circ$ , which counted the neutral particles, and  $90^\circ$  particle detector outputs, through a timing single channel analyzers, started and stopped a time-to-amplitude converter (TAC). The TAC output was collected in a PHA, and after passing through a single channel analyzer, served as an input to the linear gate. The full width at half maximum of the TAC spectrum was ~ 20 ns and a true-to-accidental ratio of ~ 5 was maintained throughout the experiment. A typical coincident spectrum for a  $2 \pm 0.2 \mu\text{g}/\text{cm}^2$  target and 25 hours of bombardment with 290 keV  $H_2^+$  ions is shown in Fig. 3 together

with the noncoincident spectrum which is obtained in 10-20 minutes. The solid line is to guide the eye. Insufficient statistics prevents us from deciding the relative intensities of peak 1 and 3. The total energy width of the coincidence distribution is  $\approx 4.5$  keV which is about 0.5 keV less than the noncoincidence distribution, indicating little post-target explosion for clusters exploding in the target. The 4.5 keV energy width is attributed to the conversion of Coulomb and vibrational energy into kinetic energy of the cluster constituents. The differences in the relative peak intensities in the two distributions are indicative of clusters with two charged nuclei that undergo post-target explosion. The coincidence distribution measures the particle distribution at the exit surface of the target and indicates that only 50% of the clusters undergo explosion in the target. Experiments with thicker targets ( $4.5 \mu\text{g}/\text{cm}^2$  and  $9 \mu\text{g}/\text{cm}^2$ ) at this cluster velocity indicate no discernable differences in the coincidence and noncoincidence distributions. From this we conclude that the relative intensity of peak 2 decreases with increasing target thickness.

We have also measured the energy distribution of the emerging neutral particles. As expected, the energy distribution is identical to the coincident energy distribution shown in Fig. 3. The measurement of the energy distribution of the emergent neutral particles is accomplished by removing the charged particles, with the aid of an electric field between the target and analyzing magnet, and ionizing the neutral particles by introducing some gas in the region between the electric and

magnetic fields. At a gas pressure of  $\sim 10^{-5}$  Torr (about an order of magnitude greater than the background pressure) we find that we ionize approximately 10% of the exiting neutral particles. The advantage of measuring the energy distribution of the neutral particles as opposed to the energy distribution of the charged particles in coincidence with the neutral particles, is that the collection time is reduced from  $\sim 25$  hours to  $\sim \frac{1}{2}$  hour.

It is possible that the occurrence of unexploded clusters is linked to molecules with internuclear distances that are larger than the screening length of the Coulomb force of moving particles in the solid. Since an  $H_2^+$  ion can be in any of 19 vibrational levels the internuclear separation can vary from 0.6 to 2.0 Å. Using internuclear separations of  $H_2^+$  given by Remillieux<sup>9</sup> and a dynamic screening length<sup>3</sup> of  $R_D = v_1/\omega_0$ , where  $\omega_0$  is the dominant response frequency of the medium ( $\omega_0 = 0.82$  a.u. for carbon), one calculates that for 300 keV incident  $H_2^+$  molecules more than 80% of the clusters should have exploded during transmission. This is a lower estimate because we assumed the internuclear distances corresponding to highly excited vibrational states of molecules. New evidence suggests that the molecule may be in the ground states.<sup>10</sup> We attempted to change these conditions by choosing a molecule with shorter internuclear distances, viz.  $HeH^+$ , and analyzed the emerging protons. Again three-peak distributions were observed. For  $HeH^+$  molecules the estimated unexploded fraction is 5% for 300 keV and 10% for 250 keV. Experimentally we find

an unexploded fraction of 40% at 300 keV and 45% at 250 keV.

The fact that we observed peaks indicative of unexploded clusters from greatly differing molecules makes it unlikely that their occurrence is due to a fortuitous cancellation, through vibrational excitation and subsequent straggling, of the explosion force while the particles are inside the solid.

The present experiments probe the screened potential of ions that move in close proximity through a solid. The theory for such multicenter potentials has not been developed. One of the models<sup>11</sup> for the charge state of ions in solids asserts that a moving proton cannot have a bound state inside a solid. A linear superposition of the screened potentials of the individual ions implies that all clusters should explode. The fact that 50% are observed not to explode signifies that the actual dynamic screening, at least for some internuclear orientations, is sufficiently strong to prevent explosion between moving ions a molecular-bond distance apart.

An alternative viewpoint is that protons retain electron bound states even in solids.<sup>12</sup> To explain our findings in these terms, at least one of the nuclei of the cluster must carry an electron during its transit time. The unexploded fraction of clusters is determined, in the simplest approximation, by twice the product of the neutral and charged fraction. Although these experiments do not prove the existence of electron bound states for moving protons in solids, the results are in qualitative agreement with this view.



Another possible explanation for the central peak can be put forward by considering electron capture by the cluster upon exiting from the target. Clearly, if no electrons are captured the nuclei are in a Coulombic potential and experience post-target explosion. This is evident by comparing the coincident and noncoincident spectra in Fig. 3. If the exiting cluster captures one electron then for diprotons, the post target potential established is that of an  $H_2^+$  molecule, which in the ground state has negative values for internuclear distances that are greater than the equilibrium internuclear distance. This will tend to inhibit explosion and hence decrease the final energy separation. This can result in the formation of the central peak. If the internuclear velocity  $v_i < (\frac{2\epsilon}{M})^{1/2}$ , where  $\epsilon$  is the potential of the  $1S\sigma$  state of  $H_2^+$  at the exiting internuclear separation, then a  $H_2^+$  molecule will be formed. For  $2 \mu\text{g}/\text{cm}^2$  targets and velocities considered here typically  $10^{-3}$  of the incident particles will satisfy this condition. The majority of clusters will have an internuclear velocity greater than this amount and the molecule will dissociate into a charged and neutral hydrogen. Hence one would expect the neutral and proton spectra to reflect the central peak. This is what is observed in Fig. 3.

To alleviate this latter ambiguity we investigated the energy distribution of the emergent neutral and charged hydrogen atoms when  $HeH^+$  molecules are the incident projectiles. Then one would expect:

<u># of electrons captured</u>	<u>Exit configuration</u>	<u>Total energy difference</u>	<u>Observed specie</u>
0	$\text{He}^{+2} + \text{H}^+$	$\Delta E_t = \Delta E_i + 2 \Delta E_c$	} $\text{H}^+$
1	$\text{He}^+ + \text{H}^+$	$\Delta E_t = \Delta E_i + \Delta E_c$	
2	$\text{He}^0 + \text{H}^+$	$\Delta E_t = \Delta E_i - \Delta E_m$	
2	$\text{He}^+ + \text{H}^0$	$\Delta E_t = \Delta E_i - \Delta E_m$	} $\text{H}^0$
3	$\text{He}^+ + \text{H}^0$	$\Delta E_t = \Delta E_i$	

where  $\Delta E_t$  is the total energy difference of the emerging particles and is the sum of the energy gained inside the target,  $\Delta E_i$ , the post target Coulombic explosion,  $\Delta E_c$ , and the energy lost overcoming the molecular potential barrier at the exit nuclear separation,  $\Delta E_m$ .

The energy distribution for the emergent protons and neutral hydrogen for 300 keV  $\text{HeH}^+$  incident molecules is shown in Figs. 4 and 5, respectively. At the present velocities the one and two electron capture processes will dominate the proton distribution. The central peak in Fig. 4 is accounted for by the two electron process and the resulting implosion, while the side peaks result from the one electron process with the additional post target explosion. At higher incident velocities the two-electron capture probability decreases resulting in the diminution, and eventual disappearance, of the central peak.

When we measure the neutral hydrogen energy distribution only the three-electron capture process is important since the yield of neutral hydrogen from the two electron capture process is - 1/5-1/10 of the yield from the three electron capture

process. This was checked experimentally by measuring the yield of charged and neutral hydrogen when fast  $\text{HeH}^+$  molecules dissociate in a gas. Hence the neutral hydrogen energy distribution reflects the energy distribution of the exiting particles. The experimental results, Fig. 5, indicate that there is explosion of the clusters inside the target. These experimental results, Fig. 4 and Fig. 5, cannot be explained in terms of hydrogen bound states in solids. We conclude that this is direct experimental evidence that there are no bound states on moving hydrogen protons in solids. A qualifier for the previous statement is required. It is possible that the results of Figs. 4 and 5 could be explained in terms of molecule formation in the target. We are presently investigating if this is a feasible mechanism.

To observe this central peak stringent requirements have to be met. The incident particle energy and target thickness have to be such that the explosion energy in the laboratory system is greater than the straggling and small-angle scattering energy, and the probability of electron capture has to be sufficiently large to detect a reasonable fraction of the total particles. This explains why the central peak has not been identified at higher incident energies.<sup>8,13</sup>

Through the study of the energy distribution of the emerging particles when molecules are the incident projectiles, one has a direct experimental method for determining the potential established by swift ions in solid targets. Experiments are in progress to exploit this result.

## References

1. L. H. Toburen, M. Y. Nakai, and R. A. Langley, Phys. Rev. 171, 114 (1968).
2. M. J. Gaillard, J. C. Poizat, A. Ratkowski, and J. Remillieux, Phys. Rev. A 16, 2323-2335 (1977).
3. See for example W. Brandt and R. H. Ritchie, Nucl. Instr. Meth. 132, 35 (1976), and references cited therein.
4. C. A. Peterson and R. Laubert, IEEE Trans. Nucl. Sci. 24, 1542 (1977).
5. H. H. Andersen and J. F. Ziegler, "Hydrogen Stopping Powers and Ranges in All Elements" (Pergamon Press, Oxford, England, 1977).
6. F. K. Chen and R. Laubert, Bull. Am. Phys. Soc. 22, 1247 (1977), and to be published.
7. See for example W. K. Chu, Phys. Rev. A 13, 2057 (1976).
8. Z. Vaber and D. S. Gemmell, Phys. Rev. Lett. 37, 1352 (1976).
9. J. Remillieux, in "Radiation Research" (Academic Press, Inc., New York, 1975), p. 302.
10. D. S. Gemmell, P. J. Cooney, W. J. Pietsch, A. J. Ratkowski, Z. Vaber, and B. J. Zabransky, VIIth International Conference on Atomic Collisions in Solids, Moscow, U.S.S.R., September 19-23, 1977, and to be published.

11. W. Brandt in "Atomic Collisions in Solids," (Plenum Press, New York, 1975), p. 261.
12. M. Cross, Phys. Rev. B 15, 602 (1977).
13. J. Golovchenko and E. Laegsgaard, Phys. Rev. A 9, 1215 (1974).

### Figure Legends

Fig. 1. Schematic of the experimental arrangement.

Fig. 2. The energy distribution of emerging protons when 100 keV (a), 200 keV (b), and 300 keV (c),  $H_2^+$  ions are incident on  $1.4 \pm 0.1 \mu\text{g}/\text{cm}^2$  carbon targets (solid points). Triangles represent the distribution of equal-velocity incident protons. The arrow marks the location of the incident energy. Figure (d) is obtained when 300 keV  $H_2^+$  and 150 keV  $H^+$  are incident on  $4.5 \pm 0.3 \mu\text{g}/\text{cm}^2$  carbon target.

Fig. 3. a) The energy distribution of emerging protons in coincidence with neutral hydrogen atoms when 190 keV  $H_2^+$  is incident on  $2.0 \pm 0.2 \mu\text{g}/\text{cm}^2$  carbon target. The solid line guides the eye. The bottom figure shows the noncoincident energy distribution for the same experimental conditions.

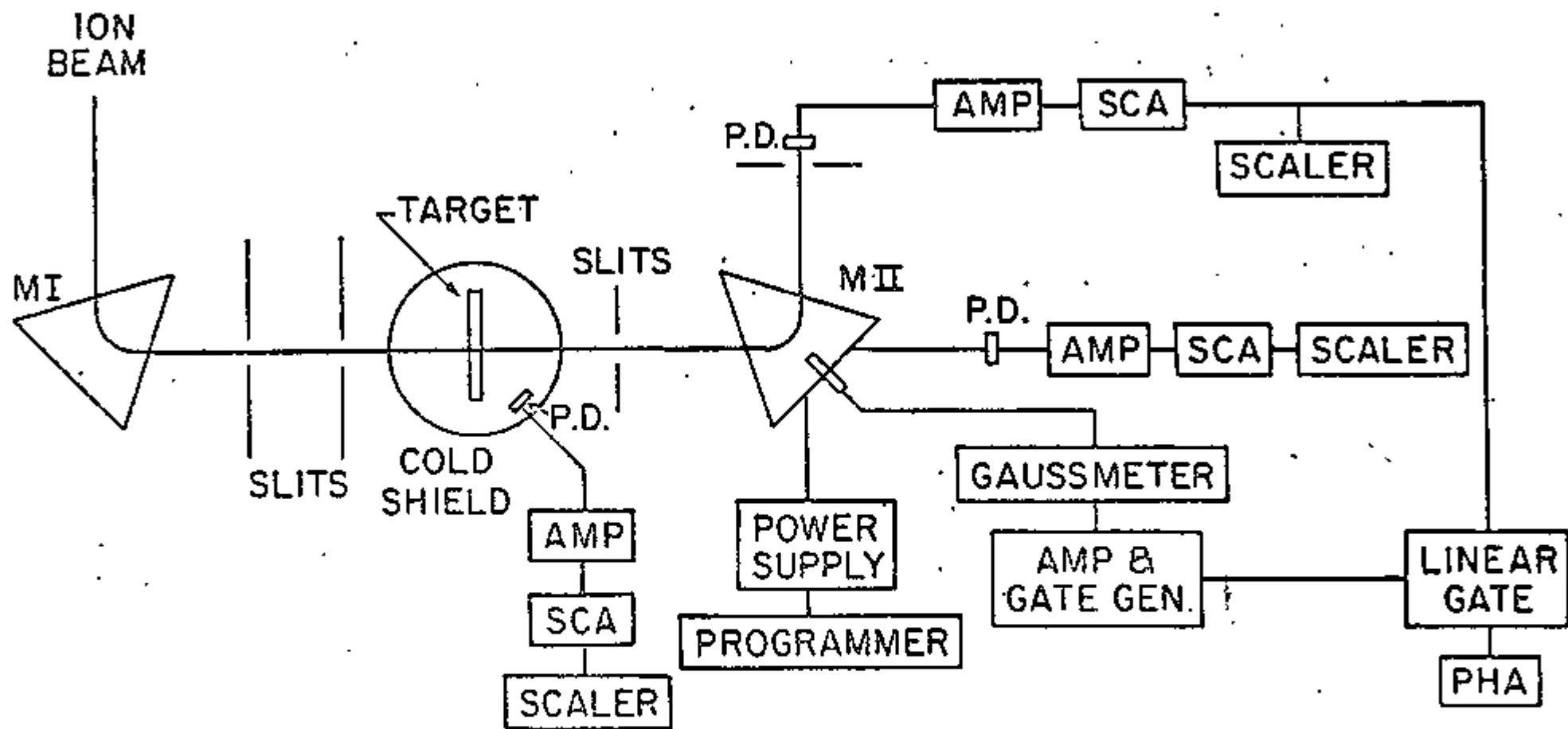


Fig. 1

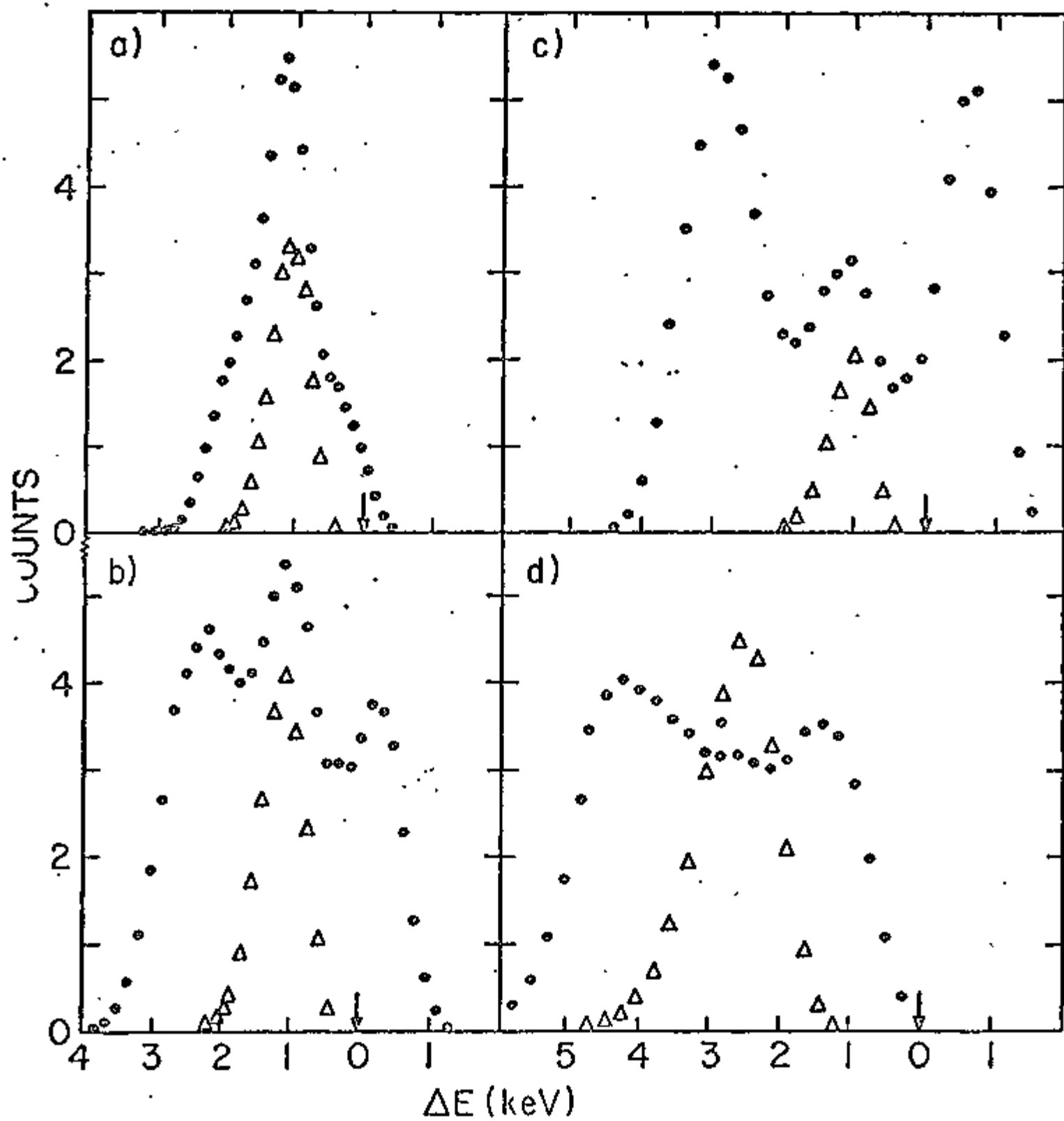


Fig. 2

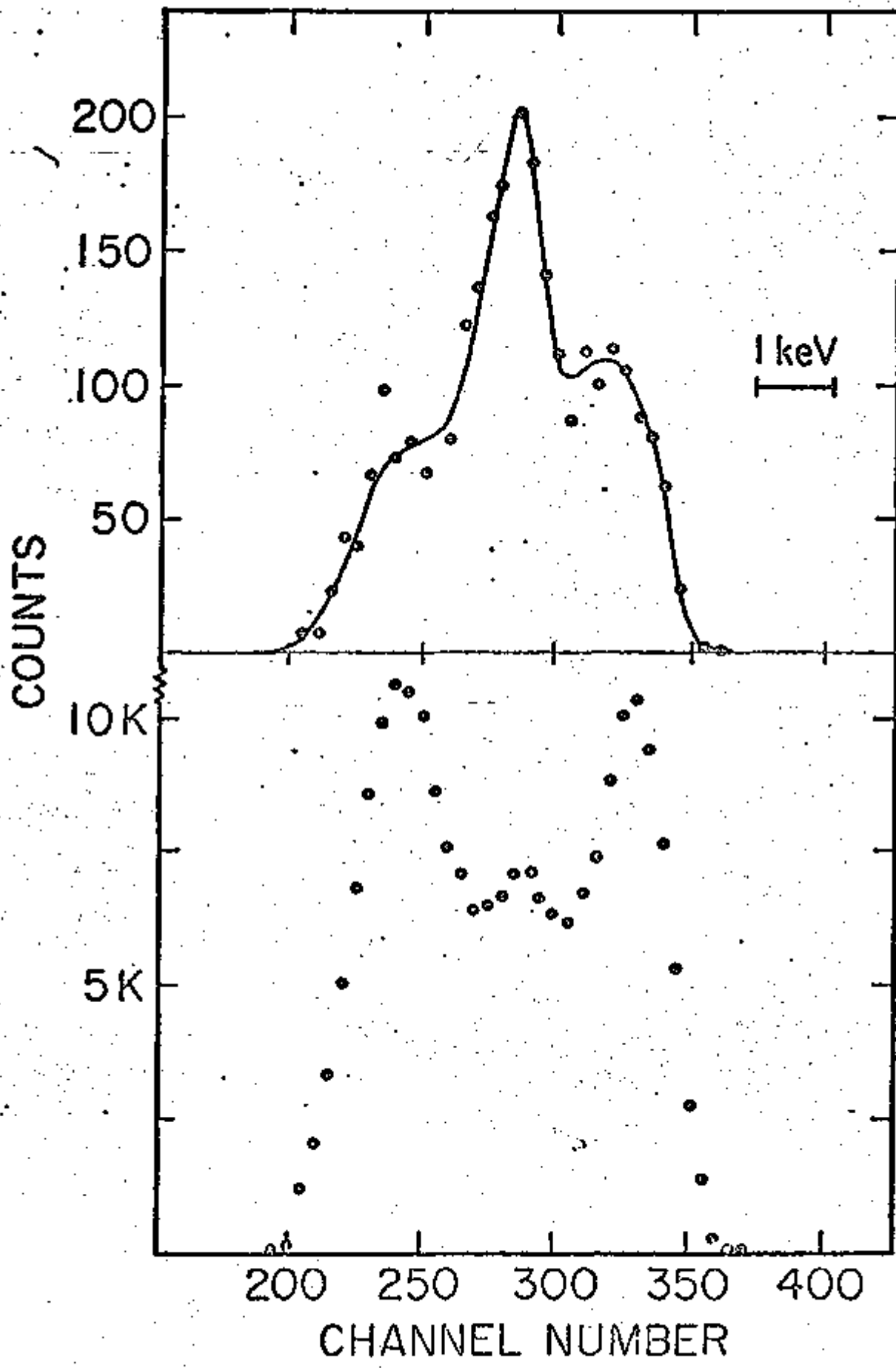


Fig. 3



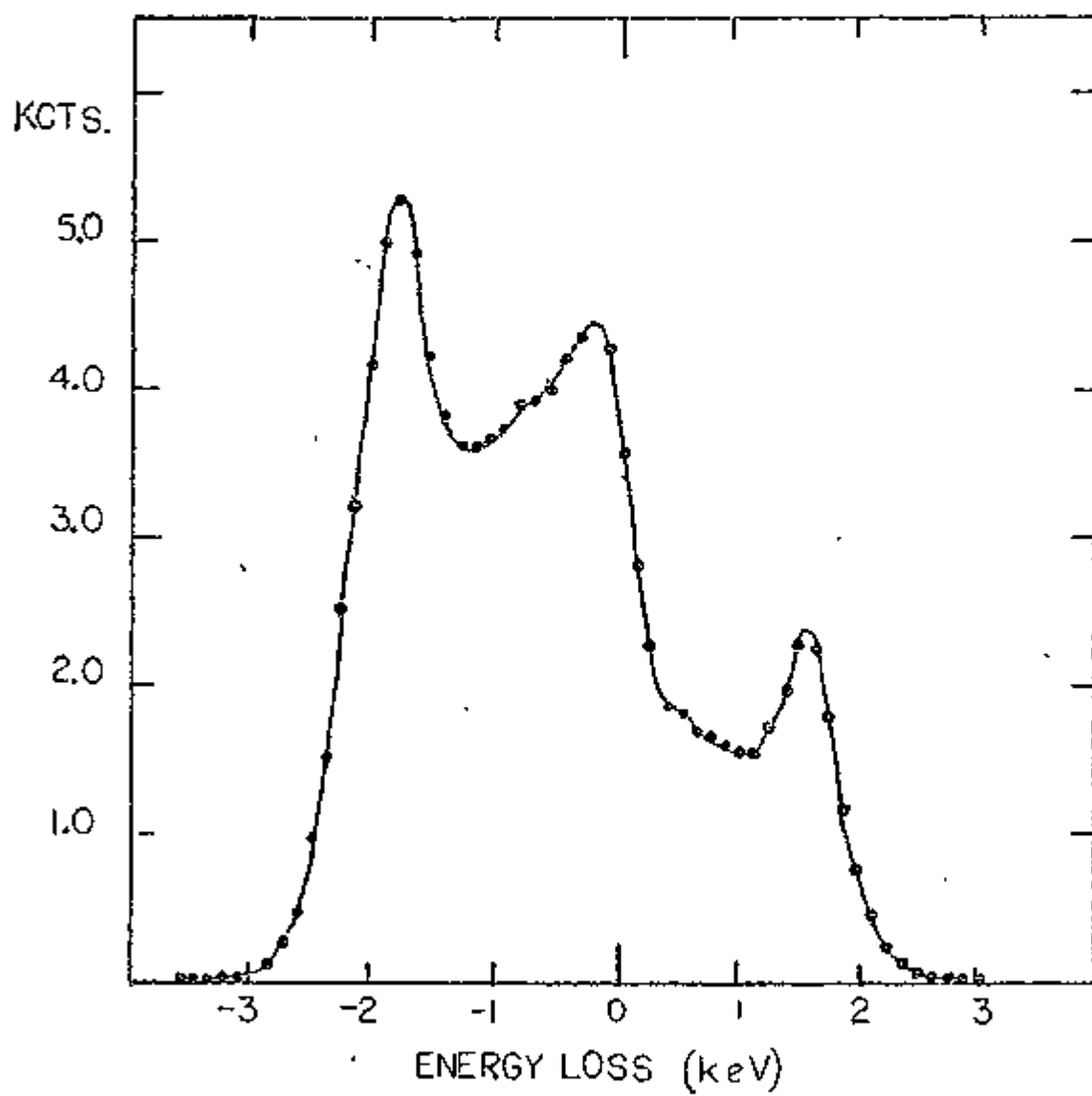


Fig. 4

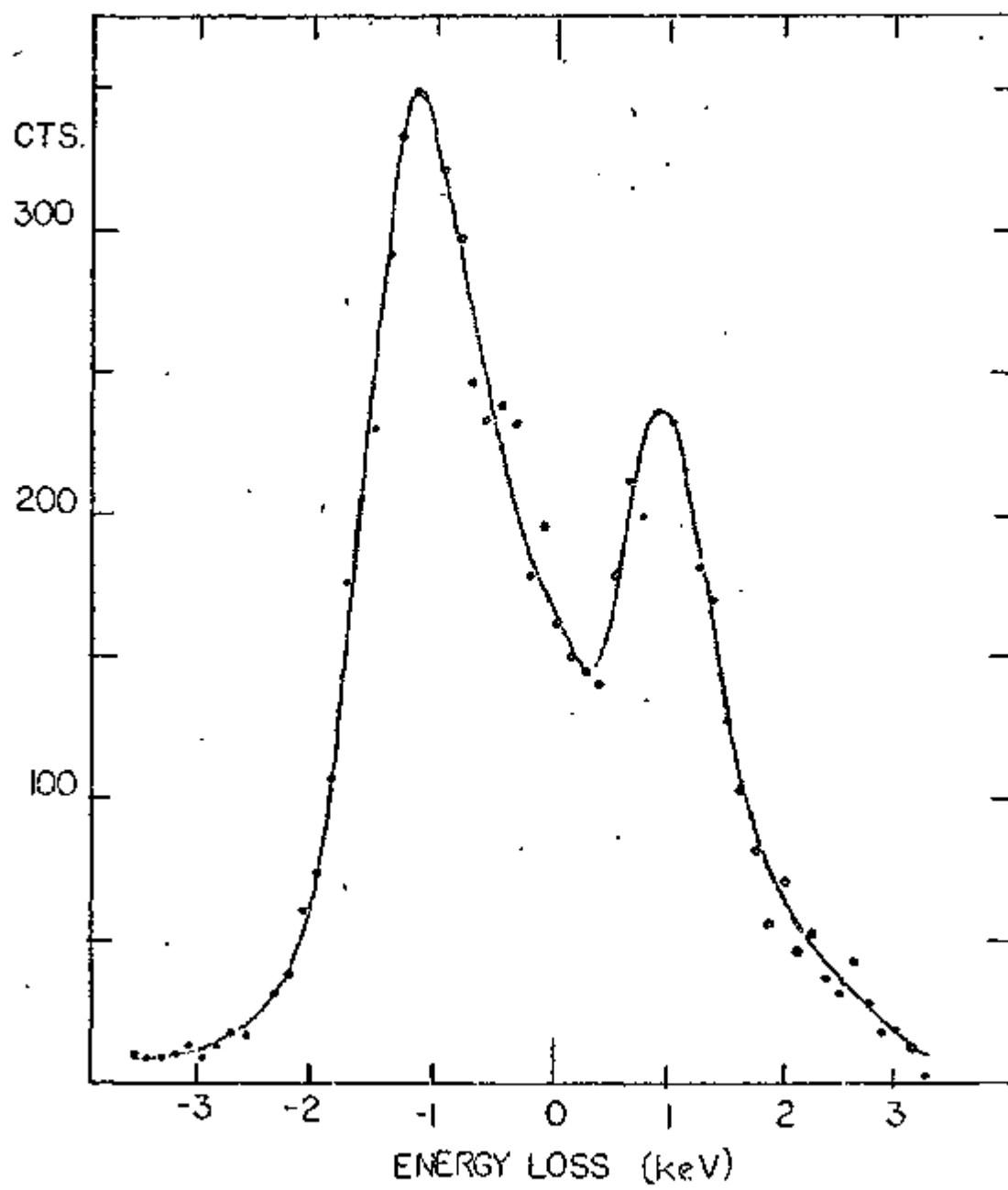


Fig. 5

Fig. 4. The energy distribution of emerging protons when 300 keV HeH<sup>+</sup> molecules are incident on  $1.4 \pm 2 \mu\text{g}/\text{cm}^2$  carbon targets.

Fig. 5. The energy distribution of emerging neutral hydrogen atoms when 300 keV HeH<sup>+</sup> molecules are incident on  $1.4 \pm 2 \mu\text{g}/\text{cm}^2$  carbon targets.

### 3. Clusters penetration through solids (Brandt, Chen, Kwang, Laubert)

To increase our understanding of the nature of the interaction of fast charged particles with matter we have undertaken an experimental and theoretical program to study the energy loss of molecular projectiles in solid targets.

The experimental procedure outlined in the previous section permits us to measure the energy distribution and energy loss of exiting charged and neutral particles about the forward ( $\theta=0^\circ$ ) direction. This is a valid experimental technique for the measurement of the average energy loss of all transmitted particles if the mean energy loss is independent of the scattering angle. To ascertain this we measured the energy distribution as a function of the exiting angle by inserting a pair of electrical plates between the target and the entrance slit of MII which allows us to select particles with the scattering angle of interest. An alternative method is to translate, in the horizontal or vertical plane, the entrance slit of MII. This method was employed in measuring the energy distribution

of neutral particles. We check, in Fig. 1, our experimental procedure by measuring the relative intensity distribution of exiting  $H^+$ ,  $H$ , and  $H^-$  as a function of scattering angle for 150 keV protons incident on a  $5.3 \mu\text{g}/\text{cm}^2$  carbon target. The solid line in Fig. 1 is the intensity distribution as calculated by the theory of Meyer<sup>1</sup>. The data agree with the theory irrespective of the experimental procedure (using electric plates or translation of entrance slit) or of the exiting particle. The mean energy loss for  $H^+$  and  $H$  exiting from the above target as measured by the centroid of the distribution as a function of scattering angle is shown in Fig. 2. Except for a slight (~ 5%) increase in the mean energy loss due to nonuniformity of the target and possible correlated electronic and nuclear energy loss (see section 7), the mean energy loss is independent of the scattering angle and the charge state of the exiting particle. Hence a measure of  $\Delta E$  at  $\theta=0$  suffices when atoms are the incident projectiles.

As is evident from Fig. 1 of the previous section, the energy distribution of the exiting particles when molecular ions are incident on solid targets is radically different. In Fig. 3 we show the energy distribution of the exiting protons as a function of the scattering angle for 150 keV/amu  $H_2^+$  incident on  $1.8 \mu\text{g}/\text{cm}^2$  carbon target. The angular distribution, as measured by the angular half width at half maximum,  $\theta_{1/2}$ , is approximately a factor three greater than the angular half width due to protons. This is shown in detail in Fig. 4 where we also note that the angular half width for  $H$  and  $H^-$  is the

same and lies between that observed from  $H^+$  from incident protons and  $H_2^+$  molecules. The half width for exiting molecules is less than that observed for protons. Figure 5 shows the half widths for incident protons and  $H_2^+$  molecules as a function of the incident energy. These measurements are analogous to, and corroborate, the energy distribution measurements.

To determine the mean energy loss when molecules are the incident projectile we need to know the mean energy loss as a function of the scattering angle of the distribution shown in Fig. 3. Although it is not apparent from Fig. 3, the mean energy loss (as determined by the centroid of the distribution) is again independent of the scattering angle. This allows us to extract the energy loss in the forward direction ( $\theta = 0$ ) and compare these results to the energy loss by incident protons in the same target. The ratio of the stopping powers, defined as

$$R = \frac{\Delta E(H_2^+, H^+)}{\Delta E(H^+, H^+)}$$

where the notation  $(H_2^+, H^+)$  refers to incident projectile, in this case  $H_2^+$ , and the exiting projectile, in this case  $H^+$ . The results as a function of the incident energy are shown in Fig. 6. They clearly indicate that at low incident energies the stopping power for clusters is less than for identical velocity protons. At higher incident energies the stopping power of clusters is greater than for atoms indicating the interaction of the wakes of the moving particles in solids. The

solid line is the theoretical result discussed in the next section.

From the above discussion and the experimental results it is evident that wake phenomena are an important consideration in the stopping of charged particles in matter and the technique of using incident molecular projectiles will help to elucidate these aspects. Work is continuing utilizing other projectiles and different target materials.

#### Figure Legends

Fig. 1. The intensity, in arbitrary units, as a function of the exit angle, in milliradians, for 150 keV  $H^+$  incident on  $5.3 \mu\text{g}/\text{cm}^2$  carbon target. The solid line is the theoretical result of Meyer. "Vertical" signifies distribution in the vertical plane while "horizontal" marks the analogous distribution in the horizontal plane.

Fig. 2. The energy loss, in keV, as a function of scattering angle, in mrad, for 150 keV  $H^+$  incident on  $5.3 \mu\text{g}/\text{cm}^2$  carbon target where the exiting charged and neutral particles are observed. The error bar marks the typical experimental uncertainty of  $\pm 3\%$ . The arrow marks the HWHM of the intensity distribution.

Fig. 3. The energy distribution at various scattering angles of exiting  $H^+$  when 150 keV/amu  $H_2^+$  molecules are incident on  $1.8 \mu\text{g}/\text{cm}^2$  carbon target.

- Fig. 4. The intensity distribution of the exiting particles ( $H_2^+$ ,  $H^+$ ,  $H$ , +  $H^-$ ) as a function of scattering angle when 150 keV/amu  $H_2^+$  molecules are incident on  $1.8 \mu\text{g}/\text{cm}^2$  carbon target. For comparison the ( $H^+$ ,  $H^+$ ) distribution is shown for the same target.
- Fig. 5. The HWHM of the intensity distribution,  $\theta_{1/2}$ , in mrad, for  $1.8 \mu\text{g}/\text{cm}^2$  carbon target as a function of the incident energy in keV/amu. The proton results are shown for comparison.
- Fig. 6. The ratio of the cluster to atom energy loss,  $\Delta E(H_2^+, H^+)/\Delta E(H^+, H^+)$ , as a function of the incident cluster energy for a solid carbon target of  $1.8 \mu\text{g}/\text{cm}^2$ . The error bar marks the experimental uncertainty of  $\pm 5\%$  for each energy loss measurement. The solid line is the theoretical result discussed in the next section.

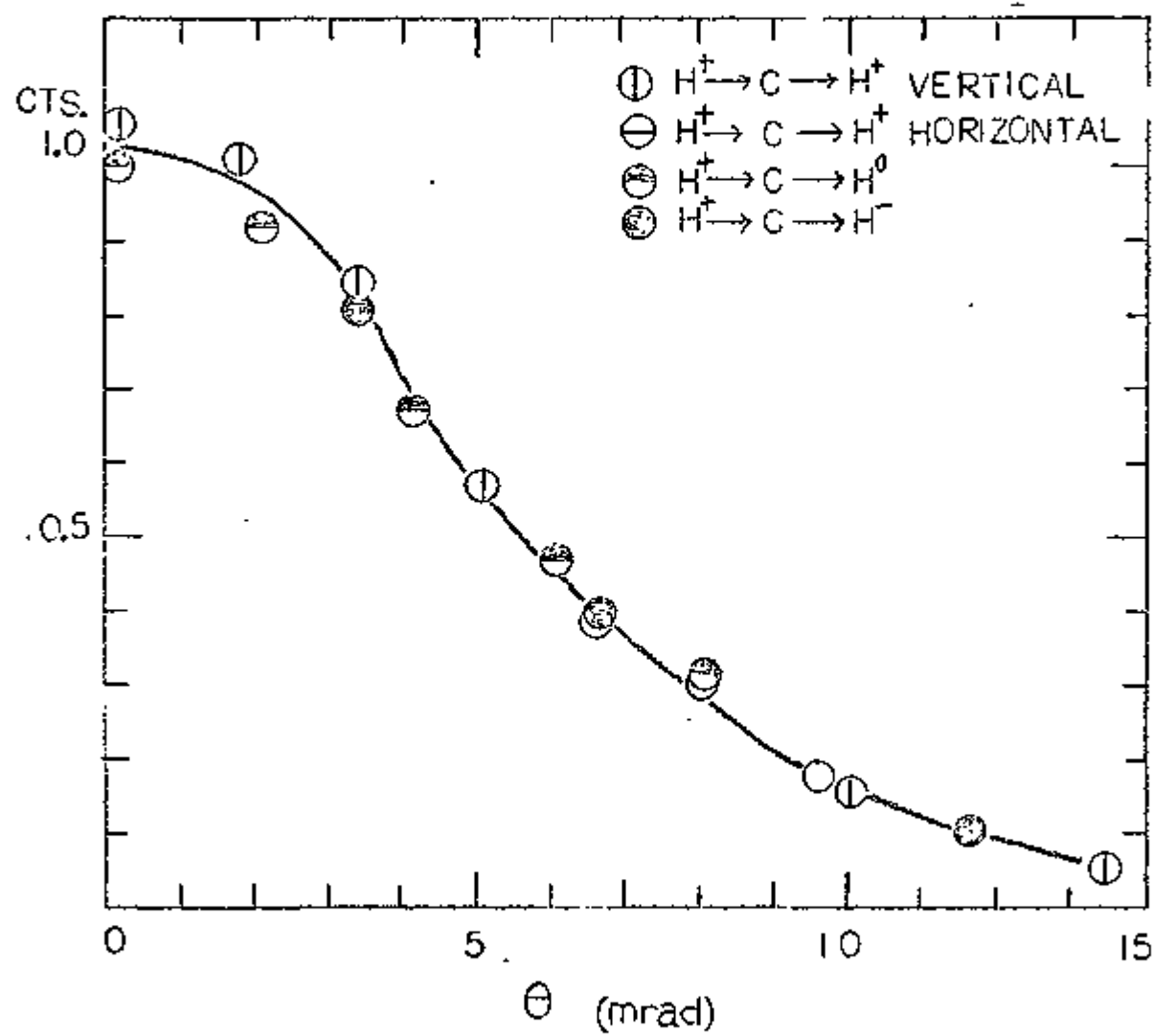


Fig. 1



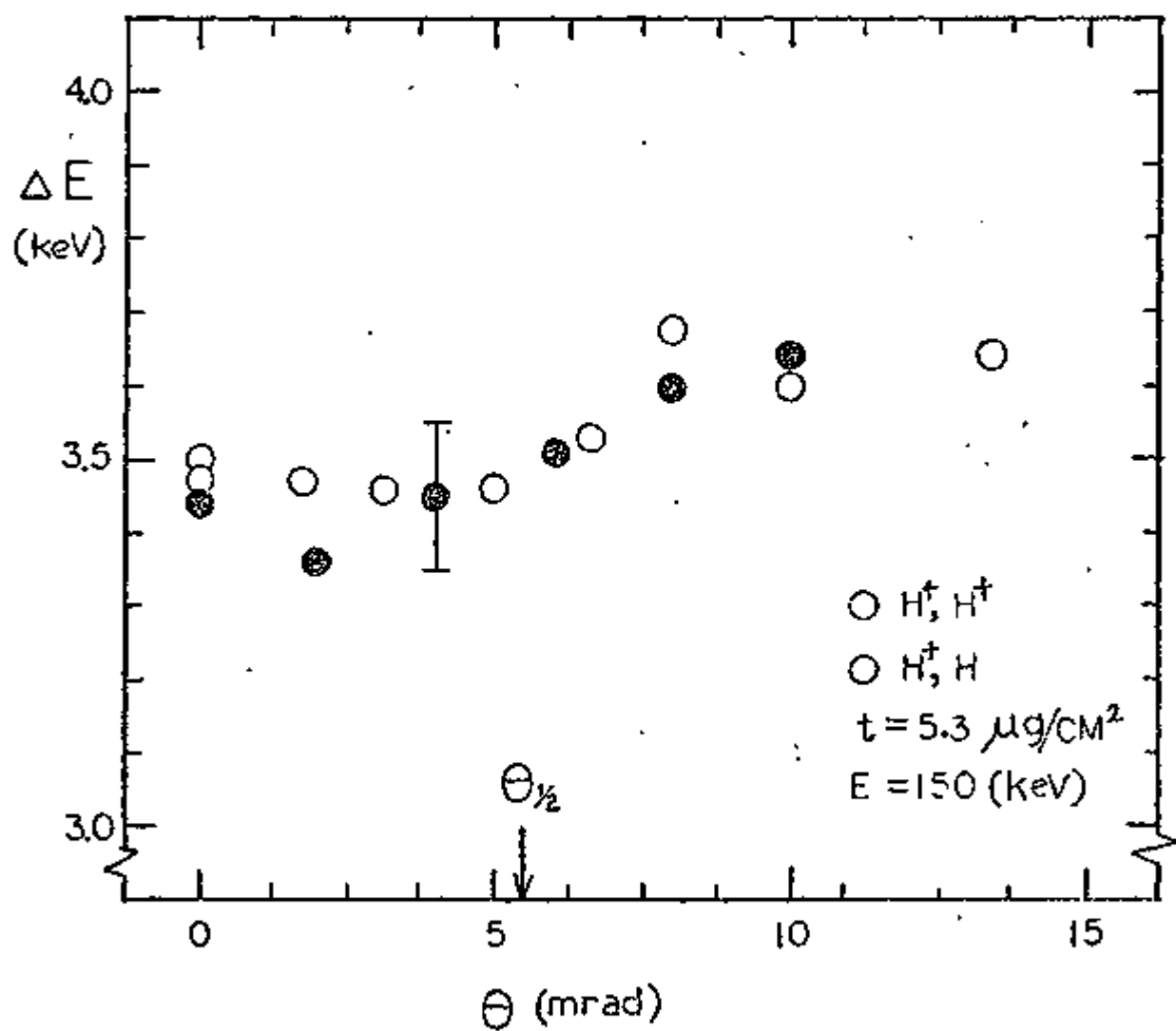


Fig. 2

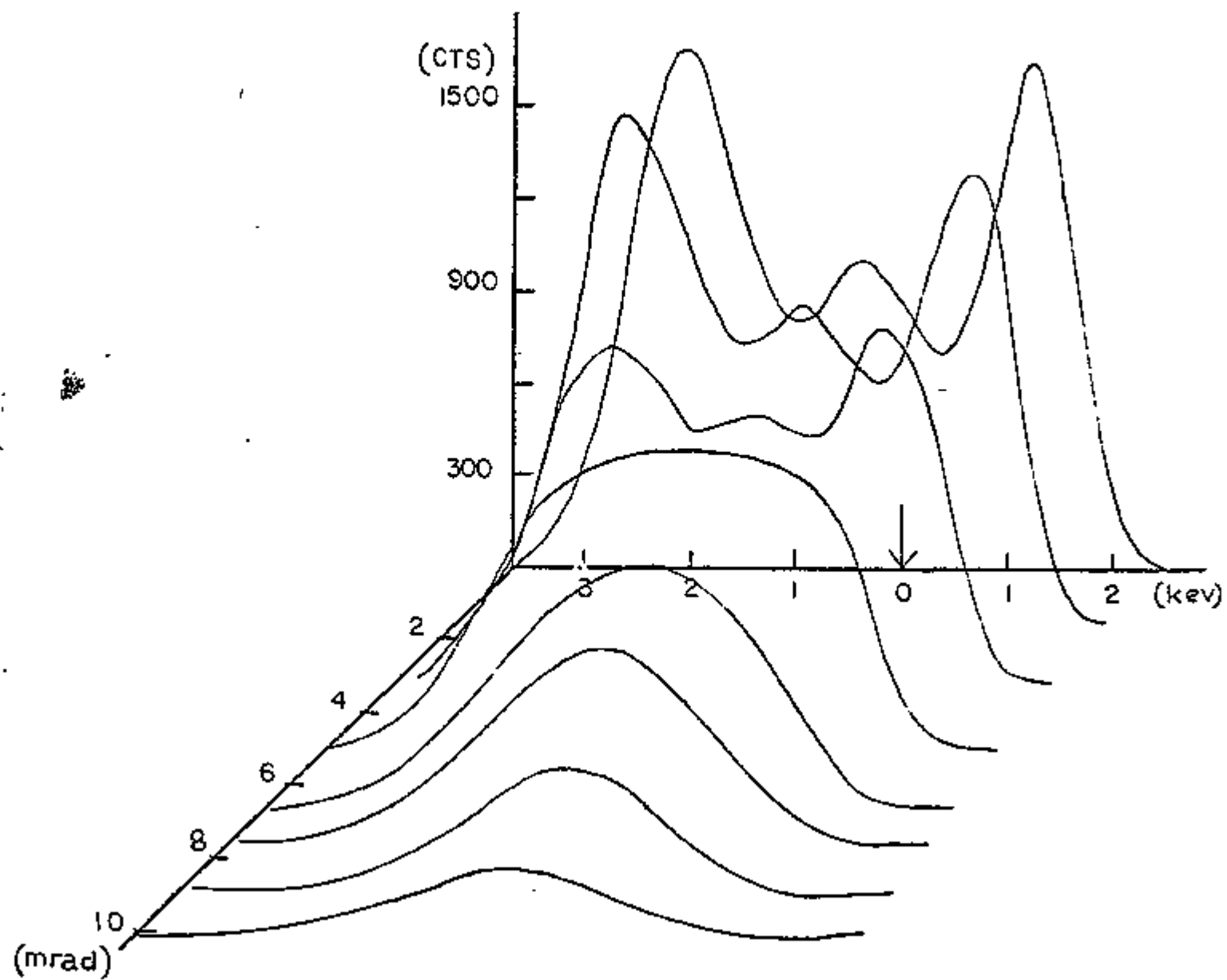


Fig. 3'

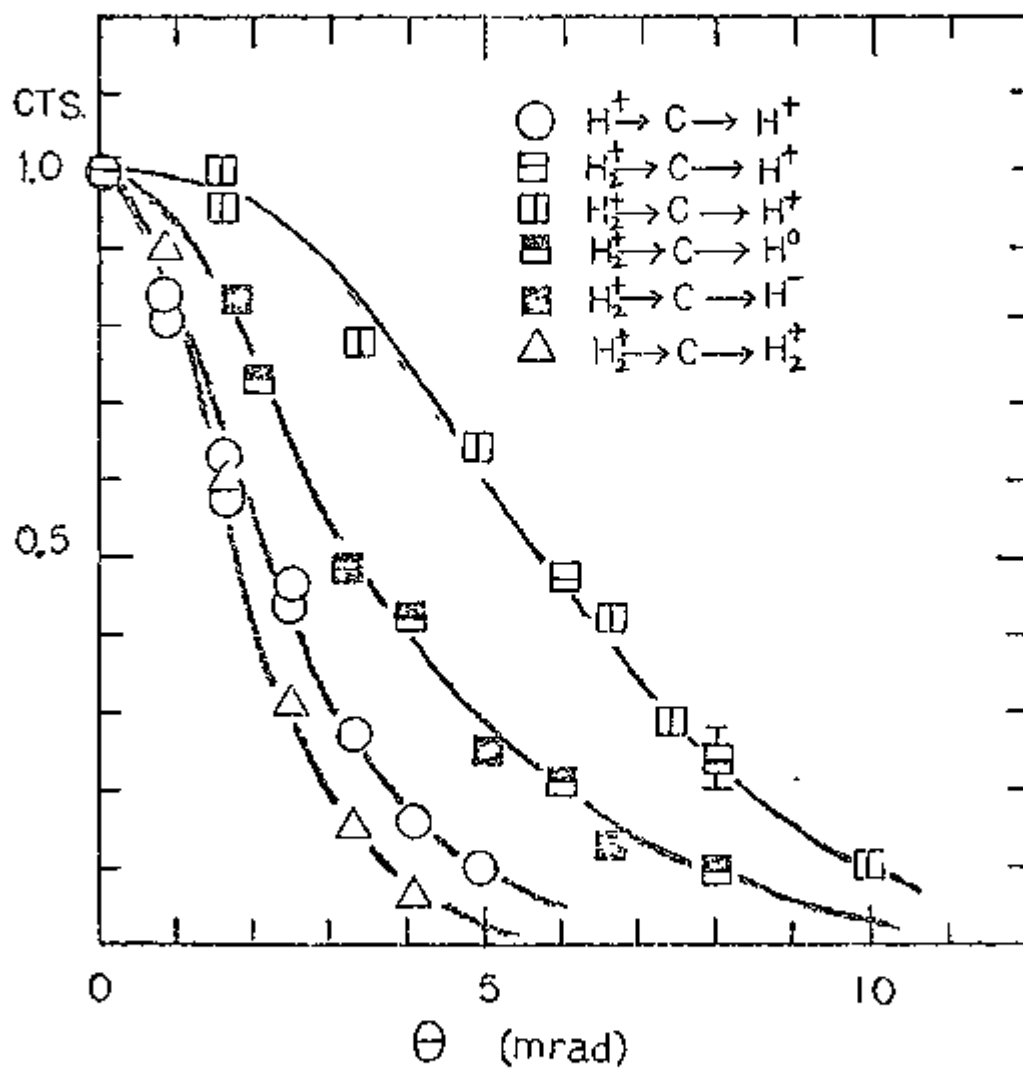


Fig. 4

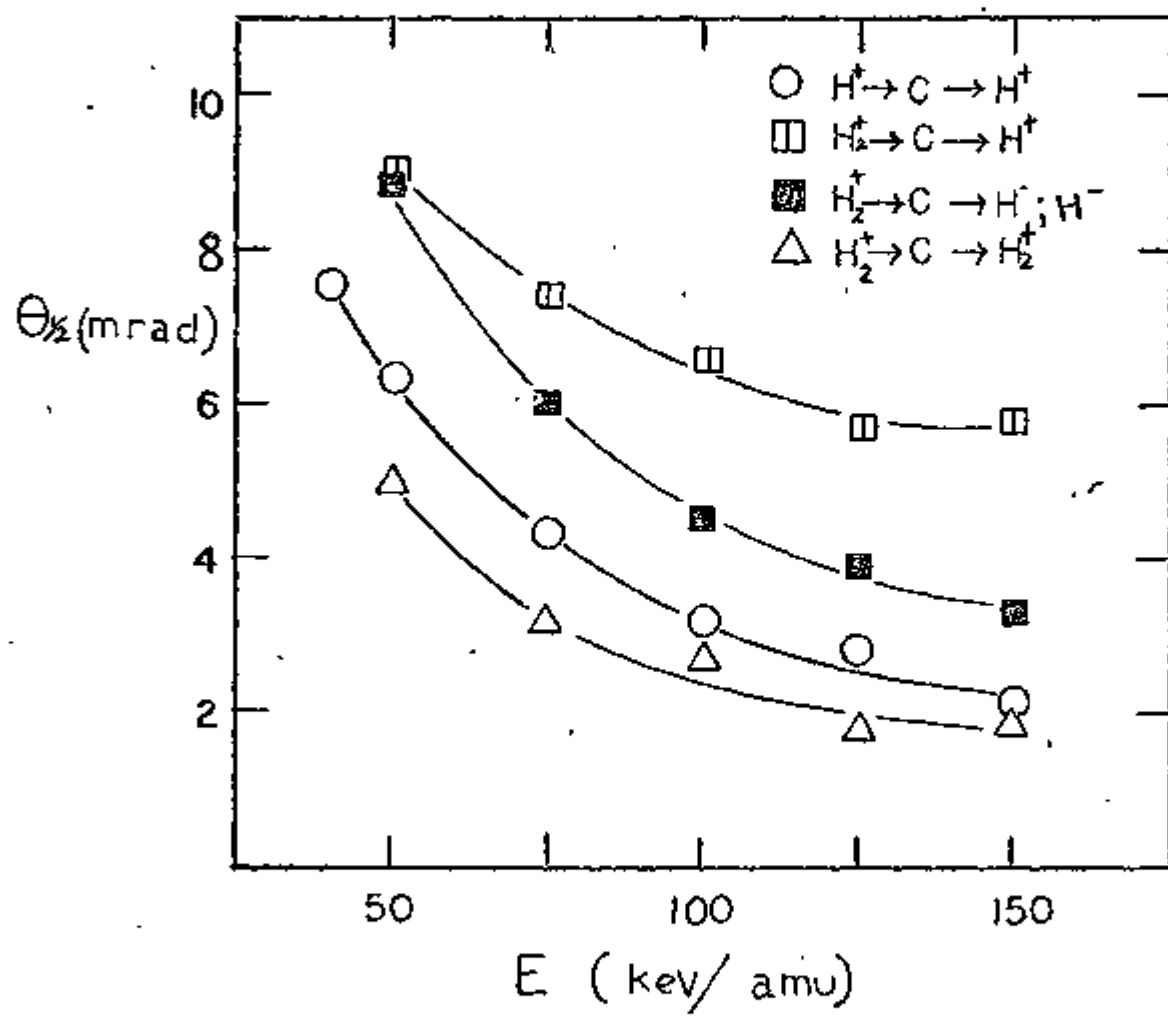


Fig. 5

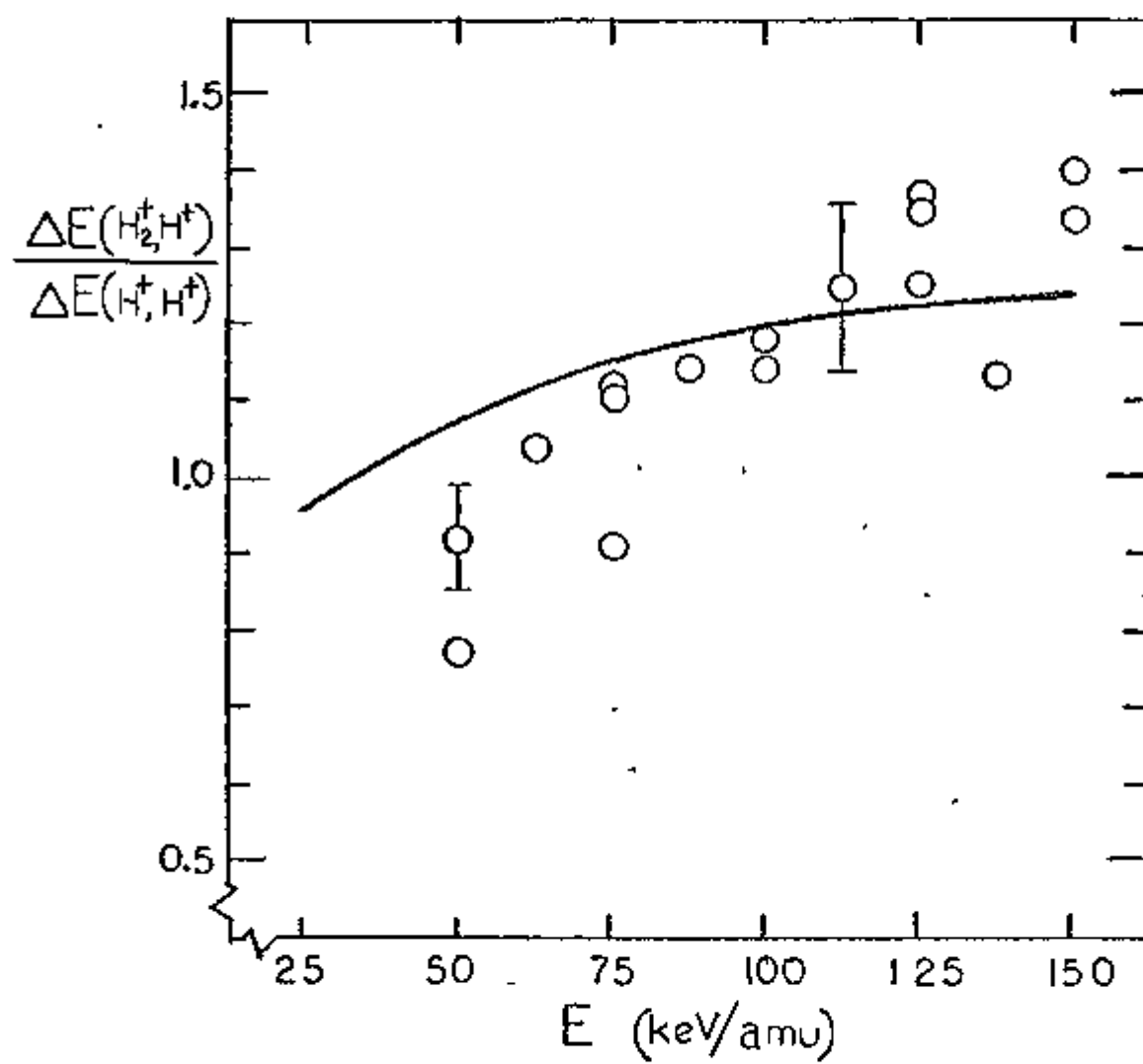


Fig. 6

#### 4. Stopping Power Maxima (Stanton)

It is well known from experiment that the electronic stopping power for any target increases as  $1/v^2$  when the velocity  $v$  of the projectile decreases and reaches a maxima before decreasing to zero with  $v$ . From the Bethe-Bloch expression for the stopping power

$$\left| \frac{dE}{dr} \right| = \frac{4\pi Z_1^2 N Z_2}{v^2} L, \quad (1)$$

where

$$L = \frac{1}{Z_2} \sum_{i,k} f_{ik} \log \frac{2v^2}{\omega_{ik}}, \quad (2)$$

$Z_1$  and  $Z_2$  are the atomic numbers for the projectile and target, respectively,  $N$  is the atomic density, and  $f_{ik}$  is the oscillator strength for a transition  $(i+k)$  of frequency  $\omega_{ik}$ . The increase of  $\left| \frac{dE}{dr} \right|$  as  $v$  decreases is evident. However, the position and shape of the maximum is incorrect, and the appearance of negative terms for  $\omega_{ik} > 2v^2$  is unphysical. Rather than seeking a different expression for  $L$ , it has been argued<sup>1</sup> that the decrease in the number of oscillators able to contribute to the stopping is more important than the form of  $L$  in determining the maximum. When the effect of the decrease in the number of effective oscillators with decreasing  $v$  becomes equal to the  $1/v^2$  increase in  $\left| \frac{dE}{dr} \right|$ , the stopping power has its maximum value.

To implement this picture we neglect negative terms which appear in  $L$ . For a statistical model of the atom, the expression for  $L$  requires an integration rather than a summation, and the

neglect of negative terms is accomplished by a cutoff in the upper limit of integration. Equation (2) becomes

$$L = \int_0^{\Omega_c = 2X} d\Omega g(\Omega) \log \frac{2X}{\Omega}, \quad (2)$$

where  $g(\Omega)$  is the differential oscillator strength distribution as a function of the scaled frequency  $\Omega = \omega/Z_2$  and  $X = v^2/v_0 Z_2$ .

In Fig. 1, the stopping cross section,  $S = \frac{1}{4\pi N Z_1^2} \left| \frac{dE}{dr} \right|$  ( $\times 10^{-15}$  eV-cm<sup>2</sup>), calculated with two different expressions for  $g(\omega)$ , is compared with proton data for  $Z_2$  ranging from 1 to 83. Both curves are universal in the variable  $X$  and are calculated using the Lenz-Jensen ground state density distribution. The solid curve uses  $g(\omega) = -1/3 \int dr r^3 \left[ 2 \frac{d\omega_0^2}{dr} + \frac{r}{4} \frac{d^2\omega_0^2}{dr^2} \right] \delta(\omega_0(r) - \omega)$ , an expression derived previously.<sup>2</sup> The dashed curve employs  $g(\omega) = \int dr r^2 \omega_0^2(r) \delta(\omega_0(r) - \omega)$ , an expression written down by Lindhard and Scharff<sup>3</sup> in heuristic analogy to a uniform electron system, and derived by Brandt and Lundquist for an atom.<sup>4</sup> In both expressions  $\omega_0^2 = 4\pi\rho_0(r)$  is a local plasma frequency for a the ground state density distribution  $\rho_0(r)$ . For  $X \geq 0.1$ , the curves cannot be distinguished and as  $X$  increases beyond the range shown. The data for all targets follow the curves closely. As one moves from higher to lower values of  $X$ , the general trend is consistent with what one should expect. Since statistical models of an atom are considered to be correct only in the limit of infinite  $Z_1$ , the data points should approach the universal curve as  $Z_2$  increases. It is also clear that the preponderance of the data from high  $Z_2$  targets tend to

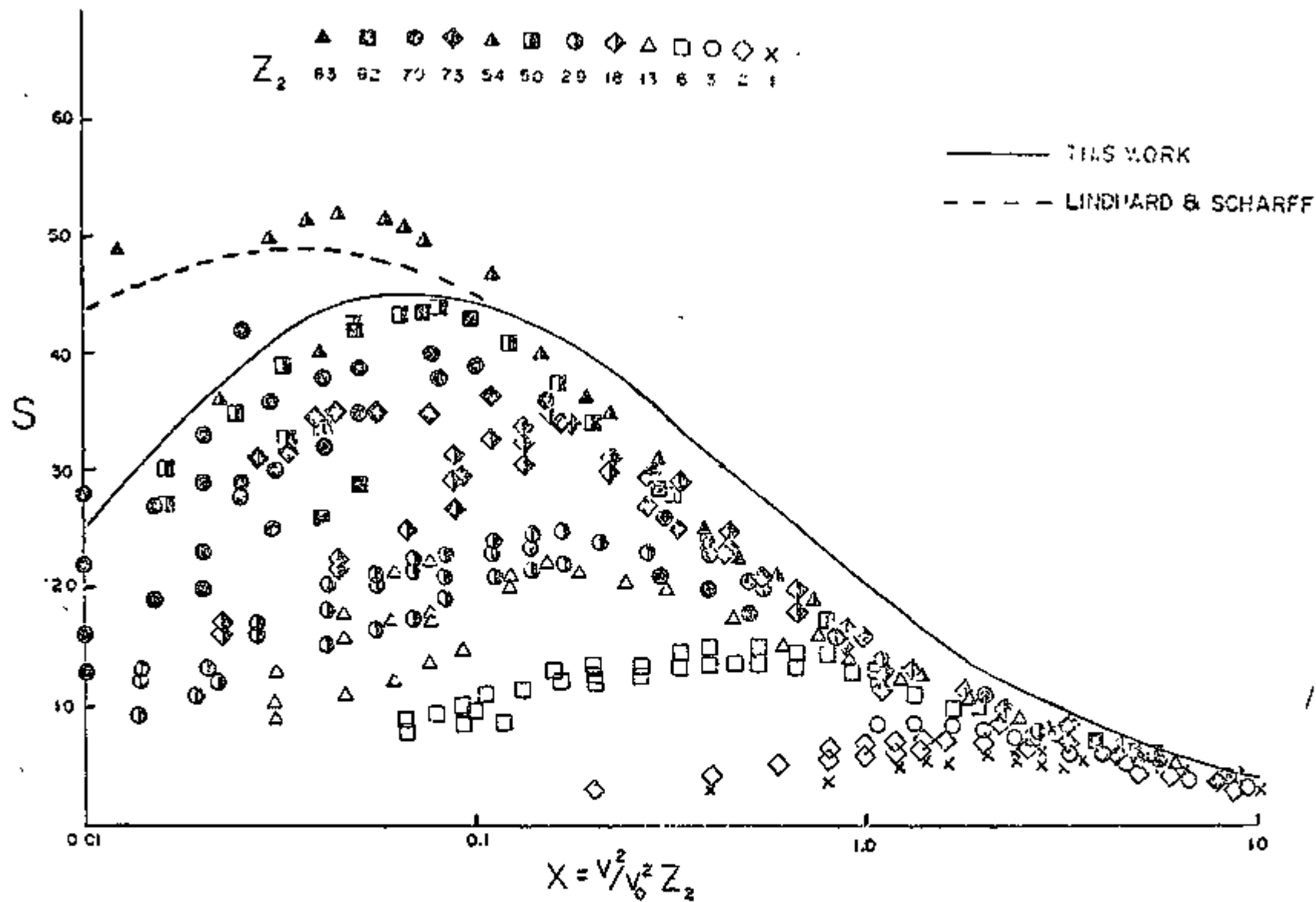
follow the solid curve rather than the dashed curve in that region where the curves exhibit a difference.

In view of the simplicity of the model, the agreement between theory and experiment is reasonable. One should not expect the maximum to occur at the same  $X$  value for every target. The gap between theory and experiment might be narrowed through the use of an appropriate set of ground state wave functions and a  $Z_2$ -dependent cutoff in the integration over frequency.

#### References

1. W. Brandt, J. Lindhard, and M. Scharff, in Proc. 2<sup>nd</sup> Intl. Conf. Physics of Electronic and Atomic Collisions, Boulder 1961 (W. A. Benjamin, Inc., New York, 1961).
2. K. Stanton, thesis, New York University (1971) (unpublished).
3. J. Lindhard and M. Scharff, Mat.-Fys. Medd. Dan. Vid. Selsk. 27, 15 (1953).
4. W. Brandt and S. Lundquist, Phys. Rev. 132, 2135 (1963).





### 5. Projectile-Charge Dependence of Stopping Powers (Brandt, Ritchie, ORNL)

The stopping power of matter for particles of charge  $Z_1e$  moving with velocity  $v_1$  is proportional to  $Z_1^2$  in the Bethe theory of energy loss.<sup>1</sup> The theory has been extended to include the polarization of the target atoms by the projectile which, to lowest order, gives a polarization term proportional to  $Z_1^3$ .<sup>2</sup> The results of this development were confirmed in a quantum-mechanical harmonic-oscillator approximation which leads to identical formulae.<sup>3</sup>

When averaged over the target atom, the  $Z_1^3$ -dependent terms contain a scaled minimum impact parameter, denoted as  $b$ . It is of order unity and essentially independent of the atomic number,  $Z_2$ , of the substance in which the projectile moves. Adjusting on relative stopping powers<sup>4</sup> of  ${}_{13}\text{Al}$  and  ${}_{73}\text{Ta}$  for  ${}^1_1\text{H}$  and  ${}^4_2\text{He}$  yielded a first trial value  $b = 1.8$ .

In new experiments Andersen, Sak, Knudsen, and Nielsen<sup>5</sup> extended the measurements to relative stopping powers of  ${}_{13}\text{Al}$ ,  ${}_{29}\text{Cu}$ ,  ${}_{47}\text{Ag}$ , and  ${}_{79}\text{Au}$  for  ${}^1_1\text{H}$ ,  ${}^4_2\text{He}$ , and  ${}^6_3\text{Li}$  ions in the range  $v_1 = 7v_0$  to  $v_1 = 12v_0$ , where  $v_0 = e^2/\hbar$ . Data have been reported by the Oak Ridge group<sup>6</sup> on the stopping of  ${}^1_1\text{H}$ ,  ${}^4_2\text{He}$ ,  ${}^6_3\text{Li}$ ,  ${}^{10}_5\text{B}$ ,  ${}^{12}_6\text{C}$ ,  ${}^{14}_7\text{N}$ ,  ${}^{16}_8\text{O}$ , and  ${}^{18}_9\text{F}$  ions in  ${}_{79}\text{Au}$  targets. It is the purpose of this note to present an analysis of these data

in terms of current theory, and to assess the importance of polarization effects and projectile charge states on the stopping power of matter. In Sec. 2, the cutoff parameter  $b$  is determined on the light-ion data. Alternate models for the polarization terms, depending on the choice of cutoff parameter, are examined in Sec. 3 and found to be in need of inner-shell corrections for their application. The data analysis for heavy ions in Sec. 4 agrees with that for light ions provided one invokes effective-charge theory.

## 2. Light ions

We write the stopping power,  $S = -dE_1/dx$ , of a medium composed of atoms with atomic number  $Z_2$  at density  $n$  for particles of non-relativistic velocity  $v_1$ , or kinetic energy  $E_1 = \frac{1}{2}M_1 v_1^2$ , where  $M_1 = A_1 M_0$  is the mass of the ion of atomic weight  $A_1$ ,  $N_0 = 1836 m$  being the atomic mass unit (amu) and  $m$  the electron mass, in the form

$$S = \frac{4\pi Z_1^2 e^4 n Z_2}{m v_1^2} (L_B + Z_1 L_1 + Z_1^2 L_2 + \dots) . \quad (1)$$

Here

$$L_B = L_0 + \phi = \log \frac{2mv_1^2}{I_0} - \frac{C_0}{Z_2} + \phi\left(\frac{Z_1 e^2}{\hbar v_1}\right) \quad (2)$$

is the Bethe-Bloch stopping number per target electron<sup>7</sup> in terms of the mean ionization potential  $I_0 = K_0 Z_2$  of the medium,  $K_0$  being the Bloch constant. The term  $C_0/Z_2$  accounts for inner-shell corrections. The function  $\phi(\xi)$ , with  $\xi \equiv \frac{Z_1 e^2}{\hbar v_1}$ , is given in terms of  $\psi$ , the logarithmic derivative of the gamma function,

$$\phi(\xi) = \psi(1) - \text{Re}\psi(1+i\xi) \quad (3)$$

It connects the classical theory, valid when  $\xi \gg 1$ , with the quantum mechanical theory, valid when  $\xi \ll 1$ .

The function  $L_1$ , averaged over the statistical Lenz-Jensen model of the target atom, can be written in the compact form<sup>2</sup>

$$L_1(b;x) = \frac{\Gamma(b/x^{1/2})}{Z_2^{1/2} x^{3/2}} \quad (4)$$

Table I where  $x \equiv v_1^2/Z_2 v_0^2 = 40E_1(\text{MeV})/A_1 Z_2$ . Table I gives values of the function  $Z_2^{3/2} L_1(b;x)$  for a range of  $b$  values. Without including  $\phi(\xi)$ , analysis of early data<sup>4</sup> gave the trial value  $b = 1.8$ . The more extensive recent data<sup>5</sup> yield, with the inclusion of  $\phi(\xi)$ ,

larger  $L_1$  values, corresponding to a new "best" parameter value  $b = 1.4 \pm 0.1$  for targets with  $Z_2 > 13$ . In fitting to the data, we set

$$L_1 + Z_1 L_2 + Z_1^2 L_3 + \dots = L_1 [1 + Z_1 \frac{L_2}{L_1} + Z_1^2 \frac{L_3}{L_1} + \dots] = L_1 \quad (5)$$

because exploratory calculations<sup>8</sup> indicate that  $\sum_{v=2}^{\infty} Z_1^v L_v / Z_1 L_1$  can have positive or negative values depending on stopping conditions, but that the absolute value in this velocity range may be  $\ll 1$ .

### 3. $Z_1^3$ terms

The polarization stopping number  $L_1$  was evaluated first with an inner cutoff distance  $a_\omega$  proportional to the orbital radius,  $r$ , of the electrons responding with frequency  $\omega(r)$ .<sup>2</sup> When averaged over the atom this yields the empirically determined parameter  $b = 1.4$ . Other models equate  $a_\omega$  with the harmonic oscillator amplitude<sup>9</sup>,  $a_\omega = (\hbar/2m\omega)^{1/2}$ , and the quantum mechanical minimum impact parameter<sup>10</sup>,  $a_\omega = \hbar/2mv_1$ . When one averages these models over the target atom, one can write

$$L_1 = \frac{3\pi e^2 G}{4mv_1^3} \int_0^\infty g(\omega) \omega d\omega \log \frac{2mv^2}{\hbar\omega} - \frac{C_1}{Z_2} \quad (6)$$

$$= \frac{3\pi e^2 G}{4mv_1^3 \hbar} W_1 \log \frac{2mv^2}{I_1} - \frac{C_1}{Z_2}, \quad (7)$$

where  $G = 1$  if  $a_\omega = (\hbar/2m\omega)^{1/2}$  and  $G = 2$  if  $a_\omega = (\hbar/2mv_1)$ ;  $g(\omega)$  is the differential oscillator strength distribution of the target atom normalized such that  $\int_0^\infty g(\omega)d\omega = 1$ , and  $C_1/Z_2$  denotes inner-shell corrections of  $L_1$ . Equation (7) introduces energies  $W_1$  and  $I_1$  as

$$W_1 = k_1 Z_2 = \hbar \int_0^\infty g(\omega)\omega d\omega, \quad (8)$$

$$\log I_1 = \log K_1 Z_2 = \hbar \int_0^\infty g(\omega)\omega d\omega \log \hbar\omega/W_1. \quad (9)$$

Similarly, the Bethe stopping number is

$$L_0 = \int_0^\infty g(\omega)d\omega \log \frac{2mv_1^2}{\hbar\omega} - \frac{C_0}{Z_2} = \log \frac{2mv_1^2}{I_0} - \frac{C_0}{Z_2} \quad (10)$$

such that

$$\log I_0 = \log K_0 Z_2 = \int_0^\infty g(\omega)d\omega \log \hbar\omega. \quad (11)$$

One may evaluate the constants  $K_0$ ,  $k_1$ , and  $K_1$  from moment integrals<sup>11-13</sup>,  $s(k)$ , defined as

$$s(k) = \int_0^\infty g(\omega)(\hbar\omega)^k d\omega, \quad (12)$$

and normalized such that  $S(0) = 1$ . Treating  $s(k)$  as an analytical function of  $k$ , one obtains the approximations

$$W_1 = s(1), \quad (13)$$

$$\log I_1 = s^{-1}(1)[ds(k)/dk]_{k=1}, \quad (14)$$

$$\log I_0 = [ds(k)/dk]_{k=0}. \quad (15)$$

Tables of  $s(k)$  are available.<sup>14,15</sup> For illustration, we have calculated the constants for some elements, using Dalgarno's interpolation formula,<sup>13</sup> with the results given in Table II. The Bloch constants  $K_0$  so obtained agree well with experimental data.<sup>16</sup>

In terms of the Lenz-Jensen statistical model of the atom<sup>2</sup> with density  $\rho^{LJ}$ , one can estimate, with  $\omega(r) = \chi[4\pi e^2 \rho^{LJ}(r)/m]^{1/2}$ ,

$$W_1^{LJ} = K_1^{LJ} Z_2 = 4\pi Z_2^{-1} \int_0^\infty \rho^{LJ}(r) \mu \omega(r) r^2 dr, \quad (15)$$

$$\log I_1^{LJ} = \log K_1^{LJ} Z_2 = 4\pi Z_2^{-1} \int_0^\infty \rho^{LJ}(r) \mu \omega(r) r^2 dr \log \mu \omega(r) / W_1^{LJ}, \quad (17)$$

and

$$\log I_0^{LJ} = \log K_0^{LJ} Z_2 = 4\pi Z_2^{-1} \int_0^\infty \rho^{LJ}(r) r^2 dr \log \mu \omega(r). \quad (18)$$

The LJ constants, with  $\chi = 1.29$ , are listed in Table II. In comparison with Eq. (4) and Eqs. (16) to (18), the constants for atoms up to  $Z = 54$ , calculated by the method of moment integrals, are larger and have additional  $Z_2$  dependences. Over the entire range of  $x$  values under discussion,  $1 \leq x \leq 11$ , these differences can only be studied and the relative merits of the two model approximations represented by the parameter  $G$  be assessed when, in analogy to  $C_0/Z_2$  for  $L_0$ , inner-shell corrections  $C_1/Z_2$  are developed for  $L_1$ .

#### 4. Heavy ions

The Oak Ridge stopping power data<sup>6</sup> of ions,  $1 \leq Z_1 \leq 9$ , moving at  $v_1 = 8.94v_0$  and  $v_1 = 11.98v_0$  in random  $^{79}\text{Au}$  foils,

were treated in a manner similar to that described in Section 2. The data for channeled ions require separate considerations.<sup>17</sup> According to the effective-charge theory<sup>18</sup>, one may write

$$S = Z_1^{*2}(v_1)S_0, \quad (19)$$

where  $Z_1^*(v_1)$  is the effective charge of the ion which depends on  $v_1$  but only weakly on the medium.  $S_0$  is the stopping power per unit charge in the limit  $Z_1 \rightarrow 0$ . Setting

Fig. 1  $Z_1^* = Z_1[1 - \exp(-0.95v_1/Z_1^{2/3}v_0)]$ , the data,  $S$ , are plotted in Fig. 1 in the form

$$L = \frac{mv_1^2}{4\pi e^4 n Z_2} \frac{S}{Z_1^{*2}} - \phi\left(\frac{Z_1^* e^2}{\hbar v_1}\right) \quad (20)$$

as a function of  $Z_1$ . Extrapolation to  $Z_1 \rightarrow 0$  yields  $L_0(8.94v_0) = 1.44 \pm 0.04$  and  $L_0(11.9v_0) = 1.86 \pm 0.05$ . By comparison, Eq. (10) gives for  $^{79}\text{Au}$ , with  $I_0 = 797$  eV and  $C_0/Z_2 = 0.27$  at  $v_1 = 8.94v_0$  and  $C_0/Z_2 = 0.38$  at  $v_1 = 11.9v_0$ , the stopping numbers  $L_0(8.94v_0) = 1.43$  and  $L_0(11.9v_0) = 1.87$ .

This permits one to extract  $L_1$  from the data, in the form  
Table III  $(L-L_0)/Z_1^*$  as collated in Table III, with mean values  $L_1(8.94v_0) = 0.10$  and  $L_1(11.9v_0) = 0.08$ . From Table I with  $b = 1.4$ , we find  $L_1(8.94v_0) = 0.104$  and  $L_1(11.8v_0) = 0.079$ . The fluctuations in Table III may be indicative of contributions from  $L_v$ ,  $v > 1$ , but they do not exceed experimental uncertainties. The trend of the  $8.94v_0$  data could signify that they may be negative, as are some results from preliminary calculations<sup>8</sup>. This merits further study.



In conclusion, current nonrelativistic stopping-power data in the ranges  $1 \leq Z_1 \leq 9$ ,  $7 \leq v_1/v_0 \leq 12$ , and  $13 \leq Z_2 \leq 79$  are consistent with the theory of  $Z_1^3$  effect, assuming that effective-charge theory applies. Comparison of experiments with calculations of the polarization stopping number  $L_1$  by the method of moment integrals and the assessment of the underlying models require the development of inner-shell corrections to the  $Z_1^3$ -proportional stopping power contributions.

## References

- \* Permanent address: Oak Ridge National Laboratory, Oak Ridge, Tennessee 37830
- † Permanent address: Department of Physics, New York University, New York, New York 10003.
1. H. A. Bethe, *Ann Physik* 5, 325 (1930).
  2. J. C. Ashley, R. H. Ritchie, and W. Brandt, *Phys. Rev. B* 5, 2393 (1972); *Phys. Rev. A* 8, 2402 (1973); *Phys. Rev. A* 10, 737 (1974). J. C. Ashley, V. E. Anderson, R. H. Ritchie, and H. Brandt,  $Z_1^3$  Effects in the Stopping Power of Matter for Charged Particles: Tables of Functions, Document No. 02195, National Auxiliary Publication Service, New York, 1974.
  3. K. W. Hill and E. Merzbacher, *Phys. Rev. A* 9, 156 (1974).
  4. H. H. Andersen, H. Simonsen, and H. Sørensen, *Nucl. Phys. A* 125, 171 (1969).
  5. H. H. Andersen, J. F. Bak, H. Knudsen, B. R. Nielsen, (to be published). See also H. H. Andersen et. al., *Nucl. Instr. Methods* 140, 537 (1977).
  6. S. Datz, J. Ganez del Campo, P. F. Dittner, P. D. Miller, and J. A. Biggerstaff, *Phys. Rev. Letters* 38, 1145 (1977).
  7. H. A. Bethe and J. Ashkin, Passage of Radiations through Matter in Experimental Nuclear Physics, Ed. E. Segrè (Wiley, New York, 1960), Vol. 1, p. 166.

8. G. Basbas, W. Brandt, and R. H. Ritchie, *Bull. Am. Phys. Soc.* 22, 487 (1977).
9. J. D. Jackson and R. L. McCarthy, *Phys. Rev. B* 6, 4131 (1972).
10. H. Esbensen, Thesis, University of Aarhus, Denmark, 1976 (unpublished); J. Lindhard, *Nucl. Instr. Methods* 132, 1 (1976).
11. W. Brandt, *Phys. Rev.* 104, 691 (1956).
12. C. L. Pekeris, *Phys. Rev.* 115, 1216 (1959).
13. A. Dalgarno, *Proc. Phys. Soc. (London)* 76, 422 (1960).
14. V. Fano and J. W. Cooper, *Rev. Mod. Phys.* 40, 441 (1968); 41, 724 (1969).
15. F. E. Cummings, *J. Chem. Phys.* 63, 4690 (1975).
16. Studies in Penetration of Charged Particles in Matter, National Academy of Sciences and National Research Council, Publication 1133, 1964, p. 225.
17. J. C. Ashley and R. H. Ritchie, *Proc. Intl. Conf. Atomic Collisions in Solids, Moscow 1977* (to be published).
18. For a discussion of effective-charge theory and experiment, see Werner Brandt, in Proceedings of the Fifth International Conference on Atomic Collisions in Solids, Gatlinburg, Tenn., 1973, Eds. S. Datz, B. R. Appleton and C. D. Moak (Plenum, New York, 1975), p. 261 ff. For a recent data analysis see B. S. Yarlagadda, J. E. Robinson, and Werner Brandt (to be published).

Table I

The  $Z_1^3$ -dependent stopping number function  $L_1$ , Eq. (1), in a target of atomic number  $Z_2$  as a function of  $x \equiv v_1^2/v_0^2 Z_2$  for various parameters  $b$ . Note that  $x = 40E_1(\text{MeV})/A_1 Z_2$ . The function  $F(w)$  is tabulated in ref. 2.

$Z_2^{1/2} L_1 = F(b/x^{1/2})/x^{3/2}$						
$x$	1.0	1.2	1.4	1.6	1.8	2.0
0.1	3.24	1.81	1.10	0.717	0.491	0.352
0.2	3.23	1.90	1.18	0.774	0.530	0.377
0.4	2.79	1.78	1.17	0.800	0.561	0.404
0.6	2.37	1.59	1.09	0.773	0.557	0.410
0.8	2.04	1.42	1.01	0.728	0.539	0.404
1.0	1.78	1.27	0.928	0.686	0.511	0.392
2.0	2.33	0.821	0.640	0.504	0.400	0.321
4.0	3.51	0.463	0.381	0.317	0.265	0.232
6.0	4.28	0.315	0.266	0.227	0.194	0.167
8.0	4.85	0.235	0.203	0.175	0.152	0.133
10	5.29	0.186	0.162	0.142	0.124	0.110
20	6.71	0.0859	0.0769	0.0692	0.0625	0.0567
40	8.20	0.0379	0.0344	0.0317	0.0292	0.0270
60	9.04	0.0230	0.0212	0.0196	0.0182	0.0170
80	9.68	0.0160	0.0149	0.0138	0.0129	0.0121
100	10.21	0.0120	0.0113	0.0105	0.00985	0.00929

Table II

Atomic constants in  $L_0$  and  $L_1$ , as estimated through Eqs. (13) to (15) from moment integrals  $s(k)$ , for  $-2 \leq k \leq 2$ . Values of  $s(k)$  from ref. 14, empirical  $K_0$  values from ref. 16 and for  $H$  calculated in ref. 1. Uncertainties in the  $s(2)$  values of Ne and Xe were resolved to yield correct  $K_0$  values. The last line is calculated for the Lenz-Jensen (LJ) statistical atom, according to Eqs. (16) to (18), with  $\chi = 1.29$  chosen for  $K_0$  to agree with experiment.

Element	$Z_2$	$k_1$ (eV)	$K_1$ (ev)	$K_0$ (ev)	$K_0$ (emp.) (ev)
H	1	18.1	24.8	14.8	(15.0)
He	2	27.8	41.7	20.9	21.0
Ne	10	43.5	166	12.9	13.1
Ar	18	48.3	177	12.2	11.7
Kr	36	55.6	264	10.2	10.6
Xe	54	60.6	299	10.2	10.3
LJ		30.6	97.6	9.8	

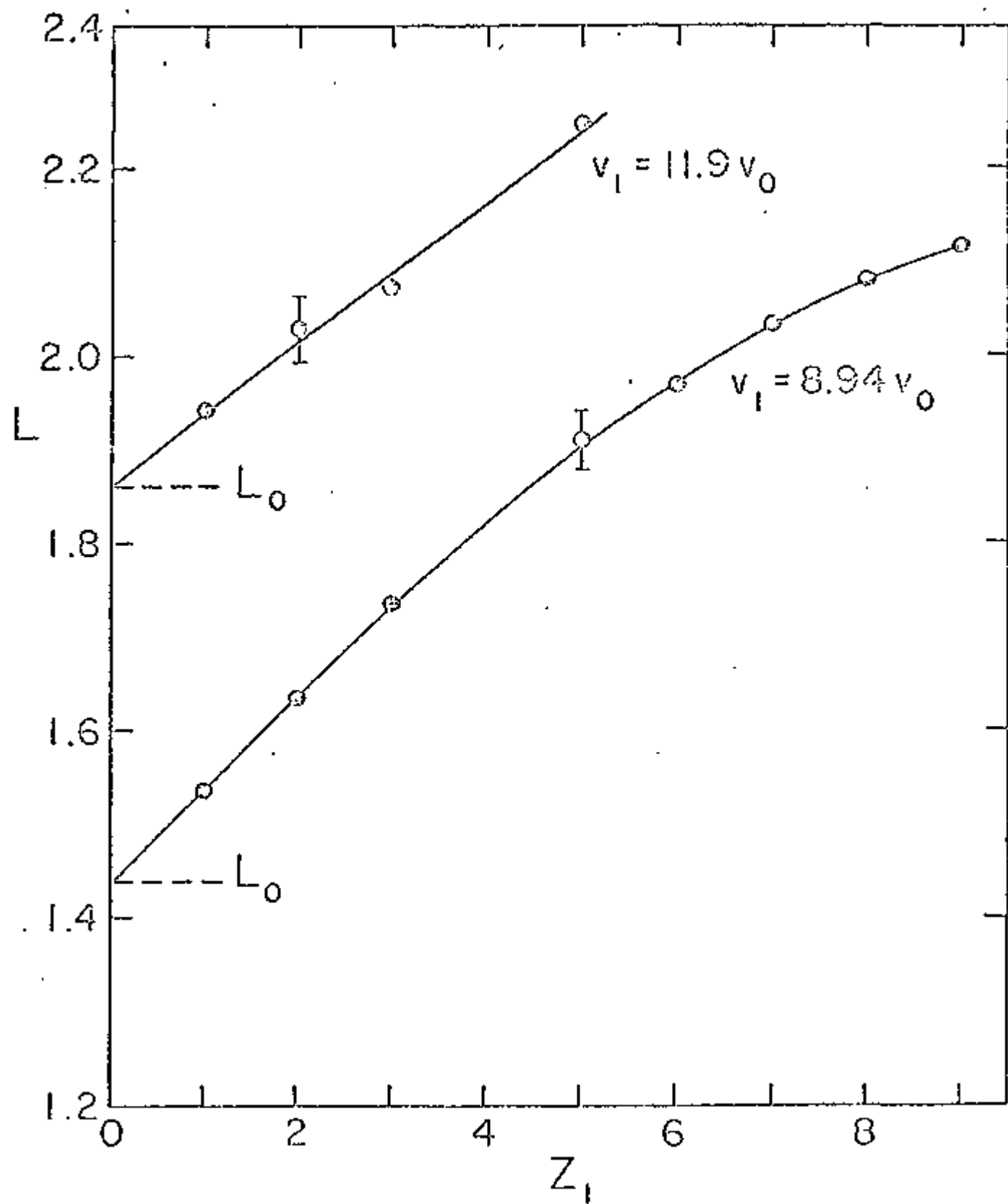
Table III

Empirical  $L_1$  values given by  $(L - L_0)/Z_1^*$  with  $L_0 = 1.44$  at  $v_1 = 8.94 v_0$  and  $L_0 = 1.86$  at  $v_1 = 11.8 v_0$ , based on measurements of ref. 6 as shown in Fig. 1. Uncertainties are ca.  $\pm 20\%$ .

Projectile	$Z_1$	$L_1$	
		$v_1 = 8.90 v_0$	$v_1 = 11.8 v_0$
H	1	0.10	0.078
He	2	0.10	0.083
Li	3	0.10	0.070
B	5	0.10	0.078
C	6	0.096	
N	7	0.095	
O	8	0.091	
F	9	0.088	

### Legend of Figure

Fig. 1. Experimental stopping number  $L$ , extracted from data<sup>6</sup> according to Eq. (20), as a function of the charge number,  $Z_1$ , of projectiles at two velocities  $v_1$  in random  ${}_{79}\text{Au}$  foils. Solid curves are drawn to aid the eye. The extrapolated values  $L_0$  for  $Z_1 \rightarrow 0$  are indicated by dashed lines. The rise of the data with  $Z_1$  is indicative of deviations from the Bethe-Bloch stopping power theory as listed in Table III.





6. Effective Charge Theory of Stopping Power (Brandt, with Yarlagadda and Robinson, ANL)

Over the past half-century a fairly complete physical understanding has developed of the electronic stopping power,  $S$ , of matter, i.e., the kinetic energy loss per unit path length by ions to electronic excitations during penetration of matter. At high ion velocities, the theories of Bethe<sup>1</sup> and of Bloch<sup>2</sup> provide a quantitative account. At low ion velocities, Fermi and Teller<sup>3</sup> have shown on very general grounds that  $S$  must be linearly proportional to the ion velocity  $v_1$ . The proportionality constant can be estimated by various methods.<sup>4,5</sup> At intermediate ion velocities one has recourse to effective ion charge models, first introduced by Bohr<sup>6</sup> and by Lamb.<sup>7</sup> Brandt<sup>8</sup> has given an effective-charge theory that successfully summarizes a large body of stopping power data for heavy ions. Extensive discussions of the field are available,<sup>9-13</sup> as are extensive compilations of interpolated stopping powers.<sup>14,15</sup>

The present study was stimulated by some recent data on heavy-ion stopping in solids, which were claimed to call into question the proportionality to  $v_1$  expected in the low velocity limit.<sup>16</sup> If in fact so, such evidence would pose very disturbing theoretical questions, and would imply important practical consequences for radiation damage calculations. However, these data do not pertain to the low velocity limit. They were taken in an intermediate velocity range where the effective projectile ion charge increases with velocity. We show in the following that when this is taken into account the putative discrepancy is resolved.<sup>17</sup> Brice has also addressed this "discrepancy" and concluded that these data conform to his three-parameter semi-empirical formulae.<sup>18</sup>

In the course of this investigation it became apparent that effective-charge theory provides a comprehensive description of electronic stopping power at all velocities from the high values of the Bethe limit down to those approaching

the Fermi-Teller regime and for all projectile-target combinations, provided that the proton stopping power in the target is known. In scrutinizing available data,<sup>19-49</sup> we find that for ion velocities greater than thrice the Bohr velocity  $v_0 = e^2/\hbar$  the effective projectile charge  $Z_1^*e$  calculated using a velocity criterion for electron stripping<sup>8</sup> agrees with experiment. The leading corrections to the  $Z_1^{*2}$ -proportional energy loss formula, which are proportional to  $(Z_1^*)^3$  and  $(Z_1^*)^4$ , were included. It is then shown that when allowance is made for an empirical effective proton charge  $Z_p^*e$ , agreement between theory and experiment extends to  $v_1 \gtrsim v_0$ . Both a velocity criterion and an energy stability criterion for stripping are considered, and a theoretical account of the effective proton charge for stopping power is given. Our results lead to a simple interpolation scheme for electronic stopping powers in the range  $0 \leq v_1 \lesssim v_0$ .

## II. ANALYSIS AND COMPARISON TO EXPERIMENT USING A VELOCITY STRIPPING CRITERION.

Effective charge theory asserts that the electronic stopping power in a target of atomic number  $Z_2$  for an ion having charge  $Z_1^*e$  and velocity  $v_1$  can be written as

$$S(Z_1, Z_2; v_1) = [Z_1^*(v_1)e]^2 S_0(Z_2; v_1) \quad (\text{II.1})$$

when  $v_1$  is greater than the velocity at which the stopping power for protons in the same target has a maximum.<sup>8</sup>  $S_0$  is then the stopping power per unit charge taken in the limit of vanishing charge. At velocities such that the effective

charge number  $Z_1^*$  is equal to the projectile atomic number  $Z_1$ , Eq. (II.1) is simply the Bethe approximation.<sup>1</sup> When higher order contributions to the stopping cross-section for a specified projectile charge need be retained, the r.h.s. of Eq. (II.1) has additional terms to which we shall come presently. According to Eq. (II.1) we can write the basic scaling relation of effective charge theory as

$$[S(Z_1, Z_2; v_1) / S_p(Z_2; v_1)]^2 = [Z_1^*(v_1) / Z_p^*(v_1)]^2, \quad (\text{II.2});$$

where  $S_p(Z_2; v_1) \equiv S(1, Z_2; v_1)$  and  $Z_p^*(v_1)e$  are, respectively, the proton stopping power and effective charge in the same target.

Rearranging Eq. (II.2) as

$$\left[ \frac{1^2}{Z_1^2} \frac{S(Z_1, Z_2; v_1)}{S_p(Z_2; v_1)} \right]^{1/2} = \frac{[Z_1^*(v_1) / Z_1]}{[Z_p^*(v_1) / 1]} \quad (\text{II.3})$$

and plotting experimental values of the l.h.s. of Eq. (II.3) as a function of  $v_1$  reveals that the r.h.s. is insensitive to the target material within an uncertainty of about 10%, as is shown in Fig. 1 for two representative examples. Accordingly, the effective charge numbers  $Z_1^*$  and  $Z_p^*$  are taken to be independent of the target. In the following, we shall refer to  $Z_1^*$  as the effective charge number or the effective charge, which are the same in atomic units with  $e = 1$ . The data shown in Fig. 1 and in subsequent graphs are based on scrutiny of all measurements available to us.<sup>20-49</sup> As is well-known, stopping power data can differ by as much as 20%, particularly in the velocity range of the proton stopping power maximum. When representative numbers are needed, we balance such data to provide them.

In Fig. 2 we plot the l.h.s. of Eq. (II.3) using all such data as a function of the reduced ion velocity  $(v_1/v_0 Z_1^{2/3})$ . If  $Z_p^*(v_1)$  were unity this would yield  $[Z_1^*(v_1)/Z_1]$ . The effective charge fraction  $(Z_1^*/Z_1)$  according to Brandt<sup>8</sup> is shown as the solid line in Fig. 2 and tabulated in Table I. The velocity criterion for electron stripping,  $v(r) \leq v_1$ , was used, with the "local orbital velocity" at  $r$  in the projectile taken to be  $v(r) = bv_F(r)$ . The local Fermi velocity,  $v_F(r) = [3\pi^2\rho(r)]^{1/3}$  in atomic units, was taken to be given by the Thomas-Fermi (TF) approximation for the electronic density  $\rho(r)$  of a neutral atom, and the parameter value  $b = 1.26$  was chosen. At high velocities ( $v_1 \gtrsim 3v_0$ ) the data are well represented by the theoretical curve for  $b = 1.26$ . The parameter value  $b=1.33$  gives a better fit to the heavy-ion data at low  $(v_1/v_0 Z_1^{2/3})$  values.<sup>50</sup> When  $v_1 \lesssim 3v_0$ , the light ion plots tend to deviate upward from the  $b = 1.26$  curve as  $v_1$  is reduced. The available heavy-ion data correspond to ion velocities  $v_1 \gtrsim 2.5v_0$ , but we conjecture that similar low-velocity departures from Brandt's curve for  $b = 1.33$  would be found for heavy ions, as is signaled by an incipient trend of the data for chlorine, potassium, and bromine projectiles.

To explore the origin of this trend we have compared the TF curve for the charge fraction with calculations based on the Lenz-Jensen (LJ) approximation<sup>51</sup> for the electronic density and the same velocity criterion, for  $b = 1$ . The results, curves a(TF) and b(LJ) in Fig 3, are virtually the same, and rule out the possibility that the upward deviations for light ions in Fig. 2 could be eliminated by using a more accurate electron density than that of the TF atom.

We have calculated the contributions to the stopping power due to the Bloch<sup>2</sup> and  $Z_1^3$  terms<sup>53</sup> for heavy ions and for the proton in the form of a correction factor  $C$  such that Eq. (II.3) is supplanted by

$$\frac{1}{C} \left[ \frac{1^2}{Z_1^2} \frac{S(Z_1, Z_2; v_1)}{S_p(Z_2; v_1)} \right]^{1/2} = \frac{[Z_1^*(v_1)/Z_1]}{[Z_p^*(v_1)/1]} \quad (\text{II.4})$$

We have

$$C = \left\{ \frac{1 + (1/L_0) \{ Z_1^* L_1 + \Psi (Z_1^* e^2 / \hbar v_1) \}}{1 + (1/L_0) \{ L_1 + \Psi (e^2 / \hbar v_1) \}} \right\}^{1/2} \quad (\text{II.5})$$

where  $L = L_0 + Z_1^* L_1$  is the stopping number per target electron and  $\Psi$  the Bloch correction which interpolates between the quantum mechanical limit ( $Z_1^* / v_1 \ll 1$ ) and the classical limit ( $Z_1^* / v_1 \gg 1$ ) of stopping power theory. In terms of the digamma function  $\psi(z) = \Gamma'(z) / \Gamma(z)$ ,  $\Psi(x) = \psi(1) - \text{Re } \psi(1+ix)$ . In the high velocity limit,  $L_0$  becomes  $\ln(2\pi m v_1^2 / I_0)$ ,  $I_0$  being the average excitation energy of the target, and  $L_1$  is the coefficient of the so-called  $Z_1^3$  effect.

No experimental point in Fig. 2 deviates significantly from Brandt's curve unless  $v_1 \gtrsim 3v_0$ , and therefore for numerical estimates, we evaluate upper limits of  $C$ , Eq. (II.5), in the low velocity domain where target ion cores do not contribute to stopping, and  $L_0$  can be approximated by  $\ln(2\pi m v_1^2 / \hbar \omega_p)$ . Here,  $\omega_p$  is the resonance (plasmon) frequency of the target valence electrons of density  $(3/4\pi r_s^3)$  with  $r_s$  in atomic units. For the typical value  $r_s = 2$ , we have  $\hbar \omega_p = 0.612$  a.u. and

$$L_1 = \frac{e^2 \omega_p}{m v_1^2} \text{I} \left[ \frac{\hbar \omega_p}{2 m v_1^2} \right] \quad (\text{II.6})$$

$$= 0.612 \left( \frac{v_0}{v_1} \right)^3 \text{I} \left[ 0.306 \left( \frac{v_0}{v_1} \right)^2 \right]$$

The function  $\text{I}(x)$  is given in Ref. 53, and we have here chosen  $\hbar/2m v_1$  for the impact parameter cutoff  $a_\omega$  of Ref. 53.

We find considerable cancellation between the  $Z_1^3$  and the Bloch contributions, in that they happen to be comparable in magnitude but opposite in sign for all ions. Values of  $C$  obtained from Eqs. (II.5) and (II.6) are overestimates at  $v_1 < 3v_0$  for the heavier projectiles, say for  $Z_1 > 17$ . For such  $Z_1$  and  $v_1$ , the alternative choice  $(\pi/2 m \omega_p)^{1/2}$  of impact parameter cutoff decreases  $C$  by roughly 20%, and, moreover,  $Z_1^* L_1$  is becoming large enough that the perturbation expansion of  $L$  should include higher order terms which are expected to reduce the correction to  $L_0$ . In Fig. 4 we show representative results of the calculation using Eq. (II.5). Examination of Fig. 4 in conjunction with Fig. 2 shows that the experimental points for the lighter ions are not brought significantly closer to the theoretical curve, and that the experimental points for heavy ions given by available data at  $v_1 \gtrsim 3v_0$  remain unchanged. Only the lowest velocity datum point for Br, at  $v_1 = 0.856v_0$ , is affected significantly in that division by  $C$  brings it close to the solid curve of Fig. 2 (but still above a curve for  $b = 1.33$ ). In this sense the rise of the Br plot at the lowest velocity measured can be taken to signal a distinguishable  $Z_1^3$  contribution. The results summarized in Fig. 4 indicate that this is the only available heavy ion datum which can be so interpreted.

We extract empirical values for  $Z_p^*(v_1)$  by using Eq. (II.4) and the theoretical charge fraction  $[Z_1^*(v_1)/Z_1]$ , and exhibit the result in Fig. 5. An effective proton charge  $Z_p^*(v_1)$  emerges which is independent of both the heavier projectiles and the target materials to which the data pertain. The solid curve in Fig. 5, which represents the locus of the data exhibited, approximates a continuation of the theoretical curve of Fig. 3 to higher arguments for  $Z_1 = 1$ . In Fig. 6 we have replotted the experimental data according to Eq. (II.4) using the mean values of  $Z_p^*(v_1)$  given by the solid line of Fig. 5 and listed in Table II. They follow the theoretical curve for  $[Z_1^*(v_1)/Z_1]$  within the uncertainty of the data.

We conclude that, when combined with Fig. 5, all available experimental data for solid targets are brought into accord with the experimental curve at all velocities  $v_1 \gtrsim v_0$  for  $Z_1$  ranging from 2 to 92.

### III. PROTON SCREENING AND STRIPPING CRITERIA

We must now test whether the empirical  $Z_p^*$  is physically reasonable and whether its values can be estimated within the framework of effective charge theory. In doing so it is necessary to take note of a few points which relate specifically to condensed-matter targets or to protons. Most commonly, discussions of effective charges have been couched in terms appropriate to gas targets, and  $Z_1^*$  interpreted as a steady-state average over a large number of discrete capture-loss processes.<sup>9</sup> Moreover, the use of a statistical model for an ion in isolation is suspect for light ions, let alone a hydrogen ion. In a solid, however, the screening corresponding to that due to the highest occupied orbitals of an isolated projectile is built up out of a macroscopic number of target electron wave functions each of which has microscopic amplitude at the projectile. In consequence, in a solid target,  $Z_1^*$  can vary continuously with small fluctuations, and statistical models are well justified even for the screened proton. Of course, a model useful and adequate for stopping power need not apply to other phenomena. In any bulk metal, if we were to include all of the screening charge density which accompanies a moving ion, we would always find  $Z_1^* = 0$ , in that perfect screening at large distances is built into the dielectric response function. We here deal with a "stopping power  $Z_1^*$ " as perceived by the medium over distances comparable to the adiabatic screening length ( $v_1/\omega_p$ ).

#### a. Stripping criteria

Velocity criteria for stripping stem ultimately from Bohr's discussion<sup>6</sup> of effective charge in terms of the  $v_1$  dependence of capture and loss cross-sections. They can be written in the form that projectile electrons of orbital

velocity  $v$  such that  $v < v_1$  are considered stripped, and the primary question is what to use as an electron "orbital velocity"  $v$ . In ordinary TF approximation, with  $v(r) = bv_F(r)$ , such a criterion can be rewritten in the form of an energy-stability condition. The parameter  $b$  then has the appearance of correcting the TF ion energy for correlation effects. Lamb's approach<sup>7</sup> primarily provides an energy criterion. We shall now sketch a heuristic derivation of such a criterion and its relation to a velocity criterion.

We consider an ion of atomic number  $Z_1$  moving with a constant velocity  $v_1$  in the bulk of a solid and take the entire system to be in its ground state for given  $v_1$  and fixed total number of electrons. We take  $N_1$  electrons moving with the ion, and seek a condition on  $N_1$  for the total system electronic energy to be a minimum. It is conceptually important to remember that in the rest frame of the target solid the energy of each projectile-ion electron increases as  $v_1^2$ . Any level in a static ion, however deep, eventually rises with increasing  $v_1$  to the lowest unoccupied level of the target medium, i.e., the Fermi level in a solid. Projectile electrons can then simply fall off into the medium provided that there is a finite transition matrix element.

Examination of those contributions to the total electronic energy of the system which change with  $N_1$  reveals that for  $v_1 > v_0$  the target solid may be treated as merely a source and sink for electrons at the Fermi level.<sup>54</sup> It is then sufficient to retain only the total projectile ion energy written as

$$\frac{1}{2}(M_1 + N_1 m)v_1^2 + E(Z_1, N_1)$$

where  $M_1$  and  $m$  are the nuclear and electron masses, respectively.  $E(Z_1, N_1)$  is the ion's ground state energy in its center of mass system. The steady-state condition is then



$$\frac{1}{2} m v_1^2 = - \frac{\partial E(Z_1, N_1)}{\partial N_1} > 0 \quad (III.1)$$

which applies to any target medium with the stipulation that differences rather than differentials are used if the electron energy and number are discrete. For discrete  $N_1$ ,  $[-\partial E(Z_1, N_1)/\partial N_1]$  is just the ionization potential at  $N_1$  and Eq. (III.1) becomes Lamb's stripping criterion.<sup>7,9</sup>

In a one-electron approximation, Koopmans' theorem<sup>55</sup> assures us that  $(\partial E/\partial N_1)$  is the orbital energy of the highest lying electron on the ion. In turn, this orbital energy is equal to the selfconsistent potential energy  $U(r)$  evaluated at the classical turning point  $r \equiv r_1$ , where the kinetic energy density vanishes. Therefore we obtain the energy-stability condition

$$\frac{1}{2} m v_1^2 + U(r_1) = 0 \quad (III.2)$$

An electron for which the l.h.s. of Eq. (III.2) is positive is to be considered stripped. In a statistical model we introduce the local velocity  $v(\underline{R} + \underline{r})$  by writing  $1/2 m v^2(\underline{R} + \underline{r}) + U(\underline{R} + \underline{r})$  for the energy of an electron at an arbitrary space point  $\underline{R} + \underline{r}$  in the system, where  $\underline{R}$  is the projectile ion center of mass. For definiteness we take the target Fermi level as the zero of energy. Since the Fermi level of the system is not shifted from that of the target by the presence of a single projectile, for an electron in the highest occupied level of the system we have

$$1/2 m v_F^2(\underline{R} + \underline{r}) + U(\underline{R} + \underline{r}) = 0 \quad ,$$

which defines a local Fermi velocity  $v_F$ . Near the moving ion the self-consistent potential  $U$  is dominated by the strong and effectively spherical field of the partially stripped projectile, independent of the position  $\underline{R}$  of the ion in the system. In consequence, near the projectile we may write

$$1/2 m v_F^2(r) + U(r) = 0 \quad (\text{III.3})$$

and interpret  $v_F(r)$  as the local Fermi velocity "in the ion". We take the classical turning point  $r_1$  for an electron in the ion and at the Fermi level of the system as a natural choice for the effective ion radius and  $v_F(r_1)$  as the relevant "orbital velocity." Comparison of Eq. (III.2) with Eq. (III.3) for  $r = r_1$  then shows that the energy criterion coincides with the velocity criterion for  $b = 1$ . Because we have concentrated on the ground state of the system, this connection takes no account of electron transfers to states above the Fermi level of the solid. Inclusion of such processes requires parameter values  $b > 1$ .

b. Screening charge density

The screening of a static proton in metals has been studied in quantitative detail,<sup>56</sup> and these studies fully justify use here of a local density approximation and a statistical model. Accurate static charge density profiles are close to those of hydrogenic 1s functions at all points inside the first node of the Friedel oscillations (which occurs close to the classical turning point).<sup>56,57</sup> We use charge density profiles appropriate to a static proton also for a moving proton. Since  $Z_1^*$  is given by  $Z_1$  minus an integral over the screening cloud, an accurate account of shape changes due to the finite velocity<sup>58</sup>

?  $|v_1|$  is not crucial. As in the calculations of  $[Z_1^*(v_1)/Z_1]$  of the preceding section, we shall use neutral atom charge densities truncated according to a stripping criterion.

c.  $Z_p^*$  estimates

With a 1s screening charge-density profile truncated at a radius  $r_1$  we calculate  $Z_p^*$  as a function of  $r_1$  and relate  $r_1$  to  $v_1$  through the stripping condition to obtain  $Z_p^*(v_1)$ . When we set  $b = 1$ , as we would for a hydrogen atom, the  $Z_p^*$  obtained using the velocity criterion (Fig. 7 curve a) rises significantly more rapidly with  $v_1$  than do the empirical values (curve c). The overall differences in slope and value are not materially reduced by varying the density profile or the value of  $b$ , and appear to be qualitative. Since such a truncated ion has no charge at  $r > r_1$ , the potential energy criterion, Eq. (III.2), may be written as

$$\frac{1}{2} m v_1^2 = Z_1^*(r_1) e^2 / r_1 \quad (III.4)$$

Use of Eq. (III.4) gives a  $Z_p^*(v_1)$  (Fig. 7 curve b) which lies within the spread of the data about the empirical curve. The small systematic overestimate of  $Z_p^*$  is to be expected, since an energy-stability criterion assumes all energetically allowed transitions to proceed with probability one.

The two criteria give different results because a local density appropriate to a neutral atom was used to determine  $v_p(r_1)$  for the velocity criterion. The potential which is consistent with that local density is the potential at  $r = r_1$  in a neutral atom, and differs from the ion potential of Eq. (III.4) by an outer screening shift which for the proton can be substantial. For example, the electron potential energy at  $r_1$  is deeper in the ion than in the neutral atom by about 9 eV at  $v_1 = v_0$  and by about 15 eV at  $v_1 = 1.5 v_0$ .

Equation (III.4) is a Hartree approximation which neglects exchange-correlation effects, but these become appreciable only at large distances,<sup>59</sup> where the screening charge density oscillates between positive and negative with a period on the scale of interatomic spacings. Indeed, our results suggest that the contributions of this oscillating tail cancel sufficiently to be neglected as compared to the central region insofar as stopping power is concerned. The greater accuracy of the energy-stability criterion for  $Z_p^*$  as compared to the velocity criterion with  $b = 1$  is analogous to the familiar experience that, in any order of perturbation theory, energies are more accurate than wave functions or densities.

#### IV. SELF-CONSISTENT EFFECTIVE CHARGE BY THE POTENTIAL ENERGY CRITERION.

All the previous calculations are based on a truncated neutral atom electronic density for the projectile. The effective projectile charge is obtained by stripping the projectile according to a velocity or potential-energy criterion. There will be redistributions of charge as the projectile is progressively ionized. To assess their influence we solve the TF equation for several ionic charges. We shall call the resulting relationship between  $\frac{Z_1^*}{Z_1}$  and  $y \equiv (v_1/v_0 Z_1^{2/3})$  the self-consistent solution.

Following conventional procedures,<sup>60</sup> the potential energy criterion leads to the relations

$$\frac{Z_1^*(x_0)}{Z_1} = -x_0 \phi'(x_0) \quad (\text{IV.1})$$

and

$$y(x_0) = 1.50329 [-\phi'(x_0)]^{1/2}, \quad (\text{IV.2})$$

where  $\phi(x)$  and  $x$  are the usual dimensionless TF potential and distance,  $\phi' = (d\phi/dx)$  and  $x_0$  is the radius of the TF ion defined by

$$\phi(x_0) = 0 \quad (IV.3)$$


The results of this calculation are shown in Fig. 8 as curve a and compared with those for the truncated-atom (curve b) and with those based on the velocity criterion (curves c and d). Satisfactory agreement of curve a with the data is obtained without any empirical parameters for  $y \leq 0.4$  provided  $Z_p^*$  is used, as seen in Fig. 9. At higher values of  $y$  this form of self-consistent solution ceases to agree with experiment.

We have also performed Thomas-Fermi-Dirac (TFD) calculations for several ions over the range  $6 \leq Z_1 \leq 92$ . The  $(Z_1^*/Z_1)$  obtained by TFD lie systematically below those found in TF, but only by amounts smaller than the spread of the data, and the shape of the  $(Z_1^*/Z_1)$  vs.  $y$  curve is the same.

#### V. INTERPOLATION FOR $0 < v_1 < v_0$ .

With allowance for proton screening the regime of reliable  $Z_1^*$ -theory reaches down to  $v_1 \approx v_0$ , but we have no basis for supposing it to reach significantly lower. We now deal with interpolating to the zero velocity limit, at which  $(S/v_1) = \text{constant}$ . Our goal is a prescription for generating acceptable values of  $S$ , at all  $v_1$ , for practical computations in which fully quantitative accuracy at low velocities is not crucial. As an example, we have in mind the account of electronic losses which is required in collision cascade-simulations.

For  $0 < v_1 < v_0$  no simple theory can be expected to be quantitatively accurate for all projectile-target combinations. While projectile shell structure effects are typically 5% corrections when  $v_1 > v_0$ , at lower velocities  $Z_1$ -oscillation amplitudes can be 50% of the "average"  $S$ .



The Lindhard<sup>5</sup> and the Firsov<sup>4</sup> theoretical estimates of the limiting  $(S/v_1)$  coefficient, despite significant successes, disagree often with each other and with experiment, and seemingly unsystematically. A detailed theoretical description of  $S$  throughout the range  $0 < v_1 < v_0$  is still lacking, and we are for practical applications led to semi-empirical interpolation.

At  $v_1 = v_0$ , the  $S$  values calculated via Eq. (II.2) agree on the average with all available data, including  $Z_1$ -oscillations, to within 20%. Simply connecting the point calculated at  $v_1 = v_0$  to the origin by a straight line, i.e., setting for  $v_1 < v_0$

$$S(Z_1, Z_2; v_1) \approx S(Z_1, Z_2; v_0) \cdot (v_1/v_0) \\ = \left[ \frac{Z_1^*(v_0)}{Z_p^*(v_0)} \right]^2 S_p(Z_2; v_0) \left( \frac{v_1}{v_0} \right) \quad (V.1)$$

should therefore give  $S$  throughout  $0 < v_1 < v_0$  with an accuracy comparable to that at the low end of the effective charge theory regime. This simple recipe preserves the generality as well as the computational efficiency of  $Z_1^*$ -theory. Table III collates several experimental values of  $S_p(Z_2; v_0)$ . In Fig. 10 we compare experimental stopping powers at  $v_1 \approx 0.41v_0$  in carbon and in aluminum to those calculated by the Lindhard and the Firsov prescriptions and by Eq. (V. 1). The solid curves are the results of interpolation according to Eq. (V. 1) for  $Z_1^*(v_0)$  obtained in two ways: from Brandt's method with the velocity criterion and  $b = 1.26$  and from the self-consistent TF ion solution (SCTF) with the potential energy criterion, corresponding, respectively, to curves d and a of Fig. 8. As these plots indicate, Eq. (V. 1) yields the mean  $Z_1$ -dependence of the stopping power at  $v_1 \approx 0.41v_0$  in both targets, and we expect the same at other velocities and for other projectile-target combinations.

TABLE I. Fractional effective charge by Brandt procedure. Calculated as discussed in the text and taken from Ref. 8. In this model  $(z_1^*/z_1)$  is a universal function of  $(1/b)(v_1/v_0 z_1^{2/3})$ .

$\frac{z_1^*}{z_1}$	$(v_1/v_0 z_1^{2/3})$	
	$b = 1.26$	$b = 1.33$
0.012	0.023	0.024
0.034	0.050	0.053
0.070	0.093	0.098
0.101	0.129	0.136
0.155	0.189	0.100
0.197	0.238	0.251
0.256	0.312	0.330
0.305	0.375	0.396
0.344	0.432	0.456
0.391	0.504	0.532
0.447	0.600	0.633
0.480	0.660	0.697
0.515	0.731	0.771
0.554	0.816	0.862
0.598	0.924	0.975
0.645	1.057	1.116
0.698	1.233	1.302
0.756	1.474	1.556
0.819	1.824	1.928
0.852	2.092	2.208
0.886	2.432	2.567
0.919	2.936	3.098
0.952	3.767	3.977
0.981	5.620	5.932

TABLE II. Empirical proton effective charge. Values of the smoothed  $z_p^*(v_1)$  data represented by the solid line in Fig. 5.

$\frac{z_p^*}{v_1}$	$z_p^*$
1.0	0.65
1.25	0.73
1.50	0.80
1.75	0.85
2.00	0.90
2.25	0.93
2.50	0.95
2.75	0.97
3.00	1.00
3.25	1.00



TABLE III. Proton stopping power at  $v_1 = v_0$  of various targets.

Target ( $Z_2$ )	$S_p$ ( $\frac{\text{ev} \cdot \text{cm}^2}{\text{atom}} \times 10^{15}$ )	Reference
C (6)	12	40
Al (13)	18 17	40 41
Ni (28)	20 14	42 37
Co (27)	15	37
Ag (47)	27	43
Au (79)	29 20	43 44,45

## REFERENCES

1. H. A. Bethe, *Ann. Physik* 5, 325 (1930).
2. F. Bloch, *Ann. Physik* 16, 285 (1933).
3. E. Fermi and E. Teller, *Phys. Rev.* 72, 399 (1947).
4. O. B. Firsov, *Sov. Phys. JETP* 36, 1076 (1959).
5. J. Lindhard, M. Scharff, and H. E. Shiott, *Kgl. Danske Videnskab. Selskab, Mat.-Fys. Medd.* 33, No. 14 (1963); J. Lindhard and M. Scharff, *Phys. Rev.* 124, 128 (1961).
6. N. Bohr, *Phys. Rev.* 58, 654 (1940), and *Phys. Rev.* 59, 270 (1941).
7. W. E. Lamb, *Phys. Rev.* 58, 696 (1940).
8. W. Brandt, in "Atomic Collisions in Solids", (Plenum Press, New York, 1973), Vol. I, p. 261.
9. H. Betz, *Rev. Mod. Phys.* 44, 465 (1972).
10. T. E. Pierce and M. Blann, *Phys. Rev.* 173, 390 (1968).
11. Ya. A. Teplova, V. A. Nikolaev, I. S. Dmitriev, and L. N. Fateeva, *Sov. Phys. J.E.T.P.* 15, 31 (1962).
12. R. S. Nelson, "The Observation of Atomic Collisions in Crystalline Solids" (North Holland, Amsterdam, 1968).
13. L. C. Northcliffe, *Ann. Rev. Nucl. Sci.* 13, 67 (1963).
14. L. C. Northcliffe and R. F. Schilling, *Nucl. Data, Sec. A* 7, 4 (1970); D. K. Brice, "Ion Implantation Range and Energy Deposition Distribution" (Plenum Press, New York, 1975).

15. Empirical correlation of solid target stopping power data on the basis of effective charge scaling has recently been treated in detail by D. Ward, J. S. Forster, H. R. Andrews, I. V. Mitchell, G. C. Ball, W. G. Davies, and G. J. Costa, Atomic Energy of Canada Limited, Report AECL-5313 (1976), (unpublished). These authors are concerned with projectile energies from 0.1 to 10 MeV/nucleon, and the data which they analyze pertain primarily to velocities above those of greatest interest in the present study. With allowance for minor differences in presentation, their empirical findings agree with our theoretical results.
16. M. D. Brown and C. D. Moak, Phys. Rev. B6, 90 (1972). See also J. Narayan, T. S. Naggle, and O. S. Oen., Bull. Am. Phys. Soc. 20, 351 (1975).
17. For a preliminary account, see B. S. Yarlagadda, J. E. Robinson, and W. Brandt, Bull. Am. Phys. Soc. 21, 407 (1976).
18. D. K. Brice, Appl. Phys. Lett. 29, 10 (1976).
19. No data pertaining to channeled projectiles have been used in the comparisons to experiment presented in the present paper. We believe that all published data for random stopping in solid targets are represented in the references that we cite, although we cannot guarantee that none has eluded our search. All data references are listed, <sup>20-49</sup>seriatim, immediately below, and are referred to in figure and table captions as appropriate. In most instances, but by no means in all, stopping power values taken from the interpolation tables of Northcliffe and Schilling<sup>14</sup> or of Brice<sup>14</sup> would have served equally as well.
20. D. I. Porat and K. Ramavataram, Proc. Phys. Soc. (Lond.) 77, 97 (1961).
21. D. I. Porat and K. Ramavataram, Proc. Phys. Soc. (Lond.) 78, 1135 (1961).
22. D. I. Porat and K. Ramavataram, Proc. Roy. Soc. A252, 394 (1959).
23. P. H. Barker and W. R. Phillips, Proc. Phys. Soc. (Lond.) 85, 379 (1965).
24. H. Nakata, Phys. Rev. B9, 4654 (1974).

25. H. Nakata, Phys. Rev. B3, 2847 (1971).
26. H. Nakata, Can. J. Phys. 46, 2765 (1968); Can. J. Phys. 47, 2545 (1969).
27. C. D. Moak, B. R. Appleton, J. A. Biggerstaff, S. Datz and T. S. Noggle "Atomic Collisions in Solids", (Plenum Press, New York, 1975), Vol. I, p. 57.
28. L. B. Bridwell and C. D. Moak, Phys. Rev. 156, 242 (1967).
29. L. B. Bridwell, L. C. Northcliffe, S. Datz, C. D. Moak and H. O. Lutz, Phys. Rev. 159, 276 (1967).
30. C. D. Moak and M. D. Brown, Phys. Rev. 149, 244 (1966).
31. R. Kalish, L. Grodzins, F. Chmara and P. H. Rose, Phys. Rev. 183, 431 (1969).
32. W. Booth and I. S. Grant, Nucl. Phys. 63, 481 (1965).
33. L. C. Northcliffe, Phys. Rev. 120, 1744 (1960).
34. D. Ward, R. L. Graham, and J. Geiger, Can. J. Phys. 50, 2302 (1972).
35. H. Schmidt-Böcking, G. Rühle and K. Bethge, "Atomic Collisions in Solids," (Plenum Press, New York, 1975), Vol. I, p. 83; P. G. Roll and F. E. Steigert, Nucl. Phys. 17, 54 (1960).
36. W. K. Chu and D. Powers, Phys. Rev. 187, 478 (1969).
37. W. White and R. M. Mueller, Phys. Rev. 187, 499 (1969).
38. B. Fastrup, P. Hvelplund and C. A. Sutter, Mat. Fys. Medd. Dan. Vid. Selsk. 35, Nr 10 (1966).
39. P. Hvelplund and B. Fastrup, Phys. Rev. 165, 408 (1968).
40. J. H. Ormrod, J. R. McDonald and H. E. Duckworth, Can. J. Phys. 43, 275 (1965).
41. G. Basbas, W. Brandt and R. Laubert, Phys. Rev. A7, 983 (1973).
42. R. L. Wolke, W. N. Bishop, E. Eichler, N. R. Johnson and G. D. O'Kelley Phys. Rev. 129, 2591 (1963).
43. A. Valenzeula, W. Meckbach, A. J. Kestleman and J. C. Eckardt, Phys. Rev. B6, 95 (1972).
44. A. H. Morson, D. A. Aldcroft and M. F. Payne, Phys. Rev. 165, 418 (1968).

45. S. K. Allison and S. D. Warshaw, *Rev. Mod. Phys.* 25, 779 (1953).
46. W. Whaling, *Handbuch der Physik*, edited by S. Flügge (Springer Verlag, Berlin (1958)), Vol. 34, p. 193.
47. R. D. Moorehead, *J. Appl. Phys.* 36, 391 (1965).
48. H. K. Reynolds, D. N. F. Dunbar, W. A. Wenzeland, W. Whaling, *Phys. Rev.* 92, 742 (1953).
49. S. D. Warshaw, *Phys. Rev.* 76, 1759 (1949).
50. A similar variation of  $b$  was found by J. H. M. Bruning, J. K. Knipp and E. Teller, *Phys. Rev.* 60, 657 (1941). Ward et al.,<sup>15</sup> parameterize the effective charge fraction in the form  $Z_1^*/Z_1 = 1 - A \exp(-Bv_1/v_0)$  and find a weak  $Z_1$ -dependence of  $A$  which is equivalent to this variation of  $b$ .
51. P. Gombas, "Die Statistische Theorie der Atoms und ihre Anwendungen," (Vienna, Springer-Verlag, 1949), p. 72.
52. J. K. Knipp and E. Teller, *Phys. Rev.* 59, 659 (1941).
53. J. C. Ashley, R. H. Ritchie and W. Brandt, *Phys. Rev.* B5, 2393 (1972).
54. The restriction to  $v_1 \gtrsim v_0$  is similar to but not identical with the approximation stated by Lamb as neglecting the binding of electrons in the target.
55. See, e.g., J. C. Slater, "Quantum Theory of Molecules and Solids", (McGraw-Hill, New York, 1963), Vol. I. p. 96.
56. See, e.g., Z. D. Popovic, M. J. Stott, J. P. Carbotte and G. R. Piercy, *Phys. Rev.* B13, 590 (1976), and references listed therein.
57. P. Jena and K. S. Singwi, *Bull. Am. Phys. Soc.* 22, 467 (1977).
58. H. Stachowiak, *Bulletin de L'Academie Polonaise des Sciences, Serie des sciences math., astr., et phys.* Vol. XXIII No. 11, p. 1213 (1975).
59. K. S. Singwi and P. Vashishta, private communication.
60. N. H. March, "Self-consistent Fields in Atoms" (Pergamon Press, New York, 1975).

## FIGURE CAPTIONS

- Fig. 1. Effective charge in various targets. Data references: carbon projectiles (20,33), iodine projectiles (27-30). Proton stopping powers were taken from 21, 25, 40-49. The approximate target independence exhibited is representative of that for all published data.
- Fig. 2. Empirical effective charge fractions obtained from data using Eq. (II.3) with  $Z_p^* = 1$ . The theoretical curve calculated by the velocity stripping criterion<sup>8</sup> with  $b = 1.26$  is adequate at high velocities for lighter projectiles, say  $Z_1 \leq 17$ , while  $b = 1.33$  is more satisfactory for heavier projectiles, e.g. for Br. Data references: He (22,25,37,41), C (20,33), N(21-25,33,11), O(20,32-35), Ne(38), Na(38), K(38), Cl(32), Br(27,28,30,39), I (27-30), Ta(31), U(16,27). Proton stopping powers (21,25,40-49). Some data used in the analysis have been omitted from the figure for clarity of presentation.
- Fig. 3. Effective charge in different models, calculated using the velocity stripping criterion<sup>8</sup> with  $b = 1$  and (a) Thomas-Fermi charge density profile, and (b) a Lenz-Jensen profile;<sup>51</sup> (c) represents the Knipp and Teller<sup>4</sup> calculation using a Thomas-Fermi profile and stripping criterion differing from that used for (a) and (b).<sup>52</sup>
- Fig. 4.  $Z_1^{*3}$  and Bloch stopping power corrections for ions of atomic number  $Z_1$ , in terms of the correction factor  $C$  defined by Eq. (II.5) as discussed in the text.

- Fig. 5. Empirical effective proton charge for stopping power. Points are  $Z_p^*$  values obtained using theoretical  $(Z_1^*/Z_1)$  and experimental  $S$  in Eq. (II.4). Averages over targets, e.g., the solid lines in Fig. 1, were used for  $S$ , so that each point represents several data. Only values deduced from light-projectile  $S$  data are shown in the plot, since heavy-ion data are available only for velocities too high to give significant deviations from theory for  $Z_p^* = 1$ , as Fig. 2 shows. The solid line is drawn through the points to aid the eye; smoothed values of  $Z_p^*$  are given in Table II.
- Fig. 6. Effective ion charges obtained using the empirical  $Z_p^*$ . Comparison to the  $b = 1.26$  curve of Fig. 2 with points obtained from light-ion experimental data by using Eq. (II.4) and the average  $Z_p^*(v_1)$  given by the solid line in Fig. 5. Target dependence for a given projectile is indicated by, e.g., several points at the same velocity. The heavy-ion data shown in Fig. 2 remain unchanged because for them  $Z_p^* \approx 1$ .
- Fig. 7. Effective charge of screened proton.  $Z_p^*(v_1)$  calculated as discussed in the text using (a) the velocity stripping criterion, and (b) the energetic stability criterion. The empirical  $Z_p^*$  of Fig. 5 is shown as (c).
- Fig. 8. Effective charge in Thomas-Fermi approximation for ions. Calculated using the energy criterion for (a) a self-consistent TF ion of finite radius, and (b) a model ion obtained by truncating the TF density for a neutral atom. Calculated using the velocity criterion and the truncated TF neutral atom density with (c)  $b = 1$ , and (d)  $b = 1.26$  (same as the curve in Figs. 2 and 6).

Fig. 9. Comparison of self-consistent effective charges with data.

$(Z_1^*/Z_1)$  is calculated self-consistently in Thomas-Fermi (SCTF) approximation for an ion, as discussed in the text and shown as curve (a) in Fig. 8. Data shown are those used in Fig. 6.

Fig. 10. Electronic stopping power at  $v_1 < v_0$ . Solid lines: obtained by linear interpolation according to Eq. (IV.1) as discussed in the text. Dashed lines: obtained from Lindhard's<sup>5</sup> and from Firsov's<sup>16</sup> estimates. Experimental S at  $v_1 = 0.4lv_0$  in (a) carbon targets,<sup>39,40</sup> and in (b) aluminum targets.<sup>40</sup>



FIG. 7

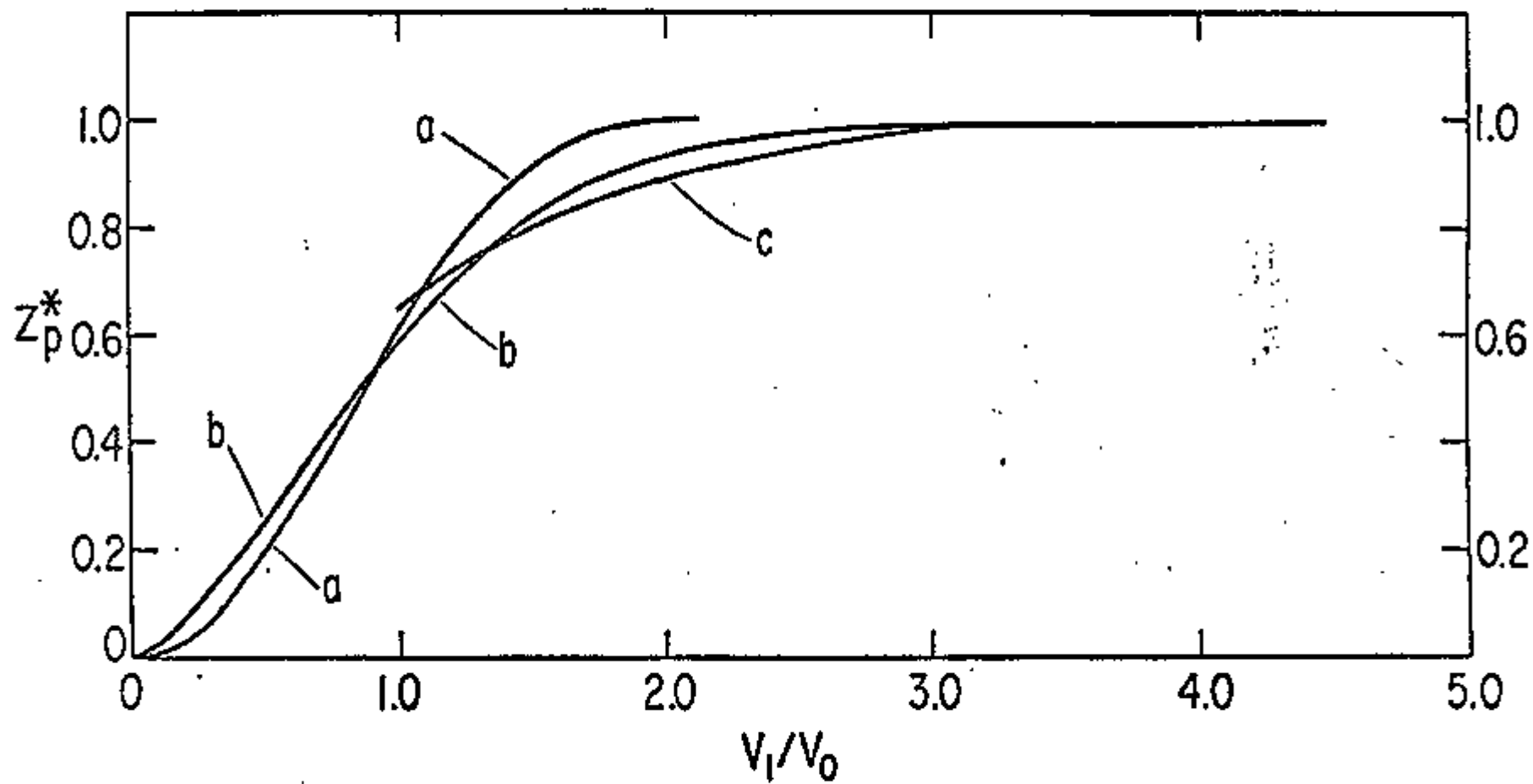


FIG. 4

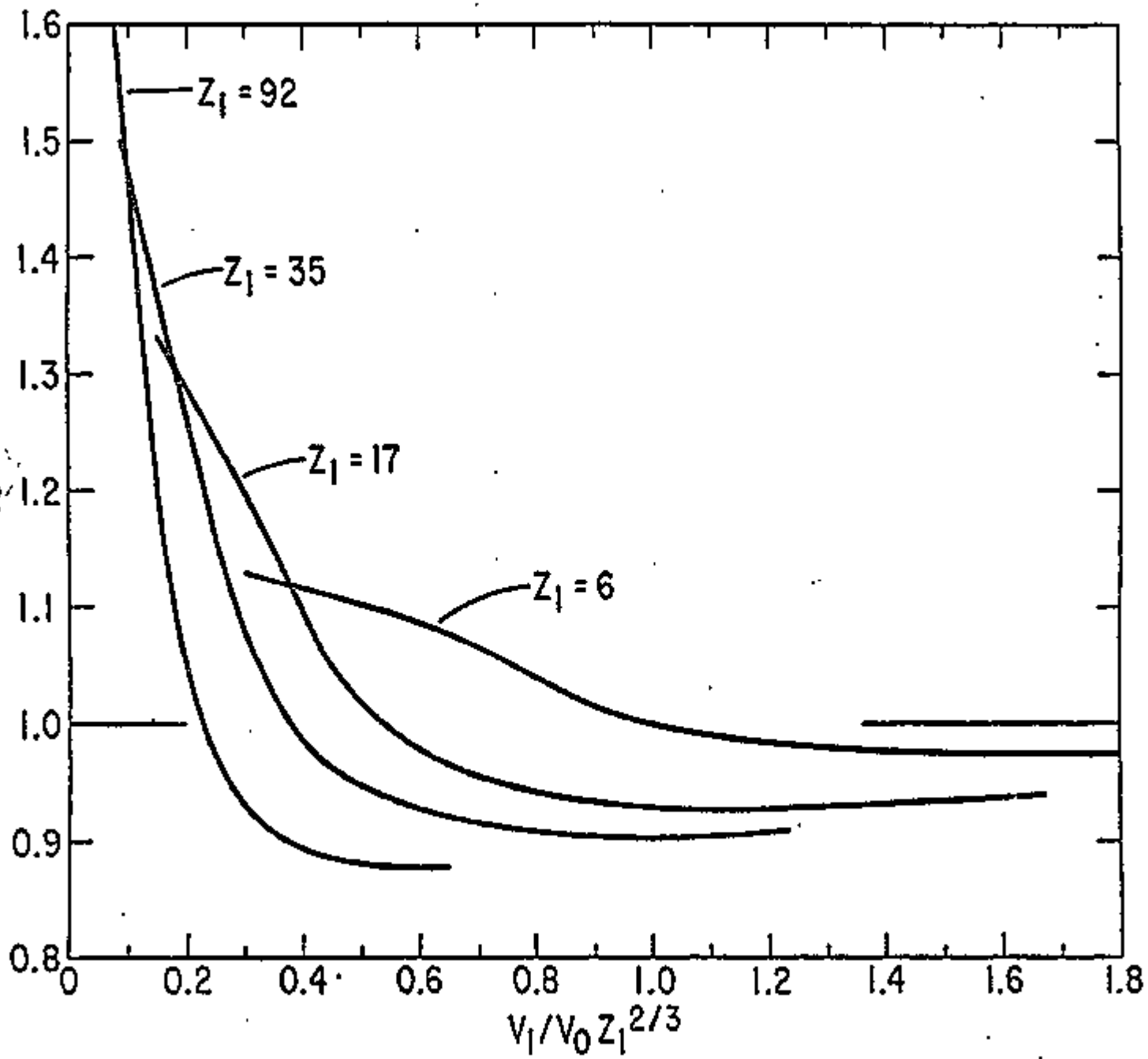


Fig. 3

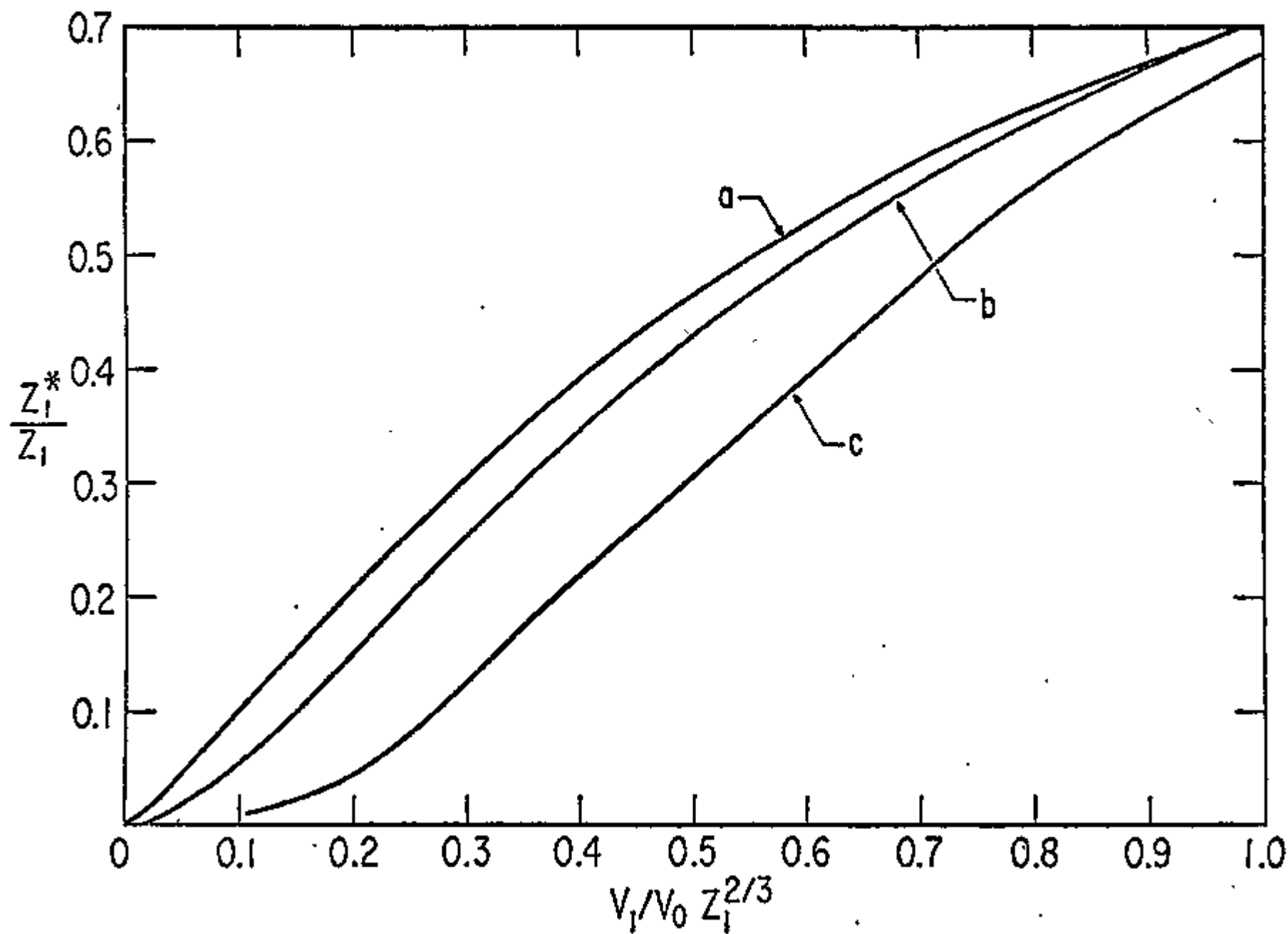


FIG. 1

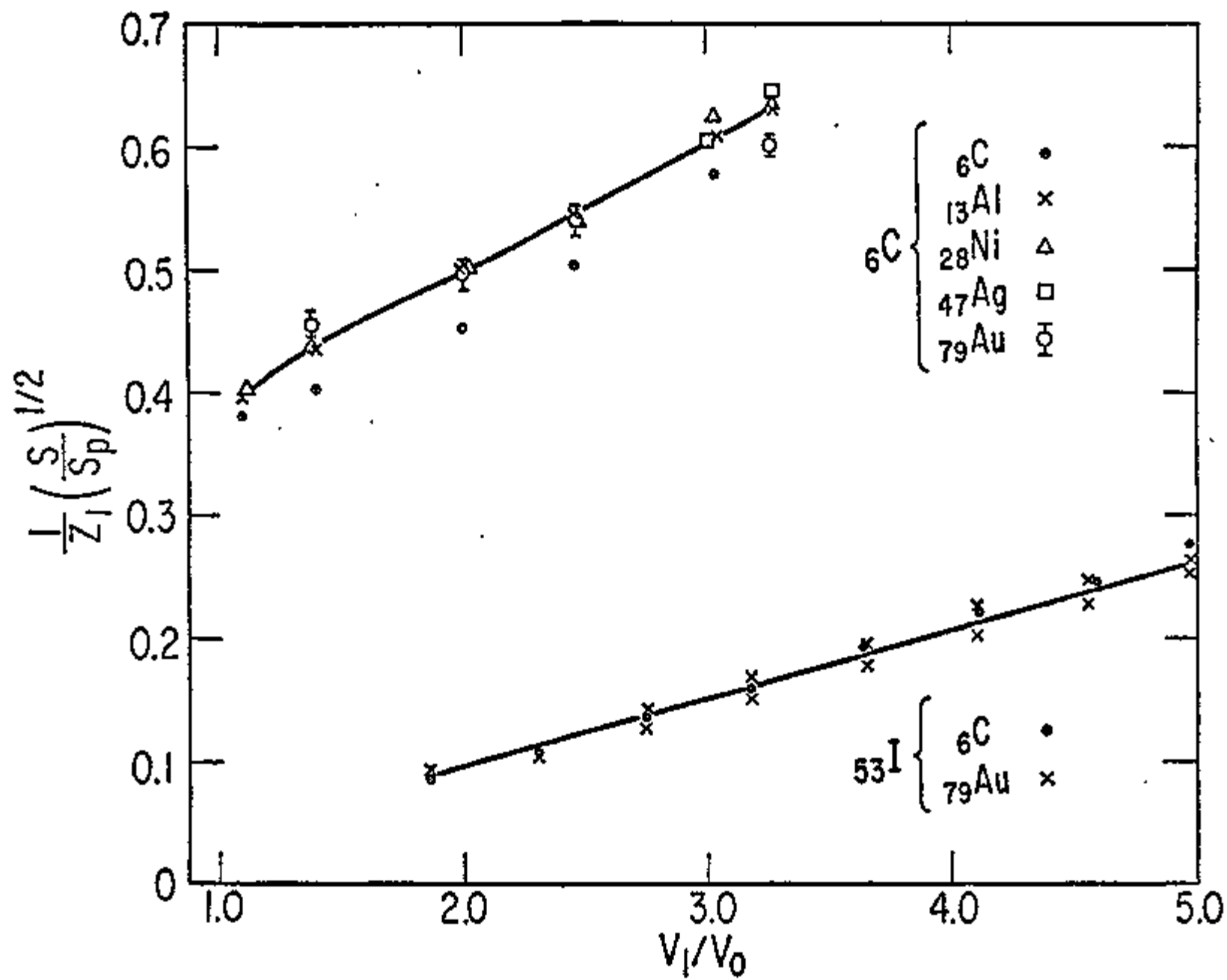


Fig. 9

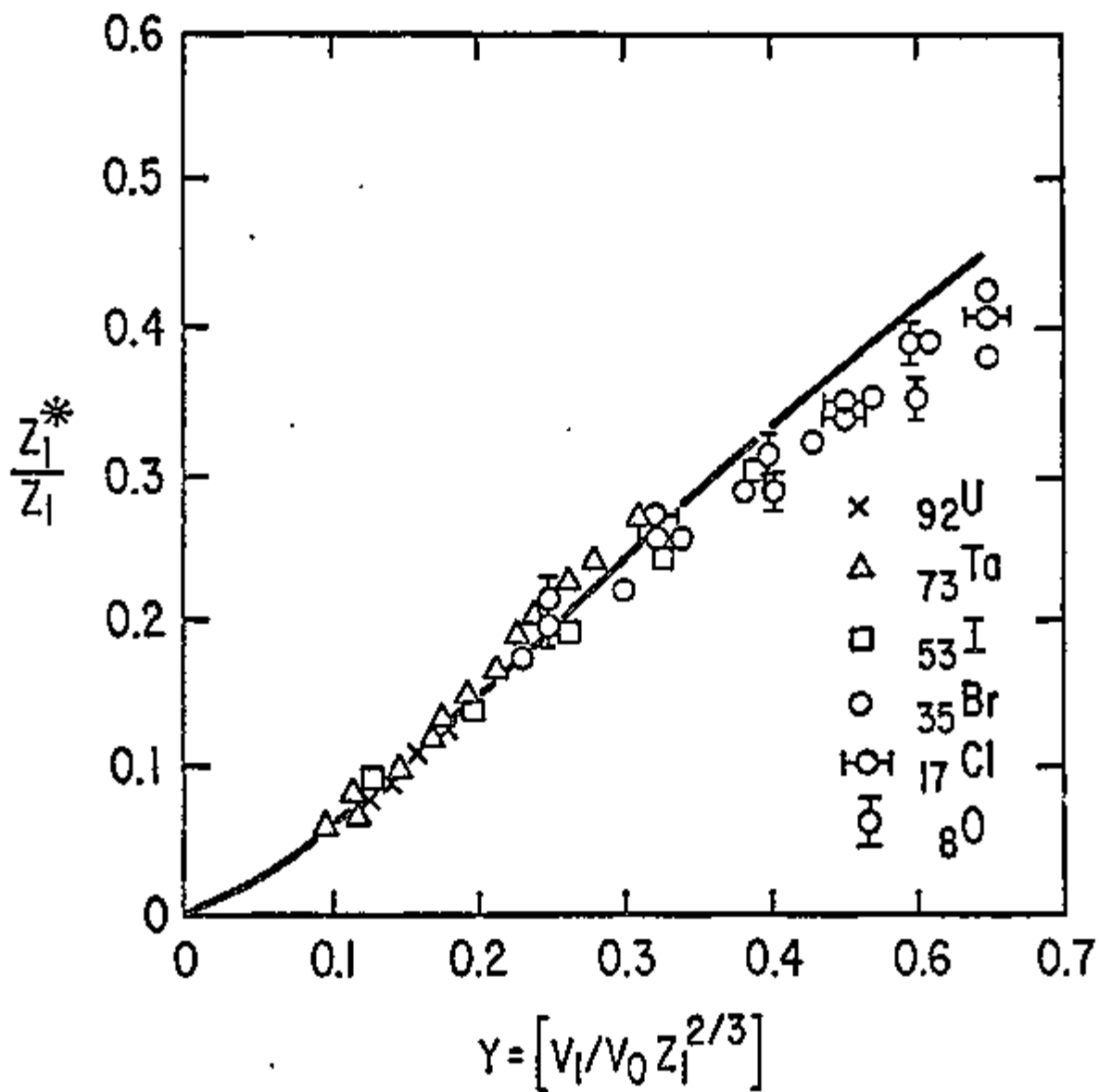
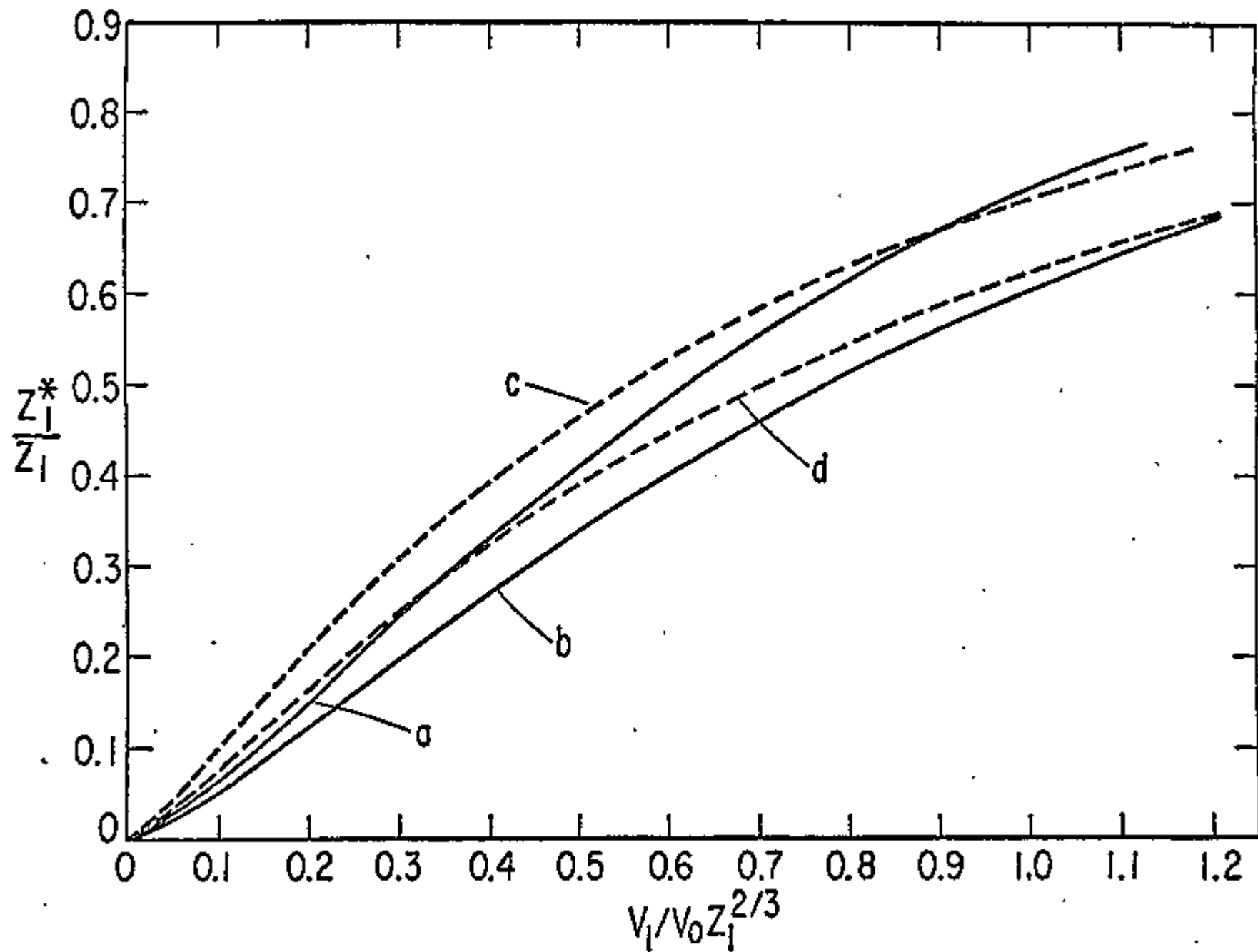


FIG. 8



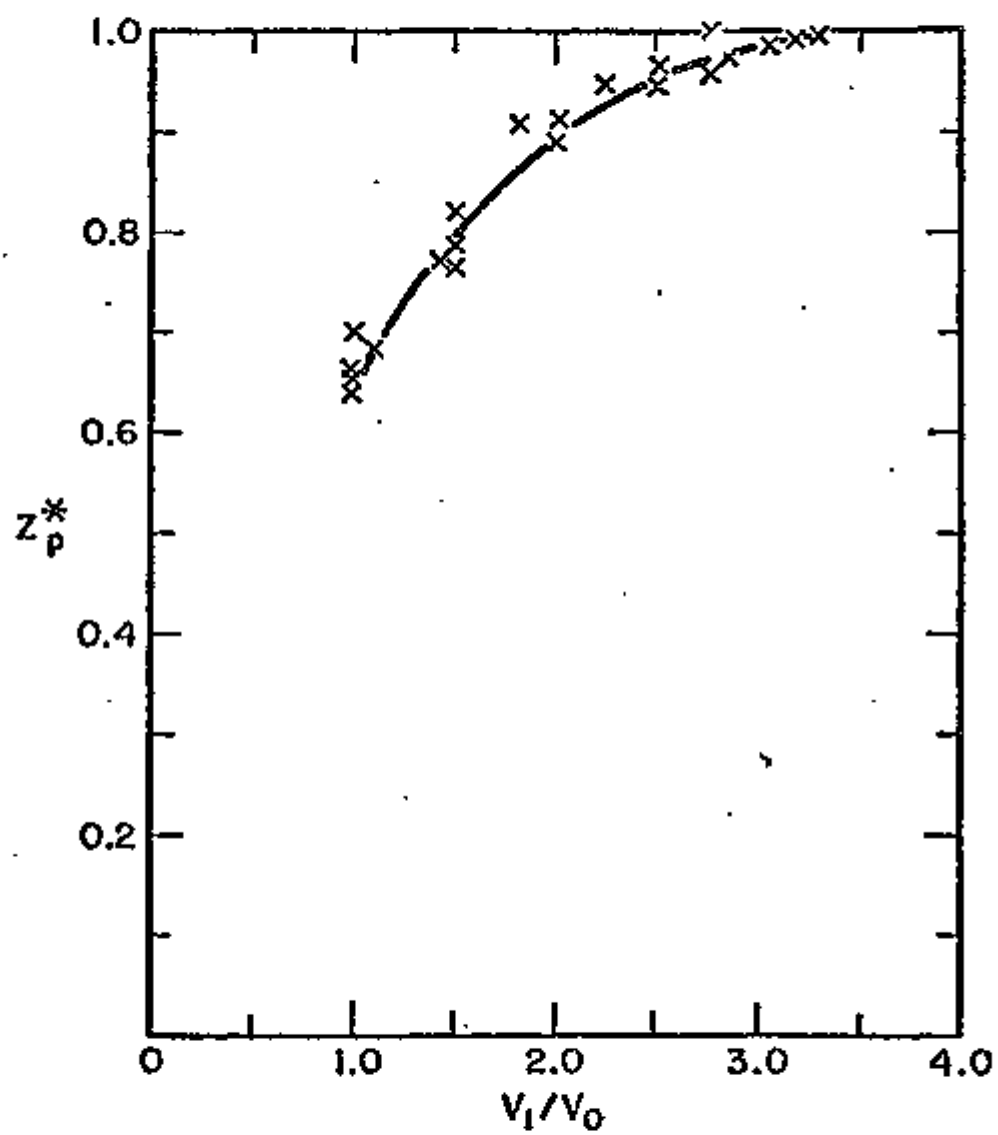
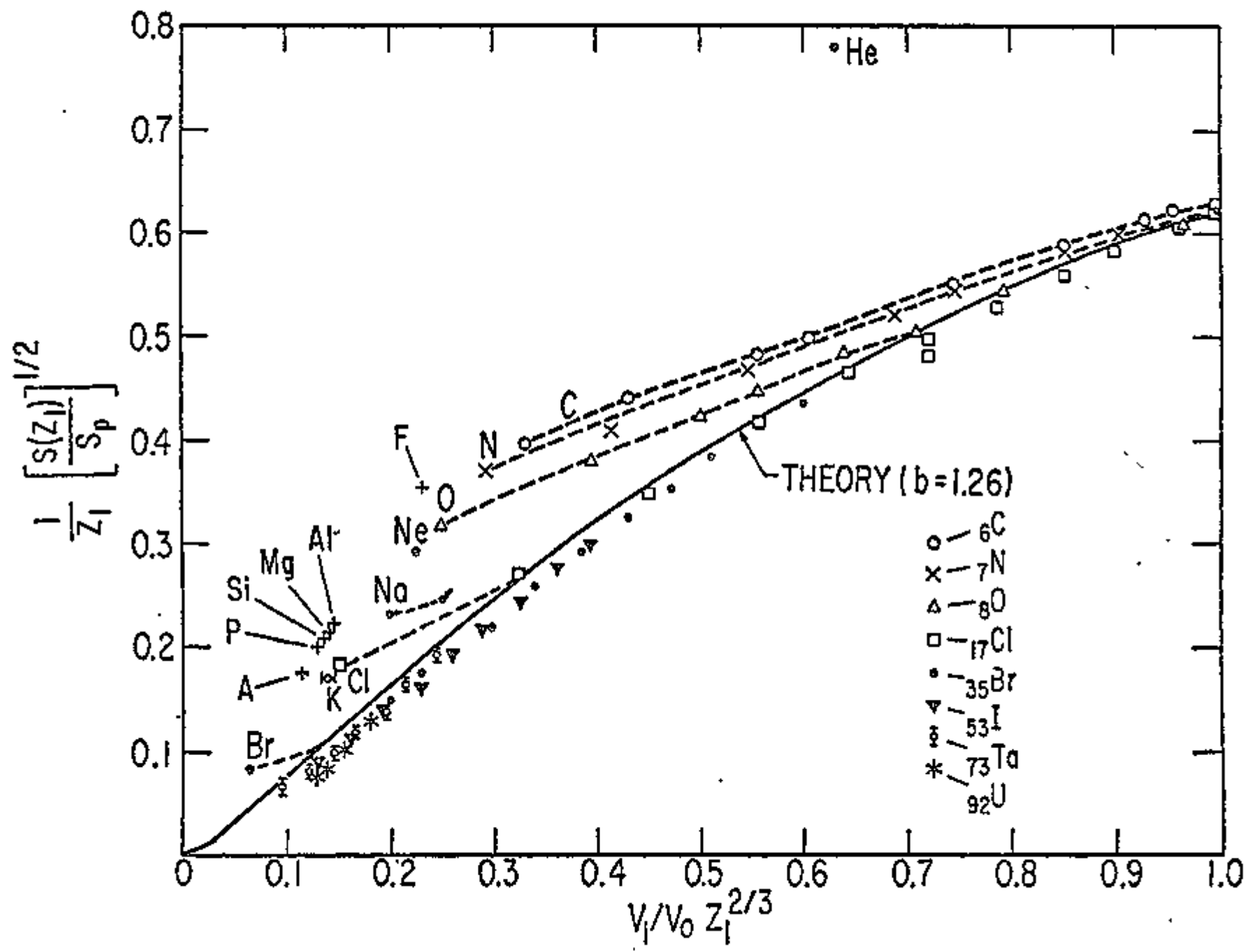


Fig. 5

FIG. 2





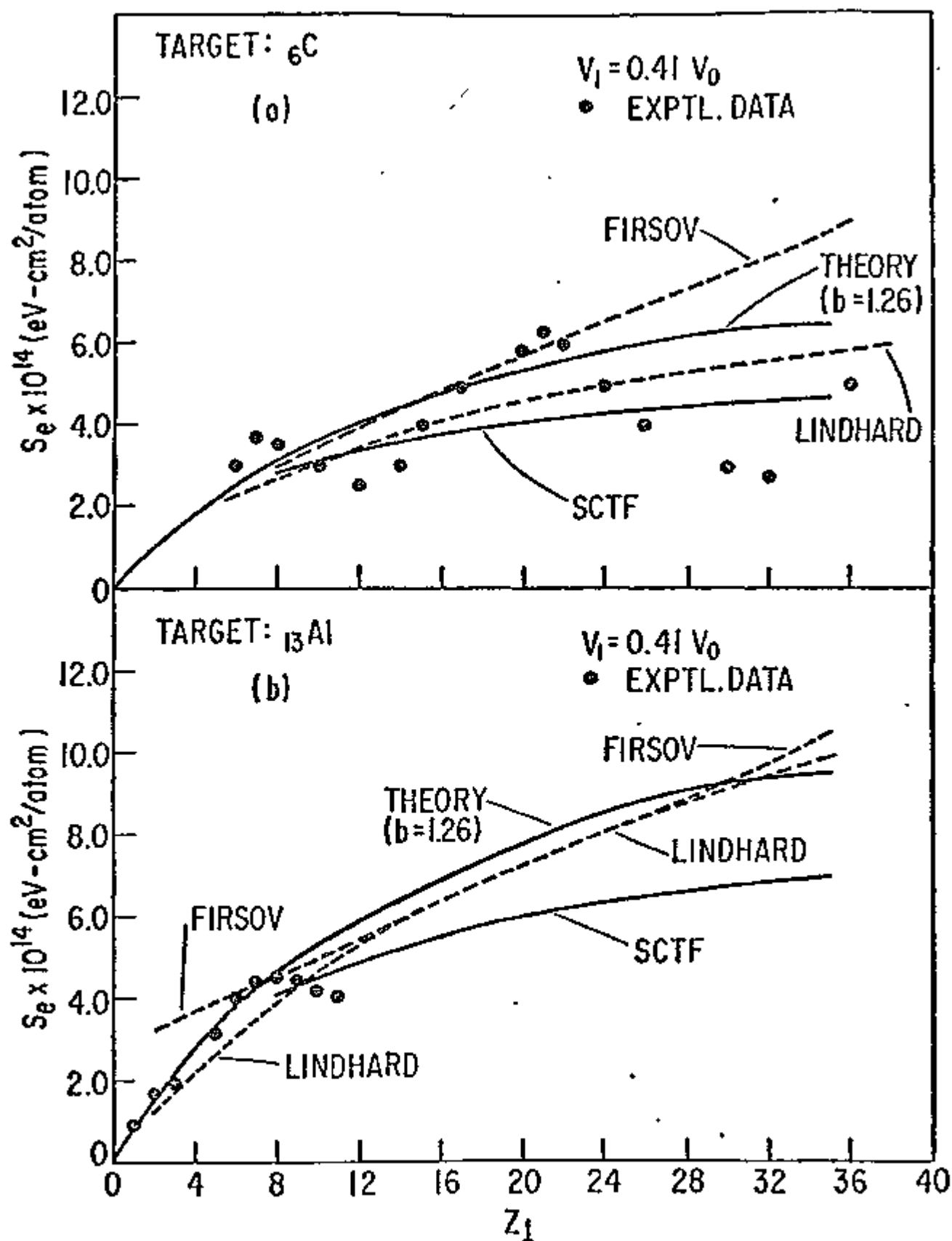


Fig. 10

## 7. Energy Straggling of Ions in Solids (Chen, Laubert)

### 1. Introduction

Energy-loss straggling of heavy ions in solids has recently received renewed attention. One of the reasons for this is the application of ion backscattering techniques in depth-profile investigations.<sup>1</sup> Unfortunately, reliable straggling measurements are difficult to perform experimentally, in part because the effects of thickness nonuniformity and of energy straggling appear in the same way. It has been demonstrated that same materials prepared differently can yield results that differ by more than a factor 2.<sup>2</sup> Hence, interpretation of the observed width as due to energy straggling appears to be in question, and recent experiment<sup>3</sup> have shown that there are discrepancies between measured and predicted energy stragglings. Further progress requires clarification of the contributions of surface nonuniformities. We present the results of our study on the effect of surface nonuniformity for thermal evaporated carbon foils with proton and He<sup>+</sup> projectiles. Since the study of each individual foil is difficult and irrelevant, we used a statistical approach which allows us to extract the straggling data from the observed energy distribution correctly and, at the same time, provides us with information about the surface nonuniformity for this particular material.

For high velocity light ions in a random target, Bohr<sup>4</sup> has given the straggling formula

$$\Omega^2 = 4\pi Z_1^2 Z_2 e^4 Nt, \quad (1)$$

where  $e$  is the charge of the electron,  $Z_1$  and  $Z_2$  are the atomic numbers of the projectile and target atoms, respectively,  $N$  is the number of target atoms per unit volume, and  $t$  is the target thickness. The straggling,  $\Omega^2$ , is defined to be the variance of a gaussian distribution of energy losses. When the projectile velocity  $v$  is no longer large compared to that of inner electrons, these electrons cannot be considered free, and Eq. (4) has to be modified. Bohr considered this case by assuming only target electrons with velocities smaller than  $v$  to be effective. This approximation of dividing atomic electrons into inner and outer shells has later been improved and refined by Lindhard and Scharff<sup>5</sup>, Bonderup and Hvelplund<sup>6</sup> (BH) and Chu.<sup>7</sup> Based on expressions for  $\Omega^2$  in an electron gas, Bonderup and Hvelplund gave the following prescription for straggling

$$\Omega^2 = 4\pi Z_1^2 e^4 N t \int 4\pi r^2 \rho(r) f(r, v) dr, \quad (2)$$

where

$$f(r, v) = 1 + \left(\frac{1}{5} + \frac{\chi^2(r)}{\sqrt{3}}\right)^2 \left(\frac{v_F(r)}{v}\right) \ln\left(\frac{v}{v_F(r)}\right)^2, \quad (3a)$$

$$= \frac{-1}{(1 + 13\chi^2(r))^{1/2}} \left(\frac{v}{v_F(r)}\right)^2, \quad (3b)$$

$$\chi^2(r) = \frac{e^2}{\pi \hbar v_F(r)}, \quad v_F(r) = \left(\frac{\hbar}{m_e}\right) (3\pi^2 \rho(r))^{1/3}.$$

For  $v \leq v_F(r)$  (3b) applies, and for  $v \geq v_F(r)$ . The expression which gives a low value of  $f(r, v)$  should be used. Thomas-Fermi or Hartree-Fock description can be used for the atomic charge distribution  $\rho(r)$ .

So far, the foil has been assumed to be uniform. If  $P_{\bar{t}}(t)dt$  is the probability for a particle to go through a thickness between  $t$  and  $t+dt$ , then it can be readily shown that

$$\Omega_{\text{exp}}^2 = \Omega^2(\bar{t}) + S^2 \Delta t^2, \quad (4)$$

where

$$\bar{t} = \int P_{\bar{t}}(t) t dt,$$

$$\Delta t^2 = \int P_{\bar{t}}(t) (t - \bar{t})^2 dt,$$

and  $S$  is the stopping. Obviously,  $\Delta t$  may vary from target to target. If one takes enough foils of the same  $\bar{t}$ , one can expect that there is a mean  $\Delta t$  for these targets, and a certain distribution of  $\Delta t$  about this mean. However,  $\Delta \bar{t}$  may still vary with  $\bar{t}$ . In the next section, we give a brief description of the experimental arrangement, and in Section III, we show how the experimental straggling measurements can be corrected for the surface nonuniformity effect from a statistical point of view.

## II. Experimental Method

Proton and  $^4\text{He}^+$  beams of 50-300 keV provided by the New York University accelerator were analyzed in a  $90^\circ$  magnet of energy resolution  $5 \times 10^{-4}$  and directed onto the carbon foil surrounded by a copper cylinder cooled by liquid nitrogen to reduce carbon build up on the foil. The beam current was typically 0.01 nA over a target area of  $1 \times 10^{-4} \text{ cm}^2$ . The target chamber pressure was about 2  $\mu\text{Torr}$ .

The arrangement used to detect the emerging ions from the foil is shown in Fig. 1 of Section III-2. The divergence of the incident beam was reduced to less than 0.5 mrad by means of two cross slits. The transmitted ions in the forward direction were analyzed in a second magnet of the same resolution. A surface barrier Si detector was used to record the energy analyzed ions. The energy distribution was obtained by sweeping the magnetic field about the mean energy of the emerging ions. A differential gauss meter which measures the changing magnetic field gives ramp signals to a linear gate which in turn converts signals from the particle detector into pulses with pulse height proportional to the ramp voltage and stores them in a PHA. To assure that no distortion of spectrum results from the non-linear response of the magnet, the sweep was so adjusted that the whole distribution always falls in the linear region. Several sweeps were taken to average out any small beam fluctuations. The sweep was calibrated by removing the target and using incident beam of known energy at several points in the sweep. A typical energy distribution is shown in Fig. 1. A second detector at 135° from incident beam direction was used to detect contaminants of the foil. In all cases such contaminants were negligible. The foil thickness was determined by using the proton stopping power  $S_H = 0.75 \text{ keV-cm}^2/\mu\text{g}$  at 75 keV,<sup>8</sup> where the proton stopping power is at its maximum. The uncertainties in the thickness measurements were estimated to be better than 5%.

### III. Results and Discussions

The variance of the energy distribution  $\Omega_{\text{exp}}^2$  as a function of incident proton and  $\text{He}^+$  energies was measured for 20 different targets ranging from 4 to 20  $\mu\text{g}/\text{cm}^2$  with a total of 500 spectra of the type shown in Fig. 1. In many cases, there were tiny pin holes within the bombarded area. This allows us to record both the incident and the transmitted energy distributions at the same time without removing the target. The HWHM of the incident energy distribution was  $\leq 50$  eV in all cases. Accordingly, no correction for instrumental spread was necessary. The transmitted energy distribution closely resembles that of a Gaussian. However, a slight asymmetry was observed (see Fig. 1). The asymmetry decreases with increasing target thickness and decreasing energy and is smaller for  $^4\text{He}^+$  than for protons. Vavilov<sup>9</sup> and Seltzer and Berger<sup>10</sup> have given a simple rule for testing the type of distribution in terms of the parameter

$$\kappa = 0.30058 \frac{m_e c^2}{\beta^2} \frac{Z_2}{Z_1} \frac{t}{T_{\text{max}}}, \quad (5)$$

where  $m_e$  is the mass of the electron,  $\beta = v/c$ ,  $Z_1$  and  $Z_2$  are the atomic and mass numbers of the target atom,  $t$  is the target thickness in  $\text{g}/\text{cm}^2$ , and  $T_{\text{max}} = (4M_e/M)E$  is the maximum energy transfer to a target electron by a projectile of mass  $M$  and energy  $E$ . If  $\kappa \gg 1$ , the distribution is Gaussian; if  $\kappa \ll 1$ , the distribution is of the Landan type. In our experiment,  $\kappa$  ranges from 11 to 2000 for  $^4\text{He}^+$  and 0.7 to 12b for protons. The correction to  $\Omega_{\text{exp}}^2$  due to this asymmetry was about 5% for the

thinnest target at the highest proton energy and smaller in other cases. Hence, no such correction was incorporated.

In Figs. 2 and 3,  $\Omega_{\text{exp}}^2/t$  is plotted as a function of the mean projectile energy  $E = E_0 - \frac{1}{2} \Delta E$ ; where  $E_0$  is the incident energy and  $\Delta E$  is the energy loss. As predicted by Bonderup and Hvelplund<sup>6</sup>,  $\Omega_{\text{exp}}^2/t$  decreases with projectile velocities for both  ${}^4\text{He}^+$  and protons. Nevertheless, they are consistently higher. It is interesting to note that data for various target thicknesses scattered much more for  ${}^4\text{He}^+$  than for protons. In addition, thicker-target data were lower and scattered less in both cases. This can not be due to uncertainties of the measurements, as reproducibility for each measurement was better than 10%. Systematic errors are also very unlikely, since measurements for different targets and different energies were taken in random orders. We conclude, therefore, that the somewhat larger scattering of He data is due to the surface nonuniformity and the higher stopping power of He as compared with that of protons. Furthermore, the lower values of  $\Omega_{\text{exp}}^2/t$  for thicker targets suggest that the surface nonuniformity, on the average, does not increase with the target thickness. On the other hand, there is no reason to believe that thicker targets are more uniform than thinner ones. We are therefore led to believe that  $\Delta \bar{t}$  is independent of target thickness for thermal evaporated carbon foils of 4-20  $\mu\text{g}/\text{cm}^2$  thickness. The mean  $\Delta \bar{t}$  can be determined provided we make sufficient measurements on many targets of different thicknesses at a given energy and fit the resulting  $\Omega_{\text{exp}}^2$  to the linear form  $\Omega_{\text{exp}}^2 = at+b$ . A comparison with Eq. (4)

immediately identifies  $b = S^2 \Delta t$ , and  $a = \Omega^2 / \bar{t}$ . Indeed, if there is a  $\Delta \bar{t}$  due to inhomogeneities, then  $b/S^2$  must be the same at all energies and for all projectiles. Plots of  $\Delta \bar{t}$  vs.  $E$  are given in Fig. 4. We found that  $\Delta \bar{t} = 0.59 \mu\text{g}/\text{cm}^2$  for protons and  $0.55 \mu\text{g}/\text{cm}^2$  for  ${}^4\text{He}^+$ . Figure 5 shows the "true straggling" per unit thickness  $a = \Omega^2 / \bar{t}$  as a function of  $E$ . Although agreement with predictions of Bonderup and Hvelplund<sup>6</sup> is improved, experiments are still higher than theoretical predictions.

In conclusion, we have investigated the effect of surface nonuniformity  $\Delta t$  on energy straggling for thermal evaporated carbon foils of thickness (4-20  $\mu\text{g}/\text{cm}^2$  with protons and  ${}^4\text{He}^+$  projectiles in the energy range of (50-300) keV. A mean  $\Delta t = 0.57 \mu\text{g}/\text{cm}^2$  was found, which was independent of the target thicknesses. In order to minimize the effect  $\Delta t$  on the straggling measurements, thicker targets should be used whenever possible. In addition, the straggling corrected for surface nonuniformity is higher than predictions. This discrepancy must be clarified theoretically.



## References

1. W. K. Chu et al., Thin Solid Films 17, 1 (1973).
2. C. J. Sofield, J. A. Cookson, J. M. Freeman and parthasaradhi, Nucl. Inst. Meth. 138, 411 (1976).
3. G. E. Hoffman and D. Powers, Phys. Rev. A 13, 2042 (1976).
4. N. Bohr, K. Dan. Vidensk. Selsk. Mat. Fys. Medd. 18, No. 8 (1948).
5. J. Lindhard and M. Scharff, K. Dan. Vidensk. Selsk. Mat. Fys. Medd. 27, No. 15 (1953).
6. E. Bonderup and P. Hvelplund, Phys. Rev. A 4, 562 (1971).
7. W. K. Chu, Phys. Rev. A 13, 2057 (1976).
8. H. R. Andersen and J. F. Ziegler, Hydrogen Stopping Powers and Ranges in All Elements (Pergamon, Oxford, England, 1977).
9. P. V. Vavilov Zh. Eksp. Teor. Fiz. 32, 320 (1957).
10. S. M. Seltzer and M. J. Berger in NAS-NRC publication No. 1133 (U.S. GPO, Washington, D.C., 1964), p. 187.

### Figure Legends

- Fig. 1. Post target energy distribution of 243 keV protons through  $11 \mu\text{g}/\text{cm}^2$  carbon foil. The arrow indicates the position of incident energy.
- Fig. 2. The measured variance per unit thickness of protons in carbon as a function of projectile energy. Fifteen targets of different thicknesses were used in obtaining these data. The dashed line is from Bohr's straggling formula<sup>4</sup>, Eq. (1), and the solid curve was prediction of Bonderup and Hvelplund.<sup>6</sup>
- Fig. 3. The measured variance per unit thickness of  $^4\text{He}^+$  in carbon foils of 5 different thicknesses. The dashed and solid curves are predictions of Bohr<sup>4</sup> and Bonderup and Hvelplund<sup>6</sup>, respectively.
- Figs. 4a and 4b. The mean surface nonuniformity  $\Delta \bar{t}$  determined at various energies. The dashed lines are averages of  $\Delta \bar{t}$ .
- Fig. 5. The energy straggling per unit thickness of protons in carbon after corrected for  $\Delta t$ . The dashed and solid curves are predictions of Bohr<sup>4</sup> and Bonderup and Hvelplund<sup>6</sup>, respectively.

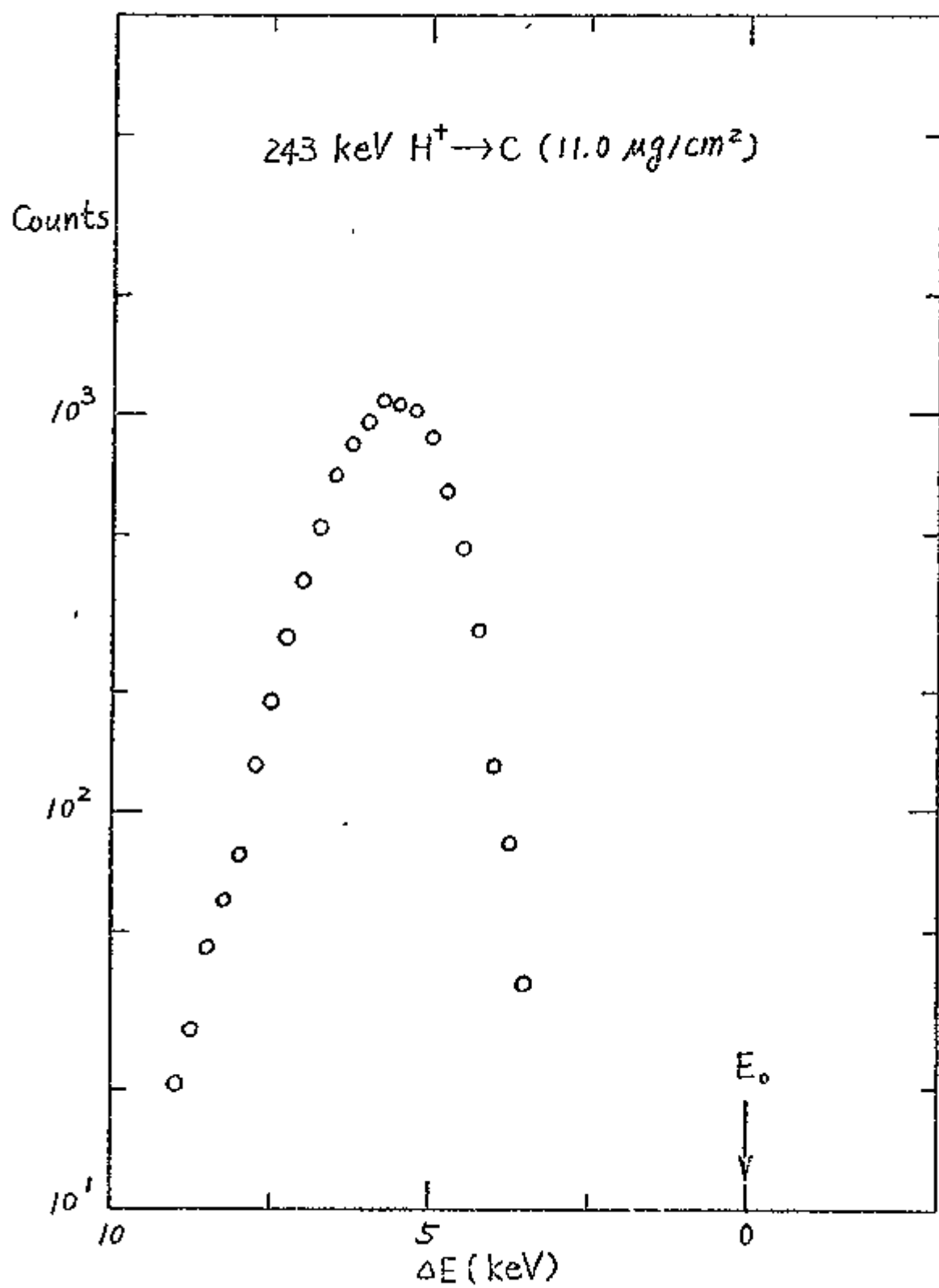


Fig. 1

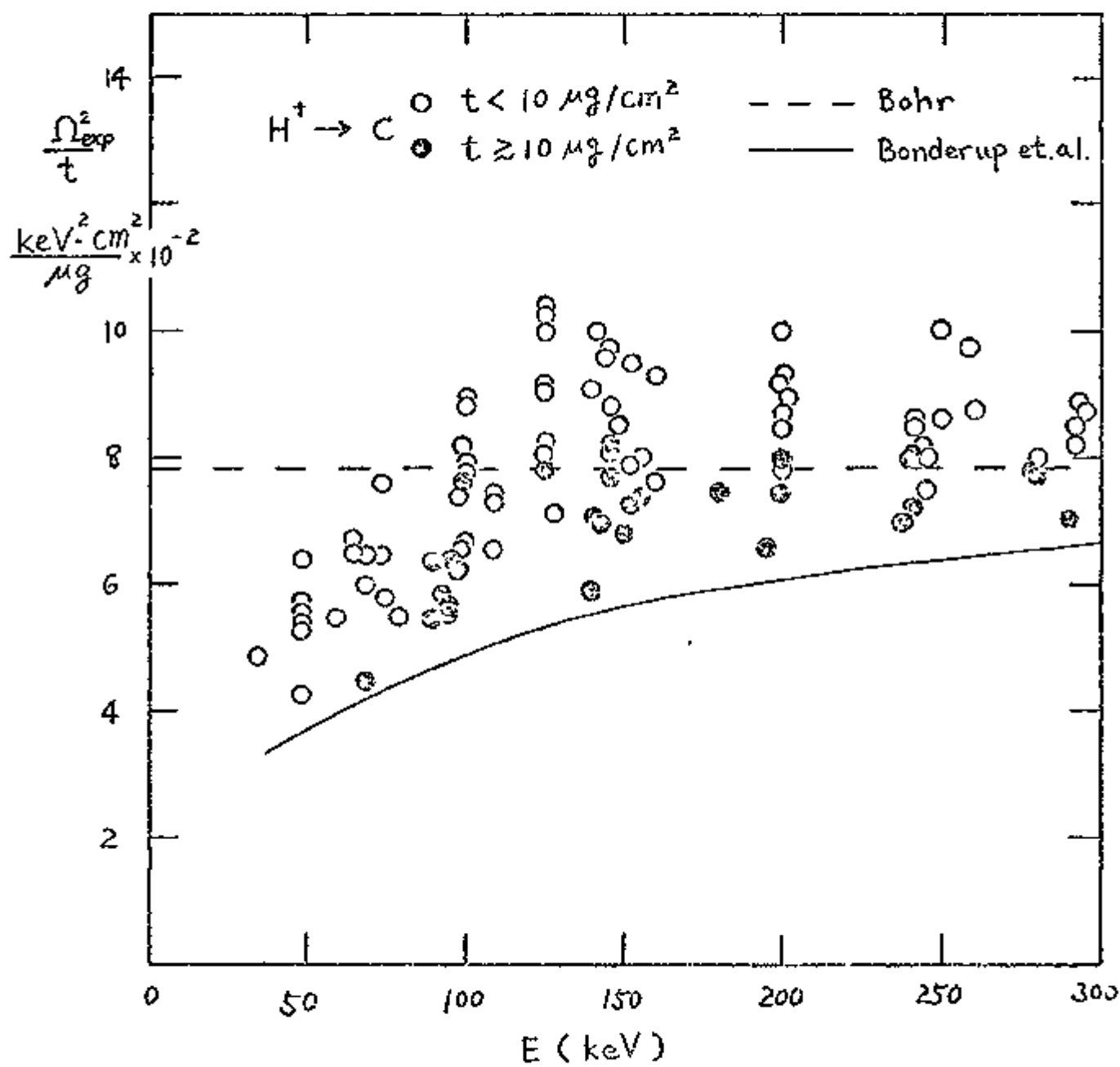


Fig. 2

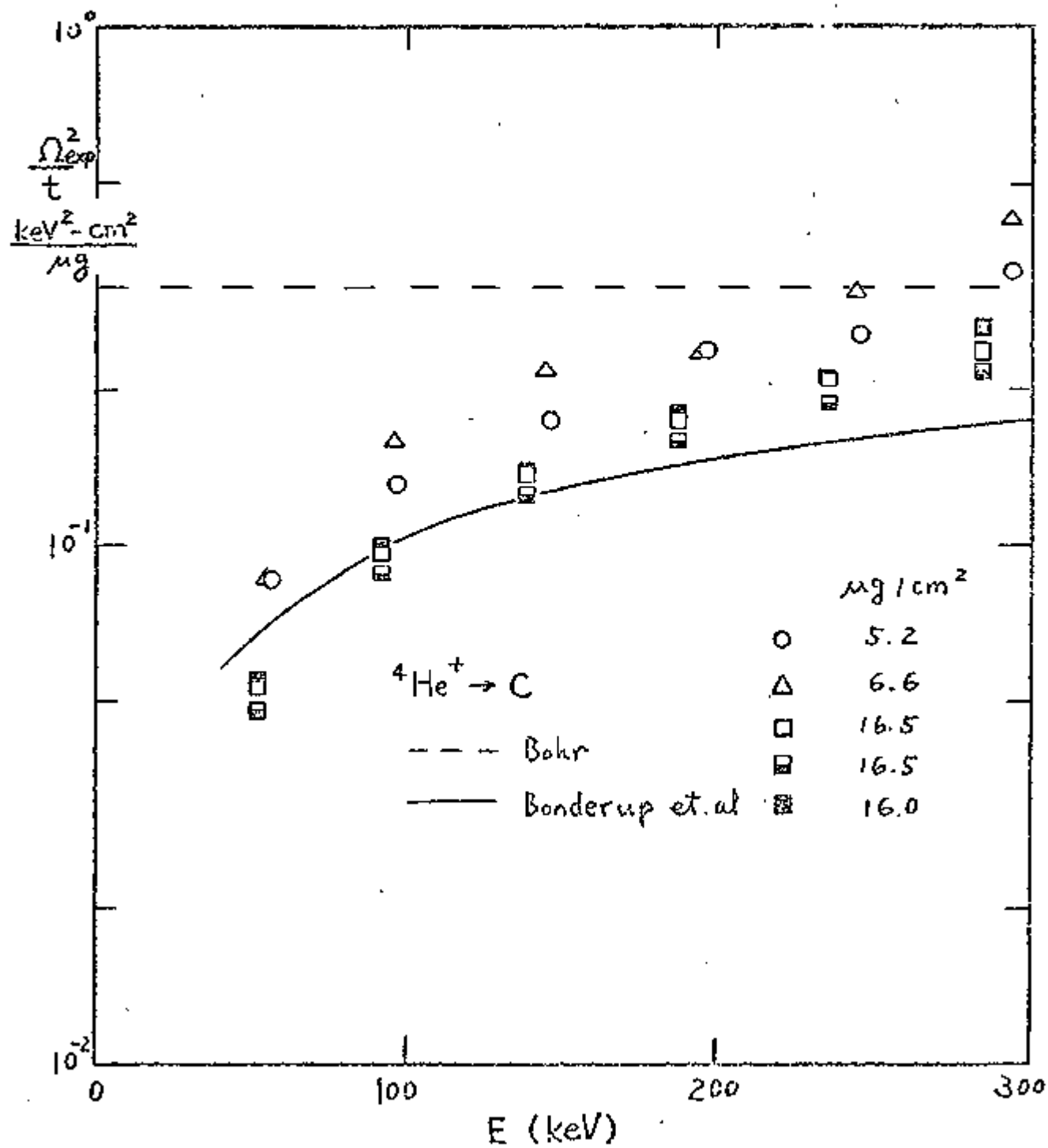


Fig. 3

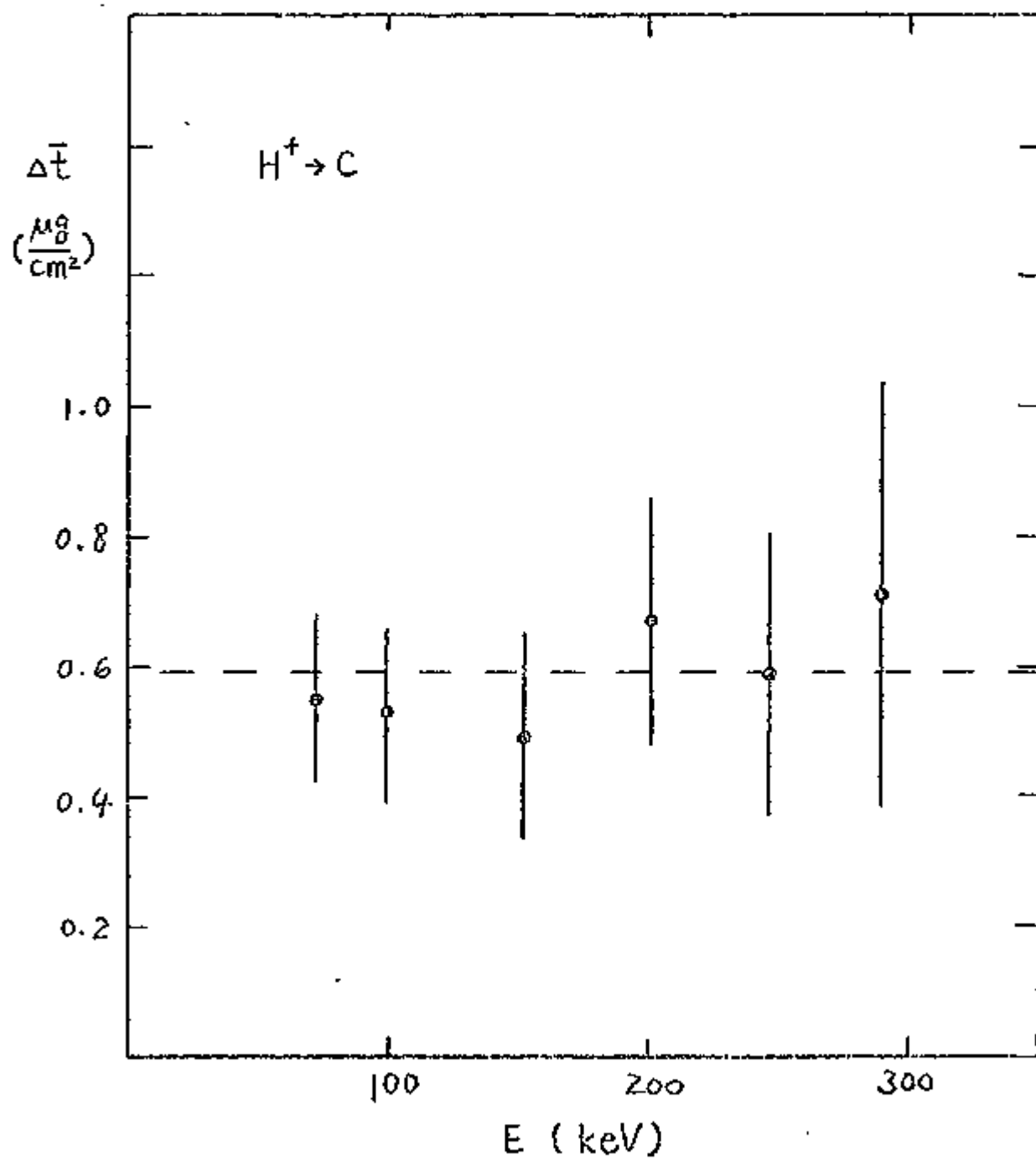


Fig. 4a

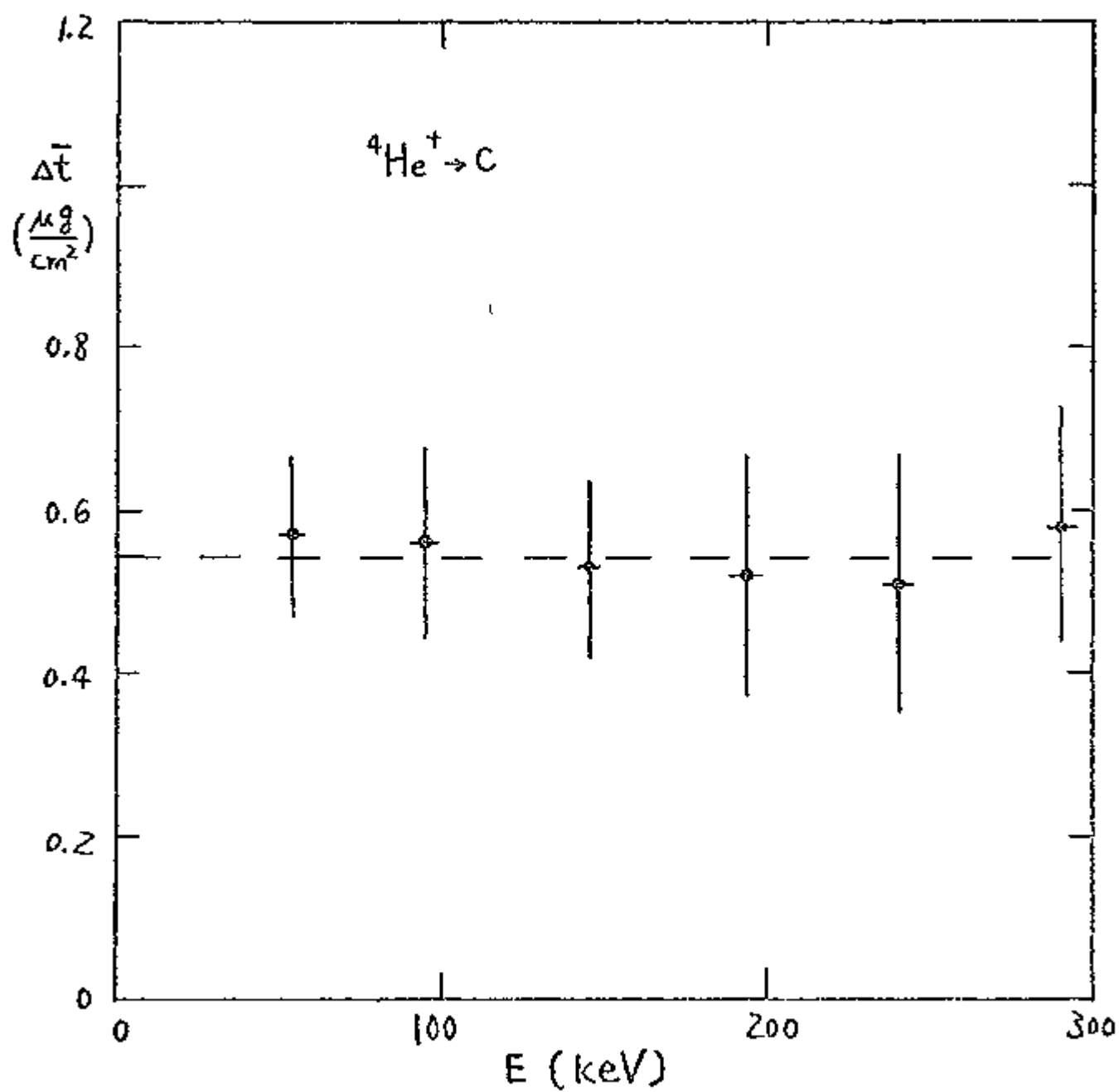


Fig. 4b

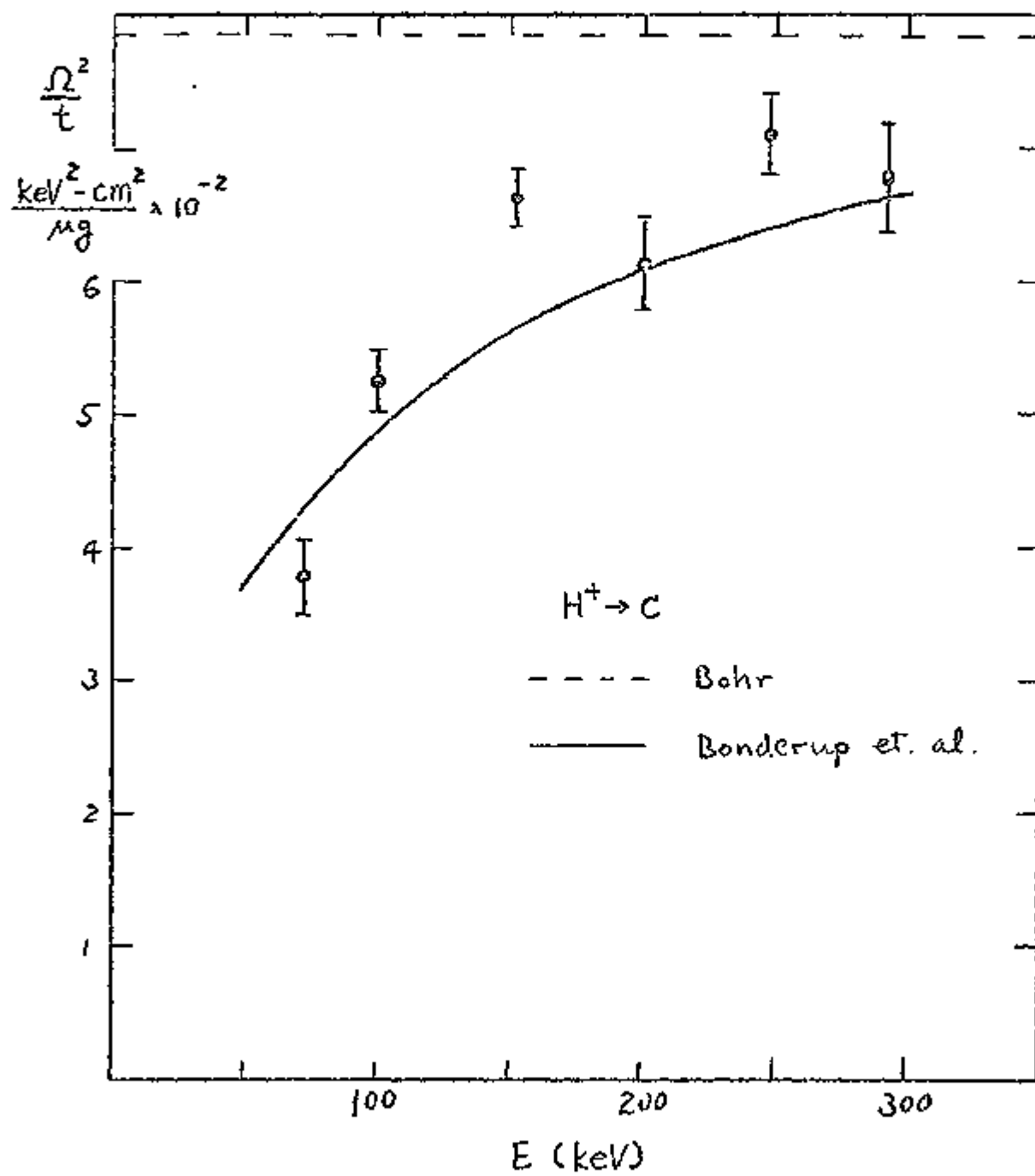


Fig. 5



IV. Informal workshop on current stopping-power problems  
New York University  
January 5 to 7, 1978

1978 is the thirtieth anniversary of the publication of Niels Bohr's treatise on *The Penetration of Atomic Particles through Matter*. The Workshop was held to concentrate on present stopping power data and the discrepancies between them, effective charge theory,  $Z_1^n$  effects for heavy and relativistic particles, and on straggling. The first Workshop on wake phenomena was held in January 1977. As then, G. Lapicki and S. Stern have prepared the report which summarizes the discussions during the Workshop and collates most of the figures shown during the presentations. The sessions were attended by some 30 scientists actively interested in the field. We are grateful to C. Peterson and other members of the Radiation and Solid State Laboratory for their help during this meeting and to the New York University Arts and Science Faculty for support.

Werner Brandt

Rufus Ritchie

## CONTENTS

List of participants	ii
Program	iii
Introductory remarks (Brandt)	1
Survey of experimental stopping powers in solids (Ziegler)	5
Comparison of recent stopping power data (Ishiwari)	25
Additivity rule (Porter)	41
Energy loss of He ions in solidified gases (Chu)	57
Energy transfer to an harmonic oscillator (Basbas)	65
Stopping power of relativistic heavy ions (Ahlen)	73
$Z_1$ dependence of stopping powers (Brandt)	87
Higher-order $Z_1$ effects in stopping of channeled ions (Datz)	91
Energy straggling due to charge-state fluctuations of C <sub>2</sub> ions in gases (Schmidt-Böcking)	101
Review of energy-loss straggling (Hvelplund)	113
$Z_2$ dependence in straggling (Chu)	127
Straggling of low energy protons in carbon (Laubert)	139
Stopping powers in high energy physics (Hagstrom)	151
Beam-density effect on stopping powers (McCorkle)	171
Resonant coherent excitation of ions (Moak)	179
Effective charge theory and stopping power in solids (Robinson)	189
Capture-loss rates in the electron gas model (Ritchie)	203

## Summary and discussion:

Preliminary remarks and comment on binary collisions (Merzbacher)	213
Finite target-infinite medium (discussion, Ritchie, Neufeld)	215
Integrity of projectile $\rightarrow Z_1, Z_{1\text{eff}}$ (discussion, Porter, Robinson, Datz)	224
Departures from $Z_1^2$ ? (Ishiwari, Ashley, discussion)	236
To Bragg, or not to Bragg? (discussion, Brandt)	243
How much do stopping properties teach (or trick) us about atomic structure? (Stanton, discussion)	248
Close collisions versus distant collisions? (Merzbacher, discussion)	256

## Participants

Steven P. Ahlen	University of California (Berkeley)
Néstor Arista	Centro Atómico Bariloche (Argentina)
James C. Ashley	Oak Ridge National Laboratory
George Basbas	North Texas State University
Martin J. Berger	National Bureau of Standards (Washington)
Christopher Bottcher	Oak Ridge National Laboratory
Werner Brandt	New York University
David K. Brice	Sandia Laboratory
Aloke Chatterjee	Lawrence Berkeley Laboratory
Felix K. Chen	New York University
Wei-Kan Chu	IBM (East Fishkill)
Sheldon Datz	Oak Ridge National Laboratory
Jene Golovchenko	Bell Laboratories (Murray Hill)
Ray Hagstrom	University of California (Berkeley)
Preben Hvelplund	Oak Ridge National Laboratory
Gerald J. Iafrate	U. S. Army ECOM (Fort Monmouth)
Ryutaro Ishiwari	Nara Women's University (Japan)
Keith W. Jones	Brookhaven National Laboratory
Brian M. Kincaid	Bell Laboratories (Murray Hill)
Gregory Lapicki	New York University
Roman Laubert	New York University
William Losonsky	Maritime College SUNY (Bronx) and NYU
Richard A. McCorkle	IBM (Yorktown Heights)
Eugen Merzbacher	University of North Carolina
Charles D. Moak	Oak Ridge National Laboratory
Jacob Neufeld	Oak Ridge National Laboratory
Leonard E. Porter	University of Montana
Rufus H. Ritchie	Oak Ridge National Laboratory
John E. Robinson	Argonne National Laboratory
Horst Schmidt-Böcking	University of Frankfurt (Germany)
Kenneth F. Stanton	New York University
Stanley Stern	New York University
James F. Ziegler	IBM (Yorktown Heights)

## V. Publications

Physics Letters 52A, 374 (1977)

Velocity Spectra of Convoy Electrons Emerging with  
Swift Ions from Solids

Werner Brandt and R. H. Ritchie

Swift ions emerging from targets carry convoys of electrons. Velocity distributions are calculated for convoy electrons that trailed ions in wakebound states inside solids. They are compared with predictions of convoy formation by charge transfer to the continuum and with experiments.

Annals of the Israel Physical Society Vol. 1, 442 (1977)

Penetration Phenomena with Heavy Projectiles

Werner Brandt

This chapter falls into four parts. The first links the energy loss of charged particles to the electronic of matter through the spectral function. The second part investigates the milieu of enhanced electron density in which a moving ion finds itself because of the reaction of the medium to the presence of the ion and briefly discusses possible consequences for the nuclear spin precession of nuclei moving in magnetized solids. The third part summarizes some of the dynamic phenomena caused by wakes of electron density fluctuations trailing

swiftly moving ions in solids. The final part touches upon some new topics which may move into the center of interest in the near future.

Yaakov Dar's idea leading to the convocation of the Haifa International Workshop on Atomic Physics Related to Nuclear Experimentation coincides with Niels Bohr's assessment,<sup>1</sup> of 1948, that the "phenomena of scattering and stopping of high speed atomic particles in passing through matter and accompanying ionization and radiation effects have, as is well known, given one of the most important sources of information regarding the constitution of atoms".

Physics Letters 65A, 113 (1978)

Analysis of Experimental Velocity Distributions of Convoy  
Electrons

W. Meckbach, N. Arista, and W. Brandt

Available data on the properties of velocity distributions of electrons accompanying ions in the velocity range from 1 to 5 au emerging from gas and solid carbon targets, for incident  $H^+$  and  $H_2^+$  beams, are presented in a consistent manner and compared with the theories of charge transfer to the continuum and of electrons in wake riding states trailing ions in solids.

Physical Review A (in publication)

Projectile-Charge Dependence of Stopping Powers

R. H. Ritchie and Werner Brandt

Recent stopping-power data of solids with atomic number  $Z_2$  ranging from 13 to 79 for ions ranging in atomic number  $Z_1$  from 1 to 9 and in velocity from  $v_0$  to  $12 v_0$  are analyzed in terms of  $Z_1^3$  effects and effective ion charges. They are found to be consistent with current theory. High-velocity forms of the  $Z_1^3$ -proportional stopping-power contributions are calculated by the method of moment integrals.

Advances in Chemistry (in publication)

Photomagnetic Positron-Annihilation Effects

Werner Brandt

The annihilation characteristics of positrons in phosphorescent substances can be altered by illumination with ultraviolet light. This phenomenon and its quantitative aspects agree with the idea that some positrons capture an electron to form ortho- or para-positronium, and that the interaction with the excited triplet states of the illuminated phosphor molecules quenches positronium through spin conversion. Spin conversion alters the channel which dictates the quantum electrodynamics selection rule for the positron-electron annihilation into gamma quanta. Photomagnetic positronium spin-conversion cross sections are very large,  $\sim 10^4 \pi a_0^2$ . They correspond to interaction ranges

of  $\sim 30 \text{ \AA}$  and are symptomatic of the wavemechanical behavior of positronium in matter. Analysis suggests that the photomagnetic effect proceeds by a process labeled spinflip in which ortho- and parapositronium interconvert under the simultaneous quenching of the excited triplet state to the singlet molecular ground state.

Physical Review B (in publication)

### Effective Charge Theory and the Electronic Stopping-Power of Solids

Werner Brandt, B. S. Yarlagadda, and J. E. Robinson

Electronic stopping powers,  $S$ , of solids for penetrating ions are analyzed on the basis of effective charge theory, and comprehensive comparisons are made to available data for random stopping. The effective projectile-ion charges,  $Z_1^*e$ , extracted from the data agree to within experimental uncertainties with those calculated in a statistical model, for projectile atomic numbers ranging from  $Z_1 = 1$  to  $Z_1 = 92$  and for projectile velocities  $v_1 \gtrsim v_0 \equiv (e^2/\hbar)$ . The rise of  $Z_1^*$  with  $v_1$  fully accounts for an often quoted apparent deviation of heavy-ion stopping power from the behavior expected in the limit  $v_1 \rightarrow 0$ . The Bloch and the  $Z_1^3$  corrections to the usual formula for  $S$  are calculated and found to make no appreciable contribution to presently available data, save possibly to one bromine datum. When  $v_0 \lesssim v_1 \lesssim 3 v_0$  the analysis requires, and provides, an empirical velocity-dependent proton effective



charge  $Z_p^* e$ . A theoretical account of  $Z_p^*$  is given in terms of velocity and energy criteria for electron stripping. Thomas-Fermi densities for heavy ions are used to calculate  $Z_1^*$ . Our results lead to an interpolation linear in  $v_1$  for the range  $0 \leq v_1 \lesssim$  which gives satisfactory values for  $S$  in this low-velocity regime.

Physical Review A (to be published)

Universal Cross Sections for K-Shell Ionization by Heavy Charged Particles. II. Intermediate Particle Velocities  
George Basbas, Werner Brandt, and Roman Laubert

Experimental K-shell ionization cross sections of  $^{13}\text{Al}$  and  $^{28}\text{Ni}$  are reported for ions of  $^1_1\text{H}$ ,  $^2_1\text{H}$ ,  $^4_2\text{He}$ ,  $^6_3\text{Li}$ , and  $^7_3\text{Li}$  with kinetic energies in the range from 2 to 36 MeV, and of  $^{28}\text{Ni}$  for ions of  $^{12}_6\text{C}$ ,  $^{16}_8\text{O}$ , and  $^{19}_9\text{F}$  in the range from 4 to 90 MeV. The theory of direct Coulomb K-shell ionization, as developed in an earlier paper labeled KI [Phys. Rev. A 7, 983 (1973)] for projectiles of atomic number,  $Z_1$ , small compared to the target atomic number,  $Z_2$ , and of velocities,  $v_1$ , small compared to the target K-shell electron velocity,  $v_{2K}$ , i.e.,  $v_1 \ll v_{2K}$ , is extended to intermediate velocities  $v_1 \sim v_{2K}$ . New effects appear. They add to the  $Z_1^2$ -proportional cross sections one derives from linear-response theories for direct ionizations. They are attributed to the polarization of the target K-shell in the field of the projectile, and to electron capture by the projectile. Guided by the perturbed

stationary-state theory of atomic collisions, the polarization effects are incorporated so that the theory retains the universal form of the cross sections derived in the plane-wave Born approximation, but where the variables now contain the non-linear effects as scaling factors. Electron-capture cross sections are added. When  $v_1 \gg v_{2K}$ , such contributions subside, and one retrieves the cross sections of the linear-response approximation. In this form, the theory predicts K-shell ionization cross sections for projectiles with  $Z_1/Z_2 < 0.5$  at all velocities in a comprehensive manner. It agrees with experimental data covering six orders of magnitude for collision partners with  $Z_1/Z_2$  ranging from 0.03 to 0.3 and  $v_1/v_{2K}$  from 0.07 to 2.

Physical Review A 16, 1312 (1977)

Screening Effect in Coulomb Excitation of Hydrogenic Atoms by Heavy Projectiles

William Losonsky

The K-shell excitation of a hydrogenic atom by atomic projectiles is treated in the first plane-wave Born approximation including the screening effect of projectile electrons. Screening causes a large decrease in cross sections, in accordance with recently reported data of Hopkins et al.

Physical Review Letters 40, 174 (1978)

Experimental Method for Testing the Potential of Moving Ions  
in Solids

Roman Laubert and Felix K. Chen

Molecular ions, which define the initial separation between nuclei, are used as a probe of the potential established by swift ions in solids. Employing 75-300 keV  $H_2^+$  and  $HeH^+$  ions one observes that a large fraction of clusters do not explode in solid targets whose thickness is much greater than the mean electron-loss distance. The results are consistent with the view that protons moving in solids carry bound electrons.

Z. Physik A 283, 329-335 (1977)

Studies of Neon L-Shell Excitation by Impact of Highly  
Ionized Heavy Ions

Roman Laubert and Felix Chen

Passage of foil-excited 1.4 MeV/A S and 1.1 MeV/A Cl ions of neon charge state  $\sim 12^+$  through neon gas targets at pressure  $\sim 100$  mTorr has been found to be accompanied by copious production of Ne II-VIII excited states. Comparable excitation cross-sections  $\sim 10^{-18}$  cm<sup>2</sup> are found for a large number of levels belonging to all of these charge states and corresponding to principal quantum numbers  $n = 2, 3, 4$ . Vacancy distributions very similar to those found in beam-foil excitation of  $\sim 1$  MeV

neon beams are found. Because the Ne recoil velocities are small compared to the fast beam velocities characteristic of the beam-foil source, it is possible to reduce both Doppler shifts and spreads by 3-4 order of magnitude for equivalent collimation. It has also been found that there is an excitation cross-section change of a factor  $\sim 5$  for a corresponding projectile charge state change from  $6^+$  to  $12^+$ , that efforts to classify K x-ray satellite spectra by L shell vacancy labels ( $KL^0, KL^1, \dots$ ) are probably inaccurate due to extensive population of  $n \geq 3$  spectator levels, that both the recoil ion and beam-foil spectra exhibit few lines with  $n \geq 4$ , and that for the allowed transitions studied here, collisional excited states quenching effects due to the  $\sim 100$  mTorr target gas pressures used are negligible.

Physical Review A 16, 1375 (1977)

Projectile Charge-State Dependence of K-Shell Ionization by Silicon Ions: A Comparison of Coulomb Ionization Theories for Direct Ionization and Electron Capture with X-Ray Production Data

Grzegorz Lapicki et al.

X-ray production cross sections measured in K-shell ionization of  ${}_{21}\text{Sc}$ ,  ${}_{22}\text{Ti}$ ,  ${}_{29}\text{Cu}$ , and  ${}_{32}\text{Ge}$  by 52-MeV  ${}_{14}^{28}\text{Si}^{+q}$  projectiles with  $q = 7$  to 14 are reported, which demonstrate, through their charge-state dependence, the validity of a recently developed electron-capture theory with a reduced

binding effect. Furthermore, the data provide evidence for the applicability of the perturbed stationary-state of direct ionization for values of  $0.44 \leq Z_1/Z_2 \leq 0.67$ .

## VI. Oral Presentation

In the past year 10 papers were presented at the American Physical Society and at international meetings. Of this number 7 were concerned with heavy ion physics while 3 talks dealt with positron physics.

# ENERGY CONVERSION PROCESSES IN ORGANIC CRYSTALS

## SUMMARY OF PAST WORK

### TABLE OF CONTENTS

	Page
INTRODUCTION.....	1
A. SUMMARY OF PAST WORK.....	6
I. EXCITON, PHOTOPHYSICS	
(a). Triplet Exciton Diffusion in Tetracene.....	6
(b). Percolation at Room Temperature.....	7
(c). Exciton Dynamics in Model and Biological Systems.....	11
II. ENVIRONMENTAL	
(a). Ultra-Accurate Measurements of Mass and Charge State of Aerosols.....	18
(b). Heterogeneous Oxidation of SO <sub>2</sub> in the Presence of Light.....	21
(c). Single Particle Photoemission Experiments.....	24
(d). Reactivities of Polycyclic Aromatic Hydrocarbons (PAH).....	27
III. RADIATION	
(a). $\alpha$ -Particle Induced Radical Production in Anthracene Beyond the Bragg Peak.....	32
B. REFERENCES.....	38
C. PUBLICATIONS.....	40
D. DOCTORAL DISSERTATIONS.....	41
E. ORAL PRESENTATIONS.....	41
F. APPENDIX OF PUBLICATIONS.....	42

## INTRODUCTION

Our work with organic crystals represents a special case of the general study of the interaction of radiation with matter. The energy range involved in our studies extends from about 1 eV to 32 MeV, with particular emphasis in the optical energy range. We have focused on the energetics and dynamics of charge and exciton behavior in solids presently characterized as polycyclic aromatic hydrocarbons (PAH). These include anthracene, tetra-cene, and many of the potent carcinogens, such as benzo(a)pyrene. In recent years, as environmental concerns have heightened, there has been an explosion in interest in these PAH compounds because they are potentially carcinogenic and because they are appearing in ever-increasing concentrations in the environment as a consequence of the combustion of solid and liquid fossil fuels. Furthermore, there is the distinct possibility that with the development of more exotic processes for the extraction of low-grade fossil fuels (such as shale oil), from the earth, the production of PAH compounds will be enhanced, necessitating a careful study of ways of minimizing the impact of these compounds on the environment. It has also been found that traces of organic compounds in the atmosphere act as catalysts in the conversion of sulfur and nitric oxides to the more pernicious corresponding acids and salts.

In our studies of the effect of radiation on organic matter over the past twenty years, our choice of the PAH as model compounds has thus provided us with an extraordinarily sound basis for understanding the different ways that these compounds can participate in creating environmental hazards. With the planned increase in the combustion of coal as petroleum stocks dwindle, there will be an increase in the emission of particulates. These particles consist of inorganic ash containing as many as 40 elements and in addition, are coated to some degree by the PAH compounds that condense upon



them in the cooler regions of the smoke stack. These particles are a source of concern because they appear to act as heterogeneous catalysts in the oxidation of  $\text{SO}_2$  to acid sulfates, and probably in the formation of acid nitrates and chlorides as well. An especially sobering thought must be that the burning of vast quantities of coal will release into the atmosphere enough particulate matter to produce a radionuclide burden that is comparable to that emitted by the operation of nuclear power plants of similar power rating. The maintenance of an interest in radiation studies is thus called for regardless of the type of fuel to be used in the nation.

This report is divided into two sections under separate covers. In the first our past work is summarized, while the second gives a proposed program for future work. The summary contains three sections that represent our main fields of interest. The first of these comprise our fundamental studies in photophysics, the results of which are used to help understand the remaining two sections, which cover our environmental and high energy radiation studies, respectively. To anticipate the discussion of the future program, it may be mentioned that during the next year, we expect to continue our studies of the interaction of high energy radiation with organic matter under the auspices of the U.S. Army Natick Laboratories, Natick, Massachusetts. Our past work dealing with exciton dynamics and radiation damage has come to the attention of the research directors of that laboratory and we were invited to submit a proposal to study the fate of radicals produced during the radiation sterilization of proteins.

In our photophysical studies, we continue our interest in the exploitation of the triplet exciton as a tracer for the presence of chemical and physical description of crystalline order. We thus have accomplished the difficult task of measuring the diffusion coefficient  $D_{ab}$  of the triplet

exciton in the  $ab$  plane of tetracene. We had in the past predicted that  $D_{ab}$  in tetracene should be anomalously high, and this has been borne out. The results are given in Section I.(a).

Another question of interest to us, and to an increasing number of other workers in the field, concerns itself with the role which crystal heterogeneity plays in altering the rate of interreaction of excitons with other species. It is becomingly evident that heterogeneity may be the basis for increased efficiency in transporting energy in biological systems, and in reducing radiation damage. Thus, a small domain makes possible the phenomenon of exciton caging which is a prototype of a healing process, and is discussed in our previous report. A related phenomenon is that of percolation. Percolation concerns itself with the transfer of matter (or energy) through a lattice containing a random mixture of conducting sites and non-conducting sites. It is not necessary for a lattice to be entirely conducting in order to insure the transfer of matter or energy. At certain critical concentrations of conducting sites, there is a dramatic increase in the probability of successful transfer across the lattice. In the absence of percolation, the conductive sites are closed off from each other and caging predominates. Now consider the situation that ensues if a fluorescing acceptor impurity is introduced in low concentration into a caged system consisting of benzocarbazole (BC)-tetracene. In this case, very few cages contain the acceptor, and the host excitation will not have the opportunity to visit other cages; in this event, fluorescence from the acceptor should drop. This occurs, as is discussed in Section I.(b). This work is of importance if attempts are to be made to direct or isolate the movements of excitons. Finally, in Section I.(c), we report on some work with high densities of excitons and show how results of biological significance can be deduced therefrom.

In Section II, we report on our environmental studies. In Section II.(a), we describe a new development in aerosol studies - a device through which precise measurements of aerosol mass and charge mass may be determined easily in the picogram level, to a precision of better than 1%. In addition, the total charge in the aerosol can be determined to within one electronic charge. This technique will greatly enlarge the capability to study the chemical and physical properties of single aerosol particles. In addition, this technique, dubbed the AMCOED (Aerosol Mass and Charge by One Electron Differentials) makes it possible to study photoemission from aerosol particles. We have previously mentioned the possibility that the presence of water around a solid aerosol greatly enhances the possibility of having photoemission of electrons from the aerosol into the aqueous system because of the high polarizability of the water. The emission of electrons into water transforms a pollution problem into one of radiation-induced radical production in water, a much-studied field. In Section II.(b) we report on the beginning phase of these studies.

In Section II.(c) we discuss an aspect of atmospheric oxidation of  $\text{SO}_2$  that we liken to a photoelectrochemical corrosion process. The PAH crystals are known to be photoconductors, and the absorption of light produces positively charge, mobile holes inside the PAH. These holes are strong oxidizing agents and should be able to oxidize  $\text{SO}_2$  to  $\text{HSO}_4^-$ . We are enormously gratified to be able to report a preliminary result that the discharge of holes in a PAH crystal by an aqueous solution containing  $\text{HSO}_3^-$  ions has resulted in the production of  $\text{HSO}_4^-$  ions with 10% quantum efficiency, and at a rate proportional to the number of positive holes discharged at the surface. This is the first and successful step in showing that holes in a PAH

crystal can catalyze the oxidation of  $\text{SO}_2$  to  $\text{HSO}_4^-$ . Section II.(d) closes with a discussion of the reactivity of PAH in biological macromolecules. This work is part of an attempt to understand why the PAH compounds are destructive inside the human cell.

Finally in Section III, we describe the successful resolution of the mystery of the origin of the deeply penetrating regions of  $\alpha$ -particle radiation induced defects. These regions extend in some cases to depths six times the nominal range of the  $\alpha$ -particles. This deep penetration has been shown to be due to proton-recoils. This information is important to those interested in using heavy particles as therapeutic agents in the treatment of disease.

All references in the summaries of work done are collected in Section B, and publications are listed in Section C. Some of this work has been supported in part by other agencies, such as the National Science Foundation and the National Institute of Health. Where papers have been published, credit has been assigned to these papers to the agencies involved. All papers have received Department of Energy support in some part.

## A. SUMMARY OF PAST WORK

I.(a). Triplet Exciton Diffusion in Tetracene

Measurement of the diffusion coefficient of triplet excitons in tetracene is important in understanding such varied phenomena as dimensionality and heterogeneity effects, photostimulation of electrical currents, scintillation under heavy ion bombardment, and radiation induced heterogeneous oxidation. Until the present work, the only information concerning this diffusion coefficient had been arrived at from the measurement of rate constants that were assumed to be diffusion limited. Picosecond measurements on exciton fission by Alfano et al<sup>1</sup> gave values for the in-plane diffusion coefficient  $D_{ab}$  of  $\geq 10^{-2} \text{ cm}^2\text{-s}^{-1}$ . Other values arrived at from the bimolecular annihilation rate of triplets are scattered with the most recent value being  $\sim 2 \times 10^{-4} \text{ cm}^2\text{-s}^{-1}$ .

In order to resolve this discrepancy, direct triplet exciton diffusion measurements were undertaken. This was accomplished by measuring the decay of the delayed fluorescence in the presence of spatially inhomogeneous excitation. By irradiating the crystal with a pulsed laser through a Ronchi ruling, a series of parallel sharply delineated regions of high triplet density is set up in the crystal, each pair of such regions being separated by an unexcited region. Upon turning off the excitation, the excitons diffuse into the unexcited regions, and the exciton density  $n$  obeys a one-dimensional diffusion equation

$$\frac{\partial n}{\partial t} = -\beta n + D \frac{\partial^2 n}{\partial x^2} \quad (1)$$

where  $\beta$  is the decay rate for excitons under homogeneous illumination and  $x$  is the distance measured in the direction perpendicular to the ruled lines.

The apparent decay of the triplet exciton density will be increased as triplets diffuse into the unexcited regions behind the opaque sections of the ruling. The change in the apparent triplet decay rate is detected from the change in the decay rate of the delayed light at different ruling densities. The results which are given in Appendix A show that the diffusion constant along the b direction in tetracene is  $(4 \pm 1) \times 10^{-3} \text{ cm}^2\text{-sec}^{-1}$ . This value gives tetracene the highest triplet diffusion rate of any linear polyacene looked at thus far. There is no way at present to rationalize the difference between our diffusion measurements and the values arrived at by Arden et al.<sup>2</sup> A theoretical estimate of the triplet exciton diffusion coefficient based on the evaluation of electronic overlap integrals would be somewhat lower than was actually measured;<sup>3</sup> there is thus good reason for additional theoretical study of this interesting material.

#### A.I.(b). Percolation at Room Temperature

In our continuing work on the photophysics of excitons we have considered the importance of moving from the study of neat molecular crystals to the study of molecular crystal alloys, in which the ratio of the mol fractions of the components can vary from 0 to 1. Aside from our basic interest in this area, a mixed crystal system has many similarities to systems encountered in nature. It is known, for example, that propagation of energy by excitons is the precursor to the chemical activity in the photosynthetic system.<sup>7</sup> It is not known with certainty what role is played by system heterogeneity (e.g., mixtures of chlorophyll-a and chlorophyll-b in the chloroplasts) in increasing the efficiency of the exciton transport process. However, heterogeneity certainly modifies the character of energy transport. For example, the energy levels in chlorophyll-b lie above those of chlorophyll-a, so the excitation must travel along the chlorophyll-a molecules when possible.

The chlorophyll-a molecules would therefore act as barriers to exciton migration, much as if they formed a picket fence.

Aside from the value of more complete knowledge of migration in biological systems, the study of mixed crystals has relevance to another important area. Thus, organic molecular crystals have been utilized in the past as scintillators for radiation detection. The luminescence in the scintillation is sometimes quenched by collisions between excitons. This effect is one consequence of exciton motion in a condensed phase. By introducing impurities which can isolate the mobile excitons, quenching should be reduced and the efficiency of the scintillator should increase.

The simplest way to produce a mixed crystal in which the components have differing energy levels is to use isotopic substitution for one of the elements in the compound under study. Thus, the use of deuterated naphthalene in normal naphthalene makes available a system in which a complete range of compositions is possible consistent with the production of a single crystal. In addition, the energy levels of the deuterated naphthalene lie above those of normal naphthalene, so these molecules would act as barriers to the migration of the triplet exciton for example, if the temperature is low enough to make the small energy level differences significant. The naphthalene d-naphthalene system has been used<sup>5</sup> to study the phenomenon of percolation. When the concentration of d-naphthalene is low, the triplet exciton would be essentially trapped because the normal naphthalene molecules would block the movement of this exciton from the d-naphthalene site to another. As the concentration of d-naphthalene increases, a point will be reached where a continuous path of d-naphthalene molecules from one surface of the

crystal to the opposite surface of the crystal becomes probable. At this concentration, triplet exciton migration is greatly enhanced, and the crystal lattice is said to percolate, even though it is the exciton that moves and not the lattice.

In the case of isotopic substitution, the energy barrier to diffusion is on the order of  $100 \text{ cm}^{-1}$ , so a room temperature study of percolation in isotopic systems is not practical. Even at  $2^\circ\text{K}$ , it is possible for tunneling to take place across barrier molecules.<sup>5</sup> Recently we have designed a mixed system with host and guest bands separated by  $\sim 1 \text{ eV}$ . This system should demonstrate isolation (i.e., non-percolation) at room temperature. In addition, since triplet transport is not well understood in the mixed systems due to the need to include tunneling, this large band separation should provide theorist with a more ideal system for applying percolation theory.

Coincident with the process of percolation is the phenomenon of caging. In the concentration range where percolation is not possible, there exist conducting regions of the crystal that are isolated from similar conducting regions. An exciton inside one of these conducting regions behaves as if it were inside a physical cage since the surrounding molecules do not permit energy transfer. We have been successful in growing tetracene crystals,  $\phi_{11}$ , with large concentrations of 2,3 benzocarbazole (BC).<sup>6</sup> The energy levels for the molecular excited states are shown in Fig. 1. As one

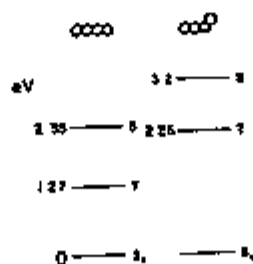


Figure 1.



can see, neither the singlet nor triplet excited states of tetracene can transfer their energy to BC. This property allows the  $\phi_4$ -BC system to demonstrate the exciton caging process. Exciton caging is particularly well demonstrated by measuring the efficiency of geminate recombination of triplet exciton pairs produced by singlet exciton fission. In our present work we are interested in observing the effects of BC on the long range transport of  $\phi_4$  excitation. To do this we have introduced a dilute (molar concentration  $\sim 1$  part in  $10^3$ ) quantity of pentacene,  $\phi_5$ , into the  $\phi_4$ -BC lattice. Pentacene acts as a trap for excitation energy because its energy levels lie below that of tetracene. In addition, pentacene fluoresces in a different wavelength region from tetracene, so the intensity of pentacene fluorescence is a measure of the local exciton concentration. With no percolation the number of new sites available to an exciton is confined to a small region of the crystal. This restricts the number of new sites that can be visited by the exciton and therefore diminishes the yield from the excited trap. In short, the cross-section of capture of excitons by the trap increases as the ability of the exciton to diffuse increases.

An example of tetracene with 1:500 impurity of pentacene is shown in Fig. 2. As one can see this dilute impurity captures most of the tetracene excitation and the spectra are easily isolated one from another at room temperature. This figure also shows a preliminary result at a mole fraction of .38 for BC.

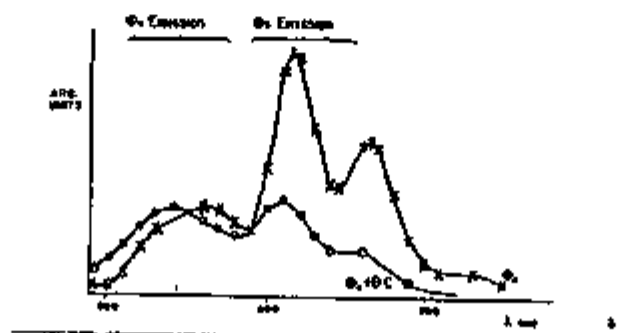


Figure 2.

The relative decrease in  $\phi_5$  fluorescence in Fig. 2 is encouraging; however, although the same concentration of  $\phi_5$  is used in the growth material, we do not have an independent measure of its concentration. The decrease in the relative yield of  $\phi_5$  should therefore be viewed cautiously. Future work (Section B) will discuss methods for the independent measurement of the pentacene concentration as well as laser induced many-body quenching processes in the BC- $\phi_4$  system.

#### A.I.(c). Exciton Dynamics in Model and Biological Systems

In this part of our overall research program we are engaged in fundamental studies of the photophysical and dynamical properties of the excited states of polycyclic aromatic compounds. These include the polycyclic aromatic hydrocarbons such as anthracene, tetracene, benz(a)anthracene, polycyclic dye molecules and chlorophyll. We are studying interactions between the excited states of polycyclic molecules under conditions of high intensity of irradiation using different modes of laser excitation.

##### 1. Model Systems

Many non-linear processes can occur when high intensity laser illumination is absorbed in a solution of polycyclic molecules. These include

- (1) Bimolecular interaction between excited states
- (2) Depletion of ground state molecules (bleaching)
- (3) Two-photon absorption
- (4) Absorption of photon by singlet or triplet excited states
- (5) Stimulated emission.

Our major interest lies in (1) above; the reactions currently under study include the bimolecular interactions between singlet-singlet, singlet-triplet and triplet-triplet excitons. Over the past two years we have investigated these bimolecular interactions in confined domains, mostly highly doped organic crystals, e.g. carbazole in anthracene. The carbazole concentration can be as high as  $\sim 50\%$  in these "exciton caging" systems. The carbazole molecules act as obstacles to the diffusion of excitons in the anthracene or tetracene domains and thus the probability of exciton-exciton interaction changes. These organic crystal systems are somewhat analogous to photosynthetic systems in which the composition of antenna pigments is highly heterogeneous; the excitons of chlorophyll-a diffuse in a matrix of higher energy level molecules such as chlorophyll-b and carotenoids.<sup>7</sup> We have thus investigated exciton annihilation processes both in these organic crystals and in Photosynthetic membranes.

Experimentally, exciton-exciton annihilation processes manifest themselves by a quenching of one of the potentially fluorescence-emitting excitons. Thus, as the intensity of the excitation and the density of excitons increases, there is a decrease in the quantum yield of fluorescence.

We have sought systems in which the size of the domains and the effect of such limited domains on exciton-exciton interactions could be demonstrated. For this purpose we have worked, within the past year, with micellar solutions of polycyclic aromatic molecules and with suspensions of membrane-like liposomes containing aromatic solute molecules of varying concentrations and of liposomes of varying sizes. The utility of the micelles is limited since only 5-10 aromatic molecules can be incorporated per particle. In the case of liposomes, we have incorporated up to 700 pyrene molecules per particle.

The expected effect of domain size is illustrated in the following schematic diagram of the fluorescence quantum yield  $\phi$  as a function of light intensity  $I$  (photon absorbed/molecule).

Physically, quenching due to bimolecular exciton annihilation phenomena is expected to set in at lower values of photons absorbed/molecule for large domains since excitons diffuse and can encounter one another even if there are only two photons absorbed per domain. For large domains, Swenberg, et al<sup>4</sup> have shown that the quantum yield  $\phi$  follows the relation

$$\phi(I) = \phi_0 \frac{1}{(\gamma/2k)I} \log \left\{ 1 + I \left( \frac{\gamma}{2k} \right) \right\} \quad (2)$$

Where  $\phi_0$  is the quantum yield as  $I \rightarrow 0$ ,  $\gamma$  is the bimolecular exciton annihilation constant and  $k$  is the unimolecular exciton decay rate.

The form of this equation is depicted in Fig. 3 (large domains). We have indeed observed experimentally that this type of curve is obtained for organic crystals, liposomes, pyrene dissolved in solution, and in photosynthetic units (see Appendices B and C for example).

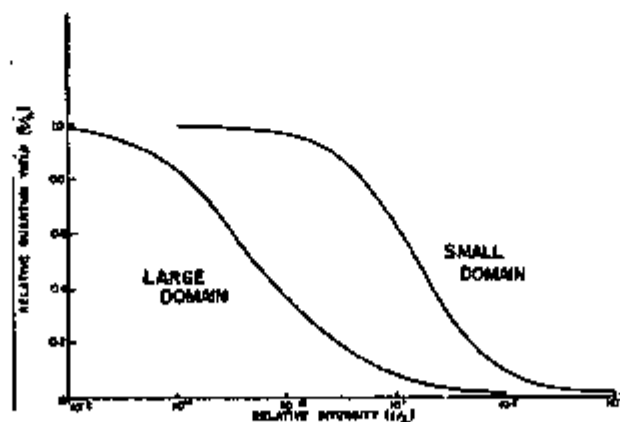


Figure 3.

If the domains are small, i.e. if there are few polycyclic molecules such as pyrene or anthracene per domain (e.g. micelles), the steep curve shown in Fig. 3 should be obtained. It is evident that quenching sets in at a much higher value of  $I$  than in the large domain case. Theoretically, such a quenching curve is represented by the Poisson photon hit distribution curve given by

$$\phi_p(x) \approx \sum_{n=1}^{\infty} \frac{\phi_o}{n} \frac{P_n}{1 - P_o(x)} \quad (3)$$

where

$$P_n(x) = \frac{(x)^n e^{-x}}{n!} \quad (4)$$

where  $x$  is the average number of photon hits per domain, and  $P_n$  is the probability that a given domain has received  $n$  hits.

We have attempted to study these small domain effects using micelles containing not more than 10 pyrene or anthracene molecules per micelle. It is evident immediately that bleaching must be taken into account in the oversimplified theory [e.g., equation (3)]. Furthermore, the concentration dependence of  $\gamma$  is an important, but unknown parameter. We have therefore decided to re-examine from a fundamental point of view all of the factors involved in these experiments, to derive theoretical equations such as equations (3)-(4) in which effects such as bleaching, two-photon excitation, stimulated emission and annihilation are included, and to test these theoretical equations experimentally.

## 2. Exciton Dynamics in PAH-DNA Complexes

The above experiments have a direct application to an understanding of the nature of the binding of polycyclic aromatic molecules to nucleic acids. One of the questions which arises is the following: when PAH

molecules bind to DNA either covalently or physically, are the PAH molecules clustered in relatively small domains, or are they distributed statistically over the entire chain length? While this question is probably not significant biologically (because of the extremely low concentration of PAH molecules in vivo), such effects might be significant in our model studies in which complexes of PAH-DNA molecules are produced in vitro (such complexes were synthesized by us to study the nature of the BP (benzo(a)pyrene) metabolite-DNA complex see below).

In these model studies we have investigated intercalation-type complexes of acridine orange (AO) physically complexed to DNA in aqueous solution. The ratio of nucleotide/dye (designated by the ratio P/D, where P stands for phosphate residue) was in the range of 10-100. If the distribution is totally random, then for  $P/D = 100$  the average distance between AO molecules is  $\sim 170\text{\AA}$ . Since typical electronic energy transfer ranges (via the Forster mechanism) are less than  $100\text{\AA}$ , little energy transfer from molecule to molecule is expected in such cases, unless there is a clustering of dye molecules in certain regions of the DNA. In the latter case, significant energy transfer is expected and subsequently there is a strong probability that fluorescence quenching at high laser excitation intensities will occur.

In addition, these polycyclic aromatic dye-DNA complexes represent limited size domains, since the chain length of the DNA molecules can be decreased at will thus confining the dye-dye energy transfer processes to essentially one-dimensional chains, neglecting, to a first approximation, the effects of coiling of the DNA in solution.

The dye-dye transfer on DNA chains has been investigated in two different time domains: (1) nanoseconds, by exciting the AO molecules with a 337 nm, 7 ns FWHM nitrogen laser pulse, and (2) by exciting with a CW

argon ion laser within the main absorption band of AO in the blue region of the spectrum.

In case (1) the fluorescence yield was measured as a function of the pulse intensity. In one experiment the effective AO molecule concentration in the DNA solution was  $10^{-5}M$ ; however, since the dye binds stoichiometrically to DNA ( $10^{-3}M$  in P residues), the real concentration within the volume occupied by the DNA molecules is much higher ( $P/D = 100$ ). In another experiment, the dye was present at the same effective concentration of  $10^{-5}M$ , but no DNA was present; the purpose of this experiment was to verify the laser pulse intensity at which the fluorescence quantum yield of AO in free solution declines due to bleaching, two-photon, excited state-absorption or stimulated emission effects. The results for the free AO and the DNA-bound AO are shown in Fig. 4. It is evident that in the AO-DNA case, quenching of the fluorescence sets in at a lower intensity than the photon flux value at which bleaching effects become noticeable in the free AO solution.

The results are presently being analyzed to see if a random (Poisson-like) distribution of AO molecules can explain these results.

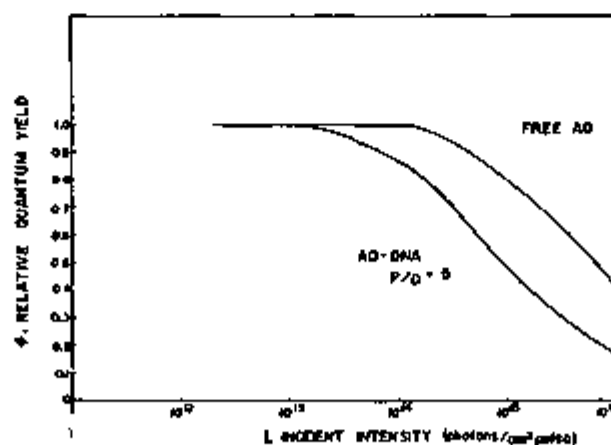


Figure 4.

In order to investigate these clustering effects further, we have investigated the variation of the delayed fluorescence intensity (DF) as a function of excitation intensity using the argon-ion laser. The DF is a function of the concentration of AO molecules in the triplet state. At high excitation intensities the triplet density becomes sufficiently high so that triplet-triplet annihilation takes place, also by a Förster mechanism. While this is a forbidden mechanism, the triplet lifetimes are  $\sim 10^6$  times longer than singlet lifetimes. Thus, such long range triplet-triplet annihilation processes are observable and manifest themselves by a decrease in the DF at high excitation intensities. Experiments of this type are shown in Fig. 5.

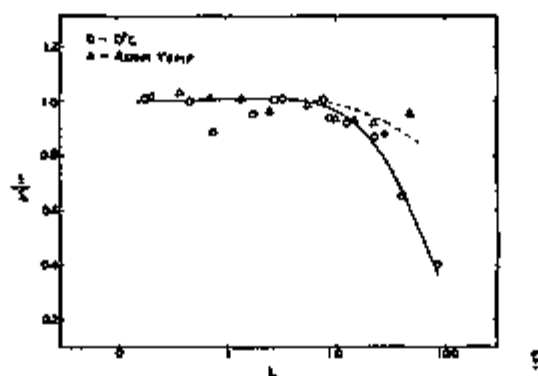


Figure 5.

These results show that significant quenching of the triplets (DF decreases) takes place at high laser intensities, while the small decline of the prompt fluorescence of AO under these same conditions indicates that bleaching and other artifacts are less important. At first it was believed that the effect on the DF was due to a physical migration of AO molecules from site-to-site on the DNA molecule, thus making it possible for even two distant triplet excited molecules to encounter one another. This mechanism is feasible since the triplet lifetime of AO bound to DNA is  $\sim 15$ -30 ms,



while it is known that dye molecule bound to DNA are desorbed and reabsorbed on time scales of about once every millisecond at room temperature. However, this molecular migration mechanism does not seem to be important in explaining these effects, because lowering the temperature to 0°C did not eliminate the quenching effect shown in Fig. 5, but enhanced it (the quenching threshold sets in at lower intensities).

These effects are presently under detailed investigation, both theoretically and experimentally. It is hoped that such experiments, using bound PAH carcinogens as triplet and singlet energy traps for the excitation energy of dye molecules bound simultaneously to the same DNA, will prove to be an additional useful tool for studying the physico-chemical properties of these complexes.

### 3. Exciton Dynamics in Photosynthetic Membranes

Using the approaches outlined in the previous sections, namely by studying the fluorescence of chloroplasts irradiated by intense laser light pulses, we have studied the dynamics of singlet and triplet excitons in the photosynthetic unit. We have been able to derive information about the modes of energy transfer from the light harvesting pigments to photosystem I and to obtain information about the dynamic properties of singlet and triplet excitons. These results are described in greater detail in some of the accompany papers.

#### A.II.(a). Ultra-Accurate Measurements of Mass and Charge State of Aerosols

Recently an instrument was designed in our laboratory for measuring photoemission rates from small particles in a Millikan Chamber [see Section II.(b)]. One of the major problems encountered in using this potentially valuable instrument is the tendency of the particle to drift

out of the field of view. The new instrument uses an electro-optic feedback system to keep a particle within the field of view of the observer over an indefinite period (i.e., weeks if necessary). Thus if an electron is removed from the particle producing an electrical imbalance, the field of the chamber is automatically adjusted to restore the balance and to keep the particle in the field of view.

Earnshaw's theorem<sup>8</sup> rules out the possibility of achieving particle stability in a purely electrostatic force field. The instrument uses periodically fluctuating fields to provide dynamic stability. The unique aspect of the apparatus is that in one of the two electric field configurations used, the field is uniform, and therefore easily described. Assuming that one can see a one-electron imbalance, aerosol mass and charge state are easily determined. The basic principle of this new method will now be described and the details of the method for determining Aerosol Mass and Charge by One Electron Differentials (AMCOED) are presented in Appendix D.

The method requires the measurement of the balance voltage on a charged aerosol particles before and after an electron is emitted from the aerosol. At balance the charge,  $q_i$  before electron emission is given by

$$q_i = \frac{Wd}{V_i} \quad (5)$$

where  $W$  is the weight of the aerosol,  $d$  is the plate separation and  $V_i$  is the potential between the plates. After emission the charge  $q_{i+1}$  is

$$q_{i+1} = q_i - e = \frac{Wd}{V_{i+1}} \quad (6)$$

where  $e$  is the electronic charge. Combining equations (5) and (6) the weight  $W$  and the charge state  $Z_i (q/e)$  are found to be

$$W = \frac{e}{d \left| \left( \frac{1}{V_{i+1}} - \frac{1}{V_i} \right) \right|} \quad (7)$$

and

$$Z_i = \frac{q}{e} = \frac{\frac{1}{V_i}}{\frac{1}{V_{i+1}} - \frac{1}{V_i}} \quad (8)$$

So one merely has to determine the voltage before and after emission of an electron in order to arrive at the particle mass and charge state.

Electrons may be emitted one at a time by using UV light of an energy that is at the threshold of ionization. Figure 6 shows the result of applying the AMCOED apparatus to mass and charge measurements. From equations (7) and (8) the mass and charge state (i.e. before the UV was turned on) of the particle in Fig. 6 are  $316.1 \pm 1.8$   $\mu\text{gm}$  and  $147.1 \pm 0.8$ , respectively.

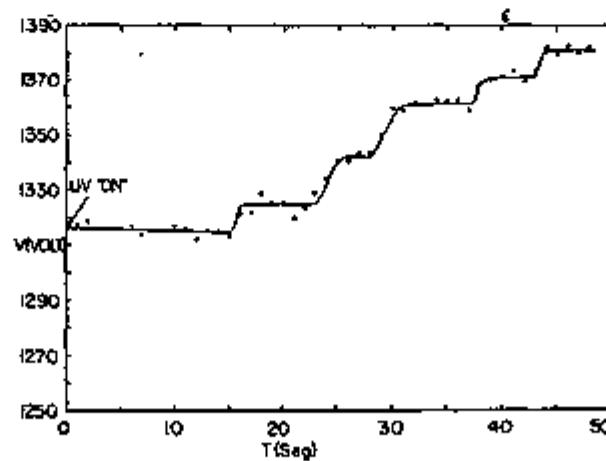


Figure 6.

Compared with sedimentation and light scattering determinations of particle mass, each of which requires a number of inputs (e.g., particle shape, viscosity and particle density) in addition to the measured quantities, the one electron differential method (AMCOED) is simple.

#### A.II.(b). Heterogeneous Oxidation of SO<sub>2</sub> in the Presence of Light

The oxidation of SO<sub>2</sub> to acid sulfates in the atmosphere is a subject of current interest.<sup>9,10,11</sup> Such occurrences as the acid rains (where the pH can drop to 2.1) in the Northeastern United States are a testament to the importance of this problem. Not only does marine life suffer from this phenomenon but sulfates almost certainly cause irritation to the respiratory system. The mode of oxidation of SO<sub>2</sub> in the atmosphere probably varies in accordance with the presence of or absence of catalytic agents however, recent studies have shown that the oxidation processes in the area of flue stacks are associated with particles leaving the stacks.<sup>13</sup> More recently airborne studies have shown that the reaction rate of this apparently heterogeneous process increases in the presence of ambient light.<sup>14</sup> The problem of heterogeneous oxidation in the presence of light is therefore of great interest. Presently we are interested in the role of photoelectrochemical "corrosion" processes on the production of sulfates in the atmosphere; in particular, we intend to study the role of photoinduced charge carriers on the oxidation processes. The absorption of light by a PAH moiety on a particle can lead to chargeseparation, the positive charge, or hole, is a powerful oxidizing agent that under the proper circumstances should be able to oxidize HSO<sub>3</sub><sup>-</sup> to HSO<sub>4</sub><sup>-</sup>. It should be understood that under present conditions of energy production the concentration of PAH on a particle is very low. It is important however to determine the conditions under which a PAH presence can enhance the pollution process.

What we propose is that solvated electrons and residual holes can become important precursors to the oxidation process. Some years ago in our laboratory we detected a near-UV induced photocurrent in an unbiased anthracene crystal which was in contact with aqueous electrodes.<sup>15,16</sup> This photocurrent was found to be due to charge carriers created by the dissociation of a singlet exciton produced by the light. This process produced a solvated electron and a residual hole. Later Jarnagin, *et al*<sup>17</sup> showed that the process involved the uptake of oxygen by the crystal and oxidation of the crystal surface. The mechanism of this oxidation has been well documented.<sup>17</sup> Basically the oxidation process proceeds by hydroxyl radicals which are created by the discharge of the  $\text{OH}^-$  ions at the crystal surface. These OH radicals oxidize the anthracene crystal preferentially. However, there is evidence that adsorbed impurities can be oxidized in lieu of anthracene. Thus Lyons and McGregor (LM)<sup>18</sup> dissolved p-anilinobenzene, sulfonic acid (PABSA) at the cathode of an anthracene crystal whose anode utilized a hole injecting solution. The current generated in the crystal under an applied field was found to oxidize PABSA. Apparently PABSA formed a monolayer on the crystal so that it was oxidized preferentially to anthracene. The efficiency of this process was found to be 100%.

In addition to this high efficiency for oxidation by holes, these carriers can be produced with ambient light in spite of the relatively high ionization energies of the organics. Thus, Kallmann and Pope showed that light of 3.15 eV was sufficient for photogeneration even though the ionization energy of the crystal in a vacuum is 5.7 eV. The lowering in energy is principally due to the solvation energy of the electron. Light of 3.15 eV is easily available in the atmosphere,<sup>9</sup> and considering that anthracene has a relatively high ionization energy compared with other polycyclic

structures including graphite, we expect such a light induced photo-oxidation process to occur in the atmosphere. What is not known is if species such as  $\text{HSO}_3^-$  or  $\text{SO}_3^{=}$  will adsorb on the crystal surface.

Apparently circumstantial evidence does exist for believing that  $\text{HSO}_3^-$  and  $\text{SO}_3^{=}$  will adsorb on anthracene. In particular, the normal UV induced oxidation described by Jarnagin, et al<sup>17</sup> is accompanied by a general degradation and loss of optical clarity of the crystal surface. However, a number of experimenters have reported that this degradation can be eliminated by dissolving sodium sulfite into solution.<sup>19</sup> This evidence seems to point to a process at the anthracene surface in which sulfite or bisulfite is preferentially oxidized as opposed to the anthracene itself. If this process occurs we would like to know the quantum efficiency for the sulfite oxidation process.

A number of methods have been investigated for detecting  $\text{SO}_4^{=}$  including nephelometry of Ba precipitates, laser Raman, Ion Chromatography (IC), ESCA and colorimetry. We have found at present that IC is the most convenient, sensitive and selective technique for our purpose.

Figure 7 shows a diagram of our present apparatus. A hole

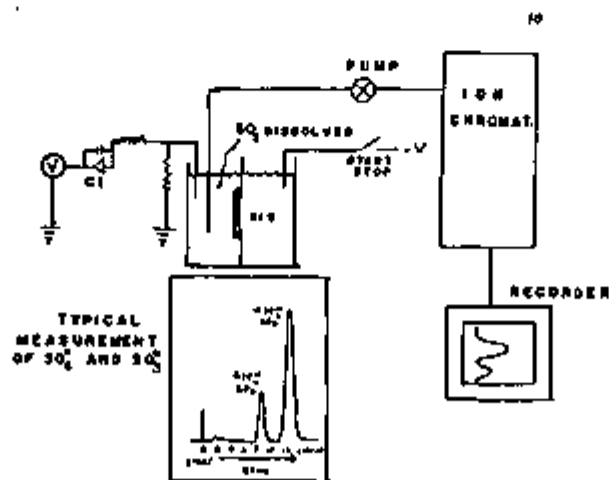


Figure 7.

injecting solution H<sub>2</sub>S is placed at the anode. A Ce(SO<sub>4</sub>)<sub>2</sub> solution is used for this purpose.<sup>20</sup> A number of holes traversing the crystal is measured with a charge integrator. A solution of Na<sub>2</sub>SO<sub>3</sub> ( $\sim 10^{-3}$ M) forms the electrode on the cathode side of the cell. After  $\sim 1000\mu\text{Coul}$  of charge has flowed ( $\sim 12$  minutes) the solution on the cathode side is pumped into an ion chromatograph and analyzed for SO<sub>3</sub><sup>-</sup> and SO<sub>4</sub><sup>=</sup>. A typical analysis run at the Environmental Laboratory at the Department of Energy in New York City is shown in Fig. 7. An Ion Chromatograph is sensitive to as little as 10ngrams SO<sub>4</sub><sup>=</sup>. At 100% efficiency as few as two holes would be required for each oxidation and the minimum charge flow for detection is 3.2 $\mu\text{Coul}$ . With a 1 $\mu\text{Amp}$  current this would take 3.2 sec; therefore IC should be an adequate method for following the oxidation process.

Other alternative methods will be explored as well as IC. These are discussed in Section B.I.(b).

#### A.II.(c). Single Particle Photoemission Experiments

Our interest in the role which light plays in the heterogeneous oxidation of SO<sub>2</sub> [see Section A.II.(b)] in the atmosphere requires information concerning the interaction of light with solid surfaces. In particular the vacuum ionization should be known in order to evaluate the influence of a fluid (e.g., water) for example, on the ionization process. In addition, as we have shown in our laboratory, solvation is not the only method of lowering the ionization thresholds. Double-quantum photoemission (as shown in Fig. 8) also occurs<sup>21,22</sup> at ambient light intensities and this process gives rise to a considerable lowering in the energy needed for ionization. In anthracene, for example, although single quantum photoemission occurs at 4.65 eV, the double quantum process begins at 3.15 eV. Other, non-intrinsic processes, can also affect the threshold for photoemission.

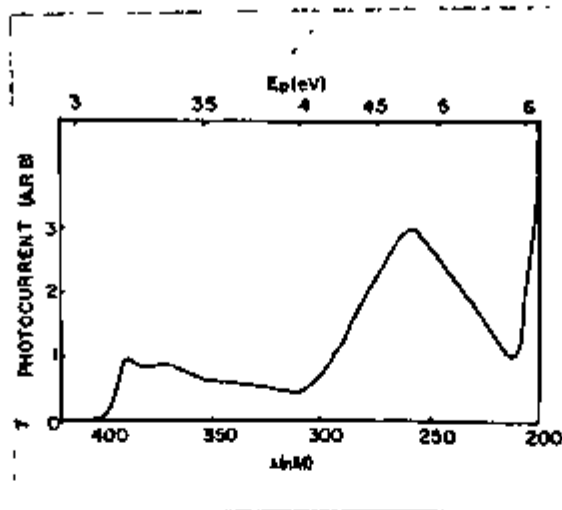


Figure 8.

Impurities which are deposited on surface cause the electron affinity of the surface to vary. Electropositive elements such as Cs have been used to create negative electron affinity photocathodes for sometime; photoemission may be extended into the infrared through this process.<sup>23</sup> The effect of adsorbed PAH on metal oxide surfaces is of interest in the atmospheric environmental area, however, little work has been done on such problems. All three of the above problems, namely:

- A) measurement of vacuum ionization of PAH;
  - B) investigation of double-quantum ionization processes in PAH;
  - C) and, elucidation of the effect of adsorbed PAH on ionization thresholds
- are the chief concern of our work in photoemission.

To date we have constructed a unique method for doing photoemission experiments directly on aerosols. The basic apparatus is almost identical to that used in our AMCOED [Aerosol Mass and Charge by One Electron Differentials, see Section A.II.(a)] technique. In addition to the AMCOED apparatus, various light sources have been added along with an on-line minicomputer. When the excitation light shines on the aerosol, electrons are emitted



and the particle balance is automatically maintained by the AMCOED servomechanism. The voltage across the plates is measured during times when the field in the chamber is uniform, and these readings are stored in the minicomputer. After sufficient charge has been removed the computer calculates the rate of charge loss and its standard deviation.

It is generally agreed for organics that the rate of charge loss  $R$  is related to the ionization energy  $I$  and the excitation energy  $E_p$  by<sup>24</sup>

$$R = A (E_p - I)^3 \quad (9)$$

Figure 9 shows a plot of  $R^{1/3}$  versus  $E_p$  for a negative tetracene microcrystal. As one can see equation (9) is obeyed for tetracene and the ionization

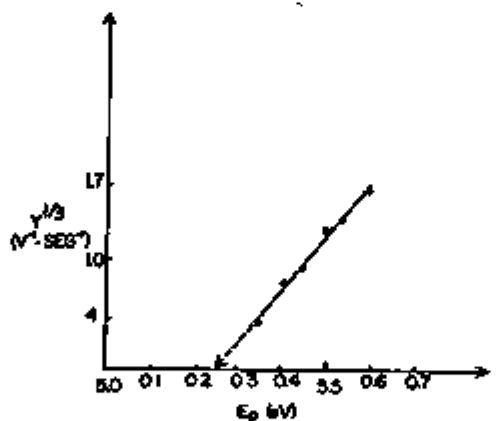


Figure 9.

energy is 5.25 eV. This energy is within 0.05 eV of the accepted value for tetracene. Apparently the  $N_2$  atmosphere in the chamber does not play an important role in the determination of  $I$ . Although single-photon ionization does not extend below 5.25 eV, ionization is found at 4 eV for substantially

higher intensities. Figure 10 shows the intensity dependence of the rate of ionization at 4 eV. As one can see this ionization process goes as the 3/2 power of the light intensity. This super-linear behavior is clearly due to a multi-quanta process. In particular, a good candidate for a one-half power law dependence is the presence of free electrons. At this time we are still in the process of determining the nature of the other quasi-particle involved in this process.

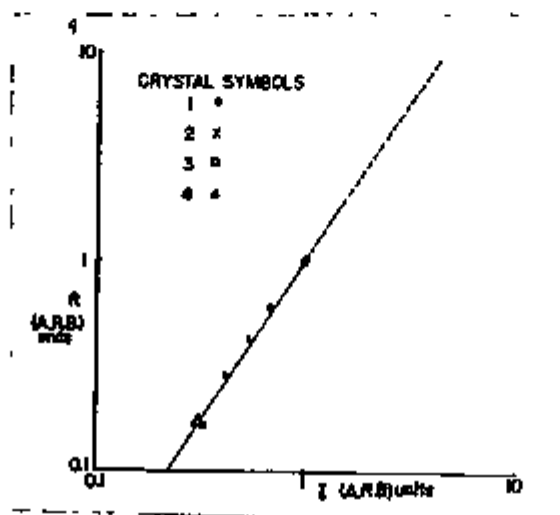


Figure 10.

#### A.II.(d). Reactivities of Polycyclic Aromatic Hydrocarbons (PAH)

Our long range research effort is concerned with an understanding of the reactivities of polycyclic aromatic hydrocarbons (PAH). Our interest is focussed on two major areas:

(1) The reactivity of PAH molecules adsorbed on soot-like particles in the presence of air and the various components of polluted atmospheres. These model studies will eventually provide an understanding of the reactivities and ultimate fate of PAH molecules emitted into the atmosphere from stacks of coal-burning plants.

(2) The reactivity and fate of PAH molecules interacting with biological macromolecules in model systems and in living cells.

Our overall approach to this problem is derived from the long-standing experience in this laboratory involving the study of the excited states of PAH molecules both in crystalline and solution phases. It involves the study of the photophysical processes which takes place when these molecules are photoexcited. Using excited singlet and triplet states of PAH molecules as probes we have developed techniques to study what happens when a PAH molecule interacts with components of the living cell. Within the last year, we have also emphasized the study of model systems, in particular exciton phenomena utilizing high levels of photoexcitation in an attempt to develop useful techniques for the study of PAH molecules complexed with biomacromolecules and with membranes. Furthermore, we have perfected our fluorescence and electric linear dichroism techniques to determine the structure of covalent benzo(a)pyrene-DNA complexes which are formed when benzo(a)pyrene (BP) is fed to and is metabolized by living cells. We have in addition developed an ultrasensitive fluorescence technique to determine the nature of the BP metabolite which binds to nucleic acids (see 1976 annual report); within the past year we have also applied this methods to a study of the metabolites of the potent carcinogen 7,12-dimethyl benz(a)anthracene (DMBA) interacting with the nucleic acids of the living cells.

Within the past year therefore, our work has emphasized the topics under (2) above, rather than those specified under (1).

The highlights of this work are summarized below, while further details may be found in the papers in the Appendix.

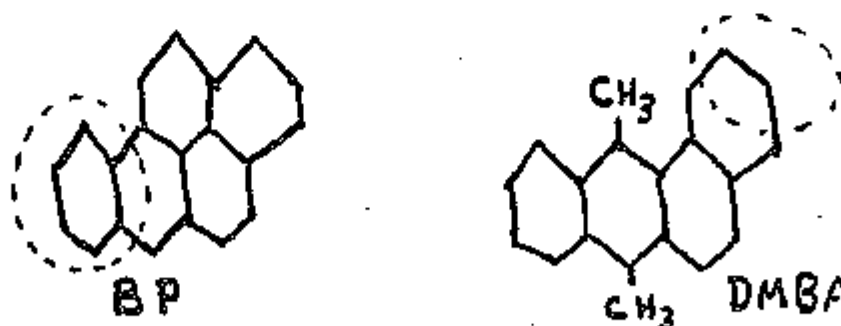
- (i) The binding of 7,12-dimethyl benz(a)anthracene to DNA in vivo studied by a fluorescence technique.

We have previously established a low-temperature fluorescence technique<sup>25</sup> to determine the site of metabolism on polycyclic aromatic

molecules. Using this technique we have established that when BP reacts with nucleic acids in vivo, metabolism takes place at the 7,8,9,10 aromatic ring of BP which is followed by a covalent attachment of the BP molecule at the 10 position to the two amino group of guanosine in DNA.<sup>26</sup> A similar approach was utilized to study the nature of the covalent binding of DMBA to nucleic acids.

DMBA was fed to hamster embryo cells in tissue culture, or a system containing DNA, and the DMBA-modified DNA was extracted by standard techniques. These DMBA-DNA adducts were analyzed by fluorescence and the results indicate that the DMBA bound to nucleic acids exhibit a 9,10-dimethyl anthracene-type fluorescence. This result is consistent with a metabolic activation of DMBA at the 1,2,3,4 ring positions of DMBA. This result, as well as the one obtained with BP, is consistent with the "bay region" theory of chemical carcinogenesis proposed by Jerina, et al.<sup>27</sup> Additional result of this type thus may lead to a general understanding as to how polycyclic aromatic hydrocarbons and allied compounds interact with cellular components, and perhaps how chemical carcinogenesis is initiated.

The structure of BP and DMBA, as well as the reactive ring positions (indicated by dotted circles), are indicated in the figure below.



- (ii) The physical structure of the benzo(a)pyrene 7,8-dihydrodiol, 9,10-oxide DNA covalent adduct.

It has been shown that benzo(a)pyrene (BP) is metabolized in vivo to about 35 different metabolites which are excreted by the living

system (see ref. 27, for example). One of these, 7,8-dihydrodial 9,10-oxide (BPDE) binds covalently to DNA and RNA in living cells. This compound is also highly mutagenic<sup>27</sup> and it is suspected that this kind of BPDE-DNA complex may give rise to important alterations of the functioning of DNA in vivo. The formation of this complex thus could be the first step in the complicated series of biochemical and physiological events termed chemical carcinogenesis.

While the chemical nature of the BPDE-DNA adduct has been established, nothing is known about its physical structure and thus the physico-chemical properties of this complex which may lead to a significant alteration of the functioning of DNA in vivo.

We have therefore undertaken a detailed investigation of the physico-chemical structure of these BPDE-DNA complexes. For this purpose, it was found necessary to develop highly specialized spectroscopic techniques. These are described in detail in the papers in Appendices E and F and only a short overview will be given here.

This work involved several phases:

1. Determination of the number of different adducts and their chemical nature when BP interacts with nucleic acids in vivo.
2. The extent of binding of the BP to nucleic acids in vivo is extremely low (one BP per 50,000-100,000 bases). These amounts are insufficient for most of the physico-chemical methods available. Thus, we developed a suitable in vitro system which provides the same type of BPDE-DNA adduct as in vivo, but in higher quantities.
3. The orientation of the pyrene-like aromatic chromophore to DNA was studied by a linear dichroism method in which the DNA is oriented in an electric field. The preliminary aspects of this work was described in last year's annual report (1976). Since then, we have subjected the experimental results to a full theoretical and experimental analysis. The final result of this

study is that a vector defining the long in-plane axis of the pyrene moiety of BPDE is oriented at an angle of  $35^\circ$  or less with respect to the axis of the helix. This result provides a strong indication that the covalently attached BPDE molecule is located externally to the DNA helix and is definitely not an intercalation type complex. In this latter type of complex, the plane of BPDE is sandwiched between the base pairs of DNA and thus the in-plane long axis would be oriented at an angle of about  $90^\circ$  with respect to the axis of the helix.

4. A sequence of experiments was designed to confirm the above conclusion about the external location of BPDE. We devised a series of fluorescence technique involving the quenching of excited singlet states of BPDE by external quenchers such as  $O_2$ ,  $I^-$ ,  $Ag^+$  and  $Hg^{++}$ . The principle of these techniques is that  $Ag^+$  and  $Hg^{++}$  ions, (quenchers of the BPDE fluorescence) bind to the bases of the helix (internal binding), whereas  $O_2$  and  $I^-$  are external quenchers. We then demonstrated that intercalated aromatic molecules are readily quenched by  $Ag^+$  and  $Hg^{++}$  ions, but are less susceptible to external quenchers such as  $O_2$  and  $I^-$ . The fluorescence of BPDE, on the other hand, was insensitive to internal quenchers, but extremely sensitive to external quenchers. These results are in complete agreement with the results of the linear dichroism studies and we thus have firm evidence that BP reacts with DNA only after it has been metabolized to BPDE by the appropriate enzymes, and by binding covalently to DNA at a site external to the double helix.

A.III.(a).  $\alpha$ -Particle Induced Radical Production in Anthracene Beyond the Bragg Peak

Recently we have developed a technique for measuring small concentrations (i.e. one part in  $10^{11}$ ) of heavy ion induced radicals within an organic crystal.<sup>28</sup> This technique termed "Exciton Sounding (ES)" utilizes the quenching of triplet excitons to probe the spatial distribution of radiation damage in organic systems. In addition to its sensitivity ES provides a high level of spatial discrimination (i.e.  $\sim 10\mu$ ), since the excitons are generated in the narrow skirt of a focussed laser. The ES technique has been applied to the measurement of the spatial distribution and yield of heavy ion induced radical with some startling results.<sup>28</sup>

Arnold, Hu and Pope<sup>28</sup> have shown that although the distribution of radicals within the range of ion follows the stopping power, radicals are also produced far beyond this range. In particular in anthracene as Fig. 11 shows radicals were found at as much as six times the range of the 27 MeV He<sup>2+</sup> ions. With the inception of the use of heavy ions for radiation therapy, an explanation for this effect has important clinical significance.

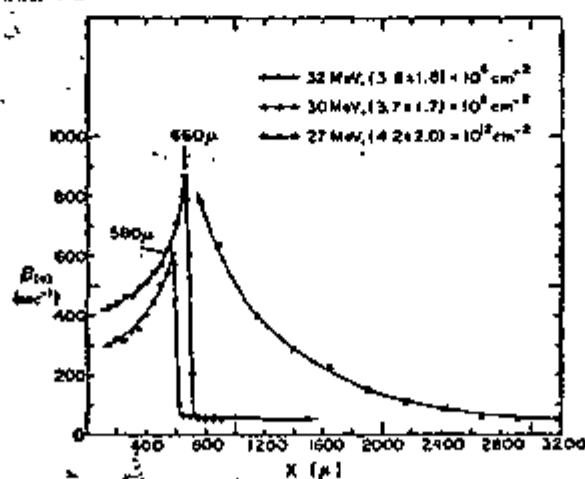


Figure 11.

Several hypotheses were proposed to explain these tails. These hypotheses may be divided into two categories:

One involves the participation of secondary radiation which causes damage through its energy degradation, and the other involves enhanced radical diffusion which allows the radicals to move beyond the  $\alpha$ -particle range in channels created for example, by recoil protons. Long range damage should be expected from any of the following secondary radiation.

- a) recoil protons.
- b)  $\gamma$ -radiation and neutrons arising from resonance excitation of carbon.
- c) bremsstrahlung from secondary electrons,  $\alpha$ -particles and secondary protons.

In addition, although the  $c'$  direction is not a channeling direction in anthracene<sup>29</sup> channeling may assist paraxial secondary charge particles in moving further than they could in an amorphous medium.

Under the circumstances a study of the energy dependence of the tails was appropriate since radical diffusion may be distinguished from nuclear processes and elastic recoil. Figure 12 shows the spatial distribution of radicals as a function of the incident energy of the  $\text{He}^{2+}$  ions.

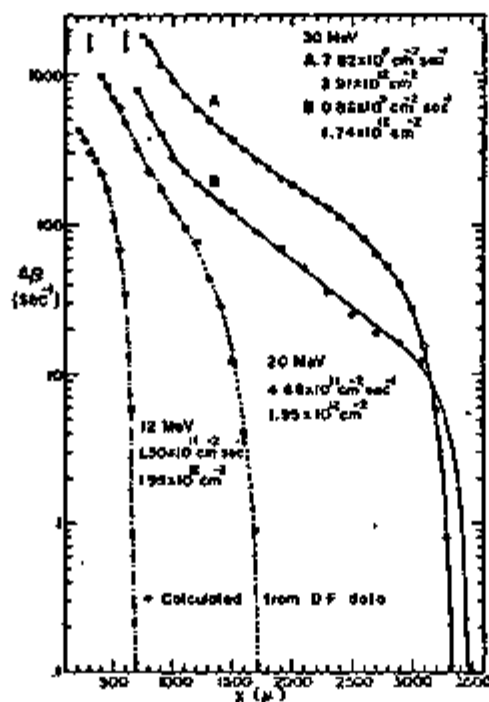


Figure 12.



As one can see the tails demonstrate an end point which increases monotonically with energy. This dependence eliminates both radical diffusion and radiation from excited nuclei from consideration as primary mechanisms for the tails. The radiation from excited nuclei may be eliminated since the process of exciting a nuclear level is not expected to be monotonic. Channeling may also be eliminated since the lateral distribution of the radicals was found to be symmetric about the  $c'$  axis which is not a channeling direction<sup>29</sup> in anthracene. The abrupt end point in the radical distribution is indicative of the stopping of heavy charged particles; proton or carbon recoils would seem appropriate. The end point range  $X_m$  plotted versus  $\text{He}^{2+}$  energy  $E_\alpha$  gives a power law of the form

$$X_m = 7.98 (E_\alpha)^{1.78} \quad (10)$$

As shown in Fig. 13.

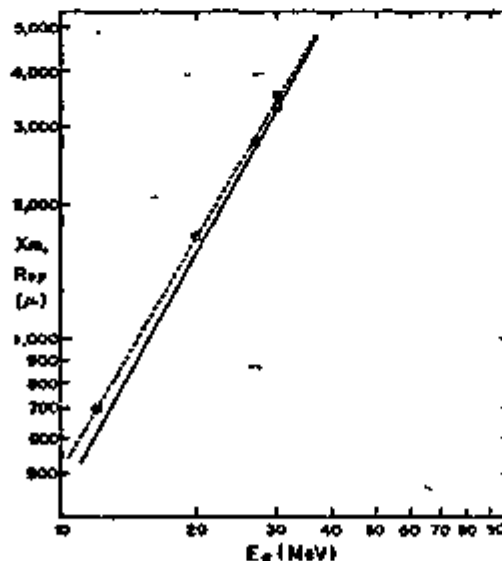


Figure 13.

Carbon recoils have too little range to account for the end point. However, the most energetic protons (i.e. those leaving from the point of entry) have ranges which agree well with the experimental points as shown by the solid line in Fig. 13.

More detailed insight into this process is gained by simulating the spatial distribution of radicals.

The density of energy deposited at any point  $\underline{R}'$ , ( $\underline{R}'$ ) due to recoil protons originating from a volume  $dV$  is

$$\rho(\underline{R}') = F_{\alpha} N_H \frac{d E_{sp}(r, E_{sp})}{dr} \frac{d(E_{\alpha}, \zeta)}{d\Omega} \frac{dV}{|\underline{R}' - \underline{R}|^2} \quad (11)$$

where  $F_{\alpha}$  is the  $\alpha$ -particle flux,  $N_H$  is the density of hydrogen,  $d\sigma_{sp}(E_{\alpha}, \zeta)/d\Omega$  is the cross-section for proton recoils,  $d E_{sp}(r, E_{sp})/dr$  is the energy loss at position  $\underline{R}'$  by a proton originating from  $dV$  with energy  $E_{sp}$ , and  $r$  is  $|\underline{R}' - \underline{R}|$ . Although stopping powers for protons in anthracene are easily arrived at from the Bragg additivity rule and stopping powers for carbon and hydrogen,<sup>30</sup> the determination of proton recoil cross-sections is more difficult. Since the center of mass energy exceeds the He Coulomb barrier, the differential cross-section  $\frac{d\sigma}{d\Omega}$  should be calculated using an attractive nuclear potential in addition to a Coulomb potential. Accordingly, these cross-sections were arrived at by solving for the S matrix using the following optical-model potential.<sup>31</sup>

$$V(r) = V_{CN}(r) + V_{SO}(r) + V_{Coul}(r) \quad (12)$$

where  $V_{CN}$  and  $V_{SO}$  are the (complex) central nuclear and spin-orbit potentials, respectively and  $V_{Coul}$  is the Coulomb potential. The parameters in the above potential were taken from fits to proton scattering experiments at 31 MeV.<sup>32</sup> The calculation of the energy density from equation (11) for a 30 MeV  $\alpha$ -particle flux of  $3.91 \times 10^{12} \text{ cm}^{-2}$  is shown in Fig. 14. As one can see, the computer simulated profile of the energy deposited along the symmetry axis is similar to the radical density profile (i.e.,  $\Delta\beta$  in Fig. 14) at the same energy. The 3% difference in cut-off depth between theory and experiment is in agreement with the semi-empirical range-energy formula and could be due to the failure to include the effects of straggling.

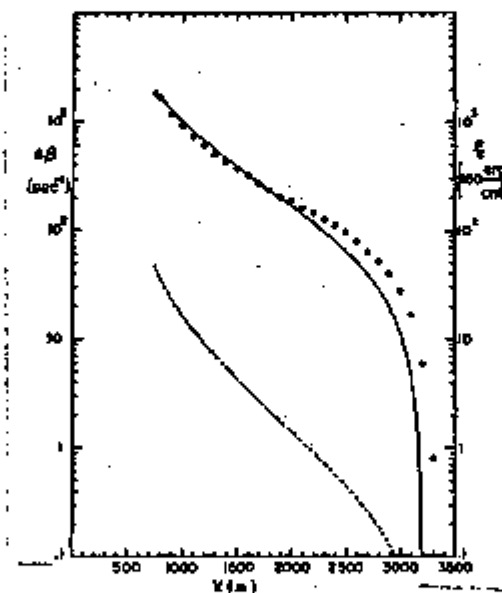


Figure 14.

Also shown in Fig. 14 is the energy density versus depth based on a Rutherford cross-section [i.e., only  $V_{Coul}(r)$  in equation (12)]. As one can see by comparison of this curve with the one corresponding to the full potential, Coulombic scattering plays a minor role in contributing to the energy deposited. The fact which is key to the occurrence of the tails will be discussed further below.

Since the energy density is calculated and the radical density is known, an average yield may be determined for the formation of radicals. This yield is approximately  $6 \times 10^8$ /erg. Although this yield is five times larger than the corresponding yield for  $\alpha$ -particles, some caution must be exercised in taking this conclusion literally. The most tenuous assumption in our calculation is that the Optical Model Parameters are independent of energy. Although this assumption is necessitated by lack of explicit data at other energies, one would expect terms in equation (12) such as the complex part of the central nuclear potential,  $\text{Im}[V_{\text{CN}}(r)]$ , to be influenced by the available energy<sup>33</sup> since this potential describes absorption into channels other than elastic scattering.<sup>34</sup>

The super-tails found in the present work appear to be a general property of the interaction of heavy ions with organic matter. The fraction of the initial energy in the secondary proton channel at 30 MeV is  $\sim 10^{-3}$ . The relative efficiency with which other ions produce tails will depend heavily on the cross-section for generating recoils. Efficiencies as high as 0.1% for ions having velocities of  $\sim 8$  MeV/AMU are a consequence of nuclear scattering and therefore will depend on the individual nuclear potentials.

The most important conclusion of the present work is that the super-tails found in the induced radical production have their origin primarily in damage by recoil protons.

## B. REFERENCES

1. R.R. Alfano, S.I. Shapiro, and M. Pope, *Optics Comm.*, 2, 388 (1972).
2. W. Arden, M. Kotani, and L.M. Peter, *Phys. Stat. Sol.(b)*, 75, 621 (1976).
3. A. Tiberghien, Ph Devaux, and G. Delacote, *Chem. Phys. Lett.*, 2, 642 (1971).
4. C.E. Swenberg, N.E. Geacintov, and M. Pope, *Biophys. J.*, 16, 1447 (1976).
5. R. Kopelman, in Topics in Applied Physics, Vol. 15: Radiationless Processes in Molecules and Crystals. By F.K. Fong (Springer, New York, N.Y., 1976).
6. S. Arnold, R.R. Alfano, M. Pope, W. Yu, P. Ho, R. Selsby, J. Tharrats, and C.E. Swenberg, *J. Chem. Phys.*, 64, 5104 (1976).
7. C.E. Swenberg, R. Dominijanni and N.E. Geacintov, *Photochem. Photobiol.*, 24, 601 (1976).
8. J.A. Stratton, Electromagnetic Theory, McGraw-Hill Book Company, New York, N.Y., 1941.
9. R.S. Berry and P.A. Lehman, *Ann. Rev. Phys. Chem.*, 22, 47 (1971).
10. P.F. Fennelly, *Amer. Sci.*, 64, 46 (1976).
11. J.N. Pitts and R.L. Metcalf, Advances in Environmental Sciences, 1, 7 (Wiley-Interscience, New York, N.Y., 1969).
12. G. Likens, *Chem. and Eng. News.*, November 22, 1976, p. 29.
13. L. Newman, J. Forest, and B. Manowitz, *Atm. Env.*, 9, 969 (1975).
14. E. Meszaws, *Aerosol. Sci.*, 4, 429 (1973).
15. H. Kallmann and M. Pope, *J. Chem. Phys.*, 30, 585 (1959).
16. H. Kallmann and M. Pope, *J. Chem. Phys.*, 32, 300 (1960).
17. R.C. Jarnagin, J. Gilliland, Jr., J.S. Kim, and M. Silver, *J. Chem. Phys.*, 39, 573 (1963).
18. L.E. Lyons, and K.G. McGregor, *Aust. J. Chem.*, 29, 21 (1976).
19. B.J. Mulder, *Phillips Research Report Supplement No. 4* (1968), p. 99.
20. W. Weston, and M. Pope, *Mol. Cryst. and Liq. Cryst.*, 25, 205 (1974).
21. M. Pope, and J. Burgos, *Mol. Cryst.*, 1, 395 (1966).
22. D. Haarer, and G. Castro, *Chem. Phys. Lett.*, 12, 277 (1971).
23. R.L. Bell, Negative Electron Affinity Devices, (Clarendon Press, Oxford, 1973).

24. A.I. Belkind, and V.V. Crechow, *Phys. Stat. Sol.(a)*, 26, 377 (1974).
25. V. Ivanovic, N.E. Geacintov, and I.B. Weinstein, *Biochem. Biophys. Res. Comm.*, 70, 1172 (1976).
26. A.M. Jeffrey, I.B. Weinstein, K.W. Jennette, K. Grzeskowiak, K. Nakaniski, R.G. Harvey, C. Harris, H. Autrup, and C. Harris, *Science*, 93, 592-595 (1976).
27. D.M. Jerina, *et al.*, In Vitro Metabolic Activation in Mutagenesis Testing (eds. F.J. de Serres, *et al.*) 1976, Elsevier/North-Holland Biomedical Press, Amsterdam, Holland.
28. S. Arnold, H.-T. R, and M. Pope, *Mol. Cryst. Liq. Cryst.*, 36, 179 (1976).
29. W. Brandt, R. Dobin, H. Jack, Jr., R. Laubert, and S. Roth, *Can. J. Phys.*, 46, 567 (1968).
30. L.C. Northcliff and R.F. Schilling, *Nuclear Data Tables A7*, 233-467 (1970).
31. J.S. Nodvik, C.B. Duke, and M.A. Melkanoff, *Phys. Rev.*, 125, 975 (1962).
32. S.M. Bunch, H.H. Forster, and C.C. Kim., *Nucl. Phys.*, 53, 241 (1964).
33. *Atomic Data and Nuclear Data Tables*, 17, 20 (1976).
34. I. Ulehla, L. Gomokak, and Z. Pluhar, Optical Model of the Atomic Nucleus, [Academic Press, New York, N.Y. (1964)].

## C. PUBLICATIONS

1. "Heterofission in Pentacene-Doped Tetracene Single Crystals", M. Pope, J. Burgos, C.E. Swenberg, and R.R. Alfano, *Phys. Stat. Sol. (b)*, 83, 249 (1977).
2. "Magnetic Field Modulated Scintillation from Tetracene-Doped Anthracene  $\alpha$ -Particle Irradiation, M. Binder, N.E. Geacintov, M. Pope and C.E. Swenberg, *Phys. Stat. Sol.(a)*, 40, 621 (1977).
3. "Triplet Exciton Diffusion and Double Photon Absorption in Tetracene", S. Arnold, J.B. Aladekomo, and M. Pope, *Phys. Stat. Sol.(b)*, 80, 333 (1977).
4. " $\alpha$ -Particle Induced Radical Production in Anthracene Beyond the Bragg Peak", S. Arnold, H.-T. Hu, and M. Pope, *Radiation Research*, 74, 231 (1978).
5. "AMCOED: Aerosol Mass and Charge by One Electron Differentials", S. Arnold, *J. Aerosol Science* (submitted, 1978).
6. "Fluorescence Study of the Physico-Chemical Properties of a Benzo(a)pyrene 7,8-Dihydrodiol 9,10-oxide Derivative Bound Covalently to DNA", T. Prusik, N.E. Geacintov, C. Tobiasz, V. Ivanovic, and I.B. Weinstein, *Photochem. Photobiol.*, in press.
7. "Cell and Microsome Mediated Binding of 7,12-Dimethyl Benz(a)anthracene to DNA Studied by Fluorescence Spectroscopy", V. Ivanovic, N.E. Geacintov, A.M. Jeffrey, P.P. Fu, R.G. Harvey, and I.B. Weinstein, *Cancer Lett.*, in press.
8. "Exciton Annihilation in the Two Photosystems in Chloroplasts at 100°K", N.E. Geacintov, and J. Breton, *Biophys. J.*, 17, 1 (1977).
9. "Picosecond and Microsecond Pulse Laser Studies of Exciton Quenching and Exciton Distribution in Spinach Chloroplasts at Low Temperatures", N.E. Geacintov, J. Breton, C.E. Swenberg, A.J. Campillo, R.C. Hyer, and S.L. Shapiro, *Biochim. Biophys. Acta.*, 461, 306-312 (1977).
10. "A Single Pulse Picosecond Laser Study of Exciton Dynamics in Chloroplasts", N.E. Geacintov, J. Breton, C.E. Swenberg, and G. Pailloton, *Photochem. Photobiol.*, 26, 629-638 (1977).
11. "Laser Pulse Excitation Studies of the Fluorescence of Chloroplasts", C.E. Swenberg, N.E. Geacintov, and J. Breton, *Photochem. Photobiol.*, in press.
12. "Photovoltages in Suspension of Magnetically Oriented Chloroplasts", J.F. Becker, N.E. Geacintov, and C.E. Swenberg, *Biochem. Biophys. Acta.*, in press.

D. DOCTORAL DISSERTATIONS

1. V. Ivanovic, Spectroscopic Studies of In Vivo and In Vitro Nucleic-Acids Carcinogen Interactions, Department of Chemistry, New York University.

E. ORAL PRESENTATIONS

The senior members of this laboratory have over the past year presented 50 lectures including presentations at 15 major universities, five international conferences and five national laboratories.



## F. APPENDIX

- A. TRIPLET EXCITON DIFFUSION AND DOUBLE PHOTON ABSORPTION IN TETRACENE.
- B. SINGLE-PULSE PICOSECOND DETERMINATION OF 735 nm FLUORESCENCE RISTIMES IN SPINACH CHLOROPLASTS.
- C. A SINGLE PULSE PICOSECOND LASER STUDY OF EXCITON DYNAMICS IN CHLOROPLASTS.
- D. AMCOED: DETERMINATION OF AEROSOL MASS AND CHARGE BY ONE ELECTRON DIFFERENTIALS.
- E. FLUORESCENCE STUDY OF PHYSICO-CHEMICAL PROPERTIES OF BENZO(A)PYRENE 7,8-DIHYDRODIOL 9,10-OXIDE DERIVATIVE BOUND COVALENTLY TO DNA.
- F. ELECTRIC LINEAR DICHROISM STUDY ON THE ORIENTATION OF BENZO(A)PYRENE-7,8-DIHYDRODIOL 9,10-OXIDE COVALENTLY BOUND TO DNA.
- G.  $\alpha$ -PARTICLE INDUCED RADICAL PRODUCTION IN ANTHRACENE BEYOND THE BRAGG PEAK.

## Triplet Exciton Diffusion and Double Photon Absorption in Tetracene

By

J. B. ALADEKOMO<sup>2)</sup>, S. ARNOLD, and M. POPE

Delayed fluorescence from tetracene crystal excited at 3600 Å is studied. The luminescence decay is interpreted in terms of a model in which singlets are generated by triplet exciton fusion and by double-photon absorption. The double-photon absorption coefficient is estimated to be  $5.8 \times 10^{-27}$  cm s. The triplet exciton diffusion coefficient along the crystal *b* axis is determined by the spatial intermittency method to be  $(4 \pm 1) \times 10^{-3}$  cm<sup>2</sup>/s. The influence of this diffusion coefficient on other processes is discussed.

Es wird die verzögerte Fluoreszenz von Tetracen-Kristallen untersucht, die bei 3600 Å angeregt wurde. Das Abklingen der Lumineszenz wird interpretiert mittels eines Modells, in dem Singulets durch Triplett-Exzitonen-Fusion und durch Zwei-Photonen-Absorption erzeugt werden. Der Koeffizient der Zwei-Photonen-Absorption wird zu  $5,8 \times 10^{-27}$  cm s abgeschätzt. Der Diffusionskoeffizient der Triplett-Exzitonen entlang der *b*-Achse wird mittels der räumlichen Intermitenz-Methode zu  $(4 \pm 1) \times 10^{-3}$  cm<sup>2</sup>/s bestimmt. Es wird der Einfluß dieses Diffusionskoeffizienten auf andere Prozesse diskutiert.

## 1. Introduction

The determination of the diffusion coefficient  $D_{ab}$  of the triplet exciton in the *ab* plane of tetracene is of special interest. Recently, Alfano et al. [1] have estimated that  $D_{ab}(\infty) \geq 10^{-2}$  cm<sup>2</sup> s<sup>-1</sup>, where the expression ( $\infty$ ) refers to a hypothetical measurement at infinite temperature. In the paper of Alfano et al. [1], the expression ( $\infty$ ) was omitted, but since  $D_{ab}$  was estimated from the fission rate constant at infinite temperature, it should have been referred to as  $D_{ab}(\infty)$ . In the absence of information on the temperature dependence of  $D_{ab}$ , it is not possible to convert  $D_{ab}(\infty)$  to a room temperature value. It appears however that according to Alfano et al. [1], if one takes the lower limit of their estimate, that  $D_{ab}^T(\text{tetracene}) \approx 100D_{ab}^T(\text{anthracene})$ . If this prediction is true, then the triplet diffusion constant in tetracene is quite anomalous. Both anthracene [2] and naphthalene [3] have diffusion constants which are within a factor of three of the predicted values based on static exciton transfer integrals [4]. The calculated transfer integrals in tetracene are only about three times those in anthracene or naphthalene [5]. Since the diffusion is proportional to the square of the transfer integrals one would expect approximately one order of magnitude increase in the diffusion in tetracene as compared to anthracene or naphthalene. The predicted hundred-fold increase is clearly at odds with existing theory. Furthermore, a paper by Arden et al. [6] has appeared recently giving a new value for the total triplet exciton fusion rate constant in tetracene,  $\gamma_{\text{tot}} = 2 \times 10^{-11}$  cm<sup>3</sup> s<sup>-1</sup>. This value is one hundred times smaller than the value previously measured, and lead Arden et al. [6] to the conclusion that  $D_{ab}$  in tetracene is rather similar to that in anthracene. It therefore appears that a direct measurement of  $D_{ab}$  is essential.

<sup>1)</sup> New York, N.Y. 10003, USA.

<sup>2)</sup> Visiting Fulbright-Hays Fellow. Permanent address: Department of Physics, University of Ifé, Nigeria.

Although direct measurements of triplet exciton diffusion have been made in anthracene and naphthalene and a number of other aromatic systems, such measurements have not been made in tetracene principally because of the weak delayed fluorescence in this system and the difficulty in growing thick crystals.

In the present work the method of spatial intermittency introduced by Avakian and Merrifield [7] is used to measure the diffusion in tetracene.

## 2. Theory

This section is divided into two parts. In the first part the decay of the triplet density will be described in the presence of traps. In the second part diffusion will be added to the kinetics and an expression for the decay of the delayed fluorescence will be derived.

### 2.1 Decay of the triplet density in the presence of traps

The basic equations governing the time dependence of a triplet exciton density  $n(t)$  generated by an incident intensity  $I(t)$  in the presence of an excess of traps in tetracene may be written as [8]

$$\frac{dn}{dt} = aI(t) - rn + gn_t, \quad (1)$$

$$\frac{dn_t}{dt} = -sn_t + pn, \quad (2)$$

where

$$r = \beta_0 + p, \quad s = \beta_t + q.$$

In the above equations  $n_t$  is the density of traps,  $\beta_0$  is the intrinsic free triplet exciton decay rate,  $p$  is the trapping rate,  $\beta_t$  is the rate of decay in the trap and  $q$  is the rate constant for escaping to the free exciton band from the trap. Bimolecular terms have been neglected [9] since the experiments are run at low enough intensities so that the luminescence is proportional to  $I^2$ . If the duration of the excitation pulse  $\Delta t$  is short compared with all other rate processes, then it can be shown in general that the solution of (1) and (2) for  $n$  will be the sum of two exponentials [8]

$$n = a e^{-\lambda t} + b e^{-\mu t}. \quad (3)$$

Experimentally, since the delayed fluorescence intensity is proportional to  $n^2$ , the rate constants,  $\lambda$ ,  $\mu$  and the ratio of amplitudes  $a/b$  may be obtained from the square root of this luminescence intensity. Once having these parameters, the rate constants  $r$  and  $s$  in equations (1) and (2), and the product  $pq$  may be arrived at from [8]

$$r = \frac{\frac{a}{b}\lambda + \mu}{\frac{a}{b} + 1}, \quad s = \frac{\frac{a}{b}\mu + \lambda}{\frac{a}{b} + 1}, \quad pq = \frac{\frac{a}{b}(\lambda - \mu)^2}{\left(\frac{a}{b} + 1\right)^2}. \quad (4)$$

### 2.2 Decay of the delayed luminescence including diffusion

Experimentally we are interested in examining the effect on the decay of the delayed fluorescence of introducing a periodic spatial distribution of excitons into a crystal. These excitons will be introduced by irradiating the crystal with a pulse of 8600 Å light through a transmission grating (Ronchi Ruling) of period  $x_0$ . Since the distribution of excitons is not uniform the analysis of the results must include

a diffusion term  $D(\partial^2 n/\partial x^2)$  in equation (1). In addition since diffusion has its greatest contribution to (1) just after the light is turned on, the analysis will include the excitation time period of duration  $\Delta t$ .

For a periodic spatical excitation,  $I(x, t)$ ,  $n(x, t)$ , and  $n_t(x, t)$  will be periodic and may be represented by the Fourier series

$$I(x, t) = \sum_{l=-\infty}^{l=+\infty} I_l(t) e^{-j\omega_l x}, \quad n(x, t) = \sum_{l=-\infty}^{l=+\infty} n_l(t) e^{-j\omega_l x}, \quad n_t(x, t) = \sum_{l=-\infty}^{l=+\infty} n_{tl}(t) e^{-j\omega_l x}, \quad (5)$$

where  $\omega_l = 2\pi l/x_0$ . By substituting (5) into (1) and (2) (with the diffusion term included in equation (1)) and doing a bit of algebra one can show that

$$\frac{d^2 n_l}{dx^2} + (\gamma + s + D\omega_l^2) \frac{dn_l}{dt} - (qp - rs - sD\omega_l^2) n_l = \alpha I_l. \quad (6)$$

The complete solution to this equation is

$$n_l(t) = A_l e^{-\delta_l t} + B_l e^{-\gamma t} - \frac{\alpha I_l}{qp - rs - sD\omega_l^2}. \quad (7)$$

where

$$\left. \begin{array}{l} \gamma_l \\ \delta_l \end{array} \right\} = \frac{(\gamma + s + D\omega_l^2) \mp \sqrt{(\gamma + s + D\omega_l^2)^2 + 4(pq - rs - sD\omega_l^2)}}{2}$$

At the instant the excitation is turned on  $n_l(0) = 0$  and  $dn_l/dt|_{t=0} = \alpha I_l$ . With these boundary conditions and equation (7),  $B_l$ , the coefficient of the slow decay, is evaluated to be

$$B_l = \frac{\delta_l \eta_l + \alpha I_l}{\delta_l - \gamma_l}. \quad (8)$$

where  $\eta_l = \alpha I_l / (qp - rs - sD\omega_l^2)$ . After the laser is turned off

$$n_l(t') = A_l e^{-\delta_l t'} + B_l e^{-\gamma_l t'}, \quad (9)$$

where  $t' = t - \Delta t$ .

By adding the boundary conditions

$$n_l(0) = n_l(\Delta t)$$

and

$$\left. \frac{dn_l}{dt} \right|_{t'=0} = \left. \frac{dn_l}{dt} \right|_{t=\Delta t} - \alpha I_l \quad (10)$$

and applying these conditions to (7) and (9),  $B_l$  is found to be

$$B_l = \frac{\alpha I_l}{\gamma_l - \delta_l} \left[ 1 + \frac{\delta_l s}{qp - rs - sD\omega_l^2} \right] (1 - e^{-\gamma_l \Delta t}) \quad (11)$$

and therefore the triplet density  $n'(t')$  after the fast decay dies away is

$$n'(t') = \sum_{l=-\infty}^{l=+\infty} B_l e^{-\gamma_l t'} e^{-j\omega_l x}. \quad (12)$$

By utilizing (12) and the Fourier coefficients of the spatial square wave of excitation, the delayed luminescence  $L$  which is proportional to the volume integral of  $n'^2$  may be shown to be

$$L \propto |B_0|^2 e^{-2\gamma t'} + 2 \sum_{l=1}^{\infty} |B_l|^2 e^{-2\gamma_l t'}, \quad (13)$$

where the prime on the summation indicates that this sum is to be carried out over only odd values of  $l$ . Experimentally we are interested in the influence of diffusion on the slow decay, and therefore data will be gathered after a time  $d$  beyond which the contribution from the fast decay is negligible. After this decay the influence of diffusion will be ascertained from the change in the rate of decay of the delayed fluorescence in the presence of the Ronchi Ruling. The amplitude normalized decay integral method [10] will be used for this purpose. In this method the ratio  $R$  of the integrated photon counts over several time constants  $(T/\tau)\tau$  to the integrated counts over a fraction of a time constant  $(d/\tau)\tau$  is measured. This ratio provides a sensitive parameter for measuring decay characteristics. In general the ratio decreases as the rate of decay increases. The effect of a diffusion term in (1) is to cause the average triplet density to decay at a greater rate, thereby increasing the rate of decay of the delayed fluorescence. The ratio  $R$  from (13) is

$$R = \frac{\int_d^{d+T} L dt}{\int_d^{d+d} L dt} = \frac{1 - e^{-2\gamma T} + 2 \sum_{l=1}^{\infty} (C_l/C_0) [1 - e^{-2\gamma l T}]}{1 - e^{-2\gamma d} + 2 \sum_{l=1}^{\infty} (C_l/C_0) [1 - e^{-2\gamma l d}]}, \quad (14)$$

where  $C_l = |E_l|^2 e^{-2\gamma l d/\gamma l}$ .

### 3. Experimental

The experimental arrangement for determining the triplet exciton diffusion in tetracene is shown in Fig. 1. Light at 8000 Å from a liquid nitrogen cooled GaAs laser diode (Laser Diode Laboratories, Inc., Model LD-68) was collimated using a lens  $L$  of short focal length and passed through a polarizer  $P$  (Polaroid HR) and an IR transmitting filter (Corning CS 7-69) to isolate the room light. The light was then passed through a Ronchi Ruling  $R$  onto the  $ab$  plane of a crystal. Polarizer  $P$  was oriented along one of the principal axes of the crystal in order to eliminate broadening of the excitation stripes within the crystal due to birefringence. The resulting delayed fluorescence was isolated from the exciting light by a green-blue filter (Corning CS 4-97) and detected by a photomultiplier (EMI-6256S). The output from this photomultiplier was conditioned for photon-counting by an amplifier-discriminator (AD). The output of this AD was sequentially channelled into a pair of scalars  $S_1$  and  $S_2$ , as explained below.

The amplitude normalized decay integral method (ANDI) was used to detect changes in the luminescence decay rate [10] as explained in Section 2.

The gating pulses for scalars  $S_1$  and  $S_2$ , SG and LG, respectively, as well as the pulse for driving the laser diode LSR was derived from a pulse sequence generator PSG whose output pulses were adjustable both individually in width and also in

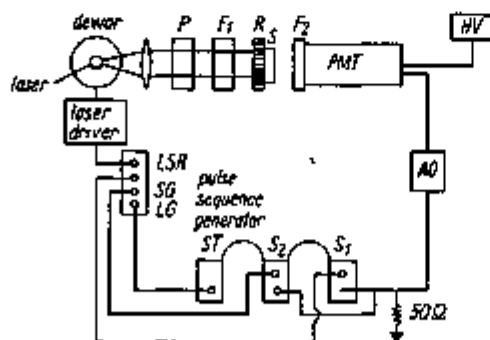
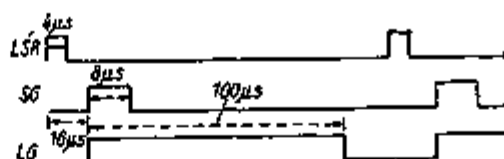


Fig. 1. Experimental setup for diffusion measurements

Fig. 2. Timing diagram for ANDI method. The repetition frequency of this sequence is 7.6 kHz.



relative sequence. The pulse width of the laser in these measurements was approximately  $2 \mu\text{s}$  including a rise and fall time of about  $0.5 \mu\text{s}$ . Both scalers  $S_1$  and  $S_2$  were slaved to a scaler-timer (ST) which counted the number of driving pulses up to a preset number of  $4 \times 10^6$ . The sequence of pulses from the PSG is shown in Fig. 2. As this figure indicates, the timing sequence was arranged such that the observation of luminescence decay was done with a delay  $d = 14 \mu\text{s}$  after the turnoff of the excitation. Experimentally the delay was necessary to eliminate the inclusion of luminescence arising from the fast decay component in the delayed fluorescence (see Section 2).

In order to correct for intensity effects due to reflection and absorption by the ruling substrate a clear glass plate of the same material as that of the Ronchi Ruling (RR) was placed in front of the crystal replacing the ruling shown in Fig. 1 (condition A). Single photon counts were then recorded in both  $S_1$  and  $S_2$  up to the preset of the scaler-timer (ST). The glass was removed, ruling inserted (condition B) and the experiment repeated for the same number of laser pulses. The changes in the ratio of the counts in the two scalers between condition A and condition B,  $E = (R_A - R_B)/R_A$  was used as a measure of exciton diffusion (see Section 2). In order to eliminate systematic errors, the experiments were done in the order A B B A A B B A ... , and analyzed pairwise. A complete set of runs involved ten pairs of readings.

An examination of the complete decay of delayed luminescence was made over a range of  $80 \mu\text{s}$  using the monophoton delayed coincidence method (MPDC) [11]. To implement this method, the output signal from the discriminator was fed into the stop channel of a time to amplitude converter TAC and to a multichannel pulse height analyzer PHA. The start pulse for this TAC was derived from the pulse sequence generator PSG such that the leading edge of the start pulse coincided with the leading edge of LSR. By running the system without a crystal, it was ascertained that the exciting laser light was completely cut off. The decay of luminescence was accumulated in the memory of the PHA.

The MPDC method was not used for the diffusion measurements because the ANDI method was found to be more reproducible. Since the ANDI method only required the recording of two readings, the rulings could be changed more quickly than the limit set in the MPDC method by the time needed to read out data. This lag time in the MPDC method was found to make systematic effects more influential in the analysis of the diffusion.

#### 4. Results

The luminescence emanating from the crystal from the time the laser is turned on is shown in Fig. 3 in terms of the square root of the luminescence intensity versus time. The curves for the two different excitation pulse widths used in these experiments have been shifted horizontally with respect to each other in order to avoid confusion due to overlap. The pulse widths may be characterized by the average time at full intensity  $I_0$ ,  $\Delta t = (\int I dt)/I_0$ . Curve a was obtained with a pulse width of  $0.25 \mu\text{s}$ . For curve b the pulse width was  $1.3 \mu\text{s}$ . The integrated luminescence detected during the laser pulse as well as that detected after the pulse were found to be proportional to the square of the incident intensity. As one can see, each of the decays shows a fast component which follows the turnoff characteristics of the laser followed by a slower

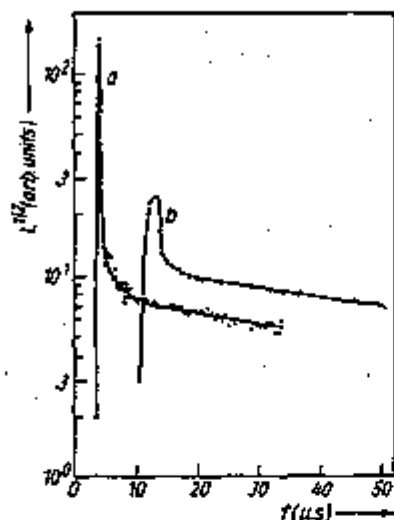


Fig. 4. The effect of diffusion on the lifetime of the long decay component in terms of  $E$  versus  $1/x_0$ . The diffusion coefficients for different curves are: (1)  $5 \times 10^{-2}$ , (2)  $4 \times 10^{-2}$ , (3)  $3 \times 10^{-2}$ , (4)  $2 \times 10^{-2}$ , (5)  $1 \times 10^{-2}$  cm<sup>2</sup>/s

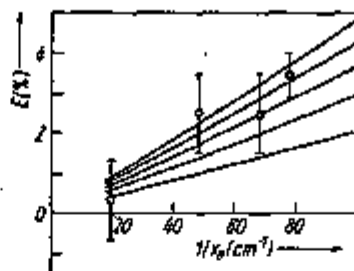


Fig. 3. Decay of luminescence excited at 8600 Å. (a) For excitation pulse width of 0.25 μs, (b) For excitation pulse width of 1.3 μs

decay which may be broken up into the sum of two exponentials. The curves have been shifted vertically so that the luminescence intensities at the start of the slow decay appear to be equal. The short pulse width (0.25 μs) is found to enhance the relative intensity above the slow decay. The lines drawn through curve a in Fig. 3 represent a fit to equation (3). The values found for  $\lambda$ ,  $\mu$  and  $a/b$  are  $5.0 \times 10^6$  s,  $1.0 \times 10^4$  s<sup>-1</sup>, and 0.5, respectively. The additional intensity above this relatively slow decay may be explained in terms of fluorescence arising from double photon excitation from the ground state to the excited singlet state (see Section 5).

The modulation of the slow decay rate in the presence of a Ronchi Ruling is represented by the factor  $E$  (see Section 3) versus ruling density  $1/x_0$  in Fig. 4. Since an increase in  $E$  corresponds to a faster decay, the data in Fig. 4 indicates that the decay rate is increased as the ruling density increases. The uncertainties in the points were calculated assuming Poisson statistics, and represents one standard error. These results indicate that the influence of diffusion is greater at higher ruling densities as predicted by theory (see Section 5).

### 5. Discussion of Results

The delayed fluorescence decays in Fig. 3 may be considered to contain two components. The first is a prompt component due to fluorescence produced by double photon absorption and the second is a delayed component arising from triplets produced by direct  $S_0 \rightarrow T_1$  absorption. The singlet population obeys the following kinetics

$$\dot{n}_s = \delta I^2 - K_s n_s + \frac{1}{2} f n^2, \quad (15)$$

where  $\delta$  is the coefficient for double photon absorption,  $K_s$  is the monomolecular decay rate of the singlets and  $\frac{1}{2} f n^2$  is the rate at which singlets are formed from fusion. Since  $K_s^{-1}$  is much smaller than the laser pulse width, the singlets may be considered to be in steady state and

$$n_s = \frac{1}{K_s} \left( \delta I^2 + \frac{1}{2} f n^2 \right). \quad (16)$$

For the 0.25  $\mu\text{s}$  pulse width the density of triplets following shortly after this pulse ( $\approx 1 \mu\text{s}$ ) may be obtained from  $n = \alpha \int I dt$ , or  $n = \alpha I_0 \Delta t$ . We see therefore that the ratio  $G$  of the density of singlets from double photon absorption at maximum intensity to that from delayed light just after the pulse

$$G = \frac{\delta}{\frac{1}{2} f \gamma a^2 \Delta t^2} \quad (17)$$

For the short pulse (0.25  $\mu\text{s}$ ) the experimental value of  $G$  is 140 and for the long pulse (1.3  $\mu\text{s}$ ),  $G$  is 4. The short pulse therefore gives thirty five times as much prompt light as compared with the long pulse in fair agreement with the value of 29 for the inverse ratio of pulse widths squared. From (17) and the value of  $G$  for the short pulse,  $\delta/(\frac{1}{2} f \gamma a^2)$  may be calculated and is found to be  $8.8 \times 10^{-12} \text{ s}^2$ . With  $\frac{1}{2} f \gamma$  taken to be  $6.6 \times 10^{-10} \text{ cm}^2/\text{s}$  [12] and  $a$  estimated to be  $10^{-3} \text{ cm}^{-1}$  [13],  $\delta$  may be estimated to be  $5.8 \times 10^{-27} \text{ cm s}$ . This result is easily within an order of magnitude of the value of  $1.5 \times 10^{-27} \text{ cm s}$  arrived at by measuring the contribution of double photon absorption to delayed light from ruby laser excitation (8). The two decays which make up the long decay in Fig. 3 may be used to determine the kinetic rates  $r$ ,  $s$ , and  $qp$  from equation (4). These calculations give values for  $r$ ,  $s$ , and  $qp$  of  $1.7 \times 10^6 \text{ s}^{-1}$ ,  $3.4 \times 10^4 \text{ s}^{-1}$ , and  $5.3 \times 10^{10} \text{ s}^{-2}$ , respectively. The values of these rates are similar to although somewhat higher than the rates found by Delannoy and Schott (8).

The values of  $r$ ,  $s$ , and  $qp$  may now be used in (14) along with the values of the diffusion constant to calculate  $E$  as a function of  $1/x_0$ . These calculations are shown in Fig. 4 along with the experimental data. As one can see the value of the diffusion coefficient in the  $b$  direction tetracene may be estimated to be  $(4 \pm 1) \times 10^{-3} \text{ cm}^2/\text{s}$ . This diffusion coefficient is more than an order of magnitude greater than the largest diffusion for anthracene ( $\approx 1.5 \times 10^{-4} \text{ cm}^2/\text{s}$ ) [14] in the  $ab$  plane. Since tetracene is triclinic the four inequivalent nearest neighbours in the  $ab$  plane will have unequal interactions with the molecule at the origin (5). This triclinic nature implies that the  $b$ -axis will not be a principal axis in tetracene. Therefore the diffusion measured in this experiment is a lower limit to the maximum diffusion. Since the spin relaxation time is expected to increase in proportion with the diffusion coefficient, a higher diffusion rate implies a longer spin relaxation time. This result is consistent with the large spin polarization found in tetracene [15]. Furthermore, such a long spin relaxation time should be evidenced in a narrowing of the spin resonance lines. We therefore would expect the spin resonance line widths to be much narrower in tetracene than in anthracene. Preliminary measurements indicate that this is indeed the case [16].

Let us return to the problem posed by the recent measurement of  $\gamma_{\text{tot}}$  by Arden et al. of  $2 \times 10^{-11} \text{ cm}^2 \text{ s}^{-1}$ . This value is one hundred times smaller than that given previously by Ern et al. [12] and Pope et al. [17] of  $\gamma_{\text{tot}} = 2 \times 10^{-9} \text{ cm}^2 \text{ s}^{-1}$ . Consider the effect of a magnetic field on the efficiency of singlet production by triplet exciton fusion in anthracene and tetracene. It can be shown by means of the Johnson-Merrifield [18] theory of this magnetic effect that the following relation holds in the absence of an applied magnetic field,

$$\gamma_s^{A,T} = \frac{1}{9} K_1^{A,T} \left( \frac{\epsilon_{A,T}}{1 + \epsilon_{A,T}/3} \right), \quad (18)$$

where  $\gamma_s^{A,T}$  is the bimolecular rate constant for the fusion of triplet excitons to produce a singlet state, and the superscripts refer to either anthracene or tetracene;  $K_1^{A,T}$  is the diffusion controlled encounter rate of the triplet excitons;  $\epsilon_{A,T}$  is the branching ratio or the ratio of the rate at which a pair of correlated triplet excitons fuse to give a singlet exciton to the rate at which the excitons backscatter to their uncorrelated



state. The branching ratio for tetracene  $\epsilon_T$  may be related through (19) to various rate constants in both anthracene and tetracene with the result that

$$\epsilon_T = \left[ 2.83 \left( \frac{\gamma_6^A}{\gamma_8^A} \right) \left( \frac{K_1^T}{K_1^A} \right) - \frac{1}{3} \right]^{-1} \quad (19)$$

with  $\epsilon_A$  taken to be 0.4. If we assume that  $K_1$  is proportional to the diffusion and that the diffusion in the present experiment is characteristic of the diffusion in the  $ab$  plane, then  $(K_1^T/K_1^A)$  is  $\approx 30$ . Based on Arden et al. [6],  $(\gamma_6^A/\gamma_8^A) = 0.54$  and  $\epsilon_T$  from equation (19) is 0.02. This value is more than an order of magnitude smaller than the value of 0.8 estimated from the magnetic anisotropy in the prompt fluorescence [19]. In fact such a value implies a much smaller magnetic field effect than that observed. On the other hand, the value for  $\gamma_8$  obtained by Ern et al. [12] and Pope et al. [17] gives a value for  $\epsilon_T$  of 1.26 which is within a factor of two of the values obtained from the magnetic field studies. We conclude therefore that it is difficult to rationalize the results of Arden et al. with the diffusion and the magnetic field measurements in the context of the Johnson-Merrifield theory of the magnetic effects. However, considering the approximations involved in making estimates from (19), the value of  $\gamma_{tot}$  arrived at by Ern et al. [12] and Pope et al. [17] is in reasonable agreement with the present diffusion measurements. In addition, the prediction of Alfano et al. [1] that  $D_{ab}^T \approx 100D_{ab}^A$  is probably too high, although the observed ratio of 30 still represents a somewhat anomalous diffusion process in tetracene.

#### Acknowledgements

We would like to thank Dr. N. Wotherspoon for building the Pulse Sequence Generator used in these experiments. We are also grateful to Prof. N. E. Geacintov at New York University and Dr. C. E. Swenberg at the National Institute for Mental Health in Washington, D.C. for their useful suggestions. This work was supported by the Energy Research and Development Administration.

#### References

- [1] R. R. ALFANO, S. I. SHAPIRO, and M. POPE, *Optics Commun.* **9**, 358 (1973).
- [2] P. AVAKIAN and R. E. MERRIFIELD, *Phys. Rev. Letters* **18**, 541 (1964).
- [3] V. ERN, *J. chem. Phys.* **51**, 6259 (1972).
- [4] A. TIBERGHIEH, Ph. DEVAUX, and G. DELACOTE, *Chem. Phys. Letters* **9**, 642 (1971).
- [5] A. TIBERGHIEH and G. DELACOTE, *Chem. Phys. Letters* **8**, 88 (1971).
- [6] W. ARDEN, M. KOTANI, and L. M. PETER, *phys. stat. sol. (b)* **78**, 621 (1976).
- [7] P. AVAKIAN and R. E. MERRIFIELD, *Phys. Rev. Letters* **18**, 541 (1964).
- [8] P. DELANNOY and M. SCHOTT, *phys. stat. sol. (b)* **70**, 119 (1975).
- [9] J. L. HALL, D. A. JENNINGS, and R. M. McCLINTOCK, *Phys. Rev. Letters* **11**, 364 (1963).
- [10] S. ARNOLD and N. WOTHERSPOON, *Rev. sci. Instrum.* **47**, 751 (1976).
- [11] Y. KOECHLIN, Thesis, University of Paris 1961.
- [12] V. ERN, J. L. SAINT-CLAIR, M. SCHOTT, and G. DELACOTE, *Chem. Phys. Letters* **10**, 287 (1971).
- [13] P. AVAKIAN, E. ABRAMSON, R. G. KEPLER, and J. C. CARIS, *J. chem. Phys.* **39**, 1121 (1963).
- [14] V. ERN, *Phys. Rev. Letters* **22**, 343 (1969).
- [15] L. YARNUS, J. ROSENTHAL, and M. CHOFF, *Chem. Phys. Letters* **16**, 477 (1972).
- [16] J. ROSENTHAL, private communication.
- [17] M. POPE, N. E. GEACINTOV, and F. VOGEL, *J. Lum.* **1/2**, 224 (1970).
- [18] R. C. JOHNSON and R. E. MERRIFIELD, *Phys. Rev. B* **1**, 896 (1970).
- [19] S. ARNOLD, C. E. SWENBERG, and M. POPE, *J. chem. Phys.* **64**, 5115 (1976).

(Received November 24, 1976)

## SINGLE-PULSE PICOSECOND DETERMINATION OF 735 nm FLUORESCENCE RISE TIME IN SPINACH CHLOROPLASTS

A. J. CAMPILLO and S. L. SHAPIRO

*University of California, Los Alamos Scientific Laboratory, Los Alamos, New Mexico 87545*

and

N. E. GEACINTOV and C. E. SWENBERG

*Department of Chemistry and The Radiation and Solid State Laboratory, New York University, New York, NY, 10003, USA*

Received 25 July 1977

Revised version received 19 September 1977

### 1. Introduction

Within the last few years there have been extensive investigations of the fluorescence from photosynthetic systems using picosecond lasers as excitation sources [1-11]. Such studies have established that the quenching of the prompt fluorescence, with increasing incident excitation intensity employing a single pulse, arises primarily from singlet-singlet exciton annihilation [2,3,7-9]. When the mode of excitation consists of a train of pulses or of a microsecond laser pulse, there exists additional quenching of the fluorescence quantum yield arising from long-lived quenchers, presumably triplet excitons [2,3,10], which either arise from intersystem crossing from the singlet manifold or from random recombination of electrons and holes formed from the autoionization final state channel of singlet fusion [8]. Recently, Geacintov et al. [8] have shown that the quantum yield quenching at emission wavelengths of 685 nm and 735 nm were identical, within experimental error, when single picosecond excitation pulses were employed. This identity in the quenching curves was interpreted in terms of the tripartite fluorescence model with bimolecular singlet fusion occurring exclusively within the light harvesting antenna system. Strong support for this interpretation was provided by the observation of an intensity-independent (for intensities below  $10^{16}$  photons  $\text{cm}^{-2}$  per pulse)

lifetime for the 735 nm emission [11]. Presumably, singlet fusion reactions are either inoperative or inefficient within the PS I antenna chlorophyll molecules, at least for intensities below  $10^{15}$  photons  $\text{cm}^{-2}$  per pulse. Within the light harvesting and PS II antenna pigments which give rise to the 685 nm emission, singlet exciton fusions do give rise to a strong decrease of the fluorescence lifetime with increasing intensity. It was concluded that the pigments which are responsible for the 735 nm emission derive their energy by singlet exciton transfer from the light harvesting system and not by direct photon absorption at 530 nm. In this paper we measure the risetime for the 735 nm emission and identify this time lag with the transfer rate from the light harvesting system to the PS I pigment molecules which give rise to the 735 nm fluorescence band at low temperatures.

### 2. Materials and methods

The experimental arrangement for fluorescence lifetime measurements was similar to that reported previously [3]. A 1060 nm, 30 ps pulse was selected from the pulse train emitted by a modelocked Nd:YAG laser, frequency shifted to 530 nm by passage through a KDP crystal, and then was allowed to excite the spinach samples. The samples, chloroplasts prepared from spinach leaves as described in [12], were

contained in a high optical quality 2 mm thick cuvette, maintained at 77°K within an optical dewar. The sample was illuminated uniformly, and the fluorescence was collected onto the slit of an Electro-photronics ICC 512 (S-20 response) streak camera with *f*/1 optics. The temporal rise and decay profiles for both the 690 nm and 735 nm fluorescence were obtained at 77°K. This was accomplished by using a narrow band pass filter at 735 nm to isolate the PS I fluorescence, whereas the PS II and light harvesting antenna pigment emission was differentiated by means of a 690 nm narrow band pass filter. In addition, appropriate filters further rejected the 530 nm radiation from the streak camera. Fluorescence streaks were imaged onto a SSR silicon vidicon optical multi-channel analyzer and then displayed on an oscilloscope after each shot. Shots could be accumulated on a Nicolet signal averager, thereby allowing detection at lower excitation intensities and hence averting exciton annihilation effects and also greatly improving the signal-to-noise ratio. Because there is considerable variation from shot to shot in the start of the streak due to electrical jitter, a reference point in time was established by allowing a weak green pulse, which bypasses the sample, to enter the streak camera a few hundred picoseconds before the arrival of the fluorescence. The zero time for the fluorescence onset and the excitation pulse shape characteristics about the zero time position could be determined by examining 530 nm light scattered off a dummy sample cuvette.

### 3. Results

As shown in fig. 1, the 735 nm emission continues to rise after termination of the excitation pulse, whereas the 690 nm emission rises abruptly with characteristics expected from the pulse shape. The risetime of the 735 nm fluorescence, taken from the 10% to 90% of peak intensity, was measured to be  $140 \pm 40$  ps, an average obtained from six separate experimental runs, each of about 30 shots. This risetime was observed over a wide range of incident intensities, from  $10^{13}$  to  $2 \times 10^{14}$  photons  $\text{cm}^{-2}$ . In fig. 1 the risetime of the 735 nm emission is comparable to the falltime of the 690 nm emission. However,

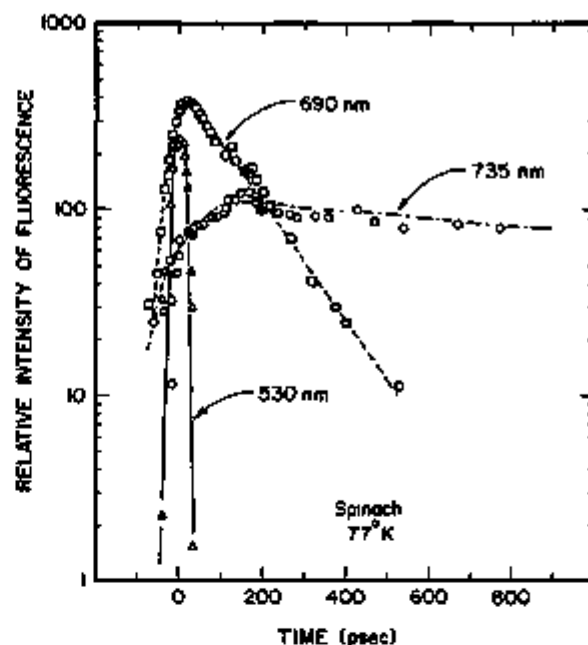


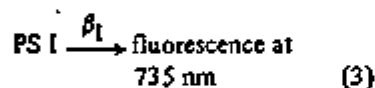
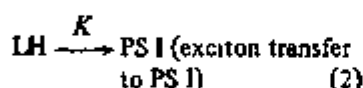
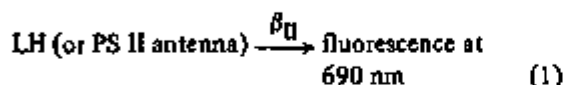
Fig. 1. Time resolved fluorescence from spinach chloroplasts at a temperature of 77°K and an incident intensity of  $2 \times 10^{14}$  photons  $\text{cm}^{-2}$ . Emission at 690 nm rises promptly, following 530 nm excitation pulse, whereas emission at 735 nm rises much more slowly.

at intensities of  $10^{13}$  photons  $\text{cm}^{-2}$  or lower, where the decay time of the 690 nm emission was measured to be about 900 ps, the risetime of the 735 nm emission remained near 140 ps. Thus, the 735 nm risetime does not correspond to the decay of the 690 nm fluorescence. The decay time of the 735 nm emission at low intensities was near to 1.5 ns, close to that reported previously. The risetime result at 735 nm, however, is in sharp conflict with the results of Yu et al. [13] obtained with high intensity pulse trains. We interpret their measurement of an abrupt rise as due to the generation of long-lived transient quenchers [14] by the pulse train and subsequent annihilation effects. Nor does our data at 690 nm agree with that observed previously by Seibert and Alfano [15,16]. Their identification of two peaks in their data [15], not observed by us, as originating from PS I (risetime  $\leq 10$  ps, lifetime  $\leq 10$  ps) and PS II (risetime 90 ps, lifetime 210 ps) leads to opposite conclusions than does this paper. Their data, like that of Yu et al. [13] was also obtained with high intensity pulse train

excitation and has lately come under much criticism [2,3,8,13,14].

#### 4. Discussion

The slower risetime of the 735 nm PS I fluorescence as compared to the risetime of the 690 nm PS II and light harvesting (LH) pigment fluorescence is consistent with our previous conclusion [11] that the 735 nm emitting pigment system derives its energy by exciton transfer from the LH pigments. An expression for the time dependence of the 735 nm fluorescence can be derived based on these considerations and which can be summarized by the following steps.



If we denote the exciton density in PS I by  $n_{\text{I}}$ , and denote the exciton density within the LH pigments by  $n_{\text{II}}$ , then the time dependence of these quantities is described by

$$\frac{dn_{\text{I}}}{dt} = K n_{\text{II}}(t) - \beta_{\text{I}} n_{\text{I}}(t) \quad (4)$$

$$\frac{dn_{\text{II}}}{dt} = G(t) - (\beta_{\text{II}} + K) n_{\text{II}}(t) \quad (5)$$

where  $G(t)$  denotes the laser pulse generation source and  $K$ ,  $\beta_{\text{I}}$  and  $\beta_{\text{II}}$  are the rate constants defined by (1)-(3). For the sake of simplicity, these equations do not include details of Kitajima and Butler's tripartite fluorescence model such as separate emission bands from LH and PS II antenna pigments, energy transfer between these two systems [17,18], and the possibility that the 735 nm fluorescence is due to a chlorophyll from C-705 which derives its energy by exciton transfer from PS I antenna pigments [19].

Treating the incident source as a delta function, a good approximation because the risetime of the

735 nm emission is at least a factor of five-times the excitation pulse width, eq. (4) and eq. (5) are easily solved:

$$n_{\text{II}}(t) = n_{\text{II}}(0) e^{-(\beta_{\text{II}} + K)t} \quad (6)$$

$$n_{\text{I}}(t) = \frac{K n_{\text{II}}(0)}{\beta_{\text{I}} - (\beta_{\text{II}} + K)} [e^{-(\beta_{\text{II}} + K)t} - e^{-\beta_{\text{I}}t}] \quad (7)$$

The first term of eq. (7) characterizes the risetime of the 735 nm fluorescence ( $140 \pm 40$  ps), while the second term characterizes the decay ( $\beta_{\text{I}}^{-1} \approx 1.5$  ns).

Equations (6) and (7) are the most simple representations of the time dependence of the 685-690 nm and the 735 nm fluorescence emissions, respectively. The data in fig. 1 indicates that  $(\beta_{\text{II}} + K)^{-1} = 140 \pm 40$  ps, which implies, according to eq. (6), that the lifetime of the fluorescence at 690 nm should display the same time dependence. However, this is not the case, since the fluorescence decay time at  $\sim 690$  nm is about 800 ps [20]. Furthermore, below intensities of  $\sim 10^{15}$  photons  $\text{cm}^{-2}$  per pulse, the 735 nm fluorescence risetime remains constant, within experimental error, while the lifetime of the 685-690 nm fluorescence varies strongly with intensity due to exciton annihilation.

At higher excitation intensities, when the quadratic term must be included in eq. (1) it can be shown [21] that the appropriate modification of eq. (6) and eq. (7) corresponds to replacing  $\beta_{\text{II}}$  by  $\beta_{\text{II}} + c\gamma_{\text{ss}}I$  where  $\gamma_{\text{ss}}$  is the singlet fusion rate,  $\alpha$  ( $\text{cm}^{-1}$ ) is the absorption coefficient,  $I$  is the incident intensity (photons  $\text{cm}^{-2}$ ), and  $c$  is a numerical constant  $\approx 0.6$ . Hence when the excitation intensity of the single pulse obeys the equation

$$I > \frac{K - \beta_{\text{II}}}{c\gamma_{\text{ss}}\alpha} \quad (8)$$

a decrease in the risetime of the 735 nm fluorescence is predicted. We indeed observe such a decrease when the excitation intensity exceeds  $I = 10^{15}$  photons  $\text{cm}^{-2}$  per pulse.

The lack of a correlation between the 735 nm fluorescence risetime and the 690 nm decay time for  $I < 10^{15}$ , and the decrease in the 735 nm risetime for  $I > 10^{15}$  photons  $\text{cm}^{-2}$  per pulse, can be understood

in terms of the following model for the LH pigment system.

There are two types of LH pigments; in one of these denoted by LH(1), the chlorophyll molecules are tightly coupled to the PS I pigment system with  $K > \beta_{II}$ , i.e., the exciton lifetime is mainly determined by energy transfer to PS I, with  $K^{-1} \approx 140$  ps. The fluorescence yield from this system is low.

The second type of LH pigments, LH(2), consists of chlorophyll molecules which are less tightly coupled to PS I (possible because of a large physical separation) and which decay mainly by the rate constant  $\beta_{II} \approx (800 \text{ ps})^{-1}$ . The fluorescence yield from this system is relatively high. The 735 nm rise-time is thus unaffected by exciton annihilation within LH(1) up to intensities of  $I \sim 10^{15}$  photons  $\text{cm}^{-2}$  per pulse when the annihilation rate begins to compete with the rapid LH(1)  $\rightarrow$  PS I transfer rate characterized by the rate constant  $K$ .

This model of the fluorescence of spinach chloroplasts at low temperatures is depicted in fig.2. It is capable of accounting for all of the observations

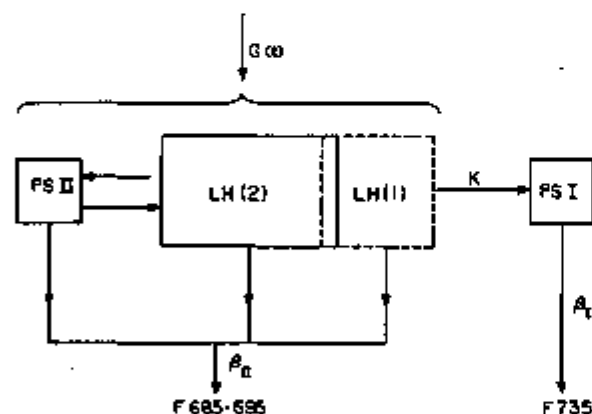


Fig.2. Modified Tripartite Fluorescence Model [17,18]. The source term  $G(t)$ , excites both the light harvesting aggregate, LH, and the PS II chlorophylls. Fluorescence emission corresponding to LH, PS II, and PS I are at 685, 695 and 735 nm [16-18], however, no differentiation is made between the PS II and LH emission in this work. The light harvesting pigment system is presumed to consist of two fractions: in LH(1) the light harvesting pigments are closely associated with PS I and energy transfer occurs with rate constant  $K$ ; in LH(2) the pigments are not closely connected to PS I and excitons decay mainly with the rate constant  $\beta_{II}$ . The decay rate of the 735 nm fluorescence, which reflects the exciton density in PS I [17], is denoted by  $\beta_I$ .

presented here, as well as for the identity of the quenching curves at 685 nm and 735 nm [11].

It is possible that LH(1) represents a relatively small fraction of the total light harvesting pigments. This is indicated by the fact that the 735 nm fluorescence reflects the exciton density within the light harvesting pigments [11], which is not primarily determined by the LH  $\rightarrow$  PS I energy transfer rate constant  $K$ , but is determined by the unimolecular rate  $\beta_{II}$  and the bimolecular exciton annihilation rate. Thus, excitons appear to communicate between LH(1) and LH(2), but the LH(2)  $\rightarrow$  LH(1)  $\rightarrow$  PS I pathway does not characterize the major pathway for excitons within the overall LH pigment system.

The model shown in fig.2 predicts that careful measurements of fluorescence decay curves at low intensities of excitation (no bimolecular exciton annihilation) may reveal two components: a fast but weak component due to exciton decay by energy transfer from LH(1)  $\rightarrow$  PS I characterized by a lifetime of  $K^{-1}$ , and a longer more intense component, which is characterized by  $\beta_{II}$ .

#### Acknowledgements

We thank K. Winn for experimental assistance and R. C. Hyer for sample preparation. We gratefully acknowledge Dr J. Breton for stimulating discussions. This work was supported by the US Energy Research and Development Administration. The portion of this work performed at New York University (N. E. Geacintov and C. E. Swenberg) was supported by National Science Foundation Grant PCM 76-14359.

#### References

- [1] Shapiro, S. L., Kollman, V. H. and Campillo, A. J. (1975) FEBS Lett. 54, 358-362.
- [2] Campillo, A. J., Shapiro, S. L., Kollman, V. H., Winn, K. R. and Hyer, R. C. (1976) Biophys. J. 16, 93-97.
- [3] Campillo, A. J., Kollman, V. H. and Shapiro, S. L. (1976) Science 193, 227-229.
- [4] Beddard, G. S., Porter, G., Tredwell, C. J. and Barber, J. (1975) Nature 258, 166-168.
- [5] Porter, G., Synowicz, J. A. and Tredwell, C. J. (1977) Biochim. Biophys. Acta 459, 329-336.
- [6] Seader, G. F. W., Barber, J., Harris, L., Porter, G. and Tredwell, C. J. (1977) Biochim. Biophys. Acta 459, 390-405.

- [7] Swenberg, C. E., Geacintov, N. E. and Pope, M. (1976) *Biophys. J.* 16, 1447-1451.
- [8] Geacintov, N. E., Breton, J., Swenberg, C. E. and Pailletin, G. *Photochem. Photobiol.* in press.
- [9] Campillo, A. J., Hyer, R. C., Monger, T. G., Parson, W. W. and Shapiro, S. L. (1977) *Proc. Natl. Acad. Sci. USA* 74, 1997-2001.
- [10] Geacintov, N. E. and Breton, J. (1977) *Biophys. J.* 17, 1-15.
- [11] Geacintov, N. E., Breton, J., Swenberg, C. E., Campillo, A. J., Hyer, R. C. and Shapiro, S. L. (1977) *Biochim. Biophys. Acta* 477, 306.
- [12] Breton, J., Roux, E. and Whitmarsh, J. (1975) *Biochem. Biophys. Res. Commun.* 64, 1274-1277.
- [13] Yu, W., Pellegrino, F. and Alfano, R. R. (1977) *Biochim. Biophys. Acta* 460, 171-181.
- [14] Breton, J. and Geacintov, N. E. (1976) *FEBS Lett.* 69, 86-89.
- [15] Seibert, M. and Alfano, R. R. (1974) *Biophys. J.* 14, 269-281.
- [16] Seibert, M., Alfano, R. R. and Shapiro, S. L. (1973) *Biochim. Biophys. Acta* 292, 493-495.
- [17] Kitajima, M. and Butler, W. (1975) *Biochim. Biophys. Acta* 408, 297-305.
- [18] Butler, W. L. and Kitajima, M. (1975) *Biochim. Biophys. Acta* 396, 72-85.
- [19] Butler, W. L. (1977) *Ann. Rev. Plant. Physiol.* in press.
- [20] Hervo, G., Pailletin, G. and Thiery, J. (1975) *J. Chim. Physique* 72, 761-766.
- [21] Campillo, A. J., Hyer, R. C., Shapiro, S. L. and Swenberg, C. E. (1977) *Chem. Phys. Lett.* 48, 495-500.

## A SINGLE PULSE PICOSECOND LASER STUDY OF EXCITON DYNAMICS IN CHLOROPLASTS

NICHOLAS E. GEACINTOV\*, JACQUES BRETON, CHARLES E. SWENBERG\*  
and GUY PAILLOTIN

Service de Biophysique, Département de Biologie, Centre d'Etudes Nucléaires de Saclay,  
BP 2, 91190 Gif-Sur-Yvette, France

(Received 6 April 1977; accepted 11 July 1977)

**Abstract**—Using single picosecond laser pulses at 610 nm, the fluorescence yield ( $\phi$ ) of spinach chloroplasts as a function of intensity ( $I$ ) ( $10^{12}$ – $10^{16}$  photons/pulse/cm<sup>2</sup>) was studied in the range of 21–300 K. The quantum yield decreases with increasing intensity and the  $\phi$  vs  $I$  curves are identical at the emission maxima of 685 and 735 nm. This result is interpreted in terms of singlet exciton–exciton annihilation on the level of the light-harvesting pigments which occurs before energy is transferred to the Photosystem I pigments which emit at 735 nm.

The yield  $\phi$  is decreased by factors of 12 and 43 at 300 and 21 K, respectively. The shapes of the  $\phi$  vs  $I$  curves are not well accounted for in terms of a model which is based on a Poisson distribution of photon hits in separate photosynthetic units, but can be satisfactorily described using a one-parameter fit and an exciton–exciton annihilation model. The bimolecular annihilation rate constant is found to be  $\gamma = (5\text{--}15) \times 10^{-9} \text{ cm}^2 \text{ s}^{-1}$  and to exhibit only a minor temperature dependence. Lower bound values of the singlet exciton diffusion coefficient ( $\geq 10^{-2} \text{ cm}^2 \text{ s}^{-1}$ ), diffusion length ( $\geq 2 \times 10^{-6} \text{ cm}$ ) and Förster energy transfer rates ( $\geq 3 \times 10^{10} \text{ s}^{-1}$ ) are estimated from  $\gamma$  using the appropriate theoretical relationships.

### INTRODUCTION

Picosecond lasers have now been used for several years in studies of the fluorescence properties of chlorophyll *in vivo* (Seibert and Alfano, 1974; Yu *et al.*, 1975; Paschenko *et al.*, 1975; Beddard *et al.*, 1975; Campillo *et al.*, 1976a, b; Breton and Geacintov, 1976). Unusually short fluorescence decay times have been reported with the use of ps laser pulses for excitation, which do not agree well with values obtained by more standard techniques utilizing low intensity excitation sources (Hervo *et al.*, 1975; Briantais *et al.*, 1972; Tumerman and Sorokin, 1967). It has been shown, however, that the fluorescence can be strongly quenched when intense laser pulses (Mauzerall, 1976a, b; Campillo *et al.*, 1976a, b; Breton and Geacintov, 1976; Geacintov and Breton, 1977; Monger *et al.*, 1976) or  $\mu\text{s}$  pulses (Delosme, 1972; Den Haan *et al.*, 1974) are utilized. This quenching which is attributable to exciton–exciton annihilation processes gives rise to the short fluorescence lifetimes determined with ps lasers and accounts for the discrepancies in lifetimes as determined by standard phase fluorimetric or photon counting techniques and ps laser techniques (Campillo *et al.*, 1976b).

We have shown elsewhere (Breton and Geacintov, 1976; Geacintov and Breton, 1977) that the fluorescence at 735 nm attributable to Photosystem I pigments is more strongly quenched than the 685 nm fluorescence (attributed to light harvesting and Pho-

tosystem II pigments) when trains of ps pulses are used. This preferential quenching of the 735 nm emission band leads to differences in fluorescence spectra determined with ps pulse trains of either low or high intensities, and is attributed to the preferential build-up of long-lived quenchers in Photosystem I.

In this paper we show that such a change in the fluorescence spectra does not occur when single ps pulses are used for excitation, although strong quenching of equal magnitude at both 685 and at 735 nm is observed. This property is unchanged in the temperature range of 21–300 K. These results are interpreted within the framework of Butler and Kitajima's (1974, 1975) tripartite model of the fluorescence of chloroplasts at low temperatures.

The shapes of the fluorescence quenching curves (yield vs pulse intensity) are interpreted in terms of a kinetic singlet exciton–exciton annihilation model proposed by Swenberg *et al.* (1976a). Using theoretical relationships relating the bimolecular annihilation coefficients  $\gamma$  to the exciton diffusion coefficient  $D$ , diffusion length  $l$ , and the energy transfer rates  $F$ , lower bounds of these quantities are estimated.

### MATERIALS AND METHODS

Chloroplasts isolated from whole spinach leaves were suspended in a sucrose (0.4 M)-Tris (20 mM, pH 8.2)-KCl (20 mM) buffer solution. A drop of this suspension was squeezed between two microscope slide cover slips so that the effective sample thickness was between 0.05 and 0.2 mm. The optical density was kept between 0.15 and 0.20 at the absorption maximum (680 nm); thus the optical density at the wavelength of excitation (around 610 nm) was always kept below 0.04. Cooling of the sample was

\* Chemistry Department and Radiation and Solid State Laboratory, New York University, New York, New York 10003.

achieved by means of a temperature regulated nitrogen or helium gas flow in a cryostat (stability  $\pm 1^\circ\text{C}$ ).

The fluorescence was excited with a mode-locked dye laser (Electro-Photonics model 33) operated with rhodamine 6G, while mode-locking was achieved with the dye 3,3'-diethyl oxadiazocyanine iodide (DODCI). The output of the mode-locked laser consisted of a train of about 300 pulses, 5–10 ps in width and spaced about 5 ns apart. The pulses were best defined in width and in amplitude within the central part of the pulse train and a pocket cell with a 3 ns gate was utilized to select a single pulse from this area of the train.

A highly attenuated portion of the excitation beam was focused onto the entrance slit of a streak camera (Electro-Photonics ICC 512). The quality of the pulse was verified for each laser shot by means of the streak camera. The data were collected only if the intensity of the selected pulse was at least 100 times larger than the intensity of the neighboring two pulses within the train.

The fluorescence spectra were recorded by means of an  $f/3.5$  spectrograph-optical multichannel analyzer (OMA) arrangement which allowed the recording of complete fluorescence emission spectra with a single pulse laser shot. The fluorescence spectra were stored in digital form in the memory of the OMA which allowed for background subtraction and signal averaging as necessary. Calibrated neutral density filters were used to attenuate the excitation pulse.

The relative fluorescence quantum yield as a function of the excitation energy was determined by dividing the digital values of the fluorescence intensities at 685 and 735 nm (recorded by the OMA) by the laser output energy. The output energy of the laser was measured by using a beam-splitter, which reflected a portion of the total energy onto the detector head of an energy meter (model R 3230, Laser Precision Corporation). The fluorescence readings were corrected for a nonlinearity of the OMA as previously described (Breton and Geacintov, 1976). At low excitation intensities the sensitivity of the OMA was

insufficient and the OMA Vidicon tube was replaced by a specially wired 56TVP Amperex photomultiplier tube. In order to insure linearity of response of this tube capacitors were placed across the last few dynodes and the dynode resistors were chosen to provide a smaller voltage drop across these last dynodes. The linearity of this tube was carefully checked over the entire range of light intensities used, a number of fluorescence quenching curves were determined using both the photomultiplier tube and the OMA system to ensure that the same results were obtained with both systems. When the photomultiplier tube was used, the following interference filters were placed in front of the spectrograph: (1) for 735 nm viewing an interference filter with a maximum transmittance at 728 nm, half maximum bandwidth 7 nm, (2) for 685 nm viewing the maximum was 680 nm, half-band width 4 nm, (3) in some experiments, particularly at the lowest intensities, a cut-off filter only (transmittance above 665 nm) was employed. This was permissible, because no difference in the relative quenching as a function of emission wavelength was observed using single ps laser pulses, the fluorescence emission spectra did not change as a function of the energy of the single ps pulses. This is in contrast to our earlier observations where ps pulse trains or  $\mu\text{s}$  pulse excitation was used (Breton and Geacintov, 1976; Geacintov and Breton, 1977).

The laser beam was focused onto the sample and the fluorescence was in turn focused onto the entrance slit (0.5 mm) of the spectrograph. The area of the sample which was excited, as well as the intensity profile of the pulse was estimated by placing the OMA detector head at the location of the sample. A strongly attenuated pulse was then imaged on the OMA detector which consists of a matrix of independent photodiodes spaced about  $8\ \mu\text{m}$  apart. Vertical arrays of diodes are read with an electron scanning beam whose resolution is about  $25\ \mu\text{m}$  (Fig. 1a). The contents of each vertical array is summed, digitized and then stored in the memory of the OMA console. All of the energy received by each vertical array of diodes

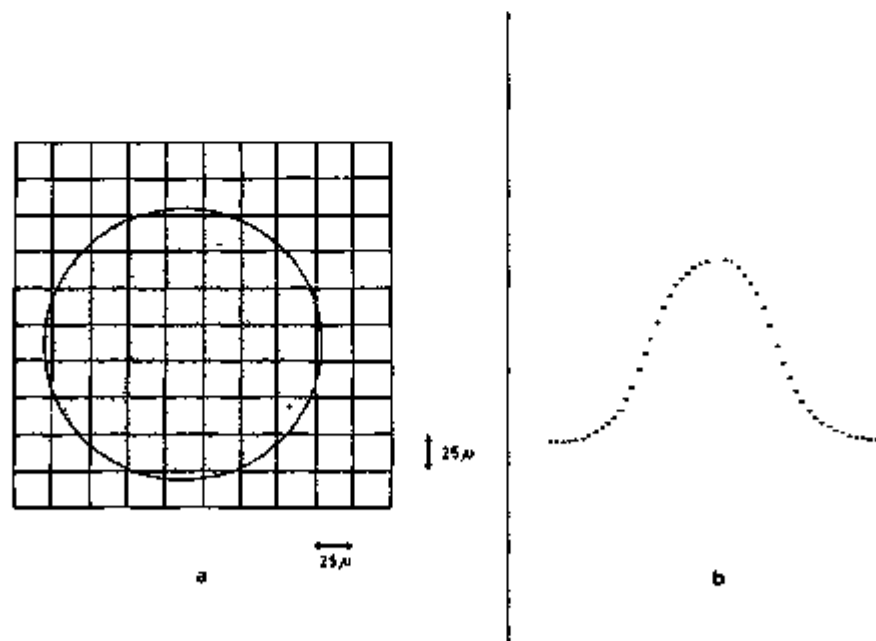


Figure 1 (a) Schematic representation of the OMA detector head which consists of a large array of photodiodes which are read by a scanning electron beam (about  $25\ \mu\text{m}$  resolution). A hypothetical circular light beam is superimposed on this array of diodes. (b) Experimentally determined laser beam profile-OMA. The vertical scale represents relative energy while the points are spaced about  $25\ \mu\text{m}$  apart.



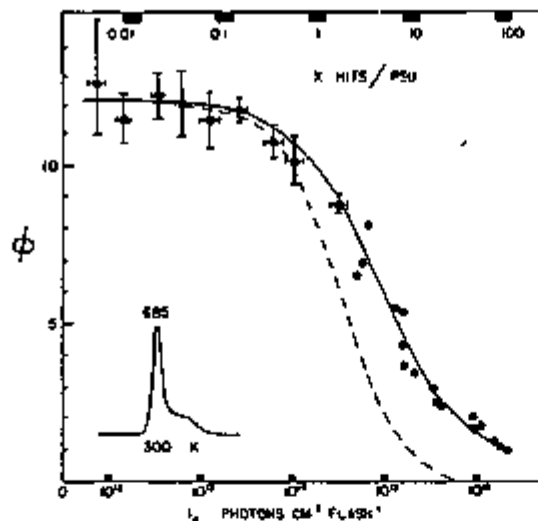


Figure 2 Relative fluorescence yield  $\phi$  as a function of the incident laser pulse intensity at 300 K.  $\times$  represents the number of photon hits per photosynthetic unit consisting of 200–300 molecules. A typical fluorescence spectrum obtained with the OMA-spectrograph is shown in the insert (maximum at 685 nm). — Theoretically calculated quenching curves according to Eq. 7 (see also the legend of Table 1), lake model of exciton quenching, ——— theoretically calculated quenching curve using the Poisson distribution of photon hits per photosynthetic unit (300 chlorophyll molecules/unit), Eq. 5, the puddle model. The vertical scale is in arbitrary units and the  $\phi$  values for the two wavelength regions were normalized with respect to each other.

was thus integrated. A typical profile of the laser pulse obtained in this way is shown in Fig. 1b, where the horizontal spacing between the dots is 25  $\mu\text{m}$  and where the amplitude represents the energy integrated over the corresponding column of photodiodes. Two different measure-

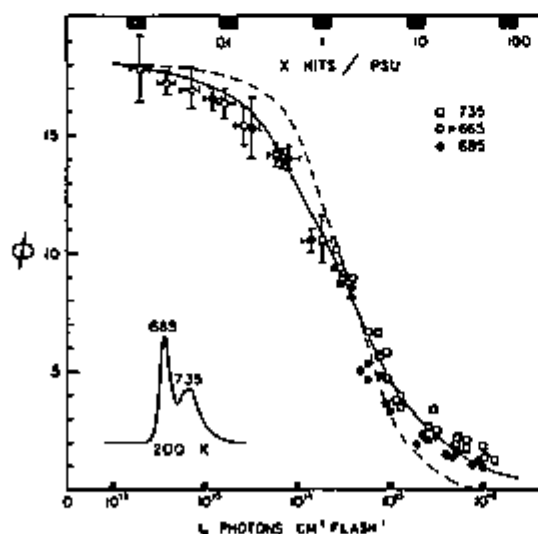


Figure 3 Relative fluorescence yield  $\phi$  as a function of the incident laser pulse intensity at 200 K. The data were obtained viewing different wavelength regions (685 or 735 nm), or the entire emission (using a 665 nm cutoff filter). Same definitions of  $X$  and the solid and dashed curves as in Fig. 2.

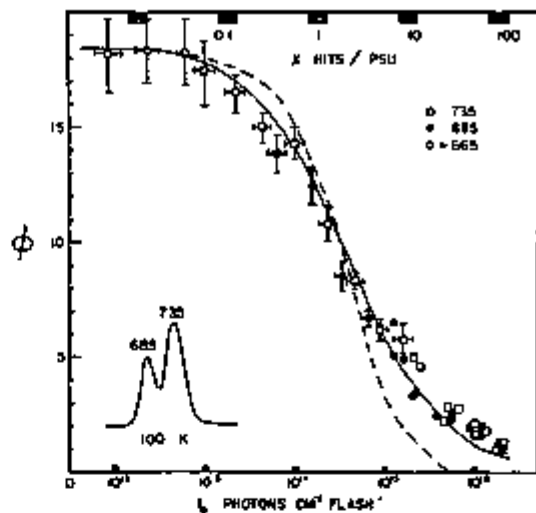


Figure 4 Relative fluorescence yield  $\phi$  as a function of the incident laser pulse intensity at 100 K. See captions of Figs. 2 and 3 for other details.

ments with the plane of the detector head rotated by 90° around the normal to this plane allowed us to probe the non circular shape of the laser beam (it was elliptical in shape) and to determine the area ( $4 \pm 1 \text{ mm}^2$ ) of the excited region of the sample.

## RESULTS

The fluorescence quantum yields (corresponding to the experimentally determined fluorescence intensity divided by the pulse energy), in relative units, as a function of the energy of the single ps pulses, are plotted in Figs. 2–5. At room temperature, only the results for the 685 nm fluorescence are plotted, since the contribution of the PS I pigment system to the overall emission is believed to be very small at 300 K. (Good-

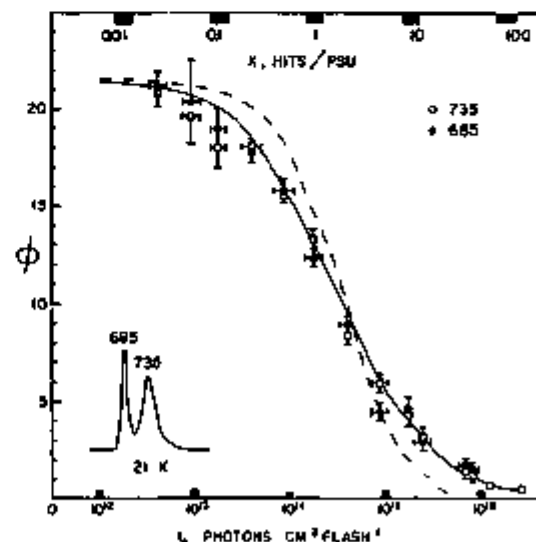


Figure 5 Relative fluorescence yield  $\phi$  as a function of the incident laser pulse intensity at 21 K. See captions of Figs. 2 and 3 for other details.

heer, 1972) At the other three temperatures (200, 100 and 21 K) the emission attributed to PS I and PS II is well resolved (Goedheer, 1972, Goedheer and Verhulsdonk, 1970, Cho *et al.*, 1966, 1970) Butler and Kitajima (1974, 1975) have recently proposed a tripartite model for the fluorescence of spinach chloroplasts at low temperatures. The 685 nm emission band is believed to emanate from light harvesting chlorophyll-protein complexes, which are capable of feeding energy to both PS I and PS II pigments. The 735 nm emission band is attributed to PS I, and a maximum, or shoulder, appearing at 695 nm is attributed to antenna pigment molecules associated with PS II. Typical emission spectra recorded with the OMA-spectrograph using a 0.5 mm slit (dispersion 26 nm/mm) are also shown in Figs 2-5. It should be noted that with this slit width, the 685 and 695 nm bands are not resolved. Using narrower slit widths however, these two maxima are clearly evident and such a spectrum obtained with our OMA system is shown elsewhere (Geacintov *et al.*, 1977). In our experiments described here, no distinction is made between the 685 and 695 nm emission peaks and this fluorescence will be collectively referred to as 685 nm, or PS II fluorescence.

Within experimental error, no differences in the fluorescence yield curves between the 685 and 735 nm emission bands can be discerned. This result is in sharp contrast to the case when ps pulse trains or  $\mu$ s excitation pulses are utilized (Geacintov and Breton, 1977).

#### DISCUSSION

A number of aspects of these results need to be interpreted. Perhaps the most striking result is the fact that there is no difference in the fluorescence yield curves at 685 and at 735 nm, whereas it is well known that these two emissions originate from different pigment systems, give rise to differences in low intensity fluorescence induction curves (Murata, 1968, Kitajima and Butler, 1975), and exhibit different singlet exciton lifetimes as determined from fluorescence decay curves (Hervo *et al.*, 1975).

Furthermore, the shape of the fluorescence yield curves as a function of the pulse energy can be interpreted in terms of either (a) the Poisson saturation model which is similar to the model proposed by Mauzerall (1976a, b) and (b) homogeneous distribution of excitons throughout the photosynthetic units and singlet-singlet exciton annihilation as described by continuum diffusion kinetics (Swenberg *et al.*, 1976a). Exciton-exciton annihilation has been invoked by Campillo *et al.* (1976a, b) to account for yield vs intensity curves and for the intensity dependence of fluorescence lifetimes in *Chlorella*.

Utilizing the reasonable assumption that the fluorescence quenching is due to the diffusive encounter and mutual annihilation of singlet excitons, informa-

tion about the diffusion parameters of excitons and their temperature dependence can be obtained.

#### Interpretation of the quenching curves

Delosme (1972) and Den Haan *et al.* (1974) using  $\mu$ s duration light flashes, Mauzerall (1976a) using ns laser flashes and Campillo *et al.* (1976a) using ps laser pulses were the first to report that fluorescence yields decrease when the number of photons absorbed per flash are substantially larger than the number required to saturate photosynthesis.

Mauzerall (1976a, b) interpreted the yield vs intensity curves in terms of Poisson distributions. When the excitations are confined domains and when the fluorescence yield depends on the number of excitations per domain, Poisson statistics are appropriate. Such a model is useful within the context of the "puddle" model of Robinson (1967) in which the excitons are confined to diffuse within one particular photosynthetic unit (PSU). The PSU is usually defined as one reaction center, or trap and its associated antenna pigment molecules. However, a domain to which the excitons are confined can also consist of 3-4 traps (Mauzerall, 1976b, Paillon, 1976). In the opposite picture, the reaction centers are distributed among a uniformly large matrix of pigments. The exciton generated within any one particular photosynthetic unit can diffuse to other units, its range being limited essentially by its lifetime. This has been referred to as the "lake" model (Robinson, 1967), or the multicentral or statistical model (Malkin, 1974). In the lake model, the creation and annihilation of excitons can be described by a standard kinetic equation (Swenberg *et al.*, 1976a). Poisson statistics do not have to be taken into account as long as the exciton distribution is completely randomized by diffusive processes on time scales which are short as compared to characteristic annihilation times (see below).

In the puddle model, or confined domain case, the annihilation of excitons gives rise to a change in the exciton density in a discontinuous manner. Since the PSU is generally considered to consist of several hundred molecules only, the use of standard kinetic equations is questionable. Using an appropriate Poisson saturation model, in which the first photon hit per PSU (or domain) gave a finite fluorescence quantum yield  $\phi_1$ , and all subsequent hits contributed no fluorescence, Mauzerall (1976b) was able to fit his experimental data using the following equation:

$$\phi(x) = \phi_1 \frac{(1 - e^{-x})}{x} \quad (1)$$

$x$  is the average number of hits per unit,  $1 - e^{-x}$  is the probability that the units have been hit at least once. With the further assumption that the maximum variation in the observed fluorescence yield  $\phi$  as a function of  $x$  cannot exceed 90% of the total yield, Mauzerall obtained a satisfactory fit to the data in the case when the reaction centers are all closed (in

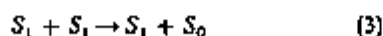
our experiments this was the case at low temperatures (thus the same considerations should apply).

We shall now attempt to fit our data to a Poisson distribution as well. In our experiments the fluorescence quantum yield varied by as little as a factor of 12 (at 300 K) with no appearance of leveling out of  $\phi(x)$  at intensities above the maximum ones used here, and by as much as a factor of 43 (at 21 K). This amounts to a quenching of about 83–98% of the total fluorescence. In our case it therefore does not appear to be justified to assume *a priori* that a fraction of the fluorescence remains unquenched.

We first consider Poisson statistics allowing for the possibility of exciton–exciton annihilation in each domain wherever there are two or more hits per domain. If we assume that this annihilation is very efficient, and that the quantum yield for each domain hit by 1, 2, 3...  $n$  photons is  $\phi_n$ , then

$$\phi_n = \frac{\phi_1}{n} \quad (2)$$

where  $\phi_1$  is the yield when there is only one hit per domain ( $n = 1$ ). These considerations follow from the exciton annihilation model



since the collision of two singlet excitons ( $S_1$ ) removes one exciton ( $S_0$  denotes a ground state chlorophyll molecule). A domain receiving  $n$  hits will have at the very least a probability of  $1/n$  to emit fluorescence with an intrinsic yield  $\phi_1$ . It should be noted that this annihilation picture is equivalent to Mauzerall's (1976b) assumption that the quantum yield of a unit is  $\phi_1$  for the first photon hit, while all subsequent hits produce a quantum yield of zero.

If the average number of hits is  $x$ , then the probability that a given unit has received  $n$  hits is given by the Poisson distribution

$$P_n(x) = \frac{(x)^n e^{-x}}{n!} \quad (4)$$

The overall quantum yield for a given number of average hits  $x$  is  $\phi_p(x)$  in the puddle model or domain case and is given by

$$\begin{aligned} \phi_p(x) &= \sum_{n=1}^{\infty} \frac{\phi_1}{n} \frac{P_n(x)}{1 - P_0(x)} \\ &= \frac{1}{1 - P_0(x)} \left\{ \phi_1 P_1 + \frac{\phi_1}{2} P_2 + \dots \right\} \quad (5) \end{aligned}$$

where  $1 - P_0(x) = 1 - e^{-x}$  is the probability that the units have been hit at least once and represents a normalization factor in Eq. 5.

If singlet–singlet annihilation leads to ionization of bulk chlorophyll molecules ( $S_1 + S_1 \rightarrow S^+ + S^-$ , where  $S^+$  and  $S^-$  correspond to chlorophyll ions), then the extent of quenching within the context of the puddle model will be even larger than predicted

by Eq. 5. In that case, all of the terms except the first one in Eq. 5 would be zero.

The number of hits per pigment molecule at any given intensity can be calculated from the values of the extinction coefficient of chlorophyll *in vivo* given by Schwartz (1972). The only assumption which must be made in calculating  $\phi_p(x)$  is the number of molecules in a photosynthetic unit. As a typical value, we have assumed a unit size of 300 pigment molecules. The number of hits per unit thus calculated is indicated by the black squares on the top of Figs. 2–5. In order to indicate how the calculated number of hits varies with unit size, the left edge of each black square on the top parts of Figs. 2–5 indicates the calculation for 300 molecules/PSU, while the right hand side indicates a calculation for 200 molecules/PSU. The calculation of  $\phi_p(x)$  thus requires only one parameter, the size of the PSU. In these calculations we have neglected the effect of the depletion of the ground state. At an incident intensity of  $5 \times 10^{15}$  photons  $\text{cm}^{-2}$ , the ground state depletion is 10%, rises to 20% at  $10^{16}$  photons  $\text{cm}^{-2}$  and to 36% at the maximum intensity of  $2 \times 10^{16}$  photons  $\text{cm}^{-2}$ . As is evident from the logarithmic intensity scale in Figs. 2–5 this neglect is justified throughout most of the intensity range studied for a comparison of the theoretical and experimental fluorescence yields.

The calculated curves according to the Poisson model Eq. 5 are plotted as the dashed curves in Figs. 2–5. We first note that if a quenching probability of less than maximum is assumed (i.e. if  $\phi_1/n < \phi_n < \phi_1$ ), this still would mean that the curves at 200, 100 and 21 K could not be fit to the experimental data in the  $x \approx 0.1$  to  $x = 2$  region. This is due to the fact that a decreased quenching efficiency would tend to raise the dashed curves, which are already above the experimental points in the  $0.1 < x < 2$  region. Since this is not the case for example at 300 K (Fig. 2), a special set of quenching efficiencies at the different values of  $n$  would have to be tried in order to obtain a satisfactory fit in this case.

Next, we consider the effect of varying the number of molecules per PSU. If more than 300 molecules per unit are assumed, the dashed curves should all be shifted to the left in Figs. 2–5. The extent of the leftward shift is larger, the larger the PSU. While this would produce a better fit at low intensities, the fit at the higher intensities would be worse. Similarly, if the assumption is made that there are less than 200 molecules per PSU, the dashed curves should be shifted to the right.

We thus conclude that the Poisson saturation model with the limited number of approximations, made here, does not well describe our experimental data. If ionization processes are important leading to a disappearance of both singlets, the quenching efficiencies will be larger than calculated by Eq. 5, but the basic conclusions will remain unchanged.

Table 1. Bimolecular rate constants inferred from fluorescence quenching curves

Temperature K	Z (cm <sup>2</sup> ) <sup>a</sup>	$\gamma/2k$ (cm <sup>2</sup> )	$\tau(\text{PS II})(\text{ns})^{**}$	$\gamma(\text{cm}^2 \text{s}^{-1})$
300	$(3 \pm 1) 10^{-13}$	$(2 \pm 0.6) 10^{-18}$	0.8	$(5.2 \pm 1.6) 10^{-9}$
200	$(9 \pm 2) 10^{-13}$	$(6.2 \pm 1.4) 10^{-18}$	0.8	$(15.6 \pm 4.0) 10^{-9}$
100	$(6 \pm 3) 10^{-13}$	$(4.4 \pm 2) 10^{-18}$	0.9	$(9.6 \pm 4.8) 10^{-9}$
21	$(9 \pm 3) 10^{-13}$	$(6.6 \pm 2) 10^{-18}$	1.1	$(12.0 \pm 4.0) 10^{-9}$

<sup>a</sup> The parameter Z was obtained from the fits to the data in Figs. 2-5 and is defined by a modified form of Eq. 7 namely  $\phi(I_0) = (\phi_0/ZI_0) \log(1 + ZI_0)$  where  $I_0$  (photons cm<sup>-2</sup> per pulse) is the experimentally determined incident intensity, whereas  $I_a$  (cm<sup>-3</sup>) in Eq. 7 is the number of absorbed photons.  $I_a$  can be calculated for a given  $I_0$  if the number of photons absorbed per cm<sup>3</sup> throughout the sample is constant (which is approximately correct for optical densities below ~0.05), from a knowledge of the extinction coefficient of chlorophyll at 610 nm (Schwartz, 1972), and the average pigment concentration *in vivo* (calculated to be about 0.1 M from the data provided by Park and Biggins, 1964). We thus find that at 610 nm  $I_0 = 10^{14}$  photons cm<sup>-2</sup> corresponds to  $I_a = 1.4 \times 10^{17}$  photons cm<sup>-3</sup>, giving  $\alpha(610 \text{ nm}) = 1400 \text{ cm}^{-1}$ ; this value was utilized in calculating values of  $\gamma/2k$  from the values of Z.

<sup>\*\*</sup> Values taken from Hervo *et al.* (1975).

We now turn to an interpretation of the data by a continuum type differential equation as previously suggested by Swenberg *et al.* (1976a):

$$\frac{dn(t)}{dt} = \alpha I(t) - kn - \frac{1}{2} \gamma n^2 \quad (6)$$

$n(t)$  denotes the time dependent singlet exciton density,  $\alpha$  (cm<sup>-1</sup>) is the absorption coefficient,  $I(t)$  (photons cm<sup>-2</sup> s<sup>-1</sup>) is the incident light intensity,  $k$  (s<sup>-1</sup>) is the unimolecular decay time of the singlet excitons in the low intensity limit, and  $\gamma$  (cm<sup>3</sup> s<sup>-1</sup>) is the bimolecular singlet exciton-exciton annihilation constant. The factor of 1/2 in the last term of Eq. 6 denotes the case where the final state channel consists of one singlet exciton which resulted from the mutual annihilation of two excitons.

The validity of Eq. 6 for singlet-singlet annihilations depends on several factors.

First, the excitons are assumed to be capable of diffusing freely within the photosynthetic membranes, from one unit to another (lake model). The size of the domains is assumed to be sufficiently large so that annihilations give rise to changes in exciton densities in a continuous manner, rather than in a discontinuous manner when a finite number of excitons are confined to a relatively small domain (this latter case will be treated in a future publication).

Furthermore, Eq. 6 assumes that annihilations do not take place before diffusive motion has completely randomized the distribution of excitons. If this is not the case, annihilation will occur before diffusion has taken place and some sort of a dependence on a Poisson distribution, or time dependent diffusion terms might be expected. If  $F$  is the molecule to molecule transfer rate, and  $\gamma n$  is a typical annihilation rate, the validity of Eq. 6 requires that  $F \gg \gamma n$ . Pailotin (1976) has estimated a lower limit of  $3 \times 10^{11} \text{ s}^{-1}$  for the nearest neighbor transfer rate. Campillo *et al.* (1976b) have shown that the fluorescence decay times at high ps pulse intensities are dominated by annihilation ( $\gamma n > k \approx 10^9 \text{ s}^{-1}$ ) particularly at high intensities. Thus, assuming  $F > 3 \times 10^{11} \text{ s}^{-1}$ , Eq. 6 is

probably valid at least up to intensities when the measured lifetimes are ~50 ps, corresponding to an average annihilation rate  $\gamma n$  of  $2 \times 10^{10} \text{ s}^{-1}$  and a relative fluorescence quantum yield of  $\sim 10^9 / (2 \times 10^{10}) \approx 1/20$ . Except in the 21 K experiment where the lowest yield measured (relative to the low intensity limit) was 1/43, the above conditions are satisfied at the other three temperatures (relative yield not less than 1/23).

The solution of Eq. 6 in which the excitation pulse has a duration of several picoseconds, has been discussed in a preliminary note by Swenberg *et al.* (1976a). If  $\phi_0$  is the quantum yield at low light intensities and  $\phi(I_0)$  is the yield when the number of photons absorbed is  $I_a = \int \alpha I(t) dt$  (with the integration extending over the duration of the pulse) then we obtain for the yield

$$\phi(I_0) = \phi_0 \frac{1}{(\gamma/2k)I_a} \log \left\{ 1 + I_a \left( \frac{\gamma}{2k} \right) \right\} \quad (7)$$

Using this equation, we can obtain excellent fits to the experimental data at all temperatures using only  $(\gamma/2k)$  as the adjustable parameter. The curves calculated according to Eq. 7 are drawn as solid lines in Figs. 2-5; the values of the parameters which were used, together with the maximum spread in these values which would place the calculated curves outside the error bars of the experimental data, are given in Table 1. Hervo *et al.* (1975) have recently remeasured the temperature dependence of the PS II and PS I fluorescence lifetimes ( $\tau(k = \tau^{-1})$ ). This allows for a calculation of the bimolecular annihilation coefficients  $\gamma$ , which are also listed in Table 1. In calculating  $\gamma$  the lifetimes determined at 685 nm were used, for reasons which will be discussed below.

From the data in Table 1 it is evident that the bimolecular constants are the same within experimental error below 200 K. The room temperature value appears to be somewhat smaller. These values are similar in magnitude to those which have been observed for singlet-singlet and singlet-triplet exciton annihilation in organic crystals (Swenberg and Gea-

cinov, 1973, Rahman and Knox (1973). In fact the same type of fluorescence quenching curves which are observed with chloroplasts (Figs 2-5) have also been demonstrated in organic solids such as anthracene and tetracene using ps laser excitation (Campillo *et al.*, 1977). The fluorescence quenching curves observed in these crystals, are also well accounted for by Eq 7. The assumption that only singlet-singlet annihilation takes place in organic crystals when single picosecond pulses are used is on rather solid grounds. Thus the similarity between the fluorescence quenching curves as a function of pulse energy observed in these systems and in chloroplasts lends further support for the kinetic model from which Eq 7 is derived.

#### Exciton diffusion parameters and their temperature dependence

The bimolecular annihilation rate constant  $\gamma$  is a function of the diffusion coefficient  $D$ . In principle it is possible to calculate  $D$  from  $\gamma$  using the appropriate theoretical relationships.

In practice however, such a calculation is difficult because a knowledge of the interaction radius  $R$  between the two excitons, which is not known, is also required. Furthermore, the constant  $\gamma$  contains a parameter  $p$  ( $\leq 20$ ) which denotes the probability that a collision will actually produce an annihilation, and that such an annihilation may remove only one or both of the excitons (the latter case is possible if ionization with the production of an ion pair occurs, thus giving rise to the maximum possible value of  $p = 20$ ).

For these reasons, only lower bound values of the diffusion constants  $D$ , diffusion length  $l$  and the Förster energy transfer rate  $F$  can be inferred from the experimentally measured values of  $\gamma$ .

The photosynthetic pigment molecules are most likely arranged in a two-dimensional network. For this reason we employ a two-dimensional system for estimating  $D$ , although similar results are obtained in three dimensions. Since the membrane thickness is of the order of 50 Å, the values of  $\gamma$  ( $\text{cm}^3 \text{s}^{-1}$ ) given in Table 1 must be multiplied by  $2 \times 10^6 \text{cm}^{-1}$  to obtain the appropriate values of the two-dimensional ( $\gamma^{(2)}$ ) values.

For a single component system, with an isotropic diffusion coefficient, the theoretical expression linking experimental values of  $\gamma^{(2)}$  to  $D$  and  $R$  is given by (Suna, 1970)

$$\gamma^{(2)} = p \frac{-4\pi D}{\ln \left\{ \frac{1}{2} \sqrt{\frac{k}{D}} R \right\} + 0.577} \quad (8)$$

where  $R$  is the effective capture radius, and  $k$  is the reciprocal of the exciton lifetime as previously defined following Eq 6 above. The  $p$  factor takes into account final states other than singlet excitons, and collisions of excitons which do not lead to annihilation. This equation is valid for the diffusion of two excitons and

annihilation within a sphere of influence  $R$  under the conditions that  $\sqrt{D/k} \gg R$ . The values of  $k$  are known to be  $\approx 10^9 \text{s}^{-1}$  (Hervo *et al.*, 1975). The average intermolecular distance between chlorophyll molecules is of the order of 20 Å (calculated from the data of Park and Biggins (1964) from which we estimate an *in vivo* chlorophyll concentration of 0.1 M). The value of 20 Å, thus represents the smallest value of the interaction radius  $R$ . Using this value of  $R$  and the values of  $k$  and  $\gamma$  given in Table 1, we can utilize Eq 8 to infer values of the diffusion coefficient  $D$ . At room temperature  $\gamma \sim 5 \times 10^{-9} \text{cm}^3 \text{s}^{-1}$ , giving  $\gamma^{(2)} \approx 10^{-2} \text{cm}^2 \text{s}^{-1}$  and  $D$  is estimated to be  $\approx 2 \times 10^{-3} \text{cm}^2 \text{s}^{-1}$ . If a larger value of  $R$ , e.g. 50 Å (Rahman and Knox, 1973) is chosen, then the calculated value of  $D$  turns out to be  $\approx 10^{-3} \text{cm}^2 \text{s}^{-1}$ . Thus, in calculating  $D$  from  $\gamma^{(2)}$ , the lack of knowledge of  $R$  still permits the calculation of values of  $D$  within a factor of 2. Since  $p \leq 20$ , the estimate of  $D \approx 10^{-3} \text{cm}^2 \text{s}^{-1}$  represents a lower bound.

At temperatures below 200 K,  $\gamma$  appears to be larger than at room temperature. Following the same procedure, but using an average value of  $\gamma \approx 10^{-8} \text{cm}^3 \text{s}^{-1}$  at these lower temperatures, yields  $D \approx 4 \times 10^{-3} \text{cm}^2 \text{s}^{-1}$ .

The condition of validity of Eq 8, namely  $\sqrt{D/k} \gg R$ , is weakly satisfied using the values of  $D$ ,  $k$  and  $R$  given above. Thus  $\sqrt{D/k}$  is of the order of 100-200 Å, while  $R$  is 20 Å. An expression relating the diffusion coefficient  $D$  to  $\gamma$  without making use of this approximation, has been developed by Yokota and Tanimoto (1967) using a scattering length formalism, using their Eq 14, we find for  $R = 20$  Å, that  $D = 7 \times 10^{-3} \text{cm}^2 \text{s}^{-1}$ . If we adopt a value of  $R = 50$  Å, then  $D = 10^{-3} \text{cm}^2 \text{s}^{-1}$ . The use of different theories relating  $D$  and  $\gamma$  will be discussed in more detail in a forthcoming publication.

The average singlet exciton diffusion length  $l$  is given by

$$l = \sqrt{4D/k} \quad (9)$$

Using the above cited values of  $k$  and lower bound values of  $D \approx 10^{-3} \text{cm}^2 \text{s}^{-1}$ , we obtain  $l > 200$  Å at room temperature, while  $l \geq 400$  Å at the lower temperatures. This represents the approximate dimensions of one photosynthetic unit consisting of 200-300 molecules. However, since  $l \propto p^{-1/2}$ , a value of  $p = 0.5$  suffices to yield a calculated diffusion length of  $\sim 800$  Å at room temperature. Since  $p$  is likely to be less than 2 it is probable that  $l$  is larger than 200 Å and that the singlet exciton in chloroplasts can range over several photosynthetic units (see for example Paillet, 1976) in the temperature range of 20-300 K.

The connection between the nearest neighbor hopping rate  $F$  and the diffusion coefficient  $D$  is complicated by our lack of knowledge of the degree of coherence (Pearlstein *et al.*, 1976, Knox, 1975). However, from the temperature dependence of  $\gamma$  and the singlet exciton lifetimes (Hervo *et al.*, 1975), a change in  $D$  as a function of temperature of less than 30%

is calculated, assuming  $R$  to be constant. Thus,  $D$  can be considered to be a constant as a function of temperature within the experimental error. This argues against phonon-scattering as the process limiting the exciton mean free path since in that case,  $D$  would be expected to vary in proportion to  $T^{-1/2}$ . This would imply a factor of  $\sim 4$  increase in  $D$  as the temperature is lowered from 300 to 21 K. Thus, the much weaker experimentally observed variation in  $\gamma$  and the values of  $D$  inferred therefrom, is consistent with an incoherent exciton transfer model. Under these conditions  $F = D/R^2$ . Using  $D > 10^{-3} \text{ cm}^2 \text{ s}^{-1}$  and  $R = 20 \text{ \AA}$  we obtain  $F > 3 \times 10^{10} \text{ s}^{-1}$  ( $F > 10^{10} \text{ s}^{-1}$  is obtained if  $R = 50 \text{ \AA}$  is chosen). Pailotin (1976) inferred values of  $F$  which are about ten times larger than these lower bound values. If  $\rho$  were equal to 0.3, then the values of  $F$  calculated would be consistent with those of Pailotin.

In the incoherent exciton limit, the lack of a strong temperature variation in  $D$ , to within  $\sim 30\%$ , implies that the transfer rate  $F$  also displays a similar lack of strong temperature dependence. The transfer rate  $F$  depends on the strength of the electronic transitions involved (donor and acceptor) and the local index of refraction of the medium. While these two parameters are not expected to vary significantly with temperature,  $F$  also depends on the overlap integral between the donor fluorescence and the acceptor absorption spectra. This overlap depends on the temperature (Pailotin, 1973). Considering the temperature dependence of  $F$  as given by Pailotin, variations in  $F$  are expected in the low temperature range (below 50 K), but not at the higher temperatures. However, this relationship was established utilizing values of the displacement between the maxima of the absorption and fluorescence maxima (Stokes shift) for chlorophyll *a* *in vitro*. Our results imply that there is no significant variation of this parameter at low temperatures, this may be due to a decrease in the Stokes shift *in vivo*.

The transfer rate also depends on the mutual orientation between the transition dipole moments. However, there is no evidence for temperature dependent phase transitions or a significant change in the orientation of bulk chlorophyll molecules (Garab and Breton, 1976).

#### *Energy transfer pathways and the origin of the PS I (735 nm) fluorescence at low temperatures*

In the previous sections we have analyzed the fluorescence quenching curves according to Eq. 7 without attempting to differentiate between PS I and PS II.

There are a number of reasons why the quenching curves at these two wavelengths are expected to be different, as indeed they are when  $\mu\text{s}$  (Geacintov and Breton, 1977) rather than ps pulses are used for excitation.

(1) The distribution of quanta among the two pigment systems. This quantity was determined recently

by Kitajima and Butler (1975). They found that for excitation below 680 nm, about 30% of the absorbed quanta contribute to the PS I fluorescence at 735 nm at 77 K, and  $\sim 70\%$  contribute to the 685 nm emission.

(2) The fluorescence decay times of the 735 nm fluorescence at low temperatures is 1.5 ns at 100 K and 2.5 ns at 23 K (Hervo *et al.*, 1975). These lifetimes are significantly longer than those determined at 685 nm (Table 1). All other parameters being the same, the increased lifetimes of the excitons in pigment system I should entail more efficient exciton annihilation, and thus more pronounced quenching in photosystem I than in photosystem II.

(3) The pigment composition in PS II is more heterogeneous than in PS I. If exciton diffusion is restricted to chlorophyll *a* molecules only (Pearlstein, 1964) and the chlorophyll *b* molecules act as antitraps (uphill energy transfer from chlorophyll *a* to chlorophyll *b* is not allowed), then the diffusion time to the PS II reaction centers may be longer in PS II than in PS I (Svenberg *et al.*, 1976b). This type of heterogeneity effect may also produce a lower  $\gamma$  in the more heterogeneous PS II system than in PS I, thus predicting a higher fluorescence quenching efficiency in PS I.

None of these effects appear to be relevant in the ps pulse quenching experiments in Figs. 2-5. Campillo *et al.* (1976a) have shown that fluorescence quenching at high pulse intensities is accompanied by a decrease in the observed fluorescence decay times. If exciton quenching occurs directly on the level of the two pigment systems giving rise to the 685 and 735 nm emission bands, then the fluorescence lifetimes should decrease at both wavelengths as the intensity of the ps laser pulses is increased. It is shown elsewhere, however, that while such a decrease is indeed observed at 685 nm, the fluorescence lifetime at 735 nm is relatively insensitive to the pulse intensity (Geacintov *et al.*, 1977). These results show that the exciton annihilation does not occur on the level of the PS I pigment system which gives rise to the 735 emission.

We thus conclude that the exciton-exciton annihilations occur within the pigment system characterized by the fluorescence emission at 685 nm. This is the system consisting of the light harvesting (LH) chlorophyll-protein complexes. The Photosystem I pigments which emit fluorescence at 735 nm appear to be present in such small concentrations that they absorb a negligible portion of the quanta at 610 nm directly. Instead energy is transferred by excitons from the LH pigments to these long-wavelength pigment forms, with subsequent emission in the 735 nm spectral region. In this manner the experimental facts, namely the identical quenching curves at 685 and 735 nm can be rationalized. This picture is consistent with Butler and Kitajima's (1974, 1975) tripartite fluorescence model for chloroplasts at low temperatures.

It should be pointed out that the identical behavior of PS I and PS II depicted in Figs. 2-5 is not repro-

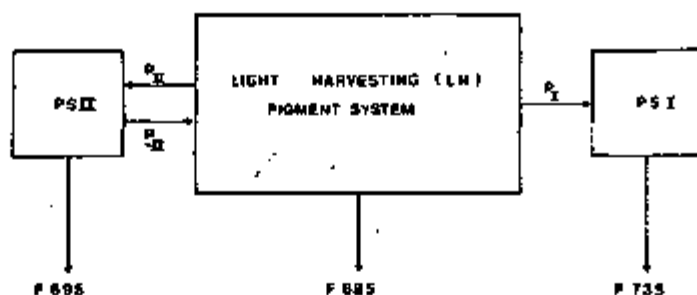
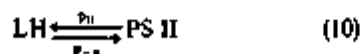


Figure 6. Tripartite model of fluorescence of chloroplasts at low temperatures after Butler and Kitajima (1974, 1975) consisting of chlorophyll molecules in the light harvesting and Photosystems I and II pigment systems. The approximate emission maxima (in nm) are indicated and  $P_{11}$ ,  $P_{12}$  and  $P_{13}$  represent probabilities of exciton transfer from one pigment system to another.

duced under steady-state excitation at reasonably low, normal intensity levels. Thus, the fluorescence changes which are observed in steady-state illumination at 685 and at 735 nm are different, when for example, the PS II reaction centers are closed. This apparent discrepancy can be resolved by considering the origins of the variable fluorescence in the picosecond and in the steady-state experiments.

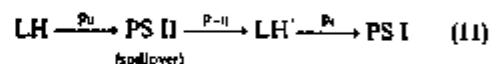
When a steady state light source is switched on and dark adapted chloroplasts are illuminated, the fluorescence increases with increasing illumination time and reaches a plateau after some time of the order of one minute or less. This phenomenon is due to the closing of the reaction centers in PS II which gives rise to an increase in the fluorescence quantum yield. Murata (1968) has studied the dependence on emission wavelength of this variable fluorescence. He has shown that the maximum increase in the fluorescence occurs at 695 nm. When the light is first turned on, the fluorescence intensity immediately rises to a level  $F_0$ , then eventually rises to a level  $F_M$ . At 695 nm  $F_M/F_0 \approx 5$ , at 685 it is  $\sim 3.3$  and is only  $\sim 1.3$  at 735 nm. Thus, the amount of variable fluorescence is lowest at 735 nm. The fluorescence of the PS I pigments themselves appears to be insensitive to the state of the P 700 reaction center (Butler and Kitajima, 1974, 1975; Satoh *et al.*, 1976), and the variable fluorescence at 735 nm is attributed to spillover of excitons from PS II to PS I pigments (Murata, 1968; Kitajima and Butler, 1975).

A schematic representation of the pigment systems and the transfer of excitons and the emission of fluorescence after Butler and Kitajima is depicted in Fig. 6. According to these authors energy transfer between the light harvesting (antenna: LH) pigments and pigment system II occurs readily in either direction, i.e.



However, the slightly smaller value of  $F_M/F_0$  observed at 685 than at 695 nm are only in part consistent with this assumption. The probability of back transfer PS II  $\rightarrow$  LH appears to be somewhat less

than the forward transfer LH  $\rightarrow$  PS II, since there is a larger fluorescence enhancement at 695 than at 685. Furthermore, as Butler and Kitajima (1974) themselves have recognized, an exciton which has been localized within the antennae of PS II and is transferred back to the system, does not have the same probability of ending up in PS I as an exciton created initially in the LH system by a photon. The two energy transfer pathways for (a) spillover (Eq. 11), and (b) for direct funneling of excitation from LH to PS I (Eq. 12) are:



and



The overall probabilities for excitons created originally in the LH pigments and eventually ending up in PS I, do not appear to be the same.

In our ps laser quenching experiments, even though the reaction centers of PS II are closed, the relative changes in the fluorescence yields are exactly the same at 735 and at 685 nm. Thus unlike in Murata's and Butler and Kitajima's fluorescence induction experiments, a change in the fluorescence yield at 685 nm is paralleled by the same relative change at 735 nm. We therefore propose that in our quenching experiments, the exciton annihilations occur within the LH pigment complexes and that these annihilations compete with energy transfers from LH to the PS II and PS I pigment systems directly. The lack of a dependence of the fluorescence lifetime on the picosecond pulse intensity at 735 nm certainly supports this statement for the LH  $\rightarrow$  PS I case. A similar verification of this statement for the LH  $\rightarrow$  PS II case is not possible, because the 695 nm PS II fluorescence is not sufficiently well resolved from the LH pigment fluorescence at 685 nm. Thus, the existence of PS II as a separate entity from the LH pigments ( $p_{11} \neq p_{12}$  in Fig. 6), and whether annihilation of excitons takes place on the level of these PS II pigments, cannot be established from our experiments.

In summary, our ps experiments essentially reflect the energy transfer pathways summarized by Eqs 11 and 12 as well as processes involving exciton transfer from LH to PS II. The fluorescence-limiting exciton annihilation processes take place on the level of the LH pigments, and the changes in the fluorescence yield at all emission wavelengths reflect the processes occurring in this antenna pigment system. In contrast, in the steady-state, fluorescence changes at the different emission wavelengths reflect the changes which occur in the PS II pigment system, in particular, the changes in the 735 nm intensity reflect spillover (Eq 11). Thus, our ps laser fluorescence quenching experiments are consistent both with Butler and Kitajima's tripartite fluorescence model of chloroplasts at low

temperatures, and the steady-state fluorescence induction experiments (Murata, 1968, Kitajima and Butler, 1975).

**Acknowledgements**—We thank Drs E. Roux at Saclay and M. Pope in New York for many stimulating discussions and their interest in this work. The authors wish to thank Prof. R. S. Knox for pointing out the scattering length method of Yokota and Tanimoto on relating the bimolecular rate to the diffusion coefficient. The portion of this work performed at New York University was supported by a National Science Foundation Grant PCM 76-14359 and in part by a United States Energy Research and Development Administration contract to the Radiation and Solid State Laboratory. In addition, one of us (N.E.G.) would like to acknowledge a useful discussion with Drs R. M. Pearlstein, R. Hemenger and W. Whitten at Oak Ridge.

#### REFERENCES

- Beddard, G. S., G. Porter, C. J. Tredwell and J. Barber (1975) *Nature* 258, 166-168.
- Breton, J. and N. E. Geacintov (1976) *FEBS Lett* 69, 86-89.
- Briantais, J. M., H. Merleto and Govindjee (1972) *Photosynthetica* 6, 133-141.
- Butler, W. L. and M. Kitajima (1974) In *Proceedings of the Third International Congress on Photosynthesis* (Edited by M. Avron) Vol. I, pp. 13-24. Elsevier, Amsterdam.
- Butler, W. L. and M. Kitajima (1975) *Biochim Biophys Acta* 396, 72-85.
- Campillo, A. J., S. L. Shapiro, V. H. Kollman, K. R. Winn and R. C. Hyer (1976a) *Biophys J* 16, 93-97.
- Campillo, A. J., V. H. Kollman and S. L. Shapiro (1976b) *Science* 193, 227-229.
- Campillo, A. J., R. C. Hyer, S. L. Shapiro and C. E. Swenberg (1977) *Chem Phys Lett* (in press).
- Cho, F. and Govindjee (1970) *Biochim Biophys Acta* 205, 371-378.
- Cho, F., J. Spencer and Govindjee (1966) *Biochim Biophys Acta* 126, 174-175.
- Delosme, R. (1972) In *Proceedings of the 2nd International Congress on Photosynthesis Research* (Edited by G. Forti, M. Avron and A. Melandri), pp. 187-195. Dr. W. Junk N.V. Publishers, The Hague.
- Den Haan, G. A., L. N. M. Duysens and D. J. N. Egberts (1974) *Biochim Biophys Acta* 368, 409-421.
- Garab, G. I. and J. Breton (1976) *Biochim Biophys Res Commun* 71, 1095-1102.
- Geacintov, N. E. and J. Breton (1977) *Biophys J* 17, 1-15.
- Geacintov, N. E., J. Breton, C. E. Swenberg, A. J. Campillo, S. L. Shapiro and R. C. Hyer (1977) *Biochim Biophys Acta* 461, 306-312.
- Goedheer, J. C. and C. A. M. Verhulsdonk (1970) *Biochim Biophys Res Commun* 39, 260-266.
- Goedheer, J. C. (1972) *Ann Rev Plant Physiol* 23, 87-112.
- Hervo, G., G. Pailotin and J. Thery (1975) *J Chim Phys* 72, 761-766.
- Kitajima, M. and W. Butler (1975) *Biochim Biophys Acta* 408, 297-305.
- Knox, R. S. (1975) In *Bioenergetics of Photosynthesis* (Edited by Govindjee), pp. 183-221. Academic Press, New York.
- Malin, S. (1974) *Biophys Chem* 2, 327-337.
- Mauzerall, D. (1976a) *Biophys J* 16, 87-91.
- Mauzerall, D. (1976b) *J Phys Chem* 80, 2306-2309.
- Monger, T. G., R. J. Cogdell and W. W. Parson (1976) *Biochim Biophys Acta* 449, 136-153.
- Murata, N. (1968) *Biochim Biophys Acta* 162, 106-121.
- Pailotin, G. (1973) Thesis Université Paris-Sud.
- Pailotin, G. (1976) *J Theoret Biol* 58, 219-252.
- Park, R. B. and J. Biggins (1964) *Science* 144, 1009-1010.
- Pashenko, V. Z., S. P. Protasov, A. B. Rubin, K. N. Timofeev, L. M. Zamazova and L. B. Rubin (1975) *Biochim Biophys Acta* 408, 143-153.
- Pearlstein, R. M. (1964) *Proc Natl Acad Sci U.S.A.* 52, 824-830.
- Pearlstein, R. M., K. Lindenberg and R. P. Hemenger (1976) In *Excited States of Biological Molecules* (Edited by J. B. Birks), pp. 591-600. Wiley, London.
- Rahman, T. S. and R. S. Knox (1973) *Phys Status Solidi (b)* 58, 715-720.
- Robinson, G. W. (1967) *Brookhaven Symp Biol* 19, 16-48.
- Sato, K., R. Strasser and W. L. Butler (1976) *Biochim Biophys Acta* 440, 337-345.
- Seibert, M. and R. R. Alfano (1974) *Biophys J* 14, 269-283.
- Schwartz, M. (1972) *Adv Enzymol* 24, 139-146.
- Suna, R. (1970) *Phys Rev B1*, 1716-1739.
- Swenberg, C. E. and N. E. Geacintov (1973) In *Organic Molecular Photophysics* (Edited by J. B. Birks) Wiley, New York.
- Swenberg, C. E., N. E. Geacintov and M. Pope (1976a) *Biophys J* 16, 1447-1452.
- Swenberg, C. E., R. Dominjanni and N. E. Geacintov (1976b) *Photochem Photobiol* 24, 601-604.
- Tumerman, L. A. and E. M. Sarokin (1967) *Mol Biol* 1, 628-638.
- Yokota, M. and O. Tanimoto (1967) *J Phys Soc Jpn*, 22, 779-784.
- Yu, W., P. P. Ho, R. R. Alfano and M. Seibert (1975) *Biochim Biophys Acta* 387, 159-164.



AMCED: DETERMINATION OF AEROSOL MASS AND CHARGE  
BY ELECTRON DIFFERENTIALS

By

Stephen Arnold

Radiation and Solid State Laboratory  
NEW YORK UNIVERSITY  
New York, N.Y. 10003

March 1970

## INTRODUCTION

In what follows an instrument is described which is capable of measuring picogram aerosol masses of a suspended particle to better than 0.5% and charge states (i.e., number of electronic charges) with an uncertainty of less than 0.1. The gravitational mass is measured directly eliminating the need for detailed information about the shape of the particles as would be necessary for masses arrived at from sedimentation or light scattering measurements.<sup>1</sup>

The sensitivity and accuracy of this method, coupled with a capability of being used in a variety of ambient atmospheres, opens new areas for the study of surface reactions involving small particles. For example, the change in mass of a carbon particle in contact with highly oxidizing gases, can be studied. This may be relevant to the response of carboniferous particulates in the upper reaches of the troposphere. As for the charge state of the particle, it recently has been shown (Chan) that increased charge has a significant effect on the deposition of aerosols in the larynx or trachea for particles smaller than  $5\mu$  in diameter.<sup>2</sup>

## THEORY IN THE PRESENT WORK

Mass and charge are measured from a one electron imbalance in a Millikan Chamber. With UV light of sufficient energy one electron can be ejected at a time from a solid or liquid aerosol. In a Millikan Chamber having a voltage  $V_1$  across plates separated by a distance  $d$  the equilibrium equation for a particle of mass  $m$  is

$$mg - B = q_i \frac{V}{d} \tag{1}$$

where  $q_i$  is the charge of the particle,  $g$  is the gravitational acceleration and  $B$  is the buoyant force.

If only one electron is knocked off a particle of charge  $q_i$  in promoting it to a charge  $q_{i+1}$  then the differential charge  $\pm e$  from equation (1) is

$$\pm e = q_{i+1} - q_i = m \left( 1 - \frac{\rho_m}{\rho_p} \right) gd \left( \frac{1}{V_{i+1}} - \frac{1}{V_i} \right) \tag{2}$$

where the  $+$  sign corresponds to a positive particle and the minus sign to a negative one and  $\rho_m$  and  $\rho_p$  are the density of the medium and particle respectively. Equation (2) may be solved for the mass of the aerosol with the result

$$m = \frac{e}{gd \left( 1 - \frac{\rho_m}{\rho_p} \right)} \left| \left( \frac{1}{V_{i+1}} - \frac{1}{V_i} \right) \right| \tag{3}$$

Since  $\rho_m/\rho_p$  is  $< 10^{-3}$  for most solids and liquids this ratio can reasonably be set to zero for masses determined to 0.3% and the resultant equation is found to be exceedingly simple. One merely has to determine two voltages in order to arrive at a particle mass. The charge state  $Z_i$  (i.e.,  $q_i/e$ ) may be determined from equations (1) and (2) with the results

$$Z_i = \frac{\frac{1}{V_i}}{\frac{1}{V_{i+1}} - \frac{1}{V_i}} = \frac{V_{i+1}}{V_i - V_{i+1}} \tag{4}$$

As one can see the charge state  $Z_i$  may be determined even if the voltage is poorly calibrated as long as the representation of the voltage is linear.

An estimate of the relationship between the fractional change in voltage for an electron step  $\Delta V/V$  and the diameter of the corresponding aerosol may be obtained by expressing the mass in equation (3) [with  $\rho_m/\rho_p = 0$ ] as a density times a volume.<sup>3</sup>

$$D^3 = \frac{6e}{\pi \rho_p g d} \left| \left( \frac{1}{V_{i+1}} - \frac{1}{V_i} \right) \right| \approx \frac{6e V}{\pi \rho_p} \left( \frac{\Delta V}{V} \right) \quad (5)$$

where  $\rho_p$  is the density of the particle,  $\Delta V$  is  $|V_i - V_{i+1}|$ ,  $V$  is the average voltage and the approximation in going to the expression at the right is that  $|V_i - V_{i+1}| \ll V_i$ . One can see from this expression that the fractional change in levitating voltage is proportional to the voltage and inversely proportional to the cube of the particle diameter. Figure 1 shows a plot of particle size versus levitating voltage for various fractional changes in voltage due to a single electron emission. The separation between the plates  $d$  is assumed to be 1 cm and  $\rho_p$  is taken to be 1 gm/cm<sup>3</sup>.

The implementation of equations (3) and (4) require the observation of the emission (or absorption) of one electron at a time. In the following section we will describe typical apparatus for detecting these electron differentials (the AMCED apparatus).

ANCED APPARATUS

A one electron imbalance is difficult to detect by eye except in the case of particle having just a few charges. The servomechanism shown in Fig. 2 may be used to automatically track the motion of a particle. Light from a He-Ne laser is introduced through a flat transparent insulated electrode in the top plate of the chamber and scatters off the suspended particle. In order to monitor the particle's position the scattered light is split and measured by two photodectors.<sup>4,5</sup> A 1:1 image of the particle is produced at the edge of the mirror in Fig. 2. With the particle more than half a diameter (or diffraction limited spot size, whichever is larger) above or below center virtually all of the scattered light will be reflected into the top or side phototube, respectively. Between these extremes both phototubes will be illuminated. Since the ratio of currents from the two phototubes contains position information which is independent of laser fluctuations, these two currents are processed by a log-ratio amplifier. The output of this amplifier is roughly proportional to the vertical displacement  $X$  of the particle when  $X$  is considerably less than the image size. The log-ratio output provides an error signal in a conventional feedback system which controls the voltage of the bottom plate (see Fig. 2) so that the particle's elevation is practically constant.

The voltage at the bottom plate is monitored by a digital voltmeter and a strip chart recorder. Both of these units integrate the output for 1 sec.

The ultraviolet excitation is provided by a 200W deuterium lamp followed by a monochromator and appropriate optics. With this source photon energies up to 7 eV are available.

The Millikan plates are enclosed within a chamber which can be evacuated and backfilled with a desired gas. In the present work nitrogen gas was used at STP.

In order to draw a particle into the laser beam the transparent insulated electrode is switched to a potential  $V_s$  (e.g., for a positively charged particle the electrode would have a negative potential).<sup>6</sup> Since this action creates a non-uniform field, measurements are only made after the electrode is brought back to the potential of the top plate (i.e., when the field is uniform).

The UV intensity must be reduced so that only one electron is ejected within the time constant of the electronics. This means that the average frequency of photoelectron events  $f$  times the response time of the system  $t_s$  should be considerably less than 1.

$$ft_s \ll 1 \quad (6)$$

In the present work, although the bandwidth of the servosystem is  $\sim 1$  kHz, the limiting time constant is that of the measuring electronics, 1 sec. Although the system can be made a great deal faster, for the present application increased speed is not necessary.

In the present experiments powders of polycyclic aromatic hydrocarbons were injected into the chamber from a conical reservoir in the top plate. Injection was accomplished by pushing the particles through a small hole with a thin wire (.006").

## RESULTS

Typical results of an experiment on a negative particle are shown in Fig. 3. In this example a segment of time is 1 sec. As one can see, the voltage increases discontinuously as electrons are emitted. Fifteen seconds after the UV light is turned on the first event occurs within 1 sec producing a plateau which remains for the next six seconds. The emission which begins at about 22 seconds is followed by an adjacent emission culminating in a plateau at 25 seconds. The third plateau also represents an additional emission of two adjacent electrons, while the fifth and sixth plateaus are single electron events.

Figure 4 is a plot of the inverse plateau voltages  $(V_i)^{-1}$  in Fig. 3 versus the number of electrons  $N_e$  emitted. Since  $(V_i)^{-1}$  is proportional to the charge on the particle from equation (1), the linearity displayed by Fig. 3 is as expected. A reduced  $\chi^2$  fit to the data gives a slope of  $-5.165 \times 10^{-6}$  (Volts) $^{-1}$  per electron emitted with a standard deviation of  $\pm 0.030 \times 10^{-6}$  (Volts) $^{-1}$ . Using this slope and a plate separation of 1 cm, the mass of the particle turns out to be  $316.1 \pm 1.8$   $\mu\text{gm}$ . This slope of the inverse voltage curve in Fig. 4 may also be used to determine the charge states corresponding to the various plateaus. These computed charge states are given in parenthesis at each point in Fig. 4.

A diameter of an equivalent sphere may be calculated from equation (5). Using the density of tetracene of  $1.30 \text{ gm/cm}^3$ , the equivalent spherical diameter is found to be  $7.74 \pm .01$ . Stokes drag measurements gave an average sedimentation velocity of  $\sim 2 \text{ mm/sec}$ . This translates into a spherical diameter of  $8.2\mu$  for sedimentation in nitrogen. Since our test particle is not spherical, the comparison of the diameters derived from electron differentials and from sedimentation can be considered to be in good agreement.

Although the uncertainty in the charge state for the example given in Fig. 3 is  $\pm 0.8$ , this uncertainty can be reduced considerably by accumulating more data (i.e., measuring more photoemission steps). In addition, as the amount of charge is reduced and the size of the steps increased, the corresponding uncertainties in mass and charge state are reduced. With  $\sim 20$  charges on a particle we have found that the uncertainty in the charge state can easily be reduced to  $\pm 0.1$ . Other organic microcrystals with masses less than a picogram have also been suspended with their masses determined to better than 0.5%.

#### DISCUSSION

Although single-electron emission by photoionization provides a convenient way of using the AMCED technique, photoionization at energies  $> 7$  eV requires the difficulty of using vacuum U.V. technology. This problem can be overcome by allowing the particle to scavenge electrons which are photoemitted from a relatively low work function surface. For example, one can emit electrons from an area of one of the Millikan plates just above or below the particle (i.e., the choice depends on whether the particle is positive or negative; top plate for a positive particle and bottom plate for a negative one).

Compared with sedimentation and light scattering determinations of particle mass, each of which requires a number of inputs (e.g., particle shape, viscosity and particle density) in addition to the measured quantities, the electron differential method (AMCED) is intrinsically simple. One only has to measure two voltages in order to arrive at the mass and charge state. Of course, all of the work thus far has been done on a single particle although the application to a stream of particles should be possible.



Another application of the apparatus in Fig. 2 is in the area of photoelectron spectroscopy. With the ability to measure the rate of loss of electrons at a particular photon energy one can measure photoelectron excitation spectra of solid and liquid particles. These measurements should lead to basic ionization constants. Future publications will deal with this application of the AMCED instrument.

## REFERENCES

1. Oster, G (1972) Physical Methods of Chemistry, Part IIIA (Edited by Weisberger, A.), J. Wiley and Sons, Inc.
2. Chan, T.L. (1977) The Characterization of Particle Deposition in the Human Tracheobronchial Tree, Ph.D. Thesis, New York University.
3. For the sake of this estimate the particle is assumed to be a sphere.
4. Ashkin, A. and Dziedzic, J.M. (1977) Appl. Phys. Lett., 30, 202.
5. Wyatt, P.J. and Phillips, D.T. (1972) J. Colloid Interface Sci., 39, 125.
6. Fletcher, H. (1914) Phys. Rev., 1, 440.

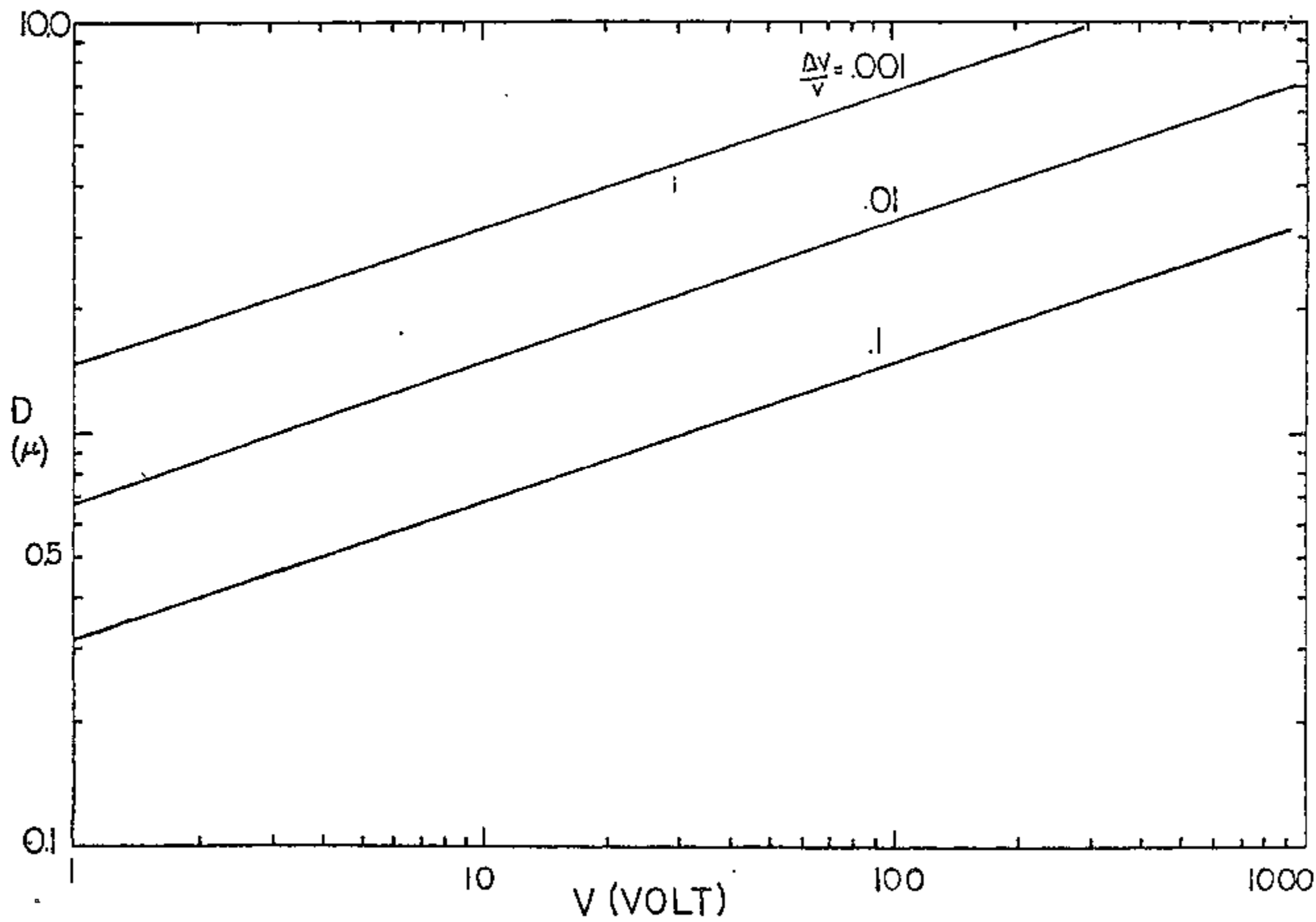
#### ACKNOWLEDGEMENTS

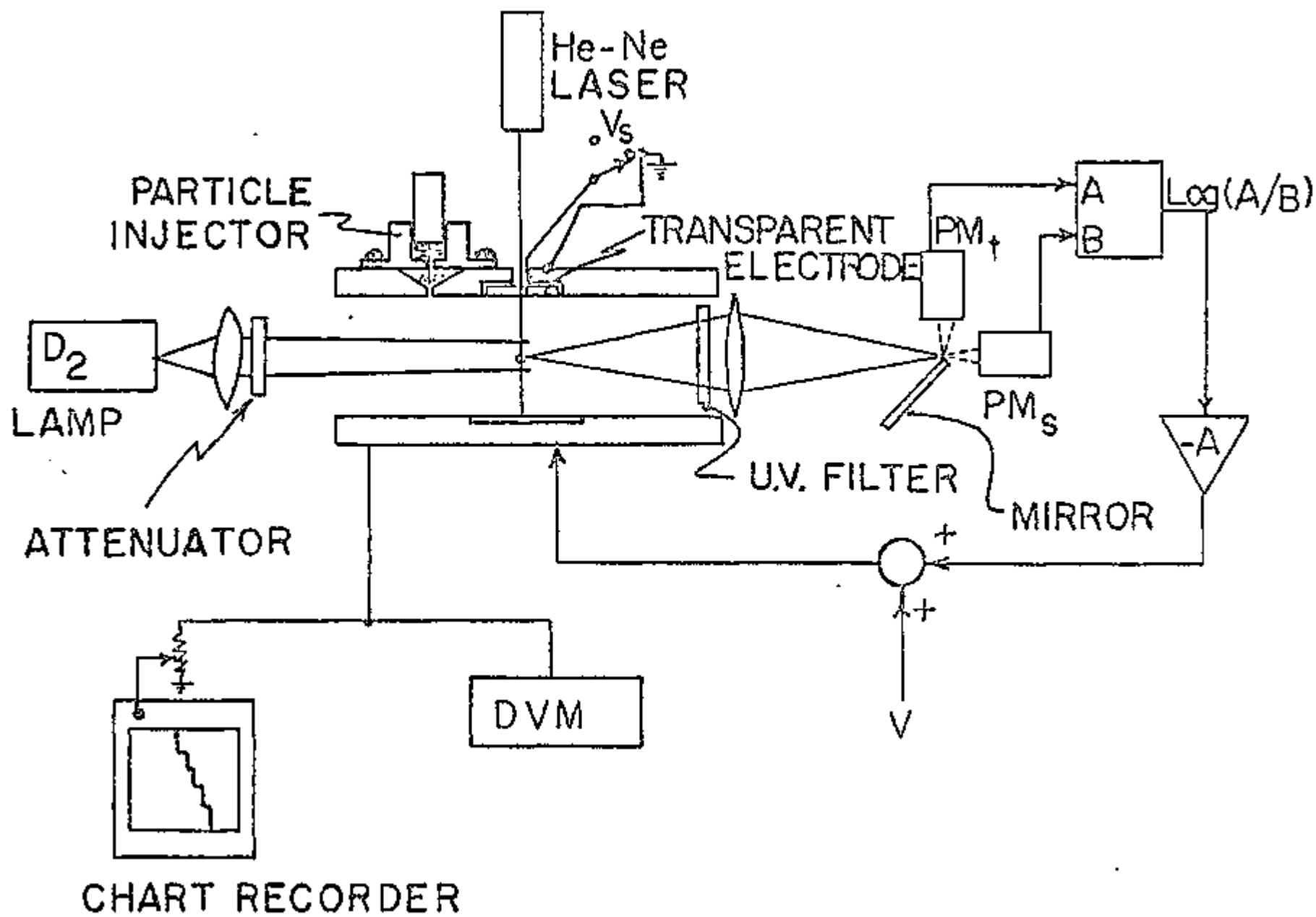
The author would like to acknowledge useful discussions with Professor D. Yeates of the Environmental Medicine Department and Professor M. Pope of the Chemistry Department of New York University.

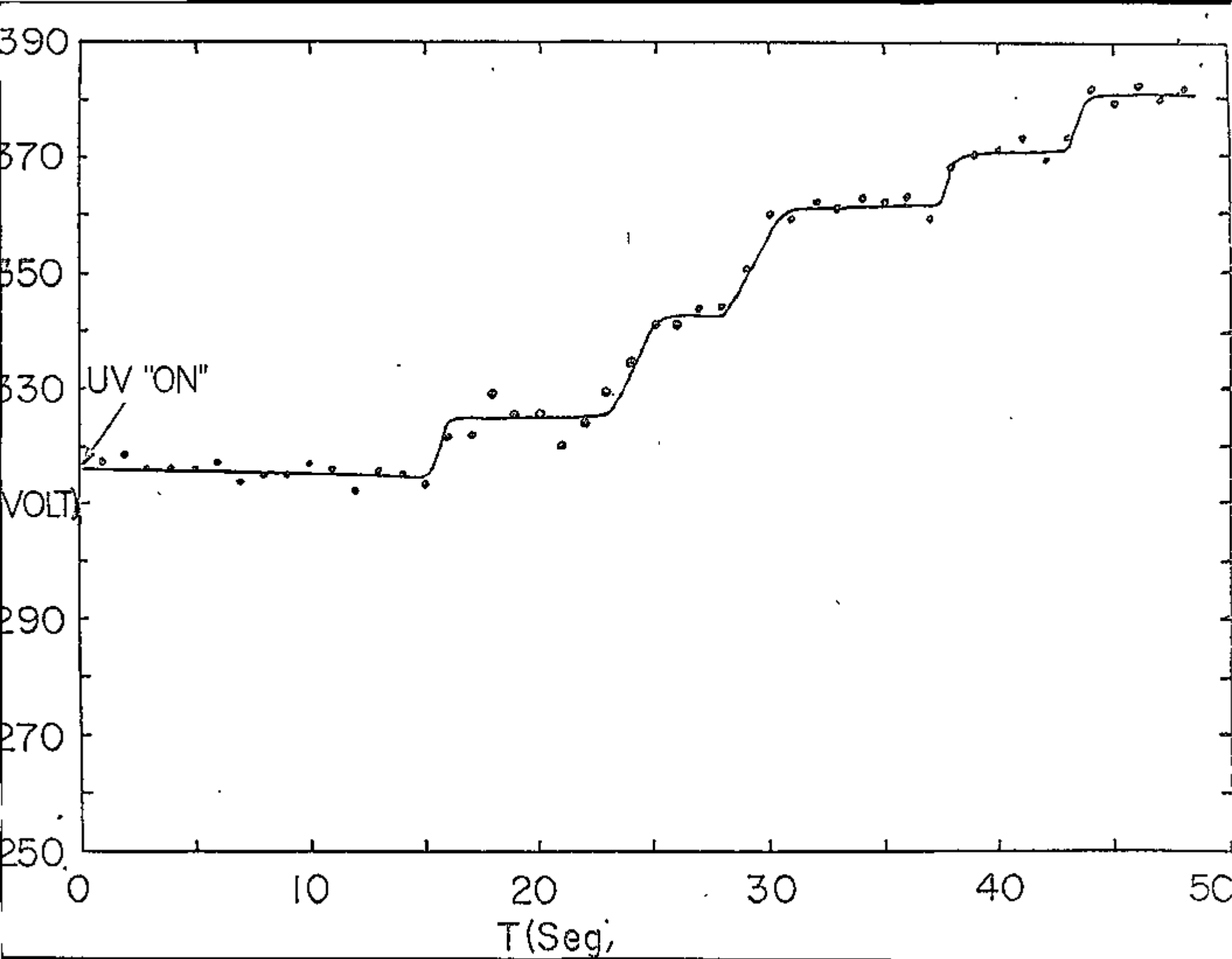
This work is supported by a research grant from the Department of Energy.

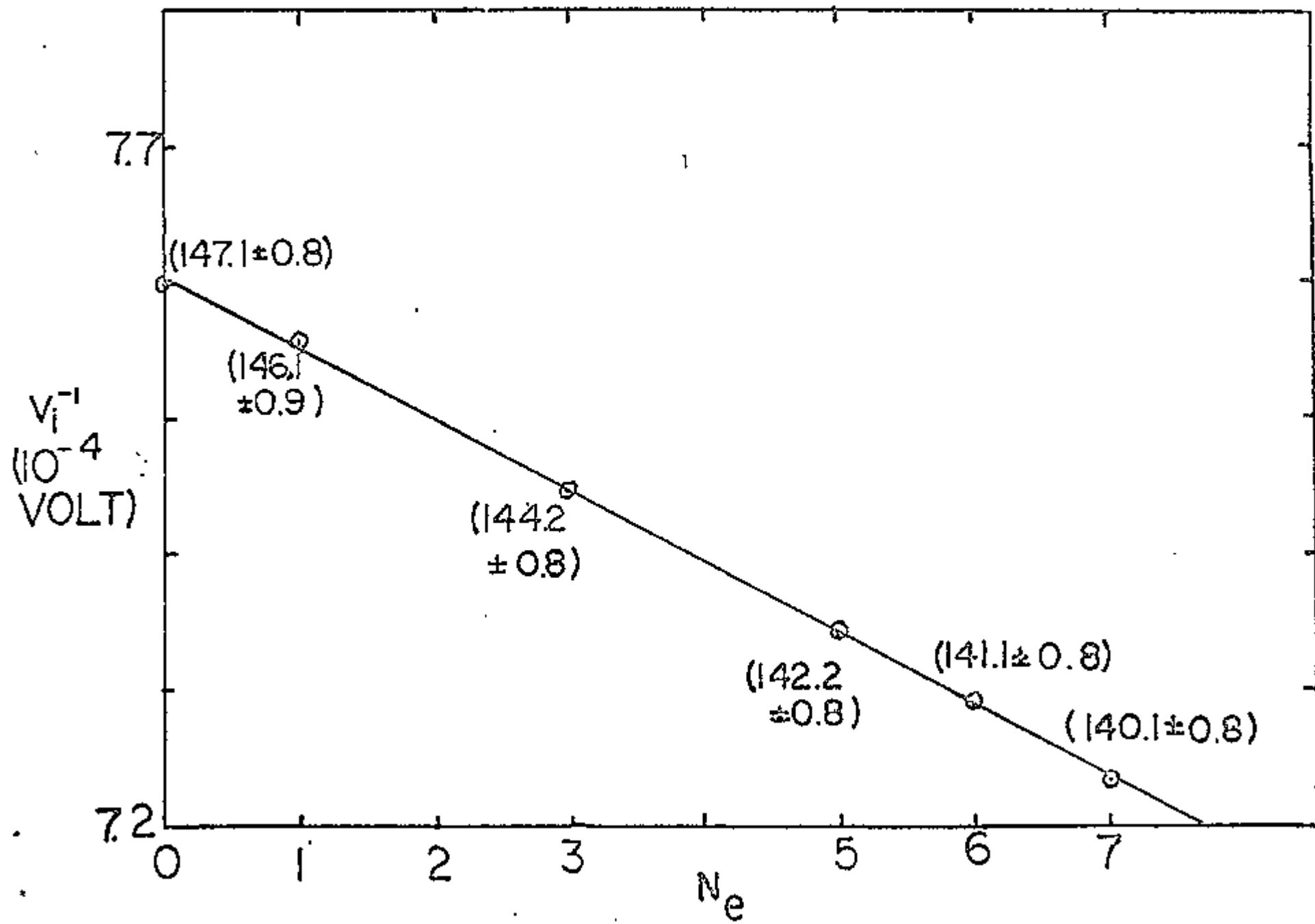
FIGURE CAPTIONS

- Fig. 1. Particle size versus levitating voltage for various fractional changes in voltage  $\frac{\Delta V}{V}$  due to an electron differential in charge.
- Fig. 2. The AMCED apparatus.
- Fig. 3. A typical segment of voltage versus time data for a tetracene microcrystal in the AMCED apparatus.
- Fig. 4. Reciprocal voltage versus number of electrons lost for the data given in Fig. 3. The charge states (i.e., number of electron charges) corresponding to each point are contained in parenthesis.











FLUORESCENCE STUDY OF THE PHYSICO-CHEMICAL PROPERTIES  
OF A BENZO(A)PYRENE 7,8-DIHYDRODIOL 9,10-OXIDE  
DERIVATIVE BOUND COVALENTLY TO DNA

by

Thaddeus Prusik, Nicholas E. Geacintov and  
Christopher Tobiasz

Chemistry Department and  
Radiation and Solid State Laboratory  
NEW YORK UNIVERSITY  
New York, N.Y. 10003

Vesna Ivanovic and I. Bernard Weinstein

Division of Environmental Sciences and  
Institute of Cancer Research  
COLUMBIA UNIVERSITY  
New York, N.Y. 10032

*submitted to  
Photochem. Photobiol.*

October 1977

## ABSTRACT

Covalent complexes between 7,8-diol 9,10 epoxide benzo(a)pyrene (BPDE) and DNA with a modification of one BPDE molecule per 1000 DNA bases were prepared in vitro. The same stereoselective and chemically homogeneous binding of BPDE to native DNA was observed, as reported earlier for human and bronchial explants. The fluorescence of the pyrene-like aromatic moiety of BPDE bound to DNA in vitro was used as a probe of the microenvironment of the BPDE molecule in order to obtain information about the structure of the BPDE-DNA complex dissolved in aqueous solution. Fluorescence techniques, based on the quenching of the singlet excited states by metal ions such as  $Ag^+$ , by iodide ions, and by molecular oxygen are described, which provide a method for differentiating between external and internal (intercalation) binding of polycyclic aromatic molecules to DNA. Silver ions, which bind to DNA by intercalation, exhibit a strong quenching effect on non-covalently bound, intercalated benzo(a)pyrene; on the other hand, there is no quenching effect on the fluorescence of BPDE in the covalent DNA adduct. Quenchers such as  $O_2$  and iodide ions, which do not specifically bind to DNA and are dissolved in the solution external to the DNA molecule, exhibit a quenching effect on the BPDE chromophore. Furthermore, the fluorescence yield of the BPDE-DNA complex decreases with increasing DNA concentration, an effect which is not observed with non-covalently bound intercalated benzo(a)pyrene-DNA complexes, and which is attributed to intermolecular DNA-DNA interactions. The results of these studies indicate that the pyrene-like chromophore in the covalent BPDE-DNA complex is not intercalated between the base pairs, and that it is located in an accessible region external to the DNA helix. Possible structures are discussed.

## INTRODUCTION

The study of the interaction of various polycyclic aromatic hydrocarbons (PAH) with DNA has been an area of active research in the field of chemical carcinogenesis. It was found that PAH molecules, which are in general very insoluble in aqueous solutions ( $10^{-7}$ - $10^{-9}$  M),<sup>1</sup> are readily solubilized by aqueous purine<sup>2</sup> and DNA solutions.<sup>3,4</sup> It was demonstrated that the size of the polycyclic hydrocarbon is an important criterion for the type and degree of physical binding to DNA.<sup>5</sup> However, there is no correlation between the ability of a PAH to physically bind to DNA and its carcinogenic potency.<sup>6</sup> The physical complexes formed between the PAH and DNA do however provide model systems for investigating the physicochemical properties of aromatic molecules bound to DNA. We have previously reported the singlet and triplet excited state properties of benzo(a)pyrene physically bound to DNA<sup>7</sup> (BP-DNA). The results of these studies were consistent with the intercalation model of binding of BP to DNA. In the intercalation model the hydrocarbon molecules are sandwiched between adjacent base pairs of the DNA helix. Evidence for the intercalation mechanism is provided by other experimental techniques including flow induced fluorescence polarization,<sup>8</sup> flow induced linear dichroism<sup>9</sup> and electrically induced linear dichroism<sup>10</sup> studies.

There is increasing evidence that the covalent binding of chemical carcinogens to cellular macromolecules, and in particular to nucleic acids, appears to be a prerequisite for their carcinogenic action.<sup>11</sup> Most carcinogens, including PAH molecules, require metabolic activation before covalent binding takes place. Recent studies indicate that the most reactive metabolite of the potent and ubiquitous carcinogen BP is the 7,8 dihydrodiol 9,10 oxide of BP (BPDE).<sup>12</sup> Several studies indicate that this derivative is the major metabolite responsible for the *in vivo* binding of BP to nucleic acids in rodent,<sup>12</sup> bovine and human cells.<sup>13,14,15</sup> BPDE has two stereoisomeric conformations each having

two enantiomeric forms.<sup>16</sup> In isomer I (7R, 8a - dihydroxy - 9a, 10a epoxy - 7,8,9,10 tetrahydro BP) the 7 hydroxyl and the 9,10 oxide groups are on opposite sides of the plane formed by the aromatic ring system, and in isomer II (7S, 8a - dihydroxy - 9B, 10B epoxy - 7,8,9,10 tetrahydro BP) the hydroxyl and oxide groups are on the same side of the plane. In human and bronchial explants, BP becomes bound to DNA essentially as a single component.<sup>13</sup> Evidence has been presented that this occurs mainly via a specific isomer of BPDE, the 7R, 8S, 9R, 10R enantiomer of isomer I (7R BPDE I), resulting in the trans addition of the 10 position of the hydrocarbon to the 2 amino group of guanine.<sup>13</sup>

Although the exact position of covalent binding of BP to DNA is known, little information is available as to the physical structure and the microenvironment of the carcinogenic moiety when it is covalently attached to DNA. To examine this aspect of the problem we have prepared an appropriate in vitro model system which mimics the in vivo system closely and provides larger quantities of modified DNA which are necessary for this spectroscopic investigation. We have modified native calf thymus DNA in vitro with racemic BPDE I under the condition where 0.1 to 0.7% of the bases were modified. The base specificity of the binding to BPDE was determined by enzymatic hydrolysis of the DNA and high pressure liquid chromatographic (HPLC) separation of the modified deoxynucleotides. Striking stereospecificity was observed, only one adduct was detected, the same 7R BPDE - guanosine adduct which is formed in DNA of human and bovine bronchial explants exposed to BP<sup>13</sup> is also found in the in vitro reaction.

The covalently bound BP retains a pyrene-like aromatic chromophore,<sup>17,18</sup> which has a relatively long excited singlet state fluorescence lifetime; this property renders the fluorescence a sensitive and convenient probe for the microenvironment of the pyrene-like chromophore of BP bound covalently to DNA. The basic approach that was utilized in this study is outlined in Fig. 1. We have

employed cations and anions and neutral molecules to quench the singlet excited state of the bound hydrocarbon. If the aromatic molecule is intercalated between the base pairs and is thus located inside the DNA helix, it will be less accessible to quenchers that cannot readily penetrate into the double helix (Fig. 1A), but will exhibit quenching by  $\text{Ag}^+$  and  $\text{Hg}^{++}$  (Fig. 1D). These ions also bind to DNA by an intercalation mechanism. On the other hand, if the chromophore is located on the outside of the helix, the reverse will be true, namely external quenchers will show large quenching effects (Fig. 1B), while metal ions bound to the DNA bases will show little or no effect (Fig. 1C). We show in this report that it is also possible for DNA itself to exhibit intermolecular quenching of the hydrocarbon fluorescence.

We have used the fluorescence properties of the hydrocarbon as a probe of its microenvironment when bound to DNA and provide evidence that the aromatic moiety of the bound BP is located outside of the DNA helix. This result is consistent with the conclusions drawn from electric linear dichroism results which are described in the accompanying paper.<sup>10</sup>

## EXPERIMENTAL SECTION

### Materials

Calf thymus DNA was purchased from Worthington Chemicals and was used without further purification. The hyperchromicity of the DNA solutions was ~ 40%. Crystalline 7,8 diol 9,10 epoxy benzo(a)pyrene and 7,8,9,10 benzo(a)-pyrene tetrol were generous gifts of Dr. R.G. Harvey. [<sup>3</sup>H] BPDE I (specific activity 220 $\mu$  Ci/ $\mu$  mole) was provided by Dr. E.V. Gelboin, N.C.I. BPDE I - guanosine markers, characterized for stereospecificity, were kindly provided by Dr. Grzeskowiak.<sup>13</sup> KI,  $\text{AgNO}_3$  and  $\text{HgCl}_2$  were reagent grade and were used without further purification. 4-amino-2,2,6,6 tetramethyl piperidinoxy was purchased from Aldrich.

## Methods

We have investigated the concentration and time dependence of the covalent binding of BPDE I at a fixed concentration of DNA. The reaction of a racemic mixture of BPDE I and the separation of the unreacted BPDE derivatives were carried out as previously described.<sup>19</sup> Solutions contained 0.05M sodium cacodylate buffer (pH = 7.1), 5% ethanol and 10  $A_{260}$  units per ml of native calf thymus DNA and various amounts of BPDE I. A racemic mixture of [<sup>3</sup>H] BPDE I was used to establish the low extent of in vitro binding for the concentration and time dependence studies. The radioactive hydrocarbon was dissolved in absolute ethanol and aliquots were added to the DNA solutions to give a final hydrocarbon concentration of  $1.4 \times 10^{-4}$  M,  $2.7 \times 10^{-4}$  M,  $4.1 \times 10^{-4}$  M and  $5.5 \times 10^{-4}$  M. The covalent binding was linearly dependent on the concentration of BPDE used, with the extent of binding relative to the mononucleotides of 0.15%, 0.33%, 0.50% and 0.70%, respectively. The incubation time of the reaction was 15 minutes at 37°C; longer incubation times did not result in higher modification. After establishing the reaction conditions, nonradioactive BPDE I was used and the amount of BPDE bound was calculated by its UV absorption characteristics<sup>19</sup> and the results obtained were in good agreement with the radioactivity studies.

The in vitro modified DNA was enzymatically hydrolyzed following the general procedure previously described.<sup>20</sup> The modified deoxynucleotides isolated by Sephadex LH 20 chromatography were co-chromatographed on a high pressure liquid chromatograph (HPLC) with various UV markers previously characterized by circular dichroism.<sup>13</sup> The HPLC separation was carried out on a Zorbax ODS column (2.1 mm I.D.) at 50°C and 2500 psi. The samples were eluted with a linear gradient of 25 to 80% methanol in water.

All absorption measurements were made on a Cary Model 14 recording spectrophotometer and all fluorescence measurements were made on a Perkin Elmer Hitachi MPF-2A fluorimeter. Fluorescence decay profiles were measured by the single photon counting technique. The apparatus used for these measurements is described elsewhere.<sup>7</sup> For the fluorescence lifetime measurements a 310 interference filter and a 7-60 Corning filter were used to select the excitation wavelengths while two 3-74, a 5-61 and a 0-52 Corning filters were used to select the fluorescence emission. Even with this filter combination there is some scattered light apparent in the decay profile. A DNA blank of the appropriate concentration was placed in the photon counting apparatus for the same amount of time as the modified sample, and these background counts were subtracted from the accumulated decay.<sup>21</sup>

All fluorescence measurements were made in square 1 cm path length quartz fluorescence cuvettes. When it was necessary to remove dissolved oxygen, the cuvette was fitted with a rubber septum and bubbled with oxygen-free nitrogen gas (purchased from the Linde Division of Union Carbide) for at least fifteen minutes. When doing quenching experiments, concentrated salt solutions were added to the cuvette with a Hamilton syringe and rebubbled for at least five minutes prior to making the measurements.

Relative fluorescence yields were measured by matching the optical density of the BPDE-DNA adduct to that of the free tetrol at 345 nm, then measuring the steady-state fluorescence at a number of different excitation and emission wavelengths and averaging the results. For absorption measurements at 345 nm containing DNA, the appropriate concentration of unmodified DNA was used in the reference compartment of the absorption spectrophotometer in order to ensure that the absorbance at 345 nm was due to the BPDE-DNA adduct and not to the DNA absorption itself. Beer's Law was checked for the BPDE-DNA adduct

in the optical density range 0.1-0.025 to ensure that there was no change in the extinction coefficient of the bound chromophore as a result of the dilution of the complexes. The samples with reported optical densities lower than 0.025, were prepared by appropriate dilution of a more concentrated sample.

## RESULTS

### The In Vitro Model System

Since the amount of adduct formed in animal systems and in cell culture systems is very small, 1 PAH per  $10^4$ - $10^5$  nucleotides, it is necessary to find a corresponding in vitro model to provide larger quantities for physical studies. Taking into consideration four possible DNA bases and four possible isomeric forms of BPDE we have anticipated a considerable degree of complexity in BPDE binding to DNA. Therefore we confined our studies to isomer I of BPDE.

Figure 2 represents the HPLC profile obtained when a 0.1% modified [ $^3\text{H}$ ] BPDE-DNA sample was digested and co-chromatographed with the UV marker BPDE-guanosine adduct whose structure and stereochemistry have been previously elucidated.<sup>13</sup> In this model compound the 2-amino group of guanine attacks position 10 of the  $\gamma\text{R}$  enantiomer of BPDE I via trans opening of the epoxide ( $\gamma\text{R}$  BPDE I-guanosine) and its structure is presented on the top of Fig. 2. As can be seen in Fig. 2, following enzymatic digestion of the [ $^3\text{H}$ ] BPDE I-DNA sample, the modified deoxynucleotides elute from the HPLC essentially as a single component with the same retention time as the  $\gamma\text{R}$  BPDE I-guanosine marker. It is observed that using the racemic mixture of [ $^3\text{H}$ ] BPDE I, only one optical enantiomer is bound to native DNA. On the other hand, when RNA is modified under the same reaction conditions, the HPLC profile of modified nucleosides reveals four distinct radioactive peaks, and several minor components (V. Ivanovic, unpublished studies). The predominance of one enantiomer bound using the racemic mixture of BPDE I suggests that the in vitro reaction with native DNA is characterized by a considerable



degree of stereospecificity and base specificity. The double stranded property of native DNA may contribute to the selectivity of its modification. The same type of HPLC profile extends to the higher modifications (up to 1%, not presented here).

Figure 2 demonstrates that the in vitro model system selected for the physical studies mimics closely the in vivo situation.<sup>13</sup> It also provides evidence that the in vitro binding to native DNA is chemically homogeneous, which is essential for further physicochemical and conformational studies.

### Spectra

Figure 3 shows the excitation and emission spectra of the BPDE-DNA adduct. The adduct has absorption and corresponding excitation maxima at 330 and 345 nm. The absorption spectra of the BP-tetrol and the diol epoxide dissolved in water have maxima at 327 and 343 nm while the fluorescence occurs at 380 and 400 nm.

When polycyclic aromatic hydrocarbons physically bind to DNA (via the intercalation mechanism), there is a larger red shift ( $\sim 10$  nm) in the absorption and fluorescence spectra of the bound hydrocarbon. This bathochromic shift can be described as arising from an increase in the molecular polarizability of the excited state, which is responsible for the fact that the stabilization of the stacked hydrocarbon by dispersive interactions with base pairs becomes stronger in the excited states.<sup>22</sup> In the case of the BPDE-DNA adduct there is a comparatively small red shift (2-3 nm) in the absorption spectrum of the bound hydrocarbon.

### Fluorescence Decay Profile and Oxygen Quenching

Figure 4A shows the time dependence of the fluorescence emission of the BPDE-DNA adduct in the presence and absence of oxygen. The first important feature of the decay is that it is strikingly nonexponential. Since, chemically,

there is only one type of covalent complex formed using the present reaction conditions, the apparent heterogeneity must arise from physically different microenvironments of the bound chromophore. The most likely cause of these differences is discussed in the section below.

The effect of molecular oxygen on the fluorescence decay curve is also shown in Fig. 4A. It can be seen that the long component of the decay is quenched in the presence of oxygen. Typical values for the long component of the decay are  $130 \pm 10$  ns in air saturated solutions and  $200 \pm 10$  ns in oxygen free solutions. These lifetimes are, within experimental error, the same as those of the diol epoxide or the tetrol dissolved in aqueous solutions without DNA. If the lifetimes of the long component are substituted into the familiar Stern-Volmer equation

$$\frac{1}{\tau} = \frac{1}{\tau_0} + K[Q] \quad (1)$$

where  $\tau$  is the lifetime in the presence of quencher of concentration  $Q$  and  $\tau_0$  is the lifetime in the absence of quencher, the bimolecular quenching constant  $K$  can be calculated.  $K$  is proportional to the encounter frequency between the chromophore and the quencher, and thus  $K$  reflects the relative accessibility of the chromophore to the quenching molecule. It has been shown that when ethidium bromide is intercalated in native DNA the oxygen quenching constant for the bound dye is  $\sim 1/30$  that of the free dye.<sup>23</sup> Similarly, the quenching of the triplet excited states of benzo(a)pyrene physically bound (intercalated) to DNA is also reduced by a factor of  $\sim 20$  as compared to the quenching of aromatic hydrocarbon triplet excited states in free solution without DNA.<sup>7</sup> These results indicate that the accessibility to oxygen is reduced upon intercalation of PAH molecules into DNA. Using equation (1) and a concentration

of oxygen of  $2.76 \times 10^{-4}$  M for an air-saturated solution, the oxygen quenching constant for the long lifetime-component of the BPDE-DNA adduct is  $9.2 \pm .7 \times 10^9$   $M^{-1} s^{-1}$ . This is the same quenching constant that is measured for either the free tetrol or the diol epoxide ( $9.9 \pm 0.9 \times 10^9$   $M^{-1} s^{-1}$ ), and which corresponds approximately to the diffusion controlled limit. There is no discernable change in the lifetime of the short component of the BPDE-DNA adduct in the presence of ambient oxygen. On the basis of equation (1) this is to be expected since this lifetime is short and the quencher concentration is relatively low.

The oxygen quenching results therefore show that the long component of the BPDE-DNA adduct is totally accessible to molecular oxygen and is not shielded by the double helix. This indicates that the chromophore corresponding to the long component is not intercalated between the base pairs; however, no information can be gained about the nature of the short component from the oxygen quenching results.

#### Factors Affecting the Fluorescence Yield

The heterogeneity of the fluorescence decay of the BPDE-DNA adduct makes qualitative and quantitative analysis of fluorescence data more complex than if there were only a single fluorescence emitting site. If it is assumed that there are only two emitting sites, the lifetime data can be fit to the equation

$$I(t) = I(o) X_1 e^{-t/\tau_1} + I(o) X_2 e^{-t/\tau_2} \quad (2)$$

where  $I(t)$  is the fluorescence intensity at time  $t$ ,  $I(o)$  is the fluorescence intensity at time zero,  $X_1$  and  $X_2$  are the fractions of binding sites radiating with lifetimes  $\tau_1$  and  $\tau_2$  respectively ( $X_1 + X_2 = 1$ ). When measuring fluorescence decays by the single photon counting technique, the displayed fluorescence profile is composed of the convolution of the lamp excitation

function with the fluorescence of the sample. When the fluorescence lifetime of the system under study is comparable to the lifetime of the excitation flash, computer analysis of the experimentally determined decay profile is necessary to determine the correct fluorescence lifetimes. Using our apparatus, it was determined that fluorescence lifetimes longer than 7 nanoseconds do not have to be treated by convolution techniques.<sup>24</sup> The data shown in the lower curve of Fig. 4A can be fit to the equation

$$\frac{I(t)}{I(0)} = 0.75 e^{-t/8.2 \text{ ns}} + 0.25 e^{-t/125 \text{ ns}}$$

From this analysis there are three times more BP molecules radiating with a short lifetime as compared to the long lived component at this concentration of DNA. The ratio of short component to long component varied from preparation to preparation and it was therefore necessary to examine the underlying causes of this variation.

Since, chemically, there is only one covalent binding site of the diol epoxide to DNA under the present reaction conditions, the existence of a non-exponential fluorescence decay implies that a fraction of the bound chromophore is being strongly quenched and that these molecules are in a physically different environment than those molecules radiating with a long lifetime. Since it is known that DNA quenches the fluorescence of physically bound BP,<sup>7</sup> the shortened fluorescence lifetime is thus probably also due to an intermolecular interaction between the aromatic hydrocarbon and the DNA. It is important to note that the lifetime of the long component of the BPDE-DNA complex is the same as that of BPDE free in aqueous solution. This finding indicates that those molecules radiating with the long lifetime are not perturbed by the presence of DNA.

It is important to determine the relative fluorescence yield of bound chromophores in this type of study to determine if there is any appreciable fraction of bound molecules which decay to the ground state nonradiatively (static quenching). If there is an appreciable amount of static quenching taking place, then the results of any fluorescence measurements are pertinent only to that group of molecules which are capable of decaying by fluorescence. In such cases it is not possible to obtain information about the subgroup of molecules that are statically quenched, i.e. which decay by nonradiative pathways.

Static quenching occurs<sup>25</sup> when the quencher is located within an active sphere surrounding the potentially fluorescence-emitting molecules, and when quenching of the excited state occurs before it has any finite probability to decay radiatively. Experimentally this phenomenon manifests itself by a decrease in the steady-state luminescence yield, while no change in lifetime of the fluorescence emitting group of molecules is observed. To determine if there is any static quenching taking place, it was necessary to compare the fluorescence quantum yield of the BPDE-DNA complex in solution to that of free BPDE dissolved in aqueous solution in the absence of DNA.

In all comparisons, BP-tetrol was used instead of the diol epoxide. This was done because of the relative instability of the diol epoxide. The relative quantum yield and singlet lifetime of equimolar solutions of the BPDE and of the BP-tetrol dissolved in water were determined to be the same, therefore it is permissible to compare the fluorescence characteristics of the BP-tetrol to that of the BPDE-DNA adduct.

The determination of the extent of static quenching was performed as previously shown,<sup>7</sup> by measuring the steady-state quantum yield of the bound BPDE-DNA adduct ( $Q_{DNA}$ ) relative to the quantum yield of the BP-tetrol in water ( $Q_{H_2O}$ ) and by using equation (3)

$$Q = \frac{Q_{\text{DNA}}}{Q_{\text{H}_2\text{O}}} = \frac{I(0)}{I_{\text{H}_2\text{O}}(0)} \left( \frac{X_1\tau_1 + X_2\tau_2}{\tau_{\text{H}_2\text{O}}} \right) \quad (3)$$

where  $X_1$ ,  $\tau_1$ ,  $X_2$  and  $\tau_2$  were previously defined and  $\tau_{\text{H}_2\text{O}}$  is the lifetime of the free BP-tetrol in water. The  $\frac{I(0)}{I_{\text{H}_2\text{O}}(0)}$  then gives the fraction of molecules bound at fluorescence emitting sites.<sup>7</sup> During the course of these studies it was discovered that DNA itself had an effect on the fluorescence yield of BPDE and that this effect varied with concentration of DNA. It was therefore necessary to investigate this effect quantitatively. This was accomplished by diluting a given BPDE-DNA sample with buffer, and by measuring the effect of this dilution on the fluorescence yield and lifetime of BPDE.

The effect of dilution on the fluorescence decay profiles is shown in Fig. 4B. The results for a 0.1% modified sample (upper curve) and the same sample diluted tenfold with buffer (lower curve) are shown. As can be seen in this figure the fraction of the long component of the decay increases upon dilution of the sample, i.e. as the effective DNA concentration is decreased. Table I summarizes the results of the quantum yield measurements of BPDE-DNA complexes relative to that of the free BP-tetrol, and the effect of dilution on the fluorescence characteristics of the BPDE-DNA adduct. As can be seen from Table I and Fig. 4B the effect of dilution on the decay characteristics of the BPDE-DNA complex is to decrease the amount of the short component of the decay curve and also to increase the overall quantum yield of the bound BPDE-DNA as the concentration of DNA is decreased. The data in Table I also show that at the highest concentration of DNA up to 18% of all molecules are quenched statically. However, the extent of static quenching becomes negligible as the sample

is diluted. Since the fluorescence lifetime and absolute quantum yield of a solution of fluorescence emitting molecules should not change as a function of BPDE molecules in this concentration range, this implies that the quenching that is observed is due to the DNA in solution. The results of this dilution experiment show that DNA is involved in quenching of the bound BPDE. In order to verify that the quenching by DNA is due to an intermolecular mechanism, the fluorescence characteristics of a 0.5% modified sample were measured, then unmodified DNA was added to the solution and the fluorescence characteristics were remeasured. The results are shown in Table II and Fig. 4C. Table II shows that as unmodified DNA is added to the solution the steady-state yield of the fluorescence decreases. Figure 4C shows the fluorescence decay of the same sample at  $1.28 \text{ A}_{260/\text{ml}}$  (upper curve) and at  $8.60 \text{ A}_{260/\text{ml}}$  (lower curve). It is clear that the fraction of the long component decreases as DNA is added, and this long component appears to be converted to the short component. This shows indeed that there is an intermolecular DNA interaction which takes place that quenches the fluorescence of the BPDE-DNA adduct. It is also noted that the lifetime of the long component is unchanged upon the addition of unmodified DNA. This quenching is atypical since the quenching of the long component is not static and it is not completely dynamic. If the quenching were static, the lifetime would not change but there would be less initial intensity. If the quenching was completely dynamic there would be only one measured lifetime. Since DNA in solution undergoes random collisions which may be "sticky" (long lived on the timescale of the fluorescence lifetime, i.e.  $\lesssim 200 \text{ ns}$ ), there are probably sites of intermolecular DNA-DNA contact at any particular instant of time. At any given DNA concentration there will be a distribution of quenched sites, the fraction of which will increase as the DNA concentration increases due to the increased rate of collisions between segments of two different DNA molecules.

The effect of DNA on the fluorescence of a physically bound BP-DNA complex was also investigated. The result of this experiment (not shown here) was that the addition of DNA to a solution containing the physical benzo(a)pyrene-DNA complex did not lead to any quenching of the fluorescence of the intercalated benzo(a)pyrene molecules. This result again shows that there is a difference in the behavior of intercalated PAH molecules and the BPDE-DNA complex; when the aromatic molecule is intercalated within the DNA helix there is no effect of additional DNA on the luminescence. However, if the fluorescence emitting molecule is located external to the helix, the quenching ability of DNA and intermolecular DNA interactions are strong enough to significantly alter the fluorescence characteristics of the hydrocarbon molecule. In fact this finding can be used to differentiate between an externally bound hydrocarbon and an intercalated one, and it also can be used as a probe of DNA-DNA interactions in solution. If the fluorescence yield in Table II is normalized to 100% at zero DNA concentration and the resultant quantum yields are plotted as  $F_0/F$ , where  $F_0$  is the fluorescence intensity of BPDE in the absence of DNA, and  $F$  is the fluorescence intensity in the presence of a given concentration of DNA, versus DNA concentration (another form of the Stern-Volmer Law), a bimolecular quenching constant of  $2 \times 10^{10} \text{ M}^{-1} \text{ s}^{-1}$  is calculated from the initial portion of the curve for the quenching of BPDE by DNA. Since this value is higher than the diffusion controlled limit, it is also indicative of intermolecular DNA-DNA interactions in solution.

#### QUENCHING OF THE FLUORESCENCE OF THE BPDE-DNA ADDUCT BY IODIDE IONS

Iodide ions have previously been used to study the interaction of aromatic dyes with DNA by quenching of the dye fluorescence.<sup>26</sup> Iodide ions cannot penetrate easily into the DNA helix. It was shown that the bimolecular quenching constant was  $\sim$  six times lower for quinacrine intercalated within



DNA as compared to the quenching constant in free solution. This lower quenching constant was interpreted as being due to the reduced accessibility of the dye molecule to the quencher as a result of being intercalated in the helix.<sup>26</sup>

We have used iodide ions as quenchers of the fluorescence to study the accessibility of the BPDE-DNA adduct and the results are shown in Fig. 5. In this Stern-Volmer graph we have plotted both the steady-state ( $F_0/F$ ) and the lifetime ( $\tau_0/\tau$ ) versus iodide ion concentration,  $[I^-]$ . It is evident that the fluorescence in the aqueous tetrol solution is quenched dynamically since both  $F_0/F$  and  $\tau_0/\tau$  are linear functions of the quencher concentration. The marked non-linearity of the  $F_0/F$  curve for a BPDE-DNA (0.03% modification) sample is also shown. This is due to the large fraction of sites exhibiting the short decay time in this complex. On the other hand, the  $\tau_0/\tau$  versus  $I^-$  plot for the long component of the fluorescence of the same BPDE-DNA complex is linear, and thus follows the Stern-Volmer relationship; the bimolecular quenching constant obtained from this latter data is the same ( $1.4 \times 10^9 \text{ M}^{-1} \text{ s}^{-1}$ ) as that of the free tetrol in solution in the absence of DNA.

As a given BPDE-DNA sample was diluted, the  $F_0/F$  versus  $[I^-]$  plots became more and more linear; thus, the Stern-Volmer law is obeyed at low DNA concentrations. It is shown in Fig. 5 that  $F_0/F$  versus  $[I^-]$  plots become linear when the BPDE-DNA solution is diluted by a factor of 50.

These iodide quenching results also indicate that the BPDE chromophore is not intercalated within the DNA. Even at a relatively high DNA concentration the long-lived fluorescence component of the BPDE-DNA complex can be quenched with the same efficiency as the free tetrol. Also, the non-linearity of the Stern-Volmer plot for the BPDE-DNA adduct at high DNA concentration confirms our conclusions about the heterogeneity of the fluorescence emitting sites and correlates with our previously described observation that the fraction of the short-lived component varies with DNA concentration.

We have also been able to quench the fluorescence of the pyrene chromophore in DNA complexes by utilizing a free radical, 4-amino-2,2,6,6 tetramethylpiperidinoxyl (density =  $0.95 \text{ g cm}^{-3}$ ). Again, the long-lived component of the fluorescence of the bound chromophore is quenched as effectively as the free tetrol even though this quencher is larger in size than any of the other quenching molecules employed in this study. The value for  $K$  is  $3 \times 10^9 \text{ M}^{-1} \text{ s}^{-1}$  for this radical.

#### Quenching by $\text{Ag}^+$ and $\text{Hg}^{++}$

Interactions between heavy metal ions and DNA have been studied extensively (see Ref. 27 for a review).  $\text{Ag}^+$  and  $\text{Hg}^{++}$  have been shown to form intercalation type complexes with the DNA bases as is shown schematically in Fig. 1. In the case of  $\text{Ag}^+$ , the binding is a function of pH. Under the conditions employed in this study, there is preferential noncovalent binding of  $\text{Ag}^+$  to guanine at  $r < 0.2$  (where  $r = \text{moles ion/moles DNA phosphate}$ ). On the other hand, it has been shown that the initial covalent binding of  $\text{Hg}^{++}$  takes place at AT rich regions of DNA.

The use of heavy metal ions in quenching the fluorescence of aromatic hydrocarbons bound to DNA has previously been studied.<sup>7</sup> It was shown that metal ions that bind to the DNA bases strongly quench the fluorescence of DNA bound hydrocarbons. It was shown that the  $\text{Ag}^+$  quenches the fluorescence by an external heavy atom effect. The fluorescence is quenched because of an increase in the rate of intersystem crossing ( $S_1 \rightarrow T_1$ ), an effect which arises because of the increase in spin orbit coupling induced by the heavy metal. This exchange type interaction requires an overlap of the orbitals of the aromatic molecule with that of the metal ion and thus a close approach between these two species is necessary.

Figure 6 shows the results obtained for both the physically intercalated BP and the covalently bound BPDE-DNA adduct. The heavy metal ions give rise to a strong quenching of the fluorescence of the intercalated hydrocarbon, but the influence of either metal ion on the fluorescence of the covalent BPDE-DNA adduct is negligible. To ensure that the metal ions in fact influence the fluorescence of the free chromophore, the quenching of the free aqueous tetrol was measured and the quenching constants were found to be  $3.9$  and  $3.6 \times 10^9 \text{ M}^{-1} \text{ s}^{-1}$  for  $\text{Ag}^+$  and  $\text{Hg}^{++}$ , respectively. It should be pointed out that the quenching of the BPDE-DNA adduct was carried out in dilute solutions to ensure that there was only one fluorescence emitting site and that there was no interference from intermolecular DNA quenching effects.

Since the metal ions are known to bind internally to the DNA and since quenching of the hydrocarbons by the metal ions necessitates close contact of the metal ions with the hydrocarbons,<sup>7</sup> the data in Fig. 6 again implies that the aromatic moiety is not located within the DNA but is located externally to the helix.

#### DISCUSSION

The first important finding is the apparent physical heterogeneity of the covalently bound BPDE. It was shown that although there is chemically only one site of DNA binding, the non-exponentiality of the fluorescence decay implies the existence of physically different microenvironments. It was shown that practically all of the bound BPDE molecules are fluorescent when compared to the free tetrol in aqueous solution in the absence of DNA, and that the heterogeneity of the decay is due to quenching of the excited state of the pyrene chromophore by DNA. It was experimentally not possible to verify directly by single photon counting that all of the short component of the fluorescence can be converted to the long-lived form; however, the iodide quenching results with the dilute BPDE-DNA sample shows no deviation from the Stern-Volmer Law and from this we

conclude that in dilute solutions of DNA, there is in fact only one fluorescence emitting site.

The results of the fluorescence quenching experiments show first that the covalently bound BPDE is totally accessible to quenchers external to the DNA helix and second, that there is no effect of DNA bound intercalated metal ions on the fluorescence of the BPDE-DNA adduct. These two facts show that the BPDE molecule is not intercalated in DNA. This is also supported by electric field induced linear dichroism results of these same samples.<sup>10</sup>

Although we can state that the bound BPDE moiety is not intercalated between the DNA base pairs, the question then arises as to where it is located. Since there is only one type of chemical complex formed in this study we can propose three different conformations of the modified region of DNA to explain the fluorescence quenching results. First, since N-2 of guanine is located in the minor groove of DNA, we could place the BPDE in the minor groove. Second, rotation of guanine by  $180^\circ$  from the anti to the syn conformation could give rise to a rotation of the BPDE to an exposed position in the major groove. Third, the local DNA region where the BPDE molecule is bound could be denatured; in this case both the BPDE and the DNA base it is bound to, would be exposed to the aqueous environment.

There appears to be no direct method to distinguish between these three different possibilities. It is not known with certainty how the bimolecular quenching constants would vary for these three possible conformations. A closer examination of the quenching results may, however, give some insight into the problem, even though an exact interpretation cannot be drawn from these results, as mentioned above.

The third conformation proposed where the BPDE and the guanine base to which it is attached are in a locally denatured environment, can easily account

for the quenching results. In this model the BPDE is totally exposed to quencher molecules within the solvent and there is no shielding by the DNA helix; one thus expects quenching by external quencher molecules to take place efficiently (Fig. 1B). In this conformation it is possible for the BPDE chromophore to interact with segments of a neighboring DNA molecule, and one would not expect quenching to take place by DNA bound metal ions for two reasons. First, the aromatic moiety would be located too far away from the bound metal ion. Second, in the case of  $Ag^+$ , since the binding of this metal ion takes place by an intercalation mechanism where the ion is sandwiched between base pairs, one does not expect the ion to bind in the same fashion to a locally denatured region as it binds to native DNA.

It has been shown that when the diol epoxide binds to DNA it induces a small local destabilization of the DNA helix.<sup>19</sup> Even at low extents of modification of DNA by BPDE, the number of base pairs broken for each BPDE molecule bound, is between zero and one. This result indicates that the microscopic region of modification of DNA at the point of attachment of the BPDE is slightly denatured. However, complete denaturation of the one modified base pair would induce destabilization of adjacent base pairs, similar to the results obtained for AAF binding to DNA.<sup>28</sup> For this reason model (3) is not likely to be the correct one.

The differences expected between the measured quenching constants for model (1) and model (2) (i.e. the BPDE is either in the minor groove or is rotated to place it in the major groove) are unknown. It is possible to state only that if the BPDE is in the major groove it is certainly in a more exposed environment than if it were located in the minor groove. Since at this time there is no known chromophore that covalently binds to DNA in such a way that it is localized in the minor groove of DNA, there is no direct verification of

the magnitude of the quenching constants which are expected in this case. It can, however, be stated that the region where the BPDE is bound to DNA must be sufficiently exposed to allow a neighboring DNA molecule to interact with the chromophore. Furthermore, the point of attachment of the hydrocarbon must be such that a negatively charged iodide ion can easily approach it despite the negatively charged phosphate groups, and also that the quenching constant measured for the relatively large free radical is also unaffected by the presence of DNA. Electric field induced fluorescence polarization studies are underway to determine which of the three proposed models of the ones described above, is the correct one.

To summarize, we have developed an in vitro system that exactly mimics the stereoselective in vivo binding of BP in DNA. Utilizing fluorescence lifetime and quenching studies we have shown that the BPDE molecule bound to native DNA is definitely not intercalated in the DNA helix, in contrast to BP physically bound to DNA.

#### ACKNOWLEDGEMENTS

We acknowledge stimulating discussions on various aspects of this work with Drs. H. Brenner, A.M. Jeffrey and M. Pope. This investigation was supported by a contract from the Energy Development and Research Administration to the Radiation and Solid State Laboratory and by grant number CA20851-01 to N.E. Geacintov and grant number CA-21111-01 to I.B. Weinstein, awarded by the National Cancer Institute, DHEW.

## REFERENCES

- ( 1 ) W.W. Davis, M.E. Krahl and G.H.A. Clowes, J. Am. Chem. Soc., 64, 108-110 (1942)
- ( 2 ) H. Weil-Malherbe, Biochem. J., 40, 351-356 (1946).
- ( 3 ) E. Boyland and B. Green, Brit. J. Cancer, 16, 507-517 (1962).
- ( 4 ) A.M. Liquori, B. DeLerma, F. Ascoli, C. Botre and M. Trasciatti, J. Mol. Biol., 5, 521-526 (1962).
- ( 5 ) M. Craig and I. Isenberg, Biopolymers, 9, 689-696 (1970).
- ( 6 ) P.O.P. Ts'o, W.J. Caspary, B.I. Cohen, J.C. Leavitt, S.A. Lesko, Jr., R.J. Lorentzen, and L.M. Schechtman, In: Chemical Carcinogenesis, Part A, P.O.P. Ts'o, J.A. DiPaolo (Eds.) pp. 113-148, Marcell Dekker, Inc New York (1974).
- ( 7 ) N.E. Geacintov, T. Prusik and J.M. Khosrofian, J. Am. Chem. Soc., 98, 6444-6452 (1976).
- ( 8 ) B. Green and J.A. McCarter, J. Mol. Biol., 29, 447-456 (1967).
- ( 9 ) C. Nagata, M. Kodama, Y. Tagashira and A. Imamura, Biopolymers, 4, 409-427 (1966).
- (10) N.E. Geacintov, A. Gagliano, V. Ivanovic and I.B. Weinstein, J. Am. Chem. Soc. (following paper).
- (11) P. Brookes and P.D. Lawley, Nature, 202, 781-784 (1964).
- (12) P. Sims, P.L. Grover, A. Swaisland, K. Pal and A. Hower, Nature, 252, 326-327 (1974).
- (13) A.M. Jeffrey, I.B. Weinstein, K.W. Jennette, K. Grzeskowiak, K. Nakanishi, R.G. Harvey, H. Autrup, and C. Harris, Nature, 269, 348-350 (1977).
- (14) I.B. Weinstein, A.M. Jeffrey, K.W. Jennette, S.H. Blobstein, R.G. Harvey, C. Harris, H. Autrup, H. Kasai, and K. Nakanishi, Science, 193, 592-595 (1976).
- (15) A.M. Jeffrey, K.W. Jennette, S.H. Blobstein, I.B. Weinstein, F.A. Beland, R.G. Harvey, H. Kasai, I. Miura, and K. Nakanishi, J. Amer. Chem. Soc., 98, 5714-5715 (1976).
- (16) K. Nakanishi, H. Kasai, H. Cho, R.G. Harvey, A.M. Jeffrey, K.W. Jennette, and I.B. Weinstein, J. Amer. Chem. Soc., 99, 258-260 (1977).
- (17) P. Daudel, M. Duquesne, P. Vigny, P.L. Grover and P. Sims, FEBS Letters, 51, 250-253 (1975).



References (continued)

- (18) V. Ivanovic, N.E. Geacintov, and I.B. Weinstein, Biochem. Biophys. Res. Comm., 70, 1172-1179 (1976).
- (19) P. Pulkrabek, S. Leffler, I.B. Weinstein, and D. Grunberger, Biochemistry, 16, 3127-3132 (1977).
- (20) K.W. Jennette, A.M. Jeffrey, S.H. Blobstein, F.A. Beland, R.G. Harvey, and I.B. Weinstein, Biochemistry, 16, 932-937 (1977).
- (21) G. Duportail, Y. Mauss, and J. Chambron, Biopolymers, 16, 1397-1413 (1977).
- (22) M.J. Mantione, Photochem. Photobiol. 17, 169-179 (1973).
- (23) J.R. Lakowicz and G. Weber, Biochemistry, 12, 4161-4170 (1973).
- (24) J. Erikson, Ph.D. Thesis, New York University, (1976).
- (25) T. Förster, "Fluoreszenz Organischer Verbindungen", Vanderhoeck and Ruprecht, Göttingen, 1951.
- (26) M. Nastasi, J.M. Morris, D.M. Rayner, V.L. Seligy, A.G. Szabo, D.F. Williams, R.E. Williams, and R.W. Yip, J. Am. Chem. Soc., 98, 3979-3986 (1976).
- (27) R.M. Izatt, J.J. Christensen, and J.H. Rytting, Chem. Rev., 71, 439-481 (1971).
- (28) P.O.O. Ts'o, W.J. Caspary, B.I. Cohen, J.C. Leavitt, S.A. Lesko, Jr., R.J. Lorentzen, and L.M. Schechtman, In: Chemical Carcinogenesis, Part A, P.O.P. Ts'o, J.A. DiPaolo (Eds.) pp. 217-253, Marcell Dekker, Inc., New York (1974).

Table 1.

Effects of dilution on the fluorescence characteristics of BPDE-DNA complex in aqueous solution.

$A_{260}^a$	$A_{345}^b$	$X_1^d$	$X_2^e$	$\frac{X_1 \tau_1 + X_2 \tau_2^f}{\tau_{H_2O}}$	$Q^g$	$\frac{I(0)^h}{I_{H_2O}(0)}$
6.4	0.10	0.82	0.19	0.28	0.23	0.82
3.2	0.05	0.72	0.28	0.38	0.32	0.84
0.64	0.01	0.58	0.42	0.53	0.52	0.98
0.064	0.001 <sup>c</sup>	---	---	---	0.66	---

<sup>a</sup>optical density at 260 nm, 1 cm path length

<sup>b</sup>optical density at 345 nm, 1 cm path length

<sup>c</sup>sample to dilute to accurately determine fluorescence decay. Profile, however there was sufficient fluorescence for steady-state measurements

<sup>d</sup> $X_1$ -fraction of molecules radiating with  $\tau_1$ , from equation

<sup>e</sup> $X_2$ -fraction of molecules radiating with  $\tau_2$ , from equation

<sup>f</sup>calculated quantum yield of BPDE-DNA complex relative to free BaP tetrol in aqueous solution based on time dependent fluorescence decay parameters

<sup>g</sup>steady-state quantum yield of BPDE-DNA complex relative to free BaP tetrol

<sup>h</sup>fraction of BPDE molecules bound to DNA radiatively decay relative to free BaP tetrol in aqueous solution.

Table 2.

Quenching of the fluorescence of BPDE covalently bound to DNA  
by the addition of unmodified DNA.

<u>A<sub>260</sub></u> <sup>a</sup>	<u>%F</u>
1.28	100 <sup>b</sup>
4.93	49
8.60	33
14.84	24

<sup>a</sup>optical density at 260 nm, 1 cm path length.

<sup>b</sup>arbitrarily assigned 100% fluorescence.

FIGURE CAPTIONS

- Fig. 1. Principles of fluorescence quenching methods. Shaded figures - bound aromatic hydrocarbon; ladder-like figures - DNA helices;  $Q_{EX}$  - external quenchers ( $O_2$ ,  $I^-$  and free radical);  $Q_{IN}$  - internal quenchers ( $Ag^+$  and  $Hg^{++}$ ). See text for explanation.
- Fig. 2 High pressure liquid chromatographic profile of DNA adducts formed by in vitro reaction with [ $^3H$ ] BPDE (—) compared to 7R BPDE I quanosine marker (—).
- Fig. 3. Excitation ( $\lambda_{fluorescence} = 400 \text{ nm}$ ) and emission ( $\lambda_{excitation} = 345 \text{ nm}$ ) spectra of BPDE-DNA.
- Fig. 4. Time decay profile of BPDE-DNA adduct. Excitation filters: 310 nm interference filter and 7-60 Corning filter; emission filters: 2 x 3-74, 5-60 and 0-52 Corning filters; 10.575 ns/ch (same filters and time scale for each decay shown).
- A. Effect of oxygen. 0.1% modified DNA ( $6.4 A_{260/ml}$ )  
upper curve - in air saturated solution, lower curve - in the absence of oxygen.
- B. Effect of sample concentration. 0.1% modified sample (air saturated).  
upper curve -  $6.4 A_{260/ml}$   
lower curve - same sample as upper curve diluted tenfold with buffer,  $0.64 A_{260/ml}$
- C. Effect of addition of unmodified DNA. 0.5% modified sample (air saturated).  
upper curve -  $1.28 A_{260/ml}$   
lower curve - same sample as above with unmodified DNA added,  $8.60 A_{260/ml}$
- Fig. 5. Stern-Volmer quenching of fluorescence of free tetrol and BPDE-DNA adduct by iodide ions (oxygen free)

A,  $\frac{\tau_0}{\tau}$ ,  $10^{-6} \text{ M BP-tetrol in } H_2O$

A,  $\frac{F_0}{F}$ ,  $10^{-6} \text{ M BP-tetrol in } H_2O$

O,  $\frac{\tau_0 \text{ long component}}{\tau \text{ long component}}$ , 0.1% modified sample ( $0.64 A_{260/ml}$ )

e,  $\frac{F_0}{F}$ , 0.1% modified sample, ( $0.64 A_{260/ml}$ )

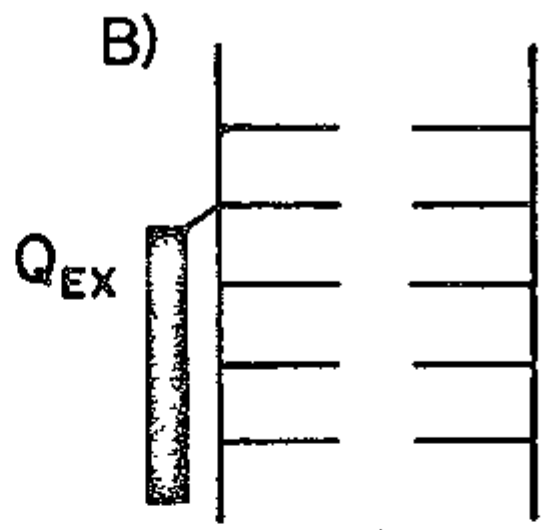
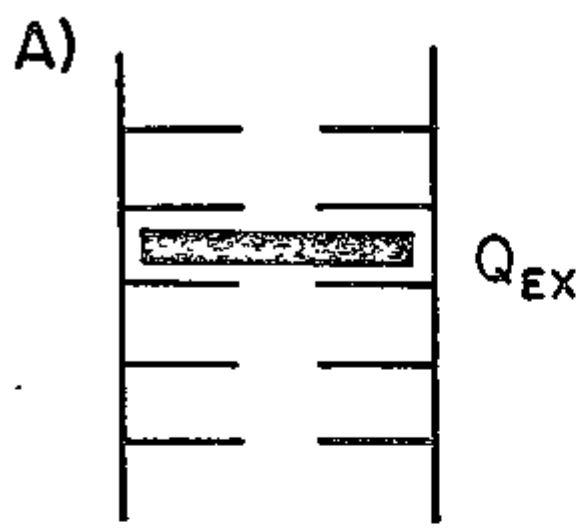
B,  $\frac{F_0}{F}$ , 0.1% modified sample,  $0.013 A_{260/ml}$

D,  $\frac{F_0}{F}$ , 0.03% modified sample, ( $4.7 A_{260/ml}$ )

Figure Captions (continued)

Fig. 6. Effect of metal ions on fluorescence of BP-DNA complexes.

- $\text{Ag}^+$  - BP physically bound to DNA ( $\sim 6 A_{260/\text{ml}}$ )
- $\text{Ag}^+$  - BPDE-DNA adduct ( $0.013 A_{260/\text{ml}}$ )
- $\text{Hg}^{++}$  - BP physically bound to DNA ( $\sim 6 A_{260/\text{ml}}$ )
- $\text{Hg}^{++}$  - BPDE-DNA adduct ( $0.013 A_{260/\text{ml}}$ )



↑  
INEFFICIENT  
QUENCHING

↑  
EFFICIENT  
QUENCHING

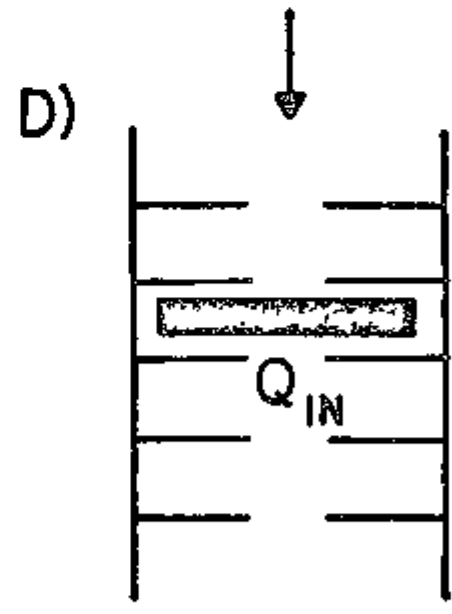
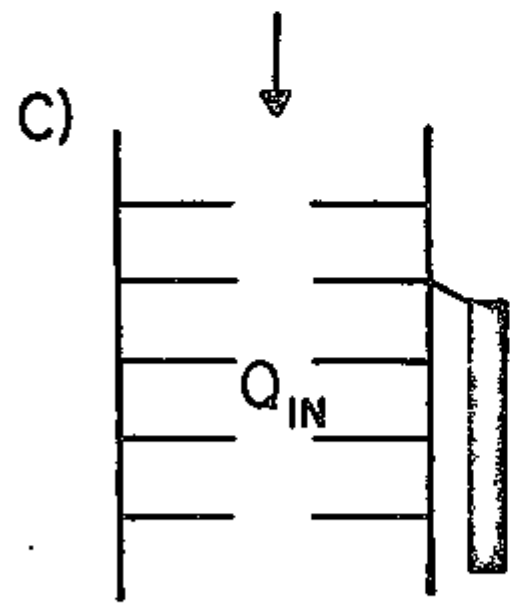


Fig 1 PRUSIK et al

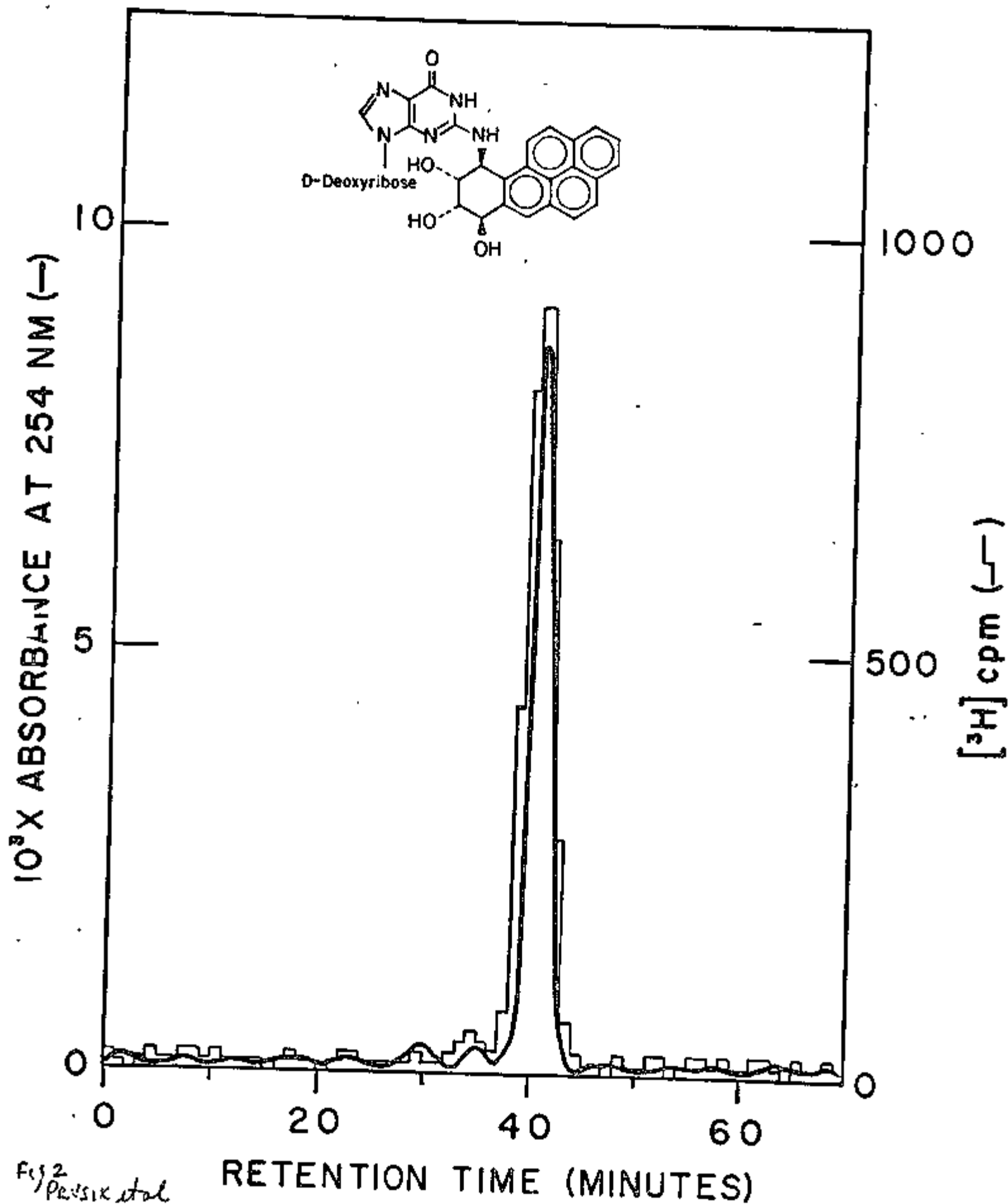
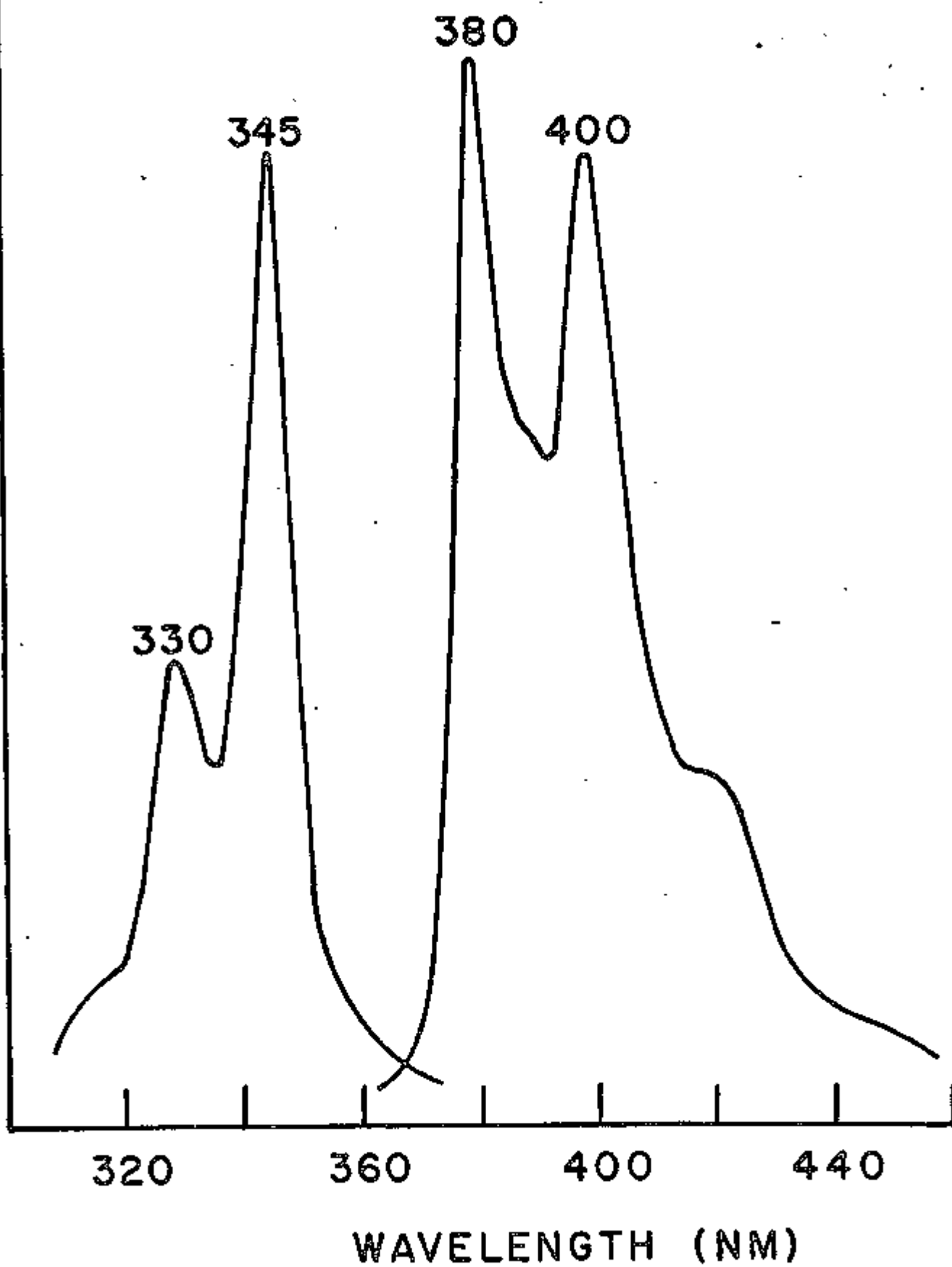


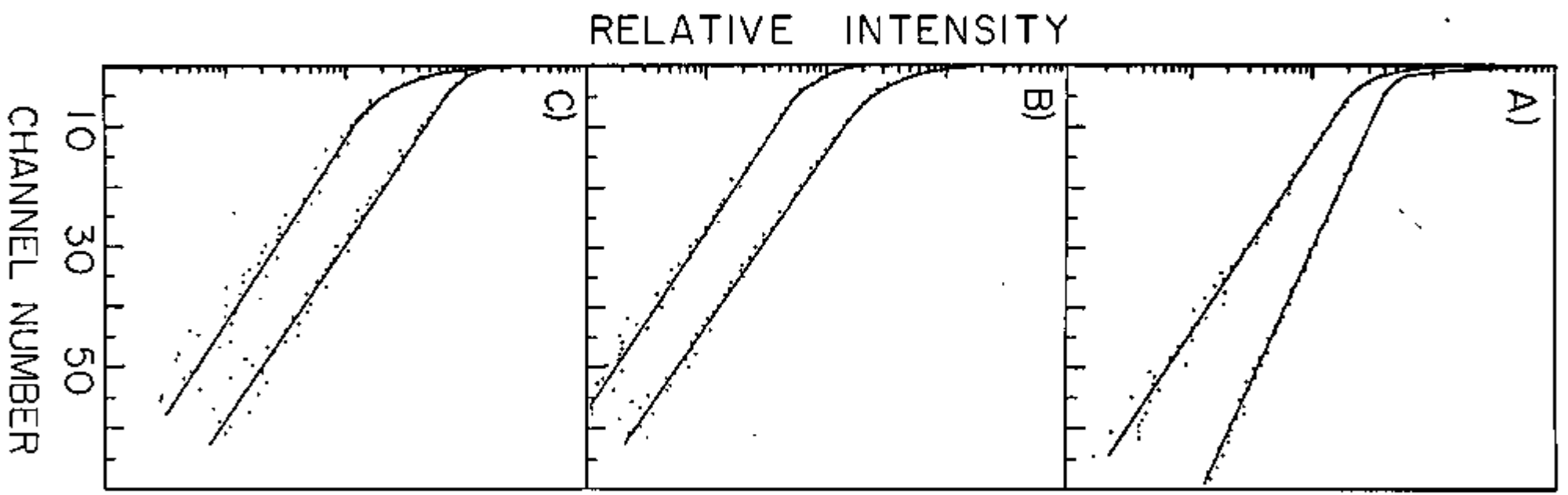
Fig 2  
Pavlik et al

RELATIVE INTENSITY





Hypovisketal



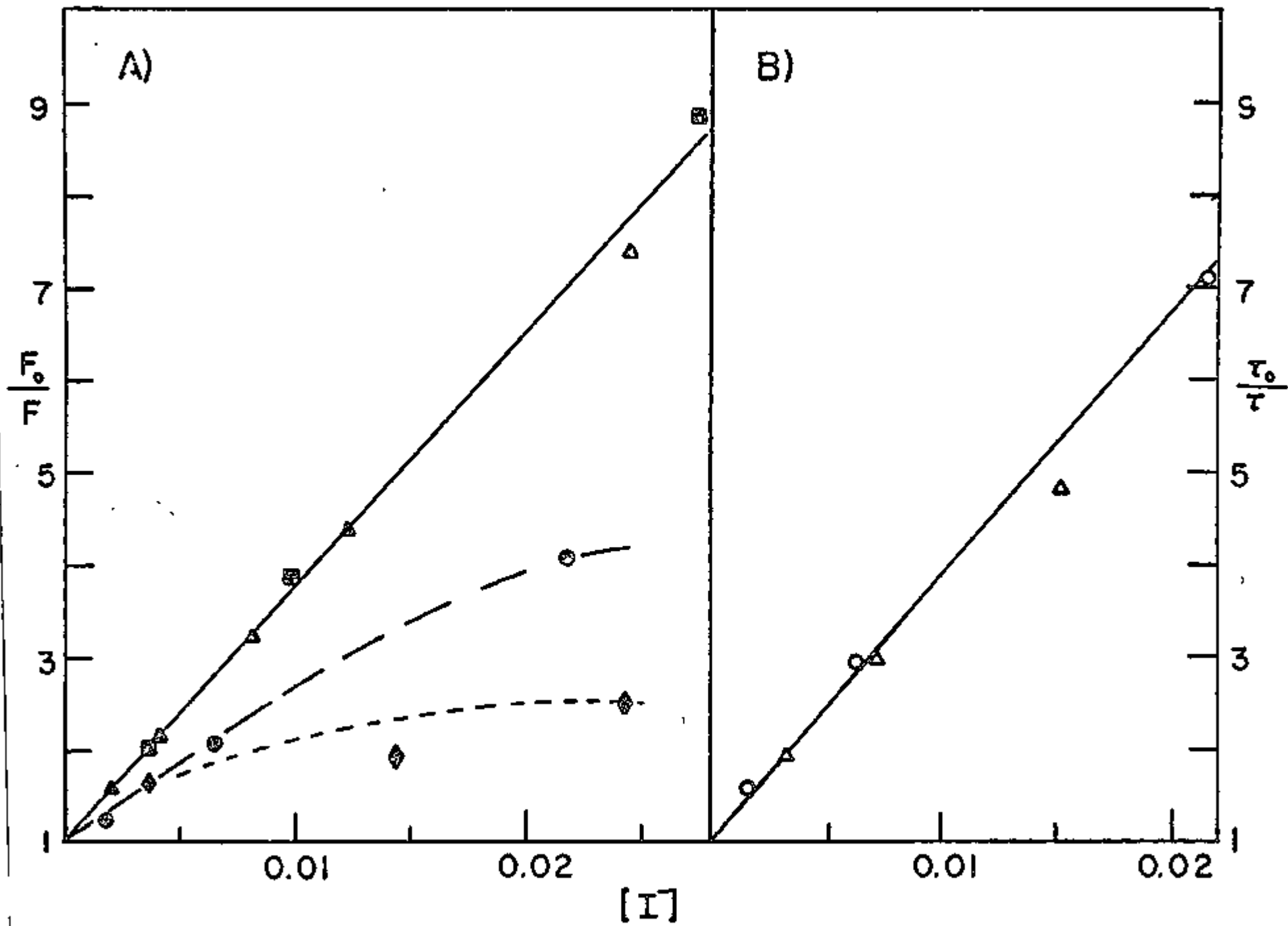


Fig 5 PWSIK

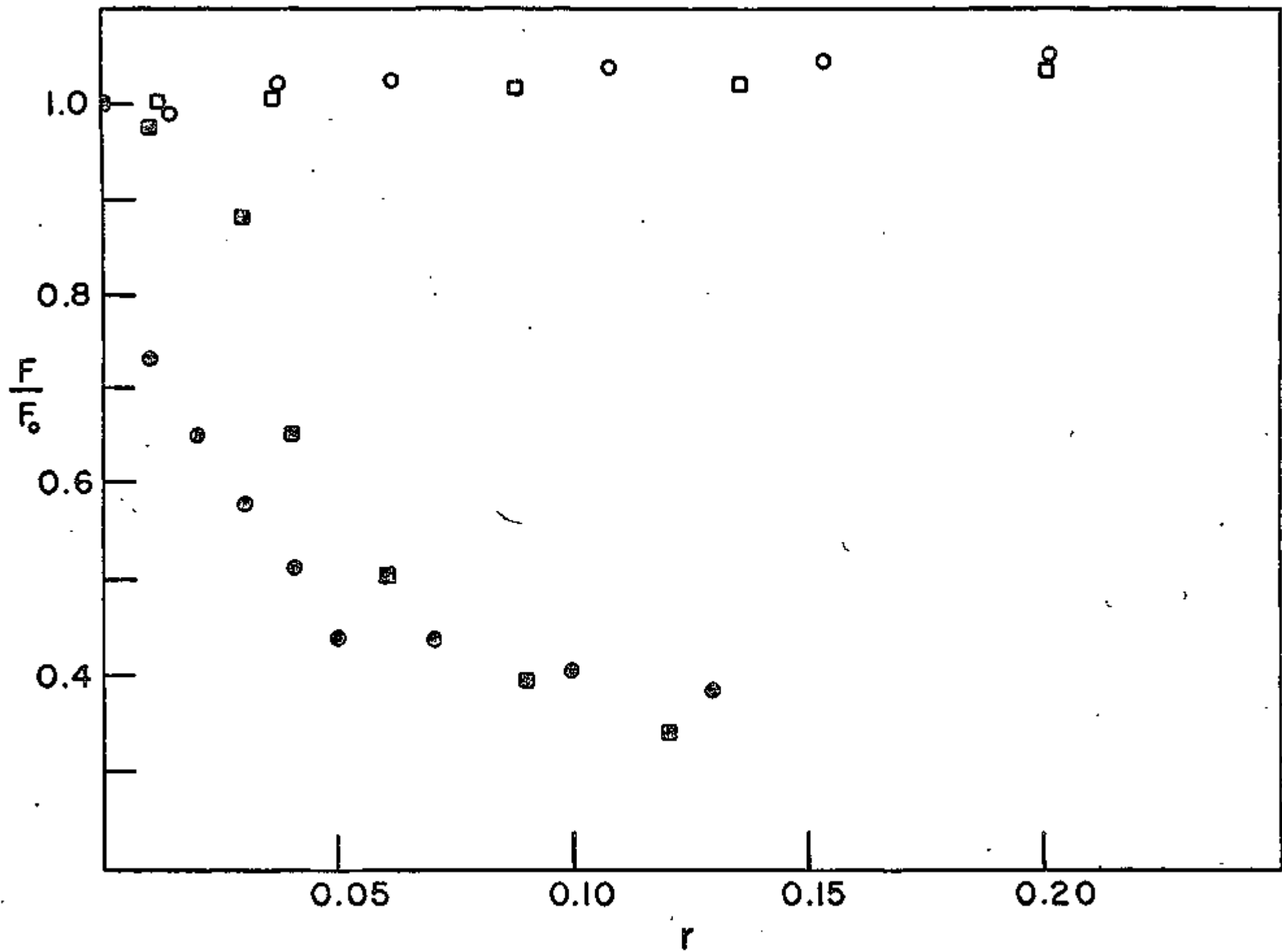


Fig 6  
PRUSIK

Revised  
Jan '77

F

ELECTRIC LINEAR DICHROISM STUDY ON THE  
ORIENTATION OF BENZO(a)PYRENE-7, 8-DIHYDRODIOL  
9,10-OXIDE COVALENTLY BOUND TO DNA

By

N.E. Geacintov  
Chemistry Department and  
Radiation and Solid State Laboratory  
NEW YORK UNIVERSITY, New York, N.Y. 10003 and  
Departement de Biologie,  
CENTRE D'ETUDES NUCLEAIRES DE SACLAY,  
91190 Gif sur Yvette, France

A. Gagliano  
Departement de Biologie,  
CENTRE D'ETUDES NUCLEAIRES DE SACLAY,  
91190 Gif sur Yvette, France and  
UNIVERSITE PARIS XI,  
Institut Universitaire de Technologie, Cachan, France

V. Ivanovic and I.B. Weinstein,  
Division of Environmental Sciences and  
Institute of Cancer Research,  
COLUMBIA UNIVERSITY,  
New York, N.Y. 10032

September 1977

To be submitted to  
Biochem.

## ABSTRACT

The electric linear dichroism spectra of native calf thymus DNA modified to a small extent (one hydrocarbon residue per 1000 bases) by reaction with (±)-7β,8α-dihydroxy-9α,10α-epoxy-7,8,9,10-tetrahydrobenzo[a]pyrene (BPDE), which binds covalently mainly to the 2-amino group of guanosine residues, and physical complexes of benzo(a)pyrene (BP) and proflavine (PF) with DNA were measured. The linear dichroism  $\Delta A$  of the covalent BPDE-DNA complex in the wavelength region of the absorption of the pyrene-like BPDE chromophore is positive. In contrast,  $\Delta A$  is negative in the absorption region of the DNA bases, as well as in the absorption region of the BP and PF molecules physically bound to DNA. It is concluded that the orientation of the BPDE moiety is not of the intercalation type as is the case for the physical BP and PF complexes. The reduced linear dichroism is wavelength dependent for the BPDE-DNA and BP-DNA complexes which indicates that there is a heterogeneity of binding sites with different orientations. The quantitative analysis of such results is discussed in detail and it is concluded that there is one major type of oriented BPDE covalently bound to DNA. The long axis of the pyrene-like chromophore of BPDE lies on the surface of a cone whose axis is that of the DNA helix and whose angle, with respect to this axis, is  $35^\circ$  or less. As expected for intercalation-type complexes the planes of BP and PF are found to be nearly parallel to the planes of the DNA bases.

## INTRODUCTION

Polycyclic aromatic hydrocarbon (PAH) carcinogens are known to bind covalently to nucleic acids in vivo. In living cells the relatively inert PAH molecules are metabolically converted to a variety of hydroxy and epoxy derivatives.<sup>1</sup> The major reactive intermediate involved in nucleic acid binding in the case of benzo(a) pyrene (BP) is a 7,8-dihydrodiol 9,10 epoxide metabolite,<sup>2-7</sup> and the structure of its ( $\pm$ )-7 $\beta$ ,8 $\alpha$ -dihydroxy-9 $\alpha$ ,10 $\alpha$ -epoxy-isomer (BPDE) is shown in Fig. 1.

The covalent binding of the bulky PAH residue to native DNA alters the local structure of the DNA<sup>8</sup> and its template activity in vitro<sup>9,10</sup>. In order to understand how the function of the modified DNA differs from that of normal DNA, it is desirable to have a knowledge of the complete physico-chemical structure and properties of regions of DNA containing the covalently bound BPDE.

In this work we have investigated the orientation of the BPDE chromophore (with respect to those of the DNA bases) in BPDE-DNA complexes. In the present study we have modified native calf thymus DNA to a small extent (one hydrocarbon residue per 1000 bases) by in vitro reaction with BPDE using the methods described elsewhere.<sup>8,11</sup> The complete structure and absolute stereochemistry of the guanosine-BPDE adduct formed by in vitro reaction with RNA and DNA has been elucidated<sup>7,13-16</sup>. The 10 position of the BPDE moiety is linked to the 2-amino group of guanine. Furthermore, this appears to be the principal DNA reaction product in vitro<sup>11</sup>, and it has the same chemical characteristics as the major BP-DNA adduct formed in vivo, when human and bovine bronchial explants are exposed to BP<sup>16</sup>.

In the accompanying paper<sup>11</sup> we have presented evidence, based on fluorescence techniques, that the BPDE moiety in these covalent BPDE-DNA complexes is located on the outside of the DNA helix. Using the electric field-induced linear dichroism technique<sup>17</sup> we show here that the long axis of the pyrene-like chromophore (Fig. 1) is not parallel to the planes of the DNA bases, as is the case of

intercalation-type complexes such as physically bound complexes of DNA and BP or proflavine (PF).

In the electric field-induced linear dichroism technique a voltage pulse is applied to an aqueous buffer solution of either the covalent BPDE-DNA complex or the physical BP-DNA or PF-DNA complexes. The electric field thus produced within the solution tends to orient the DNA and the polycyclic molecules which are either covalently or physically attached to the DNA molecule. Using polarized light, the absorbance is determined with the electric field vector of the polarizer oriented either vertically or parallel with respect to the electric field. The relative orientations of the transition moment vectors, which lie within the planes of the DNA bases and the polycyclic molecules, are then compared. The results indicate that there is a heterogeneity of binding sites with respect to the orientation angles of the BPDE chromophore, and the interpretation of linear dichroism spectra under these conditions is discussed in detail. It is shown that the usual straightforward approach<sup>18,19</sup> to calculate orientation angles from linear dichroism spectra must be modified to take this heterogeneity into account. It is shown that under certain conditions, such as in the case of the covalent BPDE-DNA complexes, a range for the most probable angle of orientation of the BPDE chromophore can be estimated.

## EXPERIMENTAL

### MATERIALS

BPDE was kindly provided by Dr. Ronald G. Harvey of the University of Chicago. Native calf thymus DNA was purchased from Worthington Company, Freehold, New Jersey, and had the following characteristics: protein content 0.1%, hyperchromicity 42% and  $S_{20,w} = 22$ .

### METHODS

Preparation of DNA complexes. The proflavine DNA complex was an aqueous solution containing sodium cacodylate buffer pH 7.1 ( $5 \times 10^{-3} M$ ), DNA ( $1.5 \times 10^{-3} M$ ) and proflavine ( $1 \times 10^{-5} M$ ). At such low concentrations of PF, this dye is fully solubilized by DNA. The intercalated PF showed the characteristic 18nm red shift in the absorption spectrum. The physical complex between BP and DNA was prepared as previously described.<sup>20</sup>

In the previous electric dichroism studies, controversial results have been obtained, due to the denatured state of DNA and/or extensive modification of DNA by N-acetoxy-N-2-acetylamino fluorene (AAF).<sup>18,19</sup> Therefore in the present study, special care has been taken in preparing the in vitro BPDE-DNA samples. The modification of DNA with BPDE was essentially the same as described in the accompanying paper.<sup>11</sup> BPDE ( $10^{-4} M$ ) and DNA (10 A260 units/ml) were incubated 95:5 (v/v) aqueous ethanol containing  $5 \times 10^{-3}$  sodium cacodylate buffer, pH 7.1. The modified DNA samples contained 1 residue of covalently bound BPDE per 1000 nucleotide residues, as detected by uv measurements and confirmed in separate studies using  $\{3_H\}$  BPDE, (the details of these methods are described in reference 8). Electric dichroism measurements were performed at 20°C on BPDE-DNA samples in aqueous solutions containing  $5 \times 10^{-3} M$  sodium cocodylate buffer pH 7.1 with concentrations of DNA in the range 1-10 A260/ml, with no detectable concentration effects in this range on the relative reduced linear dichroism values measured at 260nm (DNA absorption) and at 345 nm (BPDE absorption). There is, however, an effect of DNA concentration on the reduced linear dichroism within the absorption band of DNA, as previously reported by Yamaoka and Charney.<sup>22</sup>



Chemical characterization of the DNA-BPDE sample. The base specificity of the binding of BPDE was determined by enzymatic hydrolysis of the modified DNA and high pressure liquid chromatography of the modified deoxyribonucleosides. As described in detail in the accompanying paper<sup>11</sup>, a single BPDE-nucleoside adduct was obtained. This product results from trans addition of the 2-amino group of guanine to the 10 position of the 7R enantiomer of BPDE, or (+) BPDE derived from (-) BP 7,8 - dihydrodiol .

#### APPARATUS

The voltage source was a specially constructed transistorized power supply which is capable of delivering unipolar square wave pulses of up to 4000 volts with a duration variable from 10 $\mu$ s to 10ms over a 1000 $\Omega$  load. The sample holder consisted of a 1 x 1 cm quartz cuvette containing the electrodes mounted on a teflon block similar to the one described by Fredericq and Houssier.<sup>17</sup> The electrodes consisted of two parallel platinum strips (2 x 1 cm wide) which were held 3mm apart by teflon spacers. This entire assembly was immersed in the cuvette containing the sample. A thermocouple was inserted into a hole in one of the teflon spacers and was used to monitor the temperature of the solution.

The linear dichroism was measured using a dichrograph constructed by J. Breton<sup>21</sup> at Saclay. In this apparatus, light from a Xenon lamp is passed through a grating monochromator followed by a Glan polarizer. A photoelastic modulator (PEM 3, Morvue, Tigard, Oregon) whose driving voltage was automatically adjusted to produce a half-wave retardation at each wavelength was used to produce vertically and horizontally polarized light at a frequency of 100 KHz. The light beam, thus modulated, then passes through the sample cuvette and is incident onto a photomultiplier tube. The 100 KHz component of the photomultiplier tube output is demodulated using a lock-in amplifier which delivers a signal whose magnitude is proportional to the linear dichroism of the sample. Absolute calibration of the apparatus was obtained by using two polarizers. The sensitivity of the apparatus is such that a difference in the alignment of the two polarizers by only five

minutes of arc (corresponding to a linear dichroism of  $6 \times 10^{-5}$ , or 60 ppm) could be readily detected.

The demodulated linear dichroism signal was fed into an oscilloscope for viewing. When necessary, it was fed into an Intertechnique Didac 800 multi-channel analyzer for signal averaging. Typically, 3-5 scans were used to obtain a satisfactory signal/noise ratio. The duration of the square unipolar voltage pulses was 3 ms (apparatus response time 1 ms). Typical signals are shown in Fig. 2. The wavelength dependence of the linear dichroism was recorded point by point.

### RESULTS

The absorption spectra,  $A$ , and the linear dichroism spectra,  $\Delta A$ , of the covalent BPDE-DNA and the physical BP-DNA and PF-DNA complexes are shown in Fig. 3.

The linear dichroism  $\Delta A$  is defined by

$$\Delta A = A_{\parallel} - A_{\perp} \quad (1)$$

where  $A_{\parallel}$  is the absorbance of the sample with the polarization vector of the light oriented parallel to the electric field  $\vec{E}$  applied to the sample, and  $A_{\perp}$  refers to the absorption when the polarization vector is perpendicular to  $\vec{E}$ . As usual, the absorbance  $A$  is defined by  $\log(I_0/I)$ , where  $I_0$  is the intensity of the incident light and  $I$  is the intensity of the light after passing through the sample.

The reduced linear dichroism,  $\Delta A/A$ , for all three complexes studied is shown in Fig. 4. This quantity is constant with wavelength  $\lambda$  for the PF-DNA complex, but varies strongly as a function of  $\lambda$  for the BPDE-DNA and BP-DNA complexes. Before proceeding to a discussion of these results, we shall examine in detail the relationships between the linear dichroism and the angle of orientation of the transition moment vector of the chromophores. This is necessitated

by the fact that the  $\Delta A/A$  spectrum of the BPDE-DNA complex varies with wavelength which, as is shown below, is due to a heterogeneity of orientation angles and physical binding sites.

### DISCUSSION

Reduced Linear Dichroism for a Single Oriented Species. If the chromophore is oriented in such a way that its transition moment vector makes an angle  $\theta$  with the electric field  $\vec{E}$ , then this angle can, in principle, be calculated from the reduced linear dichroism  $\Delta A/A$ , where<sup>17</sup>

$$\frac{\Delta A}{A} = \frac{3}{2} (3 \cos^2 \theta - 1) f(\vec{E}) \quad (2)$$

$A$  denotes the absorbance of light by the sample in the absence of the orienting electric field. A plot of the dependence of the orientation function  $\frac{3}{2} (3 \cos^2 \theta - 1)$  in eq. (2) as a function of  $\theta$  is shown in Fig. 5.

The degree of orientation of the molecule or particle, is defined by the factor  $0 < f(\vec{E}) < 1.0$ , which depends on electric field strength and the temperature.<sup>17</sup> For complete orientation, which has not been achieved for DNA solutions even at field strengths<sup>17,22</sup> of 8000 volts  $\text{cm}^{-1}$ , this orientation function is unity. In our experiments, since we used a concentrated buffer solution, we utilized very low electric fields (the effective voltage was typically 200 volts, corresponding to an electric field strength of  $\approx 700$  volts  $\text{cm}^{-1}$ ). We were limited to these low voltages in order to minimize deleterious heating effects; thus, in these experiments  $f(\vec{E}) \ll 1.0$ . The orientation angle  $\theta$  of a chromophore bound to DNA can, nevertheless, be estimated by comparing the reduced linear dichroism,  $\Delta A/A$ , in the wavelength region of absorption by the chromophore, with the  $\Delta A/A$  values at 250-260 nm, where absorption is due to the transition moments of the DNA bases. The transition moment vectors at 250-260 nm are oriented within the planes of the purine and pyrimidine bases, and it is assumed that  $\theta$  would be  $90^\circ$  for complete orientation of DNA. The DNA tends to align itself with the

helix axis parallel to the applied electric field<sup>17,22</sup>, with the planes of the bases perpendicular to  $\vec{E}$ . This approach was utilized by Chang *et al*<sup>18</sup> and by Fuchs *et al*<sup>19</sup> to deduce the orientation angle of the carcinogen N-acetoxy-N-2-acetylaminofluorene (AAF) bound covalently to DNA. Using the ratio of the reduced linear dichroism for DNA and AAF, where

$$\frac{(\Delta A/A)_{\text{AAF}}}{(\Delta A/A)_{\text{DNA}}} = \frac{3 \cos^2 \theta_{\text{AAF}} - 1}{3 \cos^2 90^\circ - 1} = 1 - 3 \cos^2 \theta_{\text{AAF}} \quad (3)$$

the orientation factor  $f(\vec{E})$  cancels and the orientation angle  $\theta_{\text{AAF}}$  was calculated to be  $60 \pm 4^\circ$  by Chang *et al*<sup>18</sup> and  $82^\circ$  by Fuchs *et al*.<sup>19</sup> Discrepancies of the data have been explained by the fact that the former authors<sup>18</sup> in their studies employed denatured DNA which was very extensively modified with AAF. The later authors<sup>19</sup> have done electric dichroism studies on native DNA which was modified to only a small extent with AAF.

Equation (2) predicts that within the absorption band of the chromophore,  $\Delta A/A$  should be constant and independent of wavelength. This is an important criterion for the interpretation of linear dichroism results according to eqs. (2) and (3). In such cases the calculation of the orientation angle is straightforward. In the next section we discuss the factors which give rise to a variation of the reduced linear dichroism,  $\Delta A/A$ , as a function of wavelength, and what kind of information can be obtained in such cases.

#### Reduced Linear Dichroism in the Presence of More Than One Chromophore

We now suppose that the total absorbance  $A$  of a sample is the sum of absorbance  $A = A_1 + A_2 + \dots$   $A_i = \sum_i A_i$  where the  $A_i$  terms represent the contribution of each chromophore at a given wavelength. We further suppose that each species has a characteristic orientation angle  $\theta_i$  and thus contributes to the overall reduced linear dichroism at a particular wavelength. The reduced linear dichroism is then given by the formula:

$$\frac{\Delta A_\lambda}{A_\lambda} = \frac{3}{2} \frac{\sum_i A_i (3 \cos^2 \theta_i - 1) f_i(\vec{E})}{\sum_i A_i} \quad (4)$$

Allowance has been made for the possibility that the sample is polydisperse and that each oriented species has associated with it a different orientation factor  $f_i(\vec{E})$ . Since this factor is independent of the wavelength  $\lambda$ , it is evident that a wavelength dependence can arise only through a non-cancellation of the  $A_i$  terms in the numerator and denominator of eq. (4). The absorbance  $A_i$  of each species is given by Beer-Lambert's law  $A_i = \epsilon_i(\lambda)C_i l$ , where  $C_i$  is the concentration of species  $i$ ,  $\epsilon_i(\lambda)$  is its extinction coefficient, and  $l$  is the optical pathlength.

We now consider several different possibilities.

Case I. The extinction coefficients of all of the species have the same wavelength dependence, but their orientation angles are different ( $\epsilon_1(\lambda) = \epsilon_2(\lambda) = \epsilon_3(\lambda) = \dots$ , and  $\theta_1 \neq \theta_2 \neq \theta_3$  etc.).

Since  $\epsilon_i(\lambda)$  is the same for each species, eq. (4) reduces to

$$\frac{\Delta A_\lambda}{A_\lambda} = \frac{3}{2} \frac{\sum_i C_i (3 \cos^2 \theta_i - 1) f_i(\vec{E})}{\sum_i C_i} \quad (5)$$

which is independent of wavelength. This case is experimentally indistinguishable from the case in which there is only one species as in eq. (2), which points out the inherent limitation of all linear dichroism techniques. The experimental results do not provide an answer as to whether there is one or more oriented species. When  $\Delta A_\lambda/A_\lambda$  is independent of wavelength, it is justifiable to utilize eq. (2) to calculate the orientation angle. However, in view of eq. (5), this calculated angle reflects some weighted average of the orientation function  $(3 \cos^2 \theta_i - 1)$ .

Case II. The wavelength dependences of the absorption coefficients are different, but their orientation angles are the same ( $\epsilon_1(\lambda) \neq \epsilon_2(\lambda) \neq \epsilon_3(\lambda) = \dots$ , and  $\theta_1 = \theta_2 = \theta_3 = \dots$  etc.)

In this case the reduced linear dichroism becomes

$$\frac{\Delta A_\lambda}{A_\lambda} = \frac{3}{2} (3 \cos^2 \theta - 1) \frac{\sum_i \epsilon_i(\lambda) C_i f_i(\vec{E})}{\sum_i \epsilon_i(\lambda) C_i} \quad (6)$$

Case IIa. We further distinguish two different possibilities. If the electric field dependent orientation factors are all the same ( $f_1(\vec{E}) = f_2(\vec{E}) = f_3(\vec{E}) \dots$ ) then (6) is also independent of wavelength and this case is experimentally indistinguishable from case I.

Case IIb. For polydisperse systems, when  $f_1(\vec{E}) \neq f_2(\vec{E}) \neq f_3(\vec{E}) = \dots$  etc., a wavelength dependence in eq. (6) may arise if one or more terms in the numerator dominate over the others. Such a situation could arise for example, if there were present in the sample particles of different sizes, each displaying a different  $f_i(\vec{E})$  value at a given field strength, and each site associated with a given absorbing species defined by  $\epsilon_i$ . Since both the  $f_i$  and  $\epsilon_i$  values must differ from each other at the same time, we consider this to be a highly specialized case which most likely does not apply to our experiments. It is well known that DNA solutions behave in a polydisperse manner in the presence of electric fields.<sup>17</sup> However, it is unlikely that the  $\epsilon_i(\lambda)$  coefficient<sub>s</sub> of the bound polycyclic aromatic molecules would also vary with the size of the DNA segments. It has already been established that DNA does not undergo chain scissions

when the level of in vitro modification with BPDE is lower than 1.5%.<sup>8</sup> Therefore this highly specialized case ( $f_1 \neq f_2 \neq f_3$ ) is not likely to apply to our experiments where the modification of BPDE-DNA samples was very low (0.1%).

Case III. Both the absorption coefficients and the orientation angles differ from each other ( $\epsilon_1(\lambda) \neq \epsilon_2(\lambda) \neq \epsilon_3(\lambda) \dots$ , and  $\theta_1 \neq \theta_2 \neq \theta_3 = \dots$  etc.)

In this case, there is no cancellation of the wavelength dependent  $\epsilon_i(\lambda)$  terms and the reduced linear dichroism is given by eq. (4). If the  $\epsilon_i(\lambda)$  coefficients are strongly different from each other, i.e. if the chromophores have completely different absorption bands for example, both the  $\Delta A_\lambda$  and the  $\Delta A_\lambda/A_\lambda$  spectra may be quite complex. In such cases it is very difficult to interpret the results quantitatively. Fortunately, at least for the most important case of the BPDE-DNA complex considered in this work, the wavelength dependence of the linear dichroism  $\Delta A$  is nearly the same as the absorption spectrum of BPDE dissolved in ethanol (cf. Fig. 3a and 3b). It is therefore possible to interpret the data quantitatively. Before proceeding to a full discussion of the results obtained with the BPDE-DNA complexes, we first show, using the physical PF-DNA complex, that the general approach of calculating average orientation angles using eq. (3) is justified.

#### Linear Dichroism Exhibited by the Proflavine DNA Complex

The absorption spectrum of the physical complex between proflavine and DNA within the absorption region of the proflavine chromophore, is shown in Fig. 3a. The linear dichroism spectrum  $\Delta A$ , is shown in Fig. 3b. The sign of the linear dichroism signal is negative. Within the absorption band of the DNA bases between 240 and 290 nm,  $\Delta A$  is also negative as is demonstrated in Fig. 3b. In order to observe this linear dichroism, it was necessary to dilute the samples to bring the optical density into the range of 0.05-0.10. The contribution of the proflavine molecules to the total absorbance at 255-260 nm was negligible

at these concentrations. Since the transition moment vectors of both the PF and the DNA bases are oriented within the planes of the aromatic rings, a negative  $\Delta A$  is expected for both PF and the DNA bases if the PF residues are bound via intercalation since the axis of the helix tends to align itself parallel to the electric field.

The reduced linear dichroism for the PF-DNA complex is shown in Fig. 4. Within experimental error,  $\Delta A/A$  is constant as a function of wavelength, which is in agreement with the results of Ramstein *et al.*<sup>23</sup> According to the discussion above, this indicates that either case I or case II applies. The average orientation angle  $\theta_{PF}$  can then be calculated directly using equation (3). This angle should be equal to  $90^\circ$  for the intercalation model of binding of proflavine to DNA. The absolute values of  $\Delta A/A$  for both PF and the DNA bases are given in Table 1. Within experimental error ( $\pm 5\%$ ) these two values are the same which means that  $\theta_{PF} = 90^\circ$ , in agreement with the prediction based on the intercalation model.

Linear Dichroism and the Orientation of the Pyrene  
Chromophore in the Covalent BPDE-DNA Complex.

The absorption spectrum of the BPDE-DNA complex (Fig. 3a) reveals the typical pyrene-like absorption spectrum<sup>12</sup> with peaks at 330 and 347 nm and a shoulder at 325 nm. The BPDE moiety bound covalently to DNA displays a 2-3 nm red shift and a wider linewidth when compared to free BPDE in ethanol solution (Fig. 3a). The broader linewidth is indicative of inhomogeneous broadening. Such a broadening is due to the overlapping of different absorption bands, slightly displaced with respect to each other in wavelength, due to different physico-chemical micro-environments of the chromophore. We identify these different overlapping absorption bands with the different species characterized by the absorption coefficients  $\epsilon_i$  and concentrations  $C_i$  as discussed above.



In such cases the  $\Delta A$  spectrum essentially reflects the absorption spectrum of a particular absorbing species whose transition moment has an orientation such that the  $\Delta A$  of this species is larger than that of the other species whose absorption maxima are slightly shifted in wavelength (inhomogeneous broadening). Under these conditions there is a sharpening in the reduced linear dichroism spectrum  $\Delta A_\lambda/A_\lambda$  with respect to the overall absorption band  $A_\lambda$  to which all of the species contribute. Such a sharpening of the reduced linear dichroism spectrum has been observed in the case of poly- $\gamma$ -benzylglutamate by Charney et al.<sup>26</sup>

Since  $\Delta A_\lambda/A_\lambda$  is wavelength dependent as shown in Fig. 4, we assume that Case III applies to the covalent BPDE-DNA complex. In contrast to the wavelength dependence in the 300-350 nm region corresponding to the BPDE chromophore,  $\Delta A_\lambda/A_\lambda$  is constant within the DNA absorption wavelength region of 250-290 nm; this latter result is in qualitative agreement with the data obtained by Yamaoka and Charney<sup>22</sup> and the decreases in  $\Delta A/A$  below 250 and above 290 nm have been discussed in detail by these workers.

The linear dichroism spectrum  $\Delta A_\lambda$ , presented on Fig. 3b of the BPDE chromophore is positive, which is in contrast to the negative sign displayed by the DNA bases. The absorption of the pyrene-like chromophore in the 310-350 nm region corresponds to an excitation of the second excited electronic state. This transition is polarized along the long symmetry axis of the pyrene chromophore which passes through the central carbon atoms and is oriented within the plane of the aromatic ring system<sup>24</sup> (see Fig. 1). These results indicate that the BPDE-DNA covalent complex is not of the intercalation type and that the plane of the aromatic moiety is not perpendicular to the long axis of the DNA helix. Referring to Fig. 5, it is possible to conclude unambiguously that  $\theta_{BPDE}$  is less than  $\sim 55^\circ$ . However, utilizing the absolute values of the reduced linear dichroism in table I and the appropriate expressions based on the discussion above, it is possible to narrow down the possible range of the orientation angle still further.

The narrowness of the vibronic bands in the  $\Delta A$  spectrum of BPDE bound to DNA, which compares well with the width of the absorption bands of free BPDE in a homogeneous solution, suggests that the linear dichroism is due to one major spectroscopic species of BPDE bound to DNA. The wavelength variation of  $\Delta A_\lambda/A_\lambda$  for BPDE-DNA thus arises because of the presence of other absorbing species of BPDE which contribute less to the linear dichroism spectrum, but give rise to a broadening of the absorption spectrum. Furthermore, the total absorbance measured in the 310-350 nm region contains contributions due to the DNA itself. While the absorbance of DNA itself is weak in this wavelength region, there is considerable light scattering because of the relatively large size of the DNA molecules. This light scattering effect contributes to the total effective absorbance of the sample, particularly at shorter wavelengths, since the light scattering power is proportional to  $\lambda^{-4}$ . The scattering term thus contributes an effective absorbance term  $A_1$  (DNA) in the denominator and an effective linear dichroism term  $\Delta A_1$  (DNA) =  $3/2 A_1$  (DNA)  $(3 \cos^2 \theta_1 - 1) f_1(E)$  term in the numerator. Here,  $A_1$  refers qualitatively to the overall scattering and absorbance of DNA. We denote the absorbance of BPDE by  $A_2$  (BPDE) and the linear dichroism by  $\Delta A_2$  (BPDE); both of these terms exhibit peaks at 327 and at 345 nm. If  $A_1$  (DNA) were zero at these wavelengths, the overall  $\Delta A/A$  would be independent of wavelengths (case I). The observed wavelength dependence of  $\Delta A/A$  shown in fig. 4 follows the spectrum of  $\Delta A_2$  (BPDE) ( $\propto A_2$  (BPDE)) since the presence of the  $A_1$  (DNA) terms in eq. 4 prevent the cancellation of the wavelength dependent  $\Delta A_2$  (BPDE) term in the numerator of eq. 4, while  $\Delta A_1$  (DNA) does not exhibit any structure in this wavelength region. Therefore, this situation, i.e. the wavelength dependence of  $\Delta A/A$ , is described by case III. Different forms of BPDE, with slightly different absorption spectra  $A_3$  (BPDE),  $A_4$  (BPDE) ....etc., and different  $\Delta A_3$  (BPDE),  $\Delta A_4$  (BPDE) ....etc. values (with  $\Delta A_3, \Delta A_4 < \Delta A_2$  because of different orientation angles  $\theta_2, \theta_4$ , etc.) also fall under case III and thus can also produce a wavelength dependence of  $\Delta A/A$ . These two effects, inhomogeneous broadening of the BPDE spectrum due to multiple sites (each displaying different orientation angles),

as well as the DNA scattering background, thus contribute to the wavelength dependence of  $\Delta A/A$ . Referring to the numerator of eq. (4), it is evident that if there is one dominant species, the linear dichroism spectrum  $\Delta A_\lambda$  will resemble its absorption spectrum. We assume that this is the case for the  $\Delta A_\lambda$  spectrum of the BPDE chromophore in Fig. 3b because of the narrowness of the  $\Delta A_\lambda$  spectrum which has the same width as the BPDE absorption spectrum in a homogeneous solution; we shall label the orientation angle of this dominant species by  $\theta_1$ , its absorbance by  $A_1$  and its extinction coefficient by  $\epsilon_1(\lambda)$ . The contributions of the other terms in the numerator of eq. (4) may be small for either of two reasons: (a) the orientation angles  $\theta_i$  of the species  $i = 2, 3, 4 \dots$  are close to  $55^\circ$ ; for this angle the orientation function is close to zero (Fig. 5). (b) the species  $i = 2, 3, 4 \dots$  are randomly oriented. The linear dichroism technique cannot distinguish between these two possibilities. With these assumptions, the reduced linear dichroism is given by

$$\frac{\Delta A_\lambda}{A_\lambda} = \frac{3}{2} \frac{(3 \cos^2 \theta_1 - 1) \epsilon_1(\lambda) c_1 f_1(E)}{\epsilon_1(\lambda) c_1} = \frac{\Delta A_1}{A_1} \frac{A_1}{\sum_i A_i} \quad (7)$$

Under these circumstances  $\Delta A_\lambda$  will reproduce the absorption spectrum of the oriented species due to the presence of the term  $\epsilon_1(\lambda)$  in the numerator. Furthermore, the observed reduced linear dichroism  $\Delta A_\lambda/A_\lambda$  will be a lower limit to  $\Delta A_1/A_1$  since

$$\frac{\Delta A_1}{\sum_i A_i} < 1.0 \quad (8)$$

and we can thus write

$$\frac{\Delta A_1}{A_1} > \frac{\Delta A_\lambda}{A_\lambda} \quad (9)$$

Therefore expression (3), together with equation (9), can be utilized to estimate upper or lower bounds of the angle  $\theta_1$ . Rearranging eq. (3) we obtain the following:

$$\cos^2 \theta_1 = \frac{1}{3} \left\{ 1 - \frac{(\Delta A_\lambda/A_\lambda)_{345}}{(\Delta A_\lambda/A_\lambda)_{DNA}} \right\} \quad (10)$$

where the reduced linear dichroism values for the BPDE and DNA are taken at 345 and 260 nm respectively and are presented in Table 1. The value at 345 nm is chosen since the oriented species of BPDE gives a maximum contribution to  $\Delta A$  at this wavelength and this value is therefore most reflective of the true orientation angle. It should thus be noted that when there is a heterogeneity of absorbing species, the angles should be evaluated at the highest absorption maxima of the oriented species, rather than at different wavelengths, as is usually done<sup>18,19</sup> when  $\Delta A_\lambda/A_\lambda$  is assumed to be constant as a function of wavelength.

Using the absolute values for the reduced linear dichroism for BPDE and DNA given in Table 1, the angle of  $\theta_1 \approx 35^\circ$  is obtained. Keeping in mind the inequality in equation(9), and the fact that the reduced linear dichroism values at 345 and at 260 nm have opposite signs, the value of  $\cos^2 \theta_1$  calculated in equation (10) is a lower bound and thus the calculated angle is an upper bound. We therefore conclude that the angle of orientation of the long, in-plane symmetry axis of the pyrene chromophore (Fig. 1) is given by

$$\theta_{BPDE} = \theta_1 \lesssim 35^\circ \quad (11)$$

The planes of the aromatic chromophore thus tend to be inclined parallel to the surface of a cone whose axis is that of the DNA helix and whose angle is  $35^\circ$  or less. This result was reproducible with four different samples of BPDE-DNA with the concentration of the BPDE moiety varying between 0.1 - 0.5% (based on the nucleotide concentration).

Estimation of the Orientation angle of BP in the BP DNA-Complex.

In order to further verify the validity of our approach to calculate the range of orientation angles for the BPDE-DNA complex, we used the same method to estimate the orientation angle of the BP molecule physically bound to DNA. Benzo(a)-pyrene, when physically bound to DNA, is believed to form an intercalation complex<sup>25</sup>. Since the transition moment vector in the 390-400 nm absorption region of BP lies within the plane of the aromatic ring, the angle  $\theta_{BP}$  should be close to  $90^\circ$ .

The  $\Delta A_\lambda$  spectrum for BP in the BP-DNA complex resembles the absorption spectrum of BP only qualitatively; there is a sharp peak at 394 nm, and a weaker one at 374 nm, corresponding to the absorption bands of BP bound to DNA. The  $\Delta A_\lambda/A_\lambda$  spectrum shown in Fig. 4 is wavelength dependent, indicating here also a heterogeneity of absorbing species. As expected for an intercalation model, the sign of  $\Delta A_\lambda$  for the DNA-bound BP is negative. This immediately indicates that  $\theta_{BP} > 55^\circ$  according to Fig. 5. Using the approach embodied in eq. (10) and the data in table I, the possible range of angles can be narrowed down still further. We obtain

$$\theta_{BP} \gtrsim 81^\circ \quad (12)$$

Keeping in mind that the value of  $\Delta A_\lambda/A_\lambda$  at 394 nm is a lower bound and that the signs of the reduced linear dichroism at 260 and at 394 nm are the same, the angle of  $81^\circ$  is a lower bound value, as indicated in eq. (12). Since such an angle is expected for the intercalation model of the physical binding of BP to DNA, this result supports the validity of the calculations for BPDE bound covalently to DNA.

### CONCLUSIONS AND SUMMARY

The electric linear dichroism spectrum of BPDE bound covalently to DNA shows that the pyrene ring system is not intercalated between the base pairs of DNA. A quantitative analysis of the data indicates that the plane of the pyrene-like BPDE chromophore lies on the surface of a cone, whose axis is that of the DNA helix and whose angle is  $35^\circ$  or less. This orientation is depicted in Fig. 6.

The validity of the quantitative analysis of the electric linear dichroism data, on which the above results are based, was verified by examining the linear dichroism spectra of the intercalation type complexes that are formed when either proflavine or benzo(a)pyrene are physically bound to DNA. The same method of approach yields an angle of  $90^\circ$  for the PF and  $\geq 81^\circ$  for the BP transition moment vectors, with respect to the long axis of the DNA helix. Since these transition moment vectors lie within the planes of the aromatic ring systems, these results are totally consistent with the intercalation model of binding for these physical complexes. These results are in striking contrast to those obtained when the identical method of linear dichroism and data analysis was applied to the covalent BPDE-DNA complex.

The variation of the reduced linear dichroism  $\Delta A_\lambda / A_\lambda$  with wavelength is an important criterion for establishing whether or not there is more than one species of chromophores whose absorption spectra, while different from each other, overlap in the same wavelength region. If there is only one oriented species among these, then the linear dichroism spectrum  $\Delta A_\lambda$  reveals the absorption spectrum of this species. Under these conditions only upper or lower bounds of the orientation angles can be determined.

Finally, we note that in these experiments our DNA samples were not sonicated to obtain shorter and more easily orientable DNA segments.<sup>18,19</sup> The DNA double strand may be weakened at the sites of covalent BPDE binding and thus breaks may occur preferentially at these sites. If this is the case then the conformation

of the BPDE moiety located at the end of such a DNA segment may be quite different from what it is in whole DNA. Since we were interested only in the relative linear dichroism at 260 nm due to the DNA bases and at 345 nm due to the BPDE chromophore, the overall extent of orientation of the DNA molecule<sup>27</sup> is not important. We have therefore attempted to avoid the ambiguities which may arise because of sonication of the high molecular weight calf thymus DNA used in our experiments.

ACKNOWLEDGEMENTS

We are grateful to Dr. R.G. Harvey for providing samples of BPDE (I).

We wish to thank Dr. J. Breton at Saclay for placing his dichrograph at our disposal and for stimulating discussions. We also wish to acknowledge helpful discussions with Drs. G. Paillotin, C.E. Swenberg and M. Pope. This investigation was supported by grant number CA20851-01 to N.E.G. and grant number CA-21111-01 to I.B.W., awarded by the National Cancer Institute, DHEW. Furthermore, partial support from an Energy Research and Development contract at the Radiation and Solid State Laboratory is gratefully acknowledged.



REFERENCES

1. D.M. Jerina, and J.W. Daly, *Science*, 185, 573-582 (1974).
2. A. Borgen, H. Darvey, N. Castagnoli, T.T. Crocker, R.E. Rasmussen, and I.Y. Wang, *J. Med. Chem.*, 16, 502-506 (1973).
3. P. Sims, P.L. Grover, A. Swaisland, K. Pal and A. Hewer, *Nature*, 252, 326-327 (1974).
4. P. Daudel, M. Duquesne, P. Vigny, P.L. Grover and P. Sims, *FEBS Letters*, 57, 250-253 (1975).
5. H.W.S. King, S.R. Osborne, F.A. Beland, R.G. Harvey and P. Brookes, *Proc. Natl. Acad. Sci. U.S.A.*, 73, 2679-2681 (1976).
6. V. Ivanovic, N.E. Geacintov, and I.B. Weinstein, *Biochem. Biophys. Res. Commun.*, 70, 1172-1179 (1976).
7. I.B. Weinstein, A.M. Jeffrey, K.W. Jennette, S.H. Blobstein, R.G. Harvey, C. Harris, H. Autrup, H. Kasai, and K. Nakanishi, *Science*, 193, 592-595 (1976).
8. P. Fulkrabek, S. Leffler, I.B. Weinstein, and D. Grunberger, *Biochemistry*, 16, 3127-3132 (1977).
9. S. Leffler, P. Fulkrabek, D. Grunberger, and I.B. Weinstein, *Biochemistry*, 16, 3133-3136 (1977).
10. W.T. Hsu, E.J.S. Lin, R.G. Harvey, and S.B. Weiss, *Proc. Natl. Acad. Sci. U.S.A.*, 74, 3335-3339 (1977).
11. T. Prusik, N.E. Geacintov, C. Tobiasz, V. Ivanovic and I.B. Weinstein, preceding paper.
12. K.W. Jennette, A.M. Jeffrey, S.H. Blobstein, F. Beland, R.G. Harvey, and I.B. Weinstein, *Biochemistry*, 16, 932-938 (1977).
13. A.M. Jeffrey, K.W. Jennette, S.H. Blobstein, I.B. Weinstein, F.A. Beland, R.G. Harvey, H. Kasai, I. Muira and K. Nakanishi, *J. Amer. Chem. Soc.*, 98, 5714-5715 (1976).
14. K. Nakanishi, H. Kasai, H. Cho, R.G. Harvey, A.M. Jeffrey, K.W. Jennette, and I.B. Weinstein, *J. Amer. Chem. Soc.*, 99, 258-260 (1977).
15. M. Korgeda, P.D. Moore, H. Yagi, J.C. Yen, and D.M. Jerina, *J. Amer. Chem. Soc.*, 98, 6720-6722 (1976).
16. A.M. Jeffrey, I.B. Weinstein, K.W. Jennette, K. Grzeskowiak, K. Nakanishi, R.G. Harvey, H. Autrup, and C. Harris, *Nature*, in press (1977).
17. E. Fredericq, and C. Houssier, "Electric Dichroism and Electric Birefringence", Clarendon Press, Oxford (1973).

REFERENCES (continued)

18. C.T. Chang, S.J. Miller, and T.G. Wetmur, *Biochemistry*, 13, 2142-2148 (1974).
19. R.P.F. Fuchs, J.F. Lefevre, J. Pouyat and M.P. Daune, *Biochemistry*, 15, 3347-3351 (1976).
20. N.E. Geacintov, T. Prusik and J.M. Khosrofian, *J. Amer. Chem. Soc.*, 98, 6444-6452 (1976).
21. J. Breton, M. Michel-Villaz, and G. Paillotin, *Biochem. Biophys. Acta.*, 314, 42-56 (1973).
22. K. Yamaoka and E. Charney, *Macromol.* 6, 66 - 76 (1973).
23. J. Ramstein, C. Houssier and M. Leng, *Biochem. Biophys. Acta.*, 335, 54-68 (1973).
24. R.S. Becker, I.S. Singh, and E.A. Jackson, *J. Chem. Phys.*, 38, 2144-2171 (1963).
25. J.C. Arcos, and M.F. Argus, *Advan. Cancer Res.*, 11, 305-471 (1968).
26. E. Charney, J.B. Milstein and K. Yamaoka, *J. Amer. Chem. Soc.* 92, 2657-2664 (1970).
27. R.W. Wilson and J.A. Schellman, *Biopolymers*, 16, 2143-2165 (1977).

TABLE 1.

Values of reduced linear dichroism  $\Delta A/A \sim 700$  Volt  $\text{cm}^{-1}$  5 mM cacodylate buffer,  $10^{-3}$  M DNA phosphate concentration, room temperature

<u>Sample</u>	<u>Wavelength</u>	<u><math>\Delta A/A</math></u>
DNA	260	$-2.8 \times 10^{-2}$
BPDE-DNA <sup>a</sup>	345	$+2.7 \times 10^{-2}$
PF-DNA <sup>b</sup>	460	$-2.8 \times 10^{-2}$
BP-DNA <sup>c</sup>	394	$-2.6 \times 10^{-2}$

<sup>a</sup>BPDE-DNA---covalent complex formed by reacting (+)-7 $\beta$ , 8 $\alpha$ -dihydroxy-9 $\alpha$ , 10 $\alpha$ -epoxy-7,8,9,10 tetrahydro benzo(a)pyrene in vitro with a modification of 0.1% (one BPDE molecule bound per 1000 nucleotides). The reproducibility with 3 other samples was found to be within 10% of the value given.

<sup>b</sup>PF-DNA----physical proflavine DNA complex

<sup>c</sup>BP-DNA----physical benzo(a)pyrene DNA complex

FIGURE CAPTIONS

Fig. 1. Structure of (+)-7 $\beta$ , 8 $\alpha$ -dihydroxy-9,10-epoxy-7,8,9,10-tetrahydrobenzo(a)-pyrene (BPDE). The heavy arrow indicates the transition moment vector of the 310-350 nm absorption band.

Fig. 2. Typical Voltages and linear dichroism signals (oscilloscope tracings).

- A. Voltage  $V_0$  without cell connected (3 ms pulse duration).
- B. Effective voltage ( $V_E$ ) with cell connected. At the beginning of the pulse there is a 30% voltage drop ( $V_E \approx 0.7 V_0$ ) the effective voltage decreases further to  $V_E = 0.40 V_0$ . The effective voltages  $V_E$  given in Fig. 3 represent the values taken approximately halfway between the maximum and minimum values of  $V_E$ . Sample: covalent BPDE-DNA complex, 0.5% modification,  $A_{260}/m\ell = 4.1$  in 5 mM sodium cacodylate buffer, pH = 7.1 Cell resistance: 300 $\Omega$
- C. Linear dichroism signal at 292 nm (due to DNA)  $\Delta A$  is negative. Same sample as in B;  $V_E \approx 200$  Volt.
- D. Linear dichroism signal at 345 nm (due to the pyrene-like chromophore attached to the DNA). Same sample as in B. Dichrograph sensitivity is five times greater than in B above.

Fig. 3 BPDE-DNA;  $A_{260} = 10/m\ell$  (one BPDE/1000 bases)  
BP-DNA;  $A_{260} \approx 6.0/m\ell$  ( $\approx$  one BP/1000 bases)  
PF-DNA;  $A_{260} \approx 10.0/m\ell$  ( $\approx$  7 PF/1000 bases)  
All samples were dissolved in 5 mM cacodylate buffer. (The above abbreviations are explained in Table 1).  
 $V_E \approx 200$  Volts (the effective voltage is defined in the legend of Fig. 2).  
Cell resistance: 300 $\Omega$ .  
(A) Absorption spectra (A) of covalent BPDE-DNA complex (BPDE-DNA)———;  
BPDE in ethanol - - - - -; physical complex of benzo(a)pyrene in DNA (BP-DNA) .....; proflavine-DNA complex (PF-DNA)-----.  
(B) Linear dichroism ( $\Delta A$ ) spectra;  $\approx 700$  Volts  $cm^{-1}$ ; 5 mM cacodylate buffer solution.  
(In both (A) and (B) the BPDE-DNA solutions were diluted in order to make measurements in the DNA absorption region of 240-300 nm).  
(The vertical scales are in arbitrary units).

Fig. 4 Reduced linear dichroism spectra for the DNA complexes shown in Fig. 3;  $\Delta A/A$  is in relative units.

Fig. 5 The orientation function defined in equation (2), plotted as a function of the orientation angle  $\theta$ .

Fig. 6 Model of orientation of the in-plane axis of DNA-bound BPDE (axis defined in Fig. 1).

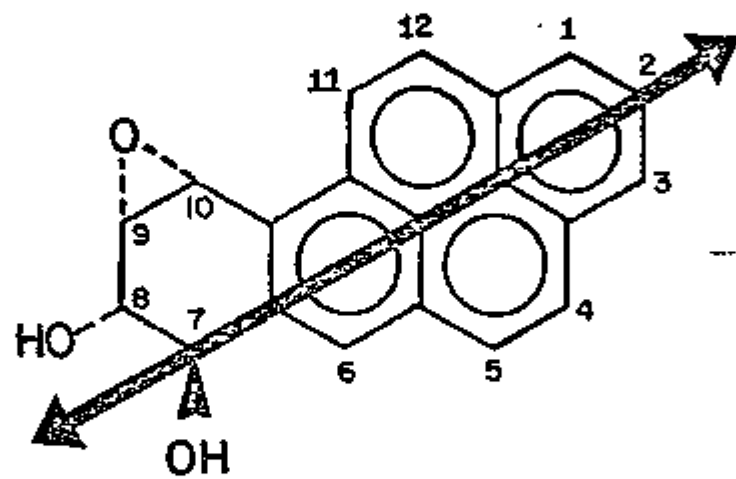


Fig. 1 Gescintov et al

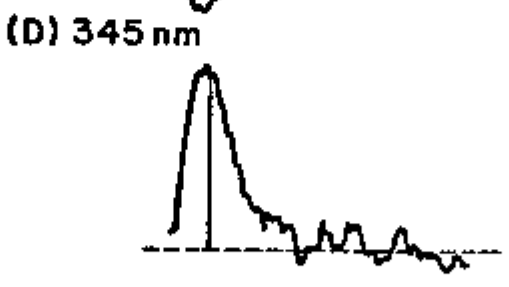
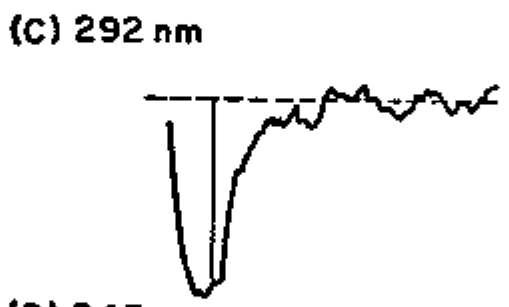
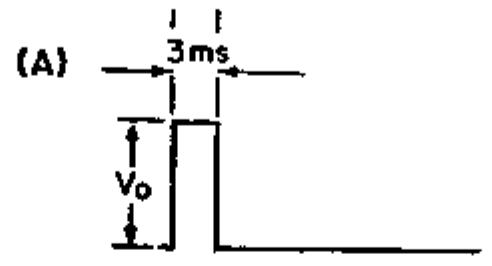


Fig. 2 Geacintov et al

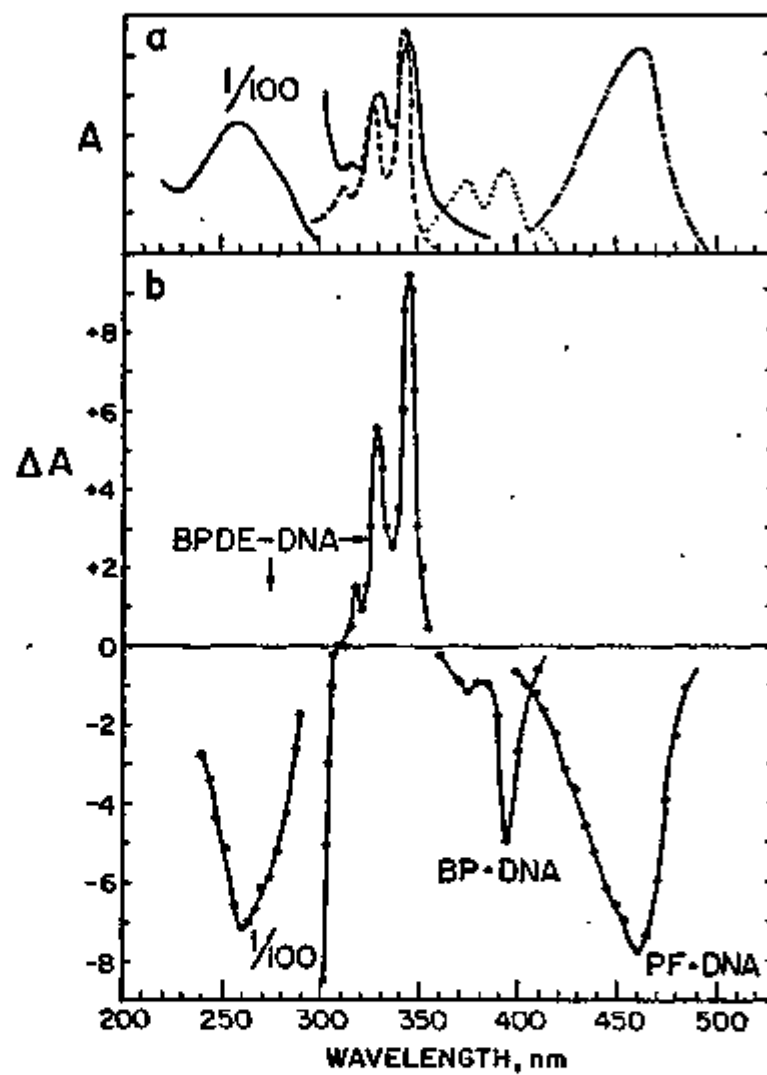


Fig. 3 Geacintov et al

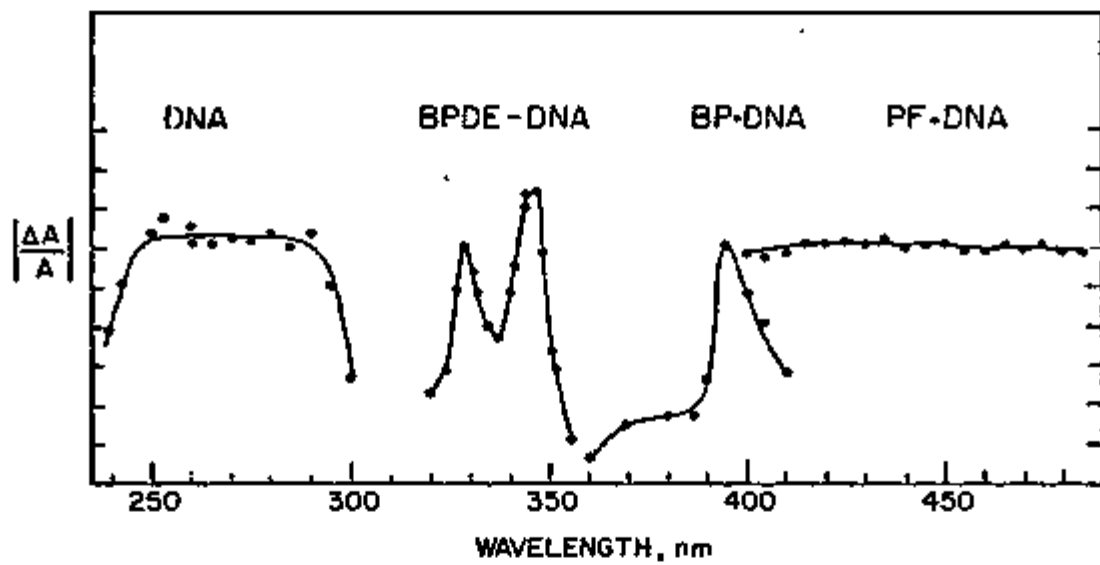


Fig. 4 Geacintov et al



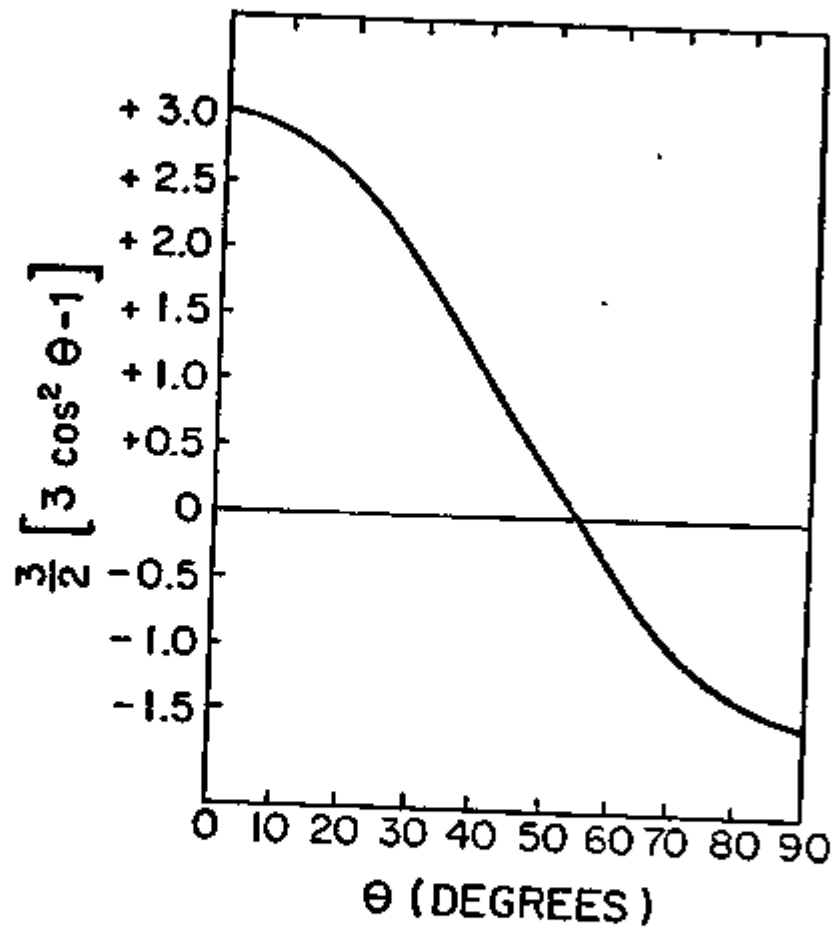


Fig. 5 Geacintov et al

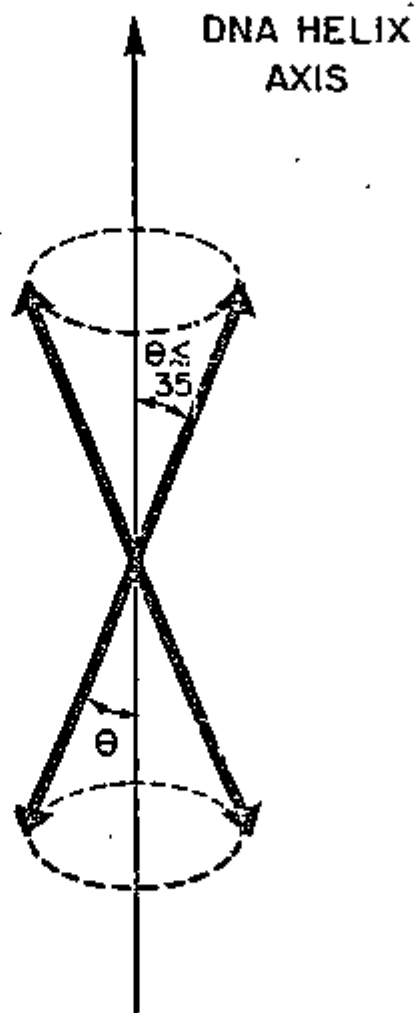


Fig. 6 Geacintov et al

Note, delete by pher

6700 R.R.

PN 4725  
0068

RADIATION RESEARCH II, III-III (1978)

## $\alpha$ -Particle-Induced Radical Production in Anthracene Beyond the Bragg Peak

H. T. HU,<sup>1</sup> S. ARNOLD,<sup>1</sup> AND M. POPE<sup>1,2</sup>

<sup>1</sup>Radiation and Solid State Laboratory<sup>1</sup> and Chemistry Department,<sup>2</sup>  
New York University, New York, New York 10003

HU, H. T., ARNOLD, S., AND POPE, M.  $\alpha$ -Particle-Induced Radical Production in Anthracene beyond the Bragg Peak. *Radiat. Res.* 74, 521-530 (1978).

Triplet excitons are used as a sensitive probe for the spatial distribution of paramagnetic defects (exciton sounding). Following  $\alpha$ -particle (12-30 MeV) bombardment of an anthracene crystal, a remarkably long tail (supertail) of paramagnetic defects (free radicals) was found, extending into the crystal for a distance of about six times that of the Bragg peak. Evidence is presented that of all possible mechanisms for this supertail, only recoil protons can account quantitatively for the observed spatial distribution. A model calculation indicates that the proton-induced radical yield is about five times that for  $\alpha$  particles. The limitations of this model are discussed.

### INTRODUCTION

In our previous work anthracene crystals were irradiated by  $\alpha$  particles moving in a direction perpendicular to *ab* plane (1). The spatial distribution of residual damage was measured by triplet exciton sounding (1). The results showed ranges for  $\alpha$  particles at 30.00 and 32.36 MeV in good agreement with the Bragg additivity rule. From the magnetic field effect on the triplet exciton lifetime (2), it was shown that the defects that quenched the triplet excitons were principally paramagnetic and that the G value for their production was about 0.02. At high radiation fluences of  $10^{22}$  cm<sup>-2</sup>, radicals were observed in a long tail extending far beyond the Bragg peak. Several hypotheses were proposed to explain these tails. The hypotheses may be divided into two categories: One involves the participation of secondary radiation which causes damage through its energy degradation and the other involves enhanced radical diffusion which allows the radicals to move beyond the  $\alpha$ -particle range in channels created, for example, by recoil protons. Long-range damage would be expected from any of the following secondary radiation.

- (a) recoil protons.
- (b)  $\gamma$  radiation and neutrons arising from resonance excitation of carbon.
- (c) bremsstrahlung from secondary electrons,  $\alpha$ -particles, and secondary protons.

0033-7587/78/0742-1111\$02.00/0

Copyright © 1978 by Academic Press, Inc.

All rights of reproduction in any form reserved.

In addition, although the  $c'$  direction is not a channeling direction in anthracene (3), channeling may assist paraxial secondary charge particles in moving farther than they could in an amorphous medium.

In order to study the damage mechanism underlying these long tails, we have made two different types of measurement.

I. The distribution of radicals within the tails was measured as a function of the incident energy of the  $\alpha$  particles.

II. The damage profiles were measured in a series of planes perpendicular to the  $\alpha$ -particle beam, these planes being situated at various distances from the irradiated surface.

The first set of experiments provided a way to distinguish enhanced radical diffusion from proton recoil or nuclear radiation. As Davies and Jespersgard (4) have shown in the case of implantation supertails in tungsten, the diffusion mechanism is expected to give exponential tails with a decrement controlled by the concentration of point defects. Therefore one would expect the length of the tails to be relatively independent of the  $\alpha$ -particle energy. In addition the energy dependence can provide useful information about the relative roles of proton recoil and nuclear radiation. Since nuclear excitation is a resonant phenomenon its energy dependence should be more abrupt than that of proton recoil.

The measurement of the lateral profile of damage in the tail gives useful information on the role of bremsstrahlung and the channeling of secondary particles. Since the probability for the emission of bremsstrahlung is known to be highest in a direction  $90^\circ$  from that of the incident beam, one would expect less damage in the forward direction than to the side. In addition, since channeling is known to take place in the  $c$  direction, which is  $34^\circ$  from the incident direction of the  $\alpha$  particles, one would expect channeling to steer the tail toward the  $c$  direction.

In what follows we will show that the primary mechanism responsible for these tails is energy deposited by secondary protons.

#### EXPERIMENTAL PROCEDURE

A detailed description of the crystal preparation, experimental setup for irradiation, and the apparatus used for radiation damage detection is given in the previous work (1). Only a brief description of the experimental procedures is given here.

The anthracene crystals used for irradiation were  $ac'$  crystal plates of anthracene typically 5 mm square in the  $ac'$  plane and 1 mm thick. The triplet exciton lifetime of the unirradiated sample was typically 21 msec. The energies of the  $\alpha$  particles were 12, 20, and 30 MeV. The number of  $\alpha$  particles absorbed were  $1.95 \times 10^{12} \text{ cm}^{-2}$  for both the 12- and 20-MeV irradiation. Two irradiations were carried out at 30 MeV with fluences of  $3.91 \times 10^{12}$  and  $1.74 \times 10^{12} \text{ cm}^{-2}$ . The  $\alpha$  particles were directed perpendicularly to  $ab$  plane (i.e., along the  $c'$  direction). The primary region of damage extended over the entire thickness of the  $ac$  plate and was either 2 or 4  $\mu\text{m}$  in length along the  $a$  direction.

The two experiments described in the Introduction were carried out as follows: The method of exciton sounding was used to determine the spatial distribution of damage within the tail as function of incident  $\alpha$ -particle energy. This method utilizes the quenching of triplet excitons by crystal defects in order to determine the defect densities. In the presence of an applied magnetic field, this method also discriminates between paramagnetic and nonparamagnetic defects; such a field is known to reduce the paramagnetic quenching process in a predictable way (2).

The quenching of triplet excitons by defects is determined by measuring the triplet exciton lifetime;  $\beta^{-1}$ ; in general  $\beta$  is increased from its intrinsic value  $\beta_0$  in the presence of defects. The change in  $\beta$ , with radiation,  $\Delta\beta$ , is given by

$$\Delta\beta = \beta - \beta_0 = \bar{\gamma}_p N_p + \sum \gamma_{ni} N_{ni} \quad (1)$$

where  $\bar{\gamma}_p$  and  $N_p$  are the average quenching rate and density of paramagnetic defects, and  $\gamma_{ni}$  and  $N_{ni}$  are the quenching rate and density of nonparamagnetic defects of the  $i$ th type. In our particular case as will be indicated by the results, the second term may be neglected since the triplet excitons are quenched almost entirely by paramagnetic defects. Therefore,  $\Delta\beta$  is essentially proportional to the density of paramagnetic quenchers.  $\beta$  is calculated from the decay rate of the luminescence produced when triplet excitons annihilate. This light, known as delayed fluorescence (DF) has a decay rate which is  $2\beta$ .

The method of exciton sounding is implemented by generating excitons in a small region of the crystal. This is accomplished by focusing the light from a He-Ne laser at 6328 Å with a spherical or cylindrical lens. The focal lengths of these lenses were 240 and 50 mm, respectively. A faithful representation of the spatial distribution of the defect densities can only be accomplished if the decay of the triplet excitons is kinetically first order. The DF under these conditions is proportional to  $I^2$ , where  $I$  is the light intensity. To remove the perturbations due to bimolecular quenching from the defect profiles the laser intensity must be lowered so that  $DF \propto I^2$ . The DF was measured by single photon counting. Since the spherical lens excited a volume of the crystal which is one-fifth of the volume excited by the cylindrical lens, one must lower  $I$  for the spherical case below that for the cylindrical case in order to eliminate bimolecular effects. Such attenuation produces luminescence within the dark count. However, since point discrimination by the spherical lens is often required for qualitative information, the results obtained with this lens were not carried out entirely in the region where  $DF \propto I^2$  and therefore can only be used for qualitative information such as angular symmetries. The information arrived at from such data are discussed in Results.

The effects of a magnetic field on the delayed luminescence were measured with a field of 3,000 G at the so-called resonance direction in the  $ac$  plane (2).

## RESULTS

Figure 1 shows the spatial variation of exciton decay rates,  $\Delta\beta$ , as a function of position from the irradiated surface for anthracene crystals irradiated at 12, 20, and 30 MeV. All of these measurements were carried out with the cylindrical

$\alpha$ -INDUCED RADICALS IN ANTHRACENE

111

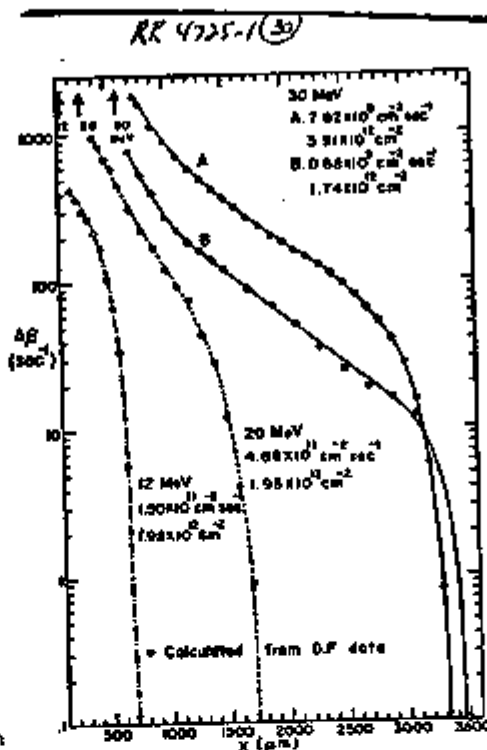


Fig. 1. The change in  $\beta$  for the samples irradiated at 12, 20, and 30 MeV. The dose rate and total absorbed dose are listed underneath the corresponding  $\alpha$ -particle energy. Distance  $X$  in micrometers is measured along the direction of the  $\alpha$ -particle beam. The range of the  $\alpha$  particles at each energy is indicated on the upper left hand of this figure.

lens. The transient lifetime of the delayed fluorescence was not measured in the region of the Bragg peak due to low luminescence in this region. However,  $\Delta\beta$ 's in this region may be estimated from the steady-state DF. Since  $\beta$  is proportional to the inverse square root of the steady-state luminescence,  $F^{-1}$ ,  $\Delta\beta$  is therefore proportional to  $\Delta(F^{-1})$ . The first several points on each curve were estimated values. As one can see  $\Delta\beta$  falls off gradually with increasing distance from the Bragg peak and then falls abruptly to zero at a position  $X_n$ . At 30 MeV this position appears to be relatively independent of particle current density. Two experiments were performed at 30 MeV as shown in Fig. 1 and although the particle current density was varied over almost an order of magnitude the values of  $X_n$  were within 3% of each other.

Figure 2 shows the lateral distribution of damage within the tail for an irradiation at 30 MeV. All measurements in this figure were carried out with the spherical lens. The lateral damage has its greatest contribution along the symmetry axis of the  $\alpha$  beam and falls off to either side. The centroids of the curves show less than 3° angular displacement as measured from the symmetry axis.

The magnetic field effect on the transient decays was measured at the resonance direction in the  $ac'$  plane at 3000 G. If  $\beta(H)$  and  $\beta(0)$  are the triplet exciton decay rates in the presence and absence of the magnetic field, respectively, then  $\beta(H)/\beta(0)$  is found to be 0.093 for points at which  $\beta \gg \beta_0$ . This value is

RR 4725-2 (30)

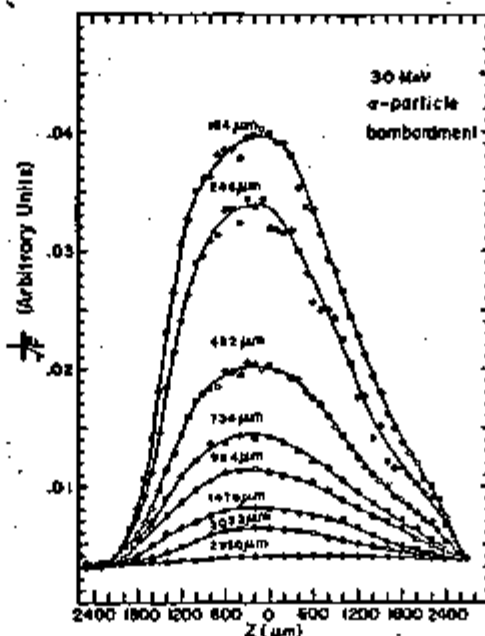


FIG. 2. Lateral distribution of the  $\alpha$ -particle beam; other values of  $z$  on either side of  $z = 0$  represent distances in a direction perpendicular to the  $\alpha$ -particle beam. Each curve represents results obtained at different distances from the position of the Bragg peak; the distances are indicated above each curve.  $P$  is the steady-state luminescence in arbitrary units.  $E_\alpha = 30$  MeV.

very close to our previously obtained values for this ratio for damage within the  $\alpha$ -particle range; as was shown, most of the quenching centers are paramagnetic (1).

RR 4725-3 (30)

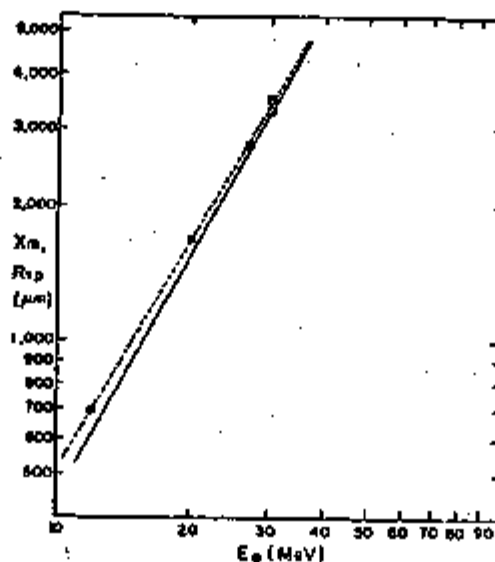


FIG. 3. Comparison of experimental,  $X_m$ , with calculated values.

of radical production (2)].

## DISCUSSION OF RESULTS

Since the values of  $\Delta\beta$  fall abruptly to zero at  $X_m$  as shown in Fig. 1, it is unlikely that photons play a major role in the production of these radicals in the region of  $X_m$  since photon intensities are attenuated exponentially.

In particular the role of bremsstrahlung in defect production should be small since Fig. 2 shows a maximum density of radicals along the beam axis which is contradictory with the mechanism of bremsstrahlung since the cross section for production of these photons is a minimum in the forward direction. In addition channeling should be unimportant in explaining the observed effect since the channeling direction is  $34^\circ$  from the symmetry axis and the centroids in Fig. 2 show less than a  $3^\circ$  angular displacement from the symmetry axis. Of course, charged particles could arise from resonance excitation; however, this is unlikely in the energy range being investigated since  $X_m$  appears to change gradually with  $E_\alpha$ , exhibiting no distinct structure. Figure 3 shows a plot of  $X_m$  versus  $E_\alpha$ . As one can see, the dependence of  $X_m$  on  $E_\alpha$  fits a power law (illustrated by the dashed line in the figure) of the following analytic form

$$X_m = 9.66(E_\alpha)^{1.72}, \quad (2)$$

where  $X_m$  is given in micrometers ( $\mu\text{m}$ ) for energy  $E_\alpha$  in millionelectron volts (MeV). The 1.72 power in Eq. (2) is suggestive of the penetration by a heavy charged particle with energy to mass ratio of several McV/amu for which the typical exponent (5) is  $\sim 1.8$ . The fact that  $X_m$  is measured from the irradiated surface implies that the charged particles responsible for radical production at  $X_m$  originate at the irradiated surface. Recoil protons, and carbon ions will be produced at the surface; however, in order that the recoils produced at the surface have the largest depth of penetration, the ratio of the recoil range to the  $\alpha$ -particle range must be greater than one. For carbon recoils this ratio is less than one. The range of protons  $R_p$  of energy  $E_p$  in anthracene can be expressed in terms of the following semiempirical equation (6):

$$R_p = 15.2E_p^{1.81}, \quad (3)$$

Since  $E_p = 4m_p m_\alpha E_\alpha / (m_p + m_\alpha)^2$  the range of forward-projected secondary protons  $R_{sp}$  leaving the front surface is then

$$R_{sp} = (15.2) \left[ \frac{4m_p m_\alpha}{(m_p + m_\alpha)^2} \right]^{1.81} E_\alpha^{1.81} = 6.78E_\alpha^{1.81}, \quad (4)$$

Figure 3 illustrates the good agreement between the experimental values of  $X_m$  and the range of recoil protons as given by Eq. (4) (the solid line in Fig. 3). Further useful information can be gained by a comparison between the shape of the  $\Delta\beta$  profiles and a computer simulation of the density of energy deposited along the symmetry axis. The density of energy deposited by recoil protons,  $d\rho$ , at a point of  $X$  on the symmetry axis, originating from a volume  $dV$  at position  $\vec{r}$ , (see Fig. 4) may be written as

$$d\rho_E = F_\alpha N_H \frac{d\sigma_{sp}(E_\alpha, \phi)}{d\Omega} \frac{dE_{sp}(E_{sp}, r)}{dr} \frac{dV}{r^2}, \quad (5)$$



where  $F_\alpha$  is the  $\alpha$ -particle flux,  $N_H$  is the density of hydrogen atoms in the crystal,  $d\sigma_{pn}(E_\alpha, \phi)/d\Omega$  is the cross section for proton recoils,  $dE_{pn}(E_\alpha, r)/dr$  is the energy loss at position  $X$  by protons originating from  $dV$  with energy  $E_\alpha$ , and  $r$  is the distance from the volume element to the position  $X$ . Therefore the overall density of energy deposited at  $X$ ,  $\rho_E$ , is given by the integration of Eq. (5), where the integration is carried out numerically over all source volumes. In order to establish the  $\alpha$ -particle energies as a function of penetration depth, the stopping powers for  $\alpha$  particles were obtained by using the Bragg additivity rule and the stopping powers for carbon and hydrogen (7). The stopping powers of protons in anthracene were calculated also by the Bragg additivity rule with appropriate data for carbon and hydrogen. Stopping power values were taken from Northcliffe (7) below 12 MeV and from Marion (8) between 12 and 20 MeV. Since the center of mass energy exceeds the He Coulomb barrier, the differential cross section  $d\sigma_{pn}/d\Omega$  was calculated using an attractive nuclear potential in addition to a Coulomb potential. Accordingly, these cross sections were arrived at by solving for the  $S$  matrix using the following optical-model potential (9):

$$U(r) = U_{CN}(r) + U_{SO}(r) + U_{Coul}(r), \quad (6)$$

where  $U_{CN}$  and  $U_{SO}$  are the (complex) nuclear and spin-orbit potentials, respectively, and  $U_{Coul}$  is the Coulomb potential. The parameters in the above potential were taken from fits to proton scattering experiments at 31 MeV (10). The calculation of the energy density from Eq. (5) for a 30-MeV  $\alpha$ -particle fluence of  $3.91 \times 10^{12} \text{ cm}^{-2}$  is shown in Fig. 5. As one can see, the computer simulated profile of the energy deposited along the symmetry axis is similar to the  $\Delta\beta$  profile at the same energy. The 3% difference in cutoff depth between theory and experiment is in agreement with the semiempirical range-energy formula and could be due to the failure to include the effects of straggling.

Also shown in Fig. 5 is the energy density versus depth based on a Rutherford cross section [i.e., only  $U_{Coul}(r)$  in Eq. (6)]. As one can see by comparison of this

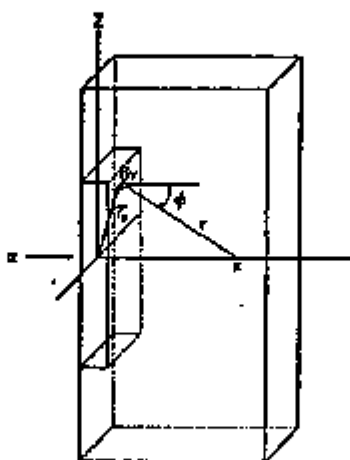


FIG. 4. The coordinate system of protons and  $X$  their destination.

is of the differential source

RR 4735-4 (30)

$\alpha$ -INDUCED RADICALS IN ANTHRACENE

111

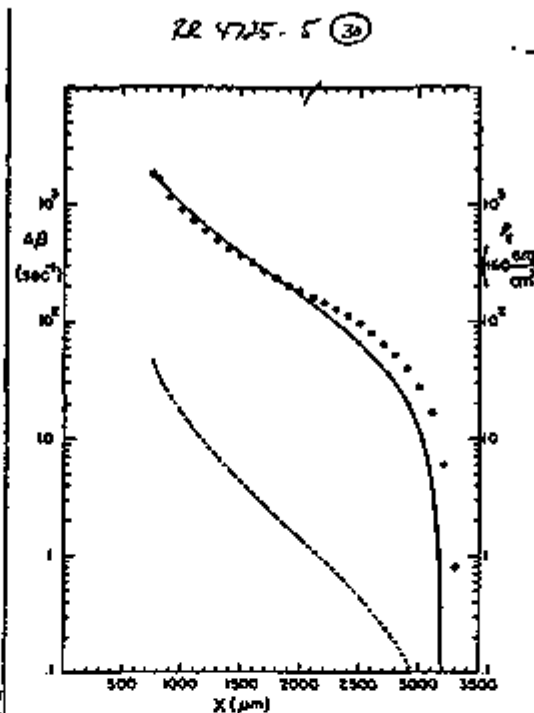


FIG. 5. Comparison of the exciton decay rate  $\Delta\beta$  (sec<sup>-2</sup>) and the particle current density  $I$  (cm<sup>-2</sup>) versus distance  $X$  ( $\mu$ m). The broken curve represents the energy density profile based on a Rutherford cross section alone.

line) and the triplet with a fluence and a  $\beta$  activity. The broken curve represents the energy density profile based on a Rutherford cross section alone.

curve with the one corresponding to the full potential, Coulombic scattering plays a minor role in contributing to the energy deposited. This fact which is key to the occurrence of the tails will be discussed below.

Although the yield  $Y$  (radical density per unit energy density) versus energy is not known for protons, one can get some idea of the average yield in the tails. We define the average yield  $\bar{Y}$  as

$$\bar{Y} = \int Y N_p dx / \int N_p dx = \bar{\gamma}_p^{-1} \int \left( \frac{\Delta\beta}{\rho E} \right) \Delta\beta dx / \int \Delta\beta dx, \quad (7)$$

where  $Y$  is  $N_p \rho E^{-1}$  and  $N_p$ , the density of paramagnetic defects is given from Eq. (1) as  $\bar{\gamma}_p^{-1} \Delta\beta$ . Using the computer-simulated energy density profiles along with the corresponding data in Fig. 1 and integrating out to 2500  $\mu$ m where the straggling should be unimportant, we obtain a value for  $\bar{\gamma}_p \bar{Y}$  of  $6.1 \times 10^{-1}$  cm<sup>2</sup>/erg-sec. Using a value of  $10^{-11}$  cm<sup>2</sup>/sec for  $\bar{\gamma}_p$  ( $J$ ), the average yield  $\bar{Y}$  is then  $6.1 \times 10^9$ /erg. This yield is approximately five times larger than the corresponding yield for  $\alpha$  particles and would imply that protons are more effective in producing radicals. In addition the yield  $Y$  appears to increase with decreasing proton energy. However, although this may indeed be the case, some caution must be exercised in taking these conclusions literally. The most tenuous assumption in our calculations is that the optical model parameters are independent of energy. Although this assumption is necessitated by lack of explicit data at other energies, one would expect terms in Eq. (6) such as the complex part of the central nuclear

potential,  $\text{Im}[U_{\text{CH}}(r)]$ , to be influenced by the available energy (11) since this potential describes absorption into channels other than elastic scattering (12).

The supertails found in the present work appear to be a general property of the interaction of heavy ions with organic matter. The fraction of the initial energy in the secondary proton channel at 30 MeV is  $\sim 10^{-3}$ . The relative efficiency with which other ions produce tails will depend heavily on the cross section for generating recoils. Efficiencies as high as 0.1% for ions having velocities of  $\sim 8$  MeV/amu are a consequence of nuclear scattering and therefore will depend on the individual nuclear potentials.

The most important conclusion of the present work is that the supertails found in the induced radical production have their origin primarily in damage by recoil protons.

#### ACKNOWLEDGMENTS

We are grateful to Dr. E. Auerbach of the Brookhaven National Laboratory for calculating the differential cross section used in this work. We would like to thank the members of the Tauden Van de Graff Group at Brookhaven for making available to us the accelerator facility used in this work. Our thanks also go to Professors W. Brandt and H. Laubert of New York University for their useful suggestions. This work was supported by the Energy Research and Development Administration.

RECEIVED: August 22, 1977

#### REFERENCES

1. E. ARNOLD, H.-T. HU, and M. POPE, Exciton sounding of  $\alpha$ -particle induced radiation defects in anthracene. *Mol. Cryst. Liq. Cryst.* 36, 179-192 (1976).
2. V. ERN and R. E. MENEFILLO, Magnetic field effect on triplet exciton quenching in organic crystals. *Phys. Rev. Lett.* 21, 609-611 (1968).
3. W. BRANDT, H. DOBBIN, H. JACK, JR., H. LAUBERT, and S. ROTM, Channeling studies through characteristic radiations. *Can. J. Phys.* 46, 537-542 (1968).
4. J. A. DAVIES and P. JENSENSON, Anomalous penetration of xenon in tungsten crystals—A diffusion effect. *Can. J. Phys.* 44, 1631-1638 (1966).
5. J. B. BIRKS, In *Theory and Practice of Scintillation Counting* (J. B. Birks, Ed.), pp. 18-20. Pergamon, Oxford, 1961.
6. G. FRIEDLANDER, J. W. KENNEDY, and J. M. MILLER, In *Nuclear and Radiochemistry*, (G. Friedlander, J. W. Kennedy, and J. M. Miller, Eds.), 2nd ed., pp. 94-98. Wiley, New York, 1964.
7. L. C. NORRCLIFF and R. F. SCHULLING, Range and stopping-power tables for heavy ions. *Nucl. Data Tables A7*, 233-464 (1976).
8. J. B. MARION and P. C. YOUNG, In *Nuclear Reaction Analysis Graphs and Tables* (J. B. Marion and P. C. Young, Eds.), pp. 15-18. Wiley, New York, 1968.
9. J. S. NOBYK, C. B. DAVIS, and M. A. MELKANOFF, Optical-model analysis of elastic scattering of protons on carbon at intermediate energies. *Phys. Rev.* 125, 975-987 (1962).
10. S. M. BUNCH, H. H. FOSTER, and C. C. KIM, Interactions of 31 MeV protons with He<sup>1</sup>. *Nucl. Phys.* 53, 241-251 (1964).
11. C. M. PERLY and F. G. PERCY, Compilation of phenomenological optical-model parameters. *At. Data Nucl. Data Tables* 17, 1-101 (1976).
12. I. ULEHRA, L. GOMOLEK, and Z. PUGHAR, In *Optical Model of the Atomic Nucleus* (I. Ulehra, L. Gomolek, and Z. Puhar, Eds.), pp. 59-91. Academic Press, New York, 1964.